A STUDY OF BONDING MECHANISMS AND CORROSION BEHAVIOUR OF COLD SPRAYED COATINGS

Tanvir Hussain, MSc

Thesis submitted to the University of Nottingham

for the degree of Doctor of Philosophy

January 2011

Abstract

Cold gas dynamic spraying (CDGS) is a material deposition technique, in which powder particles are accelerated to speeds of between 300-1200 m/s and upon impact deform plastically and adhere. The overall aims of this research project were to understand the bonding behaviour in cold spraying of copper, aluminium and titanium, and to produce corrosion resistance barrier layer of titanium coatings using cold spraying.

The mechanism of bonding in cold spraying is still a matter of some debate. In this thesis, copper has been cold sprayed onto aluminium alloy substrates, the surfaces of which had been prepared in a variety of ways. The coating - substrate bonding was assessed via a novel intermetallic growth method along with adhesive pull-off testing. The bond strength has been rationalised in terms of a modified composite strength model, with two operative bonding mechanisms, namely (i) metallurgical bonding and (ii) mechanical interlocking of substrate material into the coating. In most cases, mechanical interlocking is able to account for a large proportion of the total bond strength, with metallurgical bonding only contributing significantly when the substrate had been polished and annealed prior to spraying. In addition, grit-blasting has been shown to significantly reduce the bond strength compared to other substrate preparation methods. Aluminium has also been cold sprayed onto copper substrates, the mechanical interlocking of substrate material was not observed and the bond strength was relatively low. Titanium particles have been deposited onto three different steel substrates, namely low carbon steel, an Armco iron, and an austenitic stainless steel. Using the novel intermetallic growth method it was found that a barrier does exist at the interface of the titanium deposited onto the low carbon steel and Armco iron substrates which is not removed in either of the

stages of impact or during the heat treatment process. On the other hand, in the case of titanium deposited onto the austenitic stainless steel, the barrier is removed.

Cold spraying is believed to have the potential for the deposition of corrosion resistant barrier coatings. However, to be effective, a barrier coating must not have interconnected porosity. Titanium coatings were sprayed using nitrogen as an accelerant gas at two process gas temperatures of 600 and 800°C to reduce porosity. A modified in-situ grit blasting was used to improve the coating-substrate adhesion. The mean bond strength of the titanium deposits was ~70 MPa and tensile strength was 250 MPa. Mercury intrusion porosimetry (MIP) was used to characterize the interconnected porosity over a size range of micrometers to nanometers. The MIP results showed that in cold sprayed deposits a significant proportion of the porosity was sub-micron and so could not be reliably measured by optical microscope based image analysis. A set of free standing deposits was also vacuum heat treated to further decrease porosity levels.

The effect of porosity on the corrosion behaviour of titanium coatings onto carbon steels was investigated in 3.5 wt.% NaCl. The electrochemical measurements of the coatings showed significant substrate influence when the interconnected porosity of the coating was 11.3 vol.% but a decreased substrate influence with a porosity level of 5.9 vol.%. Salt spray (fog) tests confirmed these electrochemical findings and showed the formation of corrosion products following 24-h exposure. Laser surface melting (LSM) was used to seal the top ~140 μm of the coating to eliminate any interconnected porosity. The LSM titanium coatings showed no sign of corrosion after 100-h of salt spray tests, and the open circuit potential and passive current density values were similar to those of the bulk titanium.

Journal Publications

- Hussain, T., McCartney, D.G., Shipway, P.H., and Zhang, D., Bonding Mechanisms in Cold Spraying: The Contributions of Metallurgical and Mechanical Components. Journal of Thermal Spray Technology, 2009. 18(3): p. 364-379
- Hussain, T., McCartney, D., Shipway, P., and Marrocco, T., Corrosion Behavior of Cold Sprayed Titanium Coatings and Free Standing Deposits. Journal of Thermal Spray Technology, 2011. 20(1-2): p. 260- 274
- Marrocco, T., Hussain, T., McCartney, D., and Shipway, P., Corrosion performance of laser post-treated cold sprayed titanium coatings. Journal of Thermal Spray Technology, 2011. *(Accepted)*
- Hussain, T., McCartney, D., and Shipway, P., Impact and Bonding Behaviour in Cold-spraying of Titanium onto Various Steel Substrates. Surface and Coatings Technology, *(Under review)*

Publication on the research area but not included in this thesis:

- Li, J.F., Agyakwa, P.A., Johnson, C.M., Zhang, D., Hussain, T., and McCartney, D.G., Characterization and Solderability of Cold Sprayed Sn-Cu Coatings on Al and Cu Substrates. Surface and Coatings Technology, 2010. 204(9-10): p. 1395-1404

Conferences

- Hussain, T., McCartney, D., Shipway, P., and Marrocco, T., Metal deposition for repair of titanium based components using cold gas dynamic spraying, Gas Turbines: High Temperature Coatings and Life Extension, 9-10 Dec 2009, (London, UK),The Institute of Materials, Minerals and Mining *(Oral presentation)*
- Hussain, T., McCartney, D., Shipway, P., and Marrocco, T., Effect of Heat Treatment on Porosity and Corrosion Performance of Cold Sprayed Titanium Deposits. Thermal spray: Global Solutions for Future Application, Marple, B. R., Agarwal, A., Hyland, M. M., Lau, Y. -C., Li, C.-J., Lima, R. S., and Montavon, G., Eds., 3- 5 May 2010, (Singapore), ASM International, CD- ROM, p. 393-399
- Marrocco, T., Hussain, T., McCartney, D., and Shipway, P., Corrosion performance of laser post-treated cold sprayed titanium coatings, TSS: Cold Spray Conference, 27 – 28 Sep 2010, (Akron, Ohio USA), ASM International *(Poster presentation)*

Publication on the research area but not included in this thesis:

- Marrocco, T., Harvey, D., and Hussain, T., Characterisation of Corrosion Resistant Deposits by Cold Gas Dynamic Spray. Thermal spray: Global Solutions for Future Application, Marple, B. R., Agarwal, A., Hyland, M. M., Lau, Y. -C., Li, C.-J., Lima, R. S., and Montavon, G., Eds., 3- 5 May 2010, (Singapore), ASM International, CD-ROM, p. 496-501

Acknowledgements

I would first like to thank my supervisors Prof. Graham McCartney and Prof. Phil Shipway for their invaluable support, advice and mentoring during my three years of doctoral research. I learnt to be critical to ideas, progress logically through the course of an investigation and think rationally from working with them. It has been a life changing experience for me. I would also like to thank Keith Dinsdale, Tom Buss and Dr. Deen Zhang for all the equipment training, technical solutions and invaluable discussion. Also, a special thank you goes to my industrial supervisor Dr. Tiziana Marrocco for bringing in the commercial perspective to this project and her help in producing the coatings.

I am also very grateful to all my colleagues at Wolfson building who made my three years study at the university a pleasant one. A further thank you is extended to Jodie and Samuel for their encouragement throughout the thesis writing up period. I would like to express my deepest gratitude to my mother Nasreen Hussain and my father Motaher Hussain for their support and encouragement.

This project was sponsored by TWI Ltd, Cambridge, UK. I greatly acknowledge financial support from the university through an Overseas Research Students Awards Scheme (ORSAS) for this PhD.

Table of Contents

1 Introduction 1

1.1 Methodology 3

1.2 Scope of the thesis 3

2 Literature review 6

2.1 Surface engineering 6

2.1.1 Thermal spraying 7

2.1.2 Cold spraying 8

2.2 Gas dynamic principles in cold spraying 12

2.2.1 Flow in a convergent-divergent nozzle 12

2.2.2 Particle acceleration model 14

2.2.3 Role of gas pressure and temperature 15

2.2.4 Effect of stand-off distance and bow shock 16

2.3 Bonding mechanisms in cold spraying 18

2.3.1 Mathematical modelling using numerical methods 18

2.3.2 Experimental investigations 31

2.3.3 Summary of bonding mechanisms 38

2.4 Cold spraying of copper 39

2.5 Cold spraying of aluminium 40

2.6 Interdiffusion of Cu-Al and Ti-Fe 41

2.7 Cold spraying of titanium 43

2.7.1 Powder feedstock for titanium 44

2.7.2 Deposition efficiency and critical velocity for titanium powders 45

2.7.3 Bond strength 47

2.7.4 Porosity of the coating 50

2.7.5 Microhardness of the coating 53

2.7.6 Constituents of cold sprayed titanium 55

2.7.7 Mechanical properties of free standing deposits and coatings 60

2.7.8 Effect of heat treatment on free standing deposits and coatings 61

2.7.9 An overview of warm sprayed titanium 62

2.7.10 Summary of literature review of cold sprayed titanium 63

2.8 Corrosion 65

2.8.1 Thermodynamics of corrosion 65

2.8.2 Electrochemical corrosion 65

2.8.3 Corrosion behaviour of bulk titanium 71

2.8.4 Corrosion of sprayed titanium coatings 73

2.8.5 Summary of the literature review of corrosion 80
2.9 Aims and objectives of the research 81
3 Experimental 83
3.1 Introduction 83
3.2 Overview of cold spray equipment 83
3.2.1 Cold spraying with room temperature helium 83
3.2.2 Cold spraying with the CGT™ Kinetiks® system 84
3.3 Particle size measurements 87
3.4 Substrate composition analysis 88
3.5 Microstructural characterization 88
3.6 Surface profilometry 89
3.7 X-ray diffraction analysis 90
3.8 Microhardness measurements 91
3.9 Post spray heat treatment of titanium deposits 92
3.10 Laser surface melting 92
3.10.1 Materials 92
3.10.2 Equipment and process parameters 92
3.10.3 Primary trials to optimize settings 93
3.10.4 Production of melted areas 93
3.11 Mercury intrusion porosimetry (MIP) 94
3.12 Bond strength pull-off tests 95
3.13 Tubular coating tensile (TCT) test 97
3.14 Electrochemical tests 99
3.14.1 Sample preparation for electrochemical tests 101
3.15 Salt spray (fog) tests 102
3.15.1 Sample preparation for salt spray 102
3.16 Immersion tests 103
4 Impact behaviour and bonding mechanisms in cold spraying 104
4.1 Introduction 104
4.2 Experimental 106
4.2.1 Materials 106
4.2.2 Substrate preparations 107
4.2.3 Cold spray deposition conditions 108
4.2.4 Post spray heat treatment 110
4.3 Bonding mechanisms of copper onto aluminium 111
4.3.1 Characterization of copper powder 111
4.3.2 Single particle impact of copper onto aluminium 112

4.3.3 Characterization of different substrate surfaces 113
4.3.4 Bond strength tests and fracture surface analysis 116
4.3.5 Microstructural analysis of bond formation 121
4.4 Bonding mechanisms of aluminium onto copper 126
4.4.1 Characterization of aluminium powder 126
4.4.2 Single particle impact of aluminium onto copper 127
4.4.3 Characterization of different substrate surfaces 128
4.4.4 Bond strength tests and fracture surface analysis 131
4.4.5 Microstructural analysis of bond formation 136
4.5 Bonding mechanisms of titanium onto steels 140
4.5.1 Characterization of titanium powder 142
4.5.2 Characterization of substrates 143
4.5.3 Microstructural analysis of bond formation 144
4.6 Discussion 153
4.6.1 Bonding mechanisms of copper coatings onto aluminium substrates 154
4.6.2 Bonding mechanisms of aluminium coatings onto copper substrates 167
4.6.3 Impact and bonding behaviour of titanium particles onto steel substrates 172
4.7 Summary 182
5 Process- structure characteristics of cold sprayed and post-spray processed titanium deposits 186
5.1 Introduction 186
5.2 Materials and experimental procedures 187
5.2.1 Feedstock powder 187
5.2.2 Substrates and surface preparation 187
5.2.3 Cold spray parameters 188
5.3 Characterization of feedstock powder 190
5.4 Effect of processing conditions on coating characteristics 191
5.4.1 Effect of process gas temperature on microstructure and microhardness 191
5.4.2 Effect of process gas temperature on surface morphology 198
5.4.3 Effect of substrate types and surface preparations on coating deposition 201
5.4.4 Bond strength and cohesive strength of deposits 206
5.5 Deposit porosity and effect of post-spray processing 213
5.5.1 Porosity of as-sprayed and heat-treated titanium deposits (mercury intrusion porosimetry) 213
5.5.2 Morphological and microstructural changes following heat treatment 216

5.5.3 Laser surface melting trials 219
5.6 Discussion 225
5.6.1 General observations 225
5.6.2 Role of substrate types and surface preparations on bonding 226
5.6.3 Failure modes of titanium deposits 227
5.6.4 Porosity of as-sprayed and heat-treated deposits 229
5.6.5 Laser surface melting of the deposits 230
5.7 Summary 231
6 Corrosion performance of cold sprayed titanium coatings and free standing deposits 233
6.1 Introduction 233
6.2 Experimental methods 234
6.3 Corrosion behaviour of free standing deposits 234
6.4 Corrosion behaviour of heat-treated deposits 238
6.5 Corrosion behaviour of Ti coatings on stainless steel 241
6.6 Corrosion behaviour of Ti coatings on carbon steel 248
6.7 Corrosion behaviour of laser treated Ti coatings on carbon steel 255
6.8 Discussion 260
6.8.1 Corrosion behaviour of free standing deposits 260
6.8.2 Corrosion behaviour of coatings on stainless steel 262
6.8.3 Corrosion behaviour of coatings on carbon steel 263
6.8.4 Corrosion behaviour of laser treated coatings 264
6.9 Summary 265
7 General conclusions 267
8 Future work 271
8.1 Bonding mechanisms in cold spraying 271
8.2 Process-structure optimization of titanium coatings 272
8.3 Corrosion behaviour of cold sprayed titanium coatings 273
9 Appendix 288
9.1 Deposition efficiency measurement 288
9.2 Substrate temperature measurement 291
9.3 Williamson-Hall analysis 292

List of Tables

Table 2-1 Pull-off bond strength values of Ti coatings..... 49

Table 2-2 Porosity of cold sprayed titanium coatings reported in literature..... 52

Table 2-3 Hardness of titanium coatings reported in the literature 54

Table 2-4 Oxygen-nitrogen contents of titanium powder and cold sprayed coatings 55

Table 2-5 Microstrain determination of Ti powder and coatings..... 58

Table 3-1 Preliminary trials to optimize settings on a titanium coating deposited onto carbon steel using process gas temperature 800°C 93

Table 4-1 Chemical compositions of the low carbon steel, Armco iron, and stainless steel (304) measured using optical emission spectroscopy..... 107

Table 4-2 Near-surface hardness and surface roughness of the aluminium substrates as-prepared and following annealing. The hardness values of the bulk aluminium were 115 ± 1 kgf /mm^2 and 40 ± 1 kgf /mm^2 in the as-prepared and annealed conditions respectively. 115

Table 4-3 Bond strength values for the copper deposited onto aluminium substrates for as-prepared surfaces and following annealing treatment. 116

Table 4-4 Microscopic analysis of the material present on the substrate and on the coating after bond strength pull-off tests (All measurements were taken on BSE images with a field size of 300 ×225 μm). The polished substrate which was annealed failed in the adhesive not at the interface. 120

Table 4-5 Measurements of the fraction of the copper-aluminium interface covered with intermetallic phases after a short heat treatment of 15 min at 400°C (All measurements taken on eight BSE images of the interface cross-section comprising approximately a 2.5 mm length of the interface). 125

Table 4-6 Near-surface hardness and surface roughness of the copper substrates. As-received copper substrate hardness 90.7±0.9 and annealed copper substrate hardness 55.9±1.2 130

Table 4-7 Bond strength values for the aluminium deposited onto copper substrates for as-sprayed surfaces..... 131

Table 4-8 Microscopic analysis of the material present on the substrate and on the coating after bond strength pull-off tests (all measurements were taken on BSE images with a field size of 300 × 225 μm)..... 135

Table 4-9 Measurements of the fraction of the aluminium-copper interface covered with intermetallic phases after a short heat treatment of 15 min at 400°C (all measurements taken on eight BSE images of the interface cross-section comprising approximately a 2.5mm length of the interface)..... 140

Table 4-10 Bulk substrate microhardness of the low carbon steel, Armco iron, and stainless steel (304). The hardness value of bulk commercially pure grade 1 titanium was 145±3 kgf/ mm^2..... 144

Table 4-11 Johnson-Cook materials properties of titanium, carbon steel, Armco iron and stainless steel..... 177

Table 5-1 Process parameters of in-situ grit blasting using cold spraying gun.. 188

Table 5-2 Process parameters of cold spraying of titanium at 600 and 800°C onto cabinet grit blasted samples..... 189

Table 5-3 Microhardness values with standard error of mean measured on the polished cross-section of the coatings sprayed at 600 and 800°C temperatures..... 198

Table 5-4 Surface roughness of the cabinet grit-blasted and in-situ grit blasted carbon steel and stainless steel..... 203

Table 5-5 Microscopic analysis of the fraction of Al_2O_3 present on the substrate after grit blasting surface preparations (all measurements were taken on BSE images with a field size of 300 × 225 μm)..... 205

Table 5-6 Pull-off bond strength values for the titanium deposited onto different substrates at 800°C gas temperature. Average bond strength of the glue after 5 tests was 88 ± 2 MPa..... 207

Table 5-7 Tubular coating tensile test results of titanium deposited at 800°C process gas temperature..... 211

Table 5-8 Volume fraction of open porosity of free standing 600 and 800°C deposits before and after heat treatment (Cumulative intrusion of mercury (mL/g) was converted to vol. % assuming density of titanium is 4500 kg/m^3)..... 216

Table 5-9 Process parameters for laser surface treatment of titanium coatings deposited at 800°C process gas temperature 220

Table 6-1 OCP, Ecorr, Icorr and Ipp values of as-sprayed and heat-treated deposits tested in de-aerated 3.5% NaCl 237

Table 6-2 Corrosion parameters of 600 and 800°C coatings onto stainless steel 245

Table 6-3 Corrosion parameters of 600 and 800°C coatings onto carbon steel 252

Table 6-4 Corrosion parameters of as-sprayed and laser treated 800 °C coatings onto carbon steel in aerated 3.5% NaCl 257

Table 9-1 Deposition efficiency measurement of titanium coatings sprayed at 800°C process gas temperatures onto in-situ grit blasted carbon steel, stainless steel and Ti6Al4V substrates 290

Table 9-2 Temperatures measured at the back of the carbon steel, stainless steel and Ti6Al4V substrates during spraying of titanium at 800°C process gas temperature 291

Table 9-3 FWHM values of titanium powder, as-sprayed and heat treated 600 and 800°C deposits 292

Table 9-4 Grain size and microstrain determination of as-sprayed deposits using Williamson-Hall plots 294

List of Figures

Figure 2-1 Temperature/ velocity regimes for thermal spray and cold spray processes [8] 8

Figure 2-2 Schematic of a cold gas dynamic spray system [1] 9

Figure 2-3 Schematics of a cold gas dynamic spray de Laval nozzle [24] 12

Figure 2-4 (a) Schematic diagram of the supersonic impingement zone at the substrate (b) Schlieren images of bow shock at 10 mm standoff distance from the nozzle [33] 16

Figure 2-5 (a) Pressure field during impact (b) jetting [11] (c) SEM of a copper particle on a copper substrate [1] 20

Figure 2-6 Calculated temporal development of (a) plastic strain (b) temperature and (c) flow stress at a critical node of sprayed Cu particle from FE on Cu substrate modelling of Assadi et al. [1] 21

Figure 2-7 Schematic of relationship between particle velocity and deposition efficiency proposed by Gartner et al. [30] 22

Figure 2-8 Critical impact velocity for a 25 μm particle calculated using Schmidt's equation [11]. The dark grey level indicates the range of uncertainity 23

Figure 2-9 Minimum particle diameter for localized adiabatic shear instability for different materials [11] 25

Figure 2-10 Schematic correlation between particle velocity, deposition efficiency and impact effects at constant temperature [48, 49] 26

Figure 2-11 Critical velocity and erosion velocity as a function of particle temperature [10, 11] 26

Figure 2-12 Schematics of thermal boost up zone (TBZ) [39] 27

Figure 2-13Four cases of particle impact onto substrate (a) soft/soft (Al onto Al at 775 m/s) (b) hard/hard (Ti onto Ti at 865 m/s) (c) soft/hard (Al onto mild steel at 365 m/s) (d) hard/soft (Ti onto Al at 655 m/s) [39] ... 28

Figure 2-14 Calculated adhesion energy and rebound energy for various sized Al-Si feedstock impacting onto mild steel [56] 31

Figure 2-15 FE-TEM micrographs: bright field image of interface between aluminium powder and substrate showing aluminium oxide layer [65] ... 33

Figure 2-16 BSE image of heat-treated Cu-Al deposits showing intermetallic layer as an indicator of metal-to-metal bond formation [4] 35

Figure 2-17 Stages in coating formation in kinetic spray process [71] 36

Figure 2-18 Al-Cu phase diagram [103]..... 42

Figure 2-19 Ti-Fe phase diagram [103] 43

Figure 2-20 Typical active-passive behaviour of a metal 70

Figure 2-21 Polarization curve of cp titanium in 0.5 M NaCl [159] 72

Figure 2-22 (a) Polarization curves of free standing atmospheric plasma sprayed (APS) Ti, APS-shrouded Ti and bulk Ti in 3% NaCl (b) Polarization curves of APS/S Ti on carbon steel, Bulk Ti and carbon steel [169] 74

Figure 2-23 Anodic polarization scans of flame sprayed Ti on steel (as-sprayed), free standing Ti (detached), bulk Ti (solid) and carbon steel substrate in de-aerated 3.5% NaCl. 75

Figure 2-24 Anodic polarization curves of warm sprayed Ti coatings on carbon steel substrate and bulk Ti in de-aerated artificial seawater [175] 76

Figure 2-25 Open circuit potential measurements of bulk Ti and cold sprayed Ti in natural seawater [177]..... 77

Figure 2-26 Polarization curves of cold sprayed Ti at different process conditions of (a)1.5 MPa (b) 1.8 MPa (c) 2.0 MPa in 3.5wt.% NaCl [125] 78

Figure 2-27 Open circuit potential of plasma sprayed Ti and laser treated plasma sprayed Ti in flowing natural sea water [164]..... 79

Figure 3-1 Schematic of room temperature helium cold spray system [93] 84

Figure 3-2 CGT Kinetiks 4000/47 system mounted on a robot at TWI, Sheffield and a close up view of the cold spraying gun 85

Figure 3-3 Schematic of heated nitrogen rig cold spray system 86

Figure 3-4 Assembly view of CGT cold spray gun showing all the components and location of sensors..... 87

Figure 3-5 Schematic profiles of hardness measurements across the coating cross section. Ten indentations were made along every pass. 91

Figure 3-6 Penetrometer of the mercury intrusion test 94

Figure 3-7 Schematic of pull-off PAT tests [24]..... 96

Figure 3-8 Schematic of tensile adhesion test according to ASTM C633 [181].... 97

Figure 3-9 Tubular coating tensile (TCT) test samples after failure. (a) Plan view of the sample showing spray direction and pull-off direction in the tensile testing machine, (b) Cross-section of the samples. 98

Figure 3-10 Axi-symmetric finite element stress analysis of tubular coating tensile (TCT) test [182] 99

Figure 3-11 A schematic diagram of three electrode cell used in potentiodynamic tests 100

Figure 4-1 (a) SE image of gas atomized copper showing its morphology (b) Cumulative size distribution of copper powder measured by laser diffractometry 111

Figure 4-2 (a) SE image of copper particles on aluminium substrate. Higher magnification images of (b) copper particles on aluminium substrate (c) cross-section of a copper particle on aluminium substrate..... 112

Figure 4-3 Typical line profiles extracted from the polished, ground and grit blasted surfaces 113

Figure 4-4 Surface profiles of polished, ground and grit blasted surfaces (with identical horizontal and vertical scaling) in comparison with a disk representing a section through a 15μm diameter spherical particle. 114

Figure 4-5 Fracture surfaces, after pull off test, of as prepared Al substrate (a-c) and corresponding copper coating (d-f) with different substrate surface preparations: (a, d) polished; (b, e) ground; and (c, f) grit blasted. The bright phase is Cu and the darker one Al. The Al substrate shows the presence of individual Cu particles adhered to it and the Cu coating shows Al trapped in between Cu particles. 118

Figure 4-6 Fracture surfaces, after pull off test, of annealed Al substrate (a-b) and corresponding copper coating (c-d) with different substrate surface preparations: (a, c) ground; (b, d) grit blasted. 119

Figure 4-7 (a) High magnification image of copper coating on ground and annealed aluminium substrate showing aluminium extruded in between copper particles. (b) Fracture surface (coating side) after pull off test on the same coating-substrate combination showing rim of Al (dark) around Cu particles (bright). 119

Figure 4-8 BSE images of Cu (bright) on as-prepared Al substrate (dark) with (a) polished (b) ground (c) grit blasted surfaces. BSE images of Cu (bright) on annealed Al substrate (dark) with (d) polished (e) ground (f) grit blasted surfaces in the as-sprayed condition. Micron sized bright particles within the Al substrate are constituent intermetallics in the 6082 alloy. 122

Figure 4-9 BSE images of Cu (bright) on as-prepared Al substrate (dark) with (a) polished, (b) ground, (c) grit blasted surfaces. BSE images of Cu (bright) on annealed Al substrate (dark) with (d) polished, (e) ground, (f) grit blasted surfaces. Samples annealed at 400 °C for 15 min following deposition. Grey contrast levels in the higher magnification insets show intermetallic that formed during annealing. 124

Figure 4-10 SE image of gas atomized aluminium powder showing its morphology 127

Figure 4-11 SE image of (a) aluminium particles on copper substrate. Higher magnification image of (b) an aluminium particle on copper substrate (c) cross-section of an aluminium particle on copper substrate. 128

Figure 4-12 Typical line profiles extracted from the polished, ground, and grit-blasted surfaces 129

Figure 4-13 Surface profiles of polished, ground, and grit-blasted surfaces (with identical horizontal and vertical scaling) in comparison with a disk representing a section through a 35 μm diameter spherical particle..... 129

Figure 4-14 SE images of fracture surfaces, after pull-off test, of as-prepared Cu substrate (a-c) and corresponding aluminium coating (d-f) with different substrate surface preparations: (a, d) polished; (b, c) ground; and (c, f) grit-blasted..... 133

Figure 4-15 BSE images of fracture surfaces, after pull-off test, of as prepared Cu substrate (a-c) and corresponding aluminium coating (d-f) with different substrate surface preparations: (a, d) polished; (b, c) ground; and (c, f) grit-blasted. Arrow indicates retained Al particle..... 134

Figure 4-16 High magnification SE images of fracture surfaces, after pull-off test, of (a) as-prepared polished Cu substrate (b) corresponding aluminium deposit. Circles indicate the regions of metallurgical bonding..... 136

Figure 4-17 BSE images of Al(dark) on as-sprayed Cu substrate (bright) with (a) polished (b) ground (c) grit blasted surface. BSE images of the samples annealed at 400°C for 15 min following deposition (d) polished (e) ground (f) grit blasted surface. Arrows showing substrate deformation 138

Figure 4-18 BSE images of (a) Al(dark) on softened Cu substrate (bright) with polished surface (b) the same coating annealed at 800°C for 20 min following deposition. Arrows showing substrate deformation 139

Figure 4-19 (a) Secondary electron (SE) image of spherical titanium powder (b) SE image of angular titanium powder showing their morphology (c) Cumulative vol.% size distribution of both spherical and angular powder..... 142

Figure 4-20 Optical microscope images of etched microstructure of (a) low carbon steel, (b) Armco iron, and (c) austenitic stainless steel 143

Figure 4-21 Low-magnification SE images of spherical titanium particles as-sprayed using room temperature helium onto (a) low carbon steel, (b) Armco iron, (c) austenitic stainless steel..... 145

Figure 4-22 Higher magnification SE images of 86 ° tilted view of as sprayed titanium particles onto (a) low carbon steel, (b) Armco iron, (c) austenitic stainless steel, and cross-section of as sprayed titanium particles onto (d) low carbon steel, (e) Armco iron, (f) austenitic stainless steel 146

Figure 4-23 BSE images of spherical titanium particles sprayed using room temperature helium followed by heat treatment, for substrates as follows: (a) low carbon steel, (b) Armco iron, (c) austenitic stainless steel. (d) Higher magnification images of the intermediate phases shown in (c) (mid-grey contrast levels) 148

Figure 4-24 SEM images of angular titanium particles sprayed onto austenitic stainless steel using room temperature helium gas: (a) SE plan view; (b) SE cross–sectional image; (c) BSE cross-sectional image following heat treatment showing intermediate phase. Arrows indicate point of maximum deformation 151

Figure 4-25 SEM images of spherical titanium particles sprayed onto austenitic stainless steel using heated nitrogen gas at 800 °C and 4.0 MPa: (a) SE plan view; (b) SE cross–sectional image; (c) BSE cross-

sectional heat treated image showing formation of intermediate phases (mid-grey contrast levels) 153

Figure 4-26 Schematic illustration of jet formation on an aluminium substrate by an impinging copper particle. The jet is subsequently trapped in the copper coating by incoming copper particles. During the bond strength test fracture occurs in the aluminium jet shown by the dotted line. 156

Figure 4-27 Schematic diagram of deposit-substrate debonding at the interface, indicating failure of both the interlocked substrate and the regions of deposit-substrate metallurgical bonding; (a) prior to failure; (b) post failure. 158

Figure 4-28 Stress strain behaviour of metallurgically bonded area and mechanically interlocked area assuming that the metallurgically bonded area exhibits brittle behaviour and that the mechanically interlocked area exhibits ductile behaviour 159

Figure 4-29 Failure stresses associated with the different failure modes as indicated in equation 4.3, 4.4 and 4.6 as a function of the fraction of the metallurgically bonded material 161

Figure 4-30 Flow stress of titanium, carbon steel, Armco iron and austenitic stainless steel as a function of plastic strains at strain rate 10^7 /s and 375K according to the J-C model with data from Table 4-11..... 178

Figure 5-1 (a) SEM image of gas atomized titanium feedstock powder showing its near-spherical morphology. (b) Cumulative size distribution of the powder measured by laser diffractrometry 190

Figure 5-2 SEM images showing (a) un-etched cross section of the powder (c) etched cross section of the powder showing acicular microstructure 191

Figure 5-3 XRD profiles of titanium powder, coatings sprayed at 600 and 800°C process gas temperatures 193

Figure 5-4 OM images of un-etched titanium coatings onto stainless steel substrates at process gas temperatures of (a) 600 & (b) 800°C. Broken lines indicate the approximate locations of the inter-pass boundaries. 195

Figure 5-5 OM images of etched (15 s in Kroll's solution) titanium coatings sprayed at (c) 600 & (d) 800°C 196

Figure 5-6 Cross section of (a) 600 & (b) 800 °C coatings etched in Kroll's agent for a duration of 50 seconds 197

Figure 5-7 Topography of titanium coatings using surface profilometry: (a) 600 & (b) 800°C..... 198

Figure 5-8 Typical line profiles extracted from the top surface of 600 and 800°C coatings..... 199

Figure 5-9 Lower magnification BSE images of coatings sprayed at (a) 600 & (b) 800°C. Higher magnification BSE images of coating top layer sprayed at (c) 600 & (d) 800°C..... 200

Figure 5-10 Lower magnification images of (a) 600 & (b) 800°C coatings. Higher magnification images of (c) 600 & (b) 800°C coatings. (boxed area showing rupture of bonds, arrows showing viscous flow of material) 201

Figure 5-11 Typical line profiles extracted from conventional cabinet grit-blasted and in-situ grit blasted (a) carbon steel (b) stainless steel 202

Figure 5-12 SEM images of the top surfaces of carbon steel (a-d) and stainless steel (e-h) with different substrate surface preparations: cabinet grit blasted (a, c, e, g) and in-situ grit blasted (b, d, f, h)..... 205

Figure 5-13 BSE image of the titanium coating deposited onto in-situ grit blasted (a) carbon steel & (b) stainless steel substrate. Coating-substrate interface of (c) carbon steel & (d) stainless steel showing embedded grits. 206

Figure 5-14 Fracture surfaces of as-machined Ti6Al4V substrate (a, c) and corresponding titanium coating (b, d) 208

Figure 5-15 Fracture surfaces of carbon steel substrate (a, c) and corresponding titanium coating (b, d) 209

Figure 5-16 Fracture surfaces stainless steel (a, c) and corresponding titanium coating (b, e) 210

Figure 5-17 Fracture surfaces, after tubular coating tensile tests, of titanium deposits sprayed at 800°C. Direction of spraying from the top to bottom and load direction perpendicular to the paper surface..... 212

Figure 5-18 (a) Incremental intrusion of mercury vs. pore size distribution of as-sprayed and heat-treated deposits (b) Cumulative mercury intrusion of the same deposits..... 215

Figure 5-19 OM etched images showing changes in microstructure. As-sprayed (a) 600 & (b) 800 °C deposits. Heat-treated (c) 600 & (d) 800°C deposits. 217

Figure 5-20 SEM images of etched samples showing changes in pore structure. As-sprayed (a) 600 & (b) 800°C deposits. Heat-treated (c) 600 & (d) 800°C deposits (Arrows showing the interparticle pores) 218

Figure 5-21 SEM images of the top view of heat-treated deposits (a) 600 & (b) 800°C. Higher magnification images of the heat-treated deposits (c) 600 & (d) 800°C..... 219

Figure 5-22 Melt pool characteristics of laser treated etched titanium coatings sprayed at 800°C process gas temperature according to the process parameters shown in Table 5-9 222

Figure 5-23 (a) Etched BSE image showing the shape of the melt pool and (b) SE image showing the microstructure of the laser treated zone (run 4) 223

Figure 5-24 XRD analysis of a laser treated (condition 4) titanium coating sprayed at 800°C 224

Figure 5-25 Schematic illustration of fracture by void coalescence [204] 229

Figure 6-1 Open circuit potential of bulk titanium, as-sprayed 600 and 800 °C deposits 235

Figure 6-2 Potentiodynamic polarization scans of bulk titanium, as-sprayed 600 and 800°C deposits 236

Figure 6-3 Optical microscope images of the polished surface of (a) 600 and (b) 800 °C deposits after electrochemical tests 237

Figure 6-4 Open circuit potential of bulk titanium, heat treated 600 and 800 °C deposits 239

Figure 6-5 Potentiodynamic polarization scans of bulk titanium, heat treated 600 and 800°C deposits 240

Figure 6-6 Open circuit potentials of bulk Ti, stainless steel, 600 and 800°C coatings in (a) de-aerated (b) aerated solutions 241

Figure 6-7 Potentiodynamic polarization scans of bulk Ti, stainless steel, 600 and 800°C coatings in (a) de-aerated (b) aerated solutions 243

Figure 6-8 Immersion tests of 600°C (a, c, e) and 800°C (b, d, f) Ti coatings on stainless steel (a, b) before immersion (c, d) after 30 hours and (e, f) after 165 hours 246

Figure 6-9 SEM images of the cross section of 600°C coating (a, c) and 800 °C coating (b, d) after immersion tests of 165 hours. 247

Figure 6-10 Open circuit potentials of bulk Ti, carbon steel, 600 and 800 °C coatings in (a) de-aerated (b) aerated solutions 248

Figure 6-11 Potentiodynamic polarization scans of bulk Ti, carbon steel, 600 and 800 °C coatings in (a) de-aerated (b) aerated solutions 250

Figure 6-12 (a) Optical microscope image of 600°C coating following electrochemical tests (b) SEM image of localized corrosion 251

Figure 6-13 Salt spray (fog) samples of Ti coatings on carbon steel after 24 hours of exposure (a) 600 (b) 800 °C coatings..... 253

Figure 6-14 (a) Optical image of 600 °C Ti coating on carbon steel after 3500 hours of exposure in salt spray (fog). (b) BSE image of the cross-section. SE images of (c) the top region (d) coating-substrate interface. 254

Figure 6-15 Open circuit potential of bulk Ti, carbon steel, 800 °C coating onto carbon steel and laser treated coating in aerated 3.5% NaCl..... 255

Figure 6-16 Potentiodynamic polarization scans of bulk Ti, carbon steel, 800 °C coating onto carbon steel and laser treated coating in aerated 3.5% NaCl 256

Figure 6-17 SE images of (a) as-sprayed (b) laser treated coatings onto carbon steel after electrochemical tests. Corresponding high magnification images of the interface (c) and (d)..... 258

Figure 6-18 Salt spray (fog) sample sprayed at 800°C: (left) laser treated and (right) as-sprayed (a) before exposure (b) after 24 hours. Only laser treated section after (c) 50 hours (d) 100 hours. 259

Figure 9-1 Williamson- Hall plot for as-sprayed 600 & 800°C titanium deposits. 294

Nomenclature

A - Cross sectional area of the nozzle

A* - Cross sectional area of the throat of the nozzle

γ - Ratio of specific heats

Ma - Mach number

V - Gas velocity

T - Gas temperature

P - Gas pressure

ρ - Gas density

T_0 - Stagnation temperature

P_0 - Stagnation pressure

ρ_0 - Stagnation density

R - Universal gas constant

M_w - Molecular weight of the gas

m_p - Mass of the particle

ρ_p - Density of the particle

V_p - Velocity of the particle

V_{cr} - Critical velocity of the particle

d_{crit} - Critical diameter of the particle

c_p - Specific heat of the particle

λ_p - Thermal conductivity of the particle

A_p - Cross sectional area of the particle

C_D - Coefficient of drag

t - Time

x - Axial distance

a - Speed of sound

T_m / T_{melt} - Melting temperature of the particle

σ_u - Ultimate tensile strength of the particle

T_i - Initial particle temperature

F1, F2 - Calibration factors

T_R - Reference temperature of the particle

T_{max} - Maximum temperature of the particle

T_r / T_{trans} - Temperature of the transition point

t_i - Incubation time

t_c - Total contact time

Ad - Adhesion energy

Ad_{max} - Maximum adhesion energy

a% - Fraction of bonded atoms per unit of adhesive interface

υ - Natural frequency of Eigen-oscillations of atoms in lattice

E_a - Activation energy

T_c - Contact temperature

k - Boltzman constant

e_r - Recoil coefficient

M_a - Atomic mass

S_c - Contact area of a single particle to substrate

N_a - Total number of atoms in unit plane

E_1 - Energy of a single bond between two atoms

Re - Rebound energy

B' - Brinell hardness number of the substrate

E - Measured potential

E_o - Open circuit potential when all activities are equal to 1

F - Faraday constant

a - Chemical activity

i - External current density

i_o - Corrosion current density at equilibrium

i_a - Anodic current density

i_c - Cathodic current density

η - Total overpotential

J - Flux of the substrate which is equivalent to corrosion rate

β_a - Anodic Tafel constant

β_c - Cathodic Tafel constant

λ - Wavelength of incident wave

d - Spacing between the planes

θ - Angle between the incident ray and scattering plane

D - Pore diameter

P_a - Applied pressure

γ - Surface tension

φ - Contact angle

σ_c - Stress in the composite

σ_m - Stress in the metallurgically bonded areas

σ_i - Stress in the interlocked regions

σ_{mf} - Failure stress of the metallurgically bonded areas

σ_i' - Stress in the interlocked regions when the metallurgical bond fails

σ_c' - Stress in the composite when metallurgical bond failure occurs

σ_{ui} - Tensile strength of the interlocked material

f_m - Area fraction of the interface corresponding to metallurgical bond

f_i - Area fraction of the interface corresponding to interlocked material

f_m^T - True metallurgically bonded area fraction

σ - Equivalent flow stress

ε_p - Equivalent plastic strain

$\overline{\varepsilon_p}$ - Equivalent plastic strain rate

$\overline{\varepsilon_0}$ - Reference strain rate

T* - Normalized temperature

A - Yield stress in a simple quasi static tension/ compression test

B - Stain-hardening parameter

C - Dimensionless strain-rate hardening coefficient

n - Exponent of strain-hardening

m - Exponent of thermal-softening

r - Radius of the sphere

v - Volume of the plastic zone

r' - Radius of the hemisphere

T' - Temperature at the adiabatic shear band

C_v - heat capacity

β - Adiabatic constant (0.9)

P' - Laser power

D - Laser spot diameter

U - Laser beam traverse speed

1 Introduction

The overall aims of this thesis were to study the bonding mechanisms in cold gas dynamic spraying (CGDS) or cold spraying of metallic coatings and to develop a corrosion resistant barrier layer coating from titanium.

Cold spraying is a relatively new branch of surface engineering. Surface engineering is an interdisciplinary branch of engineering that involves design and modification of the surface of substrates to provide specific engineering advantages which the substrate alone cannot provide. Cold spraying, as a metal deposition technique, involves spraying of typically 10-40 μm particles which are accelerated by a propellant gas to 300- 1200 m/s at a temperature well below the melting point of material, and upon impact deform and adhere to the substrate. The deposition process in cold spraying occurs in a solid state. No melting of the powder occurs, which results in reduced oxidation and absence of phase changes; whereas, in thermal spraying deposition occurs of molten or semi molten particles.

Over the last decade the interest in cold spraying has increased substantially. Considerable effort has been invested in process developments and optimization of coatings like copper. However, bonding in cold spraying is still a matter of some debate. The most prevalent theory is that when a particle travels at a minimum required velocity the particle deforms at a very high strain rate upon impact and during this deformation thermal softening dominates over work hardening in impact zone and a material jet is produced [1]. This material jet removes oxides from the surface of the materials and the metal-to-metal contact is established between the freshly exposed surfaces. However, precisely how this

high strain rate deformation behaviour of material promotes bonding is still unclear and requires further investigations.

Titanium and its alloys are widely utilized in many demanding environments such as aerospace, petrochemical, biomedical etc. Titanium has excellent corrosion resistance in aqueous solutions such as salt water due to its tenacious oxide film. In the petrochemical industry, materials are exposed to harsh environments and titanium can provide suitable protection to steel substrates. Titanium clad stainless steel, as a composite material, has a wide range of applications in the nuclear industry in handling corrosive solutions [2, 3]. Also, in the aerospace industry titanium is widely used as a structural material for weight saving applications because of its high strength to weight ratio. Titanium components are very expensive to manufacture because of the costly extraction process of titanium and their difficult to machine properties. Therefore, additive manufacturing i.e., direct metal deposition from powder and repair of titanium components are of great interest to the aerospace industry using technologies such as laser deposition or cold gas spraying.

Thus cold spraying has a great potential to produce oxygen-sensitive materials, such as titanium, without significant chemical degradation of the powder. Deposition of protective coatings of titanium using thermal spraying is problematic because of its high reactivity to atmospheric oxygen at high temperatures hence forming oxide inclusions. In-flight oxidation of materials can be avoided to a great extent in cold spraying. There is a considerable interest in the scientific community in developing corrosion resistant barrier coatings using cold spraying. However, to be effective a barrier layer must not have any interconnected porosity.

1.1 Methodology

To study the bonding mechanisms, three materials namely copper, aluminium and titanium were deposited by cold spraying. The powders were sprayed using room temperature helium with the University of Nottingham cold spraying apparatus. The substrate surfaces were characterized using surface profilometry, microhardness measurements, optical microscopy and scanning electron microscopy. Pull-off tests were performed to measure the bond strengths of the deposits and the fracture surfaces were analysed using scanning electron microscopy. It was previously shown by Price et al. [4] in cold sprayed coatings that when two oxide free metal surfaces come in close contact a short heat treatment produces intermetallics. This methodology of forming intermetallic as a marker to identify metal-to-metal contact forms an important part of this thesis.

Titanium coatings were produced using heated nitrogen as a propellant gas using a CGT™ Kinetiks® 4000/47 system at TWI Ltd. The coatings were characterized using optical microscopy, scanning electron microscopy, microhardness measurements, surface profilometry and X-ray diffraction analysis. The porosity of the coatings was quantified using mercury intrusion porosimetry. The porosity of the deposits was further decreased by different post-spray treatments, namely, vacuum heat treatment and laser surface melting. In addition, bond strength and tensile tests were also performed on the cold sprayed titanium deposits. The corrosion behaviour of the free standing deposits, coatings and post-spray treated deposits were studied using electrochemical methods with a three electrode cell and also by salt spray (fog) tests.

1.2 Scope of the thesis

This thesis is composed of nine chapters and a brief overview of each chapter is presented below.

Chapter *two* presents a comprehensive literature review and is divided into three main sections. The first section summarises the proposed bonding mechanisms in cold spraying which includes both mathematical modelling using numerical methods and experimental investigations. The second section provides a current status of the cold spraying of titanium and the constituent properties reported by different researchers. Finally, the corrosion section presents the key principles of aqueous corrosion and summarises the corrosion behaviour of plasma, flame, wire, arc, warm and cold sprayed titanium coatings in aqueous NaCl solution. At the end of the chapter, the aims and objectives of the research work are defined.

Chapter *three* describes the experimental methods and presents an overview of the cold spraying apparatus used in this study and a description of all the equipment utilized to characterize the coatings.

Chapter *four* presents the study on bonding mechanisms in cold spraying. Three different coating-substrate systems were studied, namely copper coatings onto aluminium substrates, aluminium coatings onto copper substrates and titanium onto three different steel substrates. This study was performed using the cold spraying equipment at the University of Nottingham and the spraying parameters are included in this chapter. The role of substrate surface preparations was investigated using the copper-aluminium system involving analysis of intermetallic phase formation and bond strength measurements. Experimental evidence of this study led to the proposal of a bonding model with two constituents, namely a metallurgical component and a mechanical component. The metallurgical bonding of cold sprayed titanium onto three different steel substrates was also studied using this novel intermetallic growth method.

Chapter *five* presents the process-structure characteristics and effects of post-spray treatments on cold sprayed titanium coatings sprayed using the CGT Kinetiks 4000/47 system. Two different spraying parameters designed to reduce porosity were used in this work to produce titanium coatings and the microstructure of the coatings was characterized using different methods. The coatings were deposited onto low carbon steel, stainless steel and Ti6Al4V substrates. A modified grit blasting surface preparation was developed and used to improve the adhesion of the titanium deposits with the steel substrates. Pull-off bond strengths and cohesive tensile strengths of the deposits were also measured. Post-spray heat treatments and laser surface melting were used separately to reduce the level of porosity of the deposits and the effects on corrosion behaviour studied.

Chapter *six* presents the corrosion behaviour of the free standing titanium deposits and coatings onto carbon and stainless steel. The corrosion behaviour of the free standing deposits was studied using open circuit potential measurements and potentiodynamic polarization scans. Titanium coatings onto carbon steel and stainless steel were also investigated using electrochemical methods as well as immersion and salt spray tests. The corrosion performance of the laser surface treated coatings and those that had been post spray heat treated was also studied with the same solution.

Finally, chapter seven provides general conclusions of the research work in this thesis and chapter eight outlines the future work to continue this research work further for a better understanding of cold spraying.

2 Literature review

Cold gas dynamic spray was first developed by Papyrin et al. [5] in the mid-1980s at the Institute of Theoretical and Applied Mechanics of the Russian Academy of Science in Novosibirsk while working with tracer particles in supersonic wind tunnels. Since then several research groups across the world have been developing this process as a surfacing technique. In last five years, a number of cold spray research groups in Japan, South Korea, Canada, Germany, USA, Russia, Australia, Finland, India, China and UK have been active in this area. This chapter provides a comprehensive review on working principles of cold spraying and the current theories of bonding mechanisms based on experimental work and numerical modelling of impact. An overview of the properties of cold-sprayed titanium deposits and the role of different process parameters on coating performance is also included. Furthermore, the principles of electrochemical corrosion and work on the corrosion of titanium coatings are also included in this chapter.

2.1 Surface engineering

Surface engineering involves design and modification of the surface of the substrate (bulk material) to provide specific engineering advantages (e.g. improved wear resistance, corrosion resistance, bio-inertness, oxidation resistance, electronic properties, friction coefficients, thermal insulations etc) and to provide a cost effective performance which the substrate alone is unable to provide [6]. The surface can be modified using metallurgical, mechanical or chemical methods or by applying a layer of metallic or non-metallic coating using spraying.

2.1.1 Thermal spraying

Thermal spraying is a generic term for applying metallic and non-metallic coatings in which the molten or semi- molten particles are deposited onto a substrate [7]. In thermal spraying, the particles are heated and accelerated towards a substrate onto which a coating is formed. The combination of high particle temperature and/or high particle velocity results in forming a deformed splat on the substrate. Deposition of successive splats causes a coating thickness from a few microns to few millimetres to be builtup on the substrate. Thermal spray processes can be grouped into three broad categories: flame spray, electric arc spray and plasma arc spray [7]. Different energy sources (i.e., flame, electric arc and plasma) are used to melt the coating materials (in powder, wire or rod form) and propel them towards the substrate. The key advantage of thermal spraying is that material or composites which partially melt without decomposing can be sprayed. Figure 2-1 compares the particle velocity and gas temperature of different thermal spray processes. Flame spray includes low velocity powder flame, wire flame and high velocity oxy-fuel (HVOF) methods where the gas temperature is relatively low. In flame spray, the coating material is aspirated into the oxy-fuel stream, heated and carried by the flame towards the substrate [7]. In arc (wire) spray process, two consumable wire electrodes are fed into the gun. This creates an arc between them which melts the tip of the wire. The molten metal is then atomized by a gas stream and propelled towards the substrate. The velocity of the particles is low and the temperature is higher than flame spray processes [7]. However, in plasma spray process, the powder heating region is from 2500 °C to 14000 °C, significantly above the melting point of any known material. Typically argon or argon-hydrogen mixture is heated by a dc arc to produce the plasma [7]. A range of materials including ceramics can be sprayed using plasma spray. In contrast to all thermal spray processes, cold spray is a material deposition technique where the particles are accelerated to a velocity of 300-1200 m/s with nitrogen or

helium gas at a relatively low temperature of the gas, generally below the melting point of material, and for metals such as titanium and copper temperatures in the range of 400- 800 °C can be used.

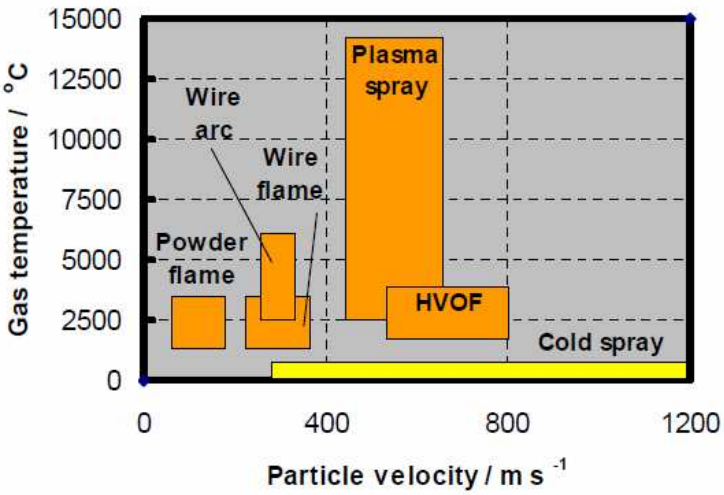

Figure 2-1 Temperature/ velocity regimes for thermal spray and cold spray processes [8]

2.1.2 Cold spraying

Cold spraying is a high strain-rate material deposition technique, in which powder particles (typically 10 - 40 μm in size) are accelerated to speeds of between 300-1200 m/s, and upon impact with a substrate (or previously deposited particles), deform plastically and adhere [1, 9-11]. The process is also referred to as cold gas dynamic spray because the process utilizes gas dynamic principle of helium or nitrogen as an accelerating gas. Deposition rates up to 14 kg/ h have also been reported in the literature [7]. Figure 2-2 shows, schematically the cold gas dynamic spraying process. In this process, a high pressure gas (helium or nitrogen) supply is used to accelerate the powder particles. A high pressure powder feeder is used to introduce the powder in the high pressure gas stream. In some systems, a gas heater is used to increase the temperature of the gas to further accelerate the particles. The key component of a cold spray process is a convergent-divergent nozzle termed a de Laval nozzle, which accelerates the gas

supersonically and gives the particles their required velocity to deposit onto a substrate. In a de laval nozzle, there are two sections: a convergent section and a divergent section. The area of the nozzle between the convergent and divergent section is called the throat.

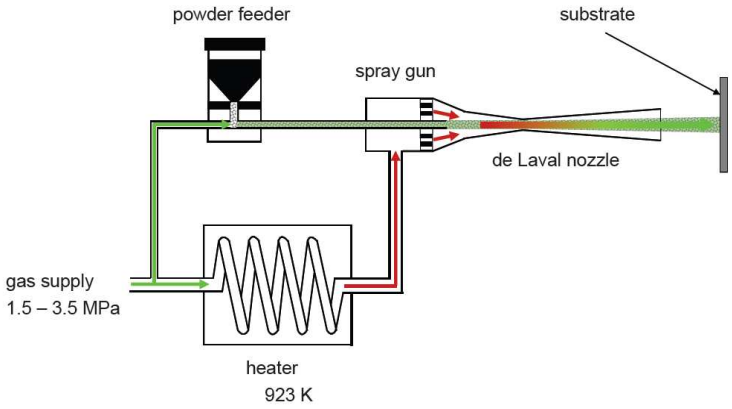

Figure 2-2 Schematic of a cold gas dynamic spray system [1]

There are two different types of commercially available cold spraying equipments: high pressure cold spraying system and low pressure cold spraying system (LPPS). Commercial high pressure cold spraying systems are manufactured by Cold Gas Technology (CGT) GmbH (Ampfig, Germany). The latest model of Kinetiks 4000/47 from CGT can achieve a pressure of 4.0 MPa with a process gas temperature of 800°C. A 47 kW heater is used as a primary gas heater and a 17 kW gun heater is used in combination with the primary gas heater. Kinetiks 4000 utilizes a WC nozzle with an elongated pre-chamber for powder mixing with the gas and can deposit high end materials like titanium, tantalum etc. There is also a portable version of the high pressure cold spray system called Kinetiks 2000 which operates below 2.0 MPa and up to 400°C. This portable cold spray system is mainly used for on site repair purposes using light materials like aluminium, copper, zinc, tin, magnesium etc [12].

Inovati Ltd (Santa Barbara, CA, USA) manufactures commercially available cold spraying model called Kinetic Metallization (KM). The Kinetic Metallization Coating Development System (KM-CDS) 3 is a fully integrated system with a 6+1 axis robot for coating development. KM-CDS model can achieve a gas temperature of 370°C while working at 1.0 MPa inlet pressure. The system utilizes friction compensated sonic nozzle made from cemented carbide for the deposition. A 2.5 kW thermal conditioning unit is integrated with the nozzle. There is also a portable version called Mobile Coating Systems (MCS) which is used for onsite repair work [13].

Supersonic Spray Technology (SST), which is a division of Centerline Ltd, manufactures commercially available low pressure cold spray systems. The low pressure Dymet model utilizes pressures below 1.0 MPa and a gas temperature below 600°C for coating deposition. The powders used in this low pressure cold spraying system typically include ceramics which helps in hammering the particles and thus facilitating particle deposition. In contrast to high pressure system where powder is introduced at the converging section of the nozzle, in this low pressure cold spray system the powder is introduced at the diverging section of the nozzle [14].

In the cold spraying process, the gas and particle temperatures remain well below the melting temperature of the spray materials and therefore the particles are in solid state, and formation of coatings occurs due to the kinetic energy of the particles on impact [1]. Unlike thermal spraying, where the particles are molten or semi molten, the deposition of particles in the solid state by cold spraying has various advantages. Some of the key advantages of cold spray are mentioned as follows [15].

- High deposition efficiency, values as high as 100% for titanium [16] and copper have been reported.
- High deposition rate, up to 14 kg/ h for various materials [17].
- Substrate preparation by grit-blasting is not required for ductile materials as the process can be viewed as a combination of grit-blasting, spray coating and shot peening [15].
- Low porosity coating because of visco-plastic deformation of the particles during deposition [1]. Also the particles from the trailing edge of the moving plume sputter away any loosely bonded particles and shot-peen the underlying layer to reduce porosity.
- Minimal thermal input to the substrate because of the absence of any high temperature jet to heat the substrate.
- Compressive residual stress in the coating because of plastic deformation in the solid state, which enhances fatigue properties of the coating.
- No phase change, no oxidation and no grain growth due to a lack of heating of the powders.
- High thermal and electrical conductivity of coatings can be produced from metals ,like copper, due to a low porosity and negligible oxide [18].
- High strength and hardness of the cold sprayed coatings compared to the bulk material because of the high degree of plastic deformation of the particles [19].
- In addition, corrosion resistant coating like tantalum [20] and aluminium [21] produced from cold spraying showed bulk like properties in corrosion tests.

2.2 Gas dynamic principles in cold spraying

The convergent- divergent nozzle or de Laval nozzle is a key component in the cold spraying system. To understand the cold spray deposition mechanisms it is important to understand the gas dynamic principles of flow through a convergent-divergent nozzle. High pressure gas is fed into the back of the convergent section of a de Laval nozzle. Figure 2-3 shows the schematics of a de Laval nozzle used in cold spraying. In a de Laval nozzle the flow can be accelerated or decelerated by changing the flow areas [22, 23]. The compressible nature of a gas allows the de Laval nozzle to operate. At the throat of the nozzle, the gas reaches sonic condition (Mach no. =1). At the divergent section of the nozzle, the gas continues to accelerate to supersonic velocities. As the gas accelerates in the divergent section of the nozzle, the temperature and pressure decrease from their original stagnation values [22]. The particles accelerate as they pass along the nozzle gaining kinetic energy from the supersonic gas [24].

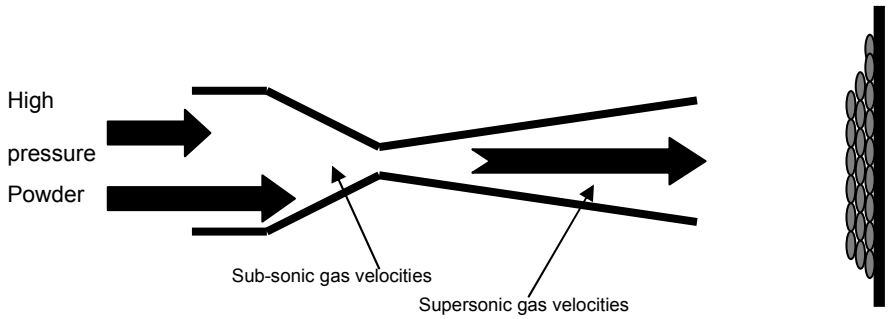

Figure 2-3 Schematics of a cold gas dynamic spray de Laval nozzle [24]

2.2.1 Flow in a convergent-divergent nozzle

This section describes the key equations for a compressible flow inside a de Laval, convergent-divergent nozzle. It is assumed that the gas flow is isentropic (adiabatic and frictionless), one dimensional, a perfect gas with a constant specific heat and external forces (i.e gravitational effects) are negligible [22, 24,

25]. The following equation shows the relationship between change in area with the change in velocity of an isentropic fluid

$$\frac{dA}{dV} = (Ma^2 - 1)\frac{A}{V} \qquad \text{equation 2.1}$$

where A is the cross sectional area, V is the velocity of the gas and Ma is Mach number. Because A and V are positive, it may be concluded from the equation that:

- If Ma<1, the flow is subsonic, i.e., decreasing the area increases the velocity. The flow in the convergent section of the nozzle.
- If Ma>1, the flow is supersonic, i.e., increasing the area increases the velocity. The flow in the divergent section of the nozzle.
- If Ma=1, then dA/ dV =0, A has to be minimum, i.e., at the throat of the nozzle.

If it is assumed that the exit area of the nozzle is known and then the Mach number at the exit of the nozzle (Ma) has the following relationship with the throat area (A*)

$$\left(\frac{A}{A^*}\right) = \frac{1}{Ma}\left[\frac{2}{\gamma+1}\left(1+\frac{\gamma-1}{2}Ma^2\right)\right]^{\frac{\gamma+1}{2(\gamma-1)}} \qquad \text{equation 2.2}$$

where γ is the ratio of specific heat. When the exit Mach number is known, the other gas parameters can be obtained using the isentropic gas flow equations and have the following final form with the stagnation conditions ($_0$) where T is temperature, P is pressure and ρ is density.

$$T = \frac{T_o}{\left[1+\left(\frac{\gamma-1}{2}\right)Ma^2\right]} \qquad \text{equation 2.3}$$

$$P = \frac{P_o}{\left[1+\left(\frac{\gamma-1}{2}\right)Ma^2\right]^{\frac{\gamma}{\gamma-1}}} \quad \text{equation 2.4}$$

$$\rho = \frac{\rho_o}{\left[1+\left(\frac{\gamma-1}{2}\right)Ma^2\right]^{\frac{1}{\gamma-1}}} \quad \text{equation 2.5}$$

The velocity can be obtained using the following equation

$$V = Ma\sqrt{\gamma RT} \quad \text{equation 2.6}$$

2.2.2 Particle acceleration model

In cold spraying, the adequacy of the cold spray process is determined by velocity of the particles not the gas stream. It is assumed that the two phase flow (gas and particle) is dilute enough. The mass times the acceleration of the particle can be equated to the drag force of the particle [22, 26] as follows

$$m_p \frac{dV_p}{dt} = m_p V_p \frac{dV_p}{dx} = \frac{C_D A_p \rho \ (V - V_p)^2}{2} \quad \text{equation 2.7}$$

where V_p is the particle velocity, A_p is the cross-sectional area of the particle, C_D is co-efficient of drag, m_p is mass of the particle, t is time and x is the axial distance travelled by the particle. This equation can be integrated if the gas velocity and density are held constant and the drag coefficient is assumed constant. After integration

$$\log\left(\frac{V - V_p}{V}\right) + \frac{V}{V - V_p} - 1 = \frac{C_D A_p \rho x}{2m_p} \quad \text{equation 2.8}$$

For low values of spray particle velocity compared to gas velocity, the equation can be simplified as follows [22]

$$V_p = V\sqrt{\frac{C_D A_p \rho x}{m_p}} \qquad \text{equation 2.9}$$

This relationship states that the spray particle velocity is proportional to square root of the distance travelled over the particle diameter. It should be noted that the drag coefficient and gas density vary over the length of the nozzle [26, 27]. In addition, it has been shown [28-30] that the particle velocity increases with the decrease of particle size and a particle of lower density under the same conditions will reach a higher velocity. However, this high velocity of smaller particles does not necessary contribute to deposition in cold spray due to bow shocks, external to the nozzle which will be explained in section 2.2.4.

2.2.3 Role of gas pressure and temperature

The velocity of the particles in cold spraying is affected by the type of gas used, gas pressure and gas temperature. In the previous section, we have seen how the gas properties depend on the Mach number. However, Mach number is nothing but the ratio of the speed of an object in the medium to the speed of sound in that medium. The equation for speed of sound (a) is expressed as follows

$$a = \sqrt{(\gamma RT / M_w)} \qquad \text{equation 2.10}$$

Where γ is the ratio of specific heats, R is the gas constant, T is the gas temperature, M_w is the molecular weight of the gas. The gas velocity will increase if a gas with lower molecular weight is used (such as helium) or the gas temperature is increased. Van Steenkiste et al. [31] reported that when the pressure downstream of the convergent divergent nozzle is equal to 52.8% of the pressure upstream, in the case of air, the throat of the nozzle is choked (sonic condition). Increase in pressure at upstream will not result in an increase in gas velocity through the throat of the nozzle as a result of this. However, increase in pressure will result in an increase in density, and mass flow rate is a function of

density. So the mass flow rate will increase linearly as a result of pressure increase while the gas velocity remains constant.

2.2.4 Effect of stand-off distance and bow shock

Interaction of particles with the substrates from a fluid mechanics point of view in the cold spraying has been subjected to much research [26, 29, 32-36]. Computational fluid dynamics (CFD) codes and Schlieren images were both used to study the gas and particle properties beyond the nozzle exit. Yin et al. [36] reported a complex wave structure at the nozzle exit which are composed of oblique shock due to overexpansion, expansion waves as a result of interaction with atmospheric boundaries and bow shock due to interaction with the substrate.

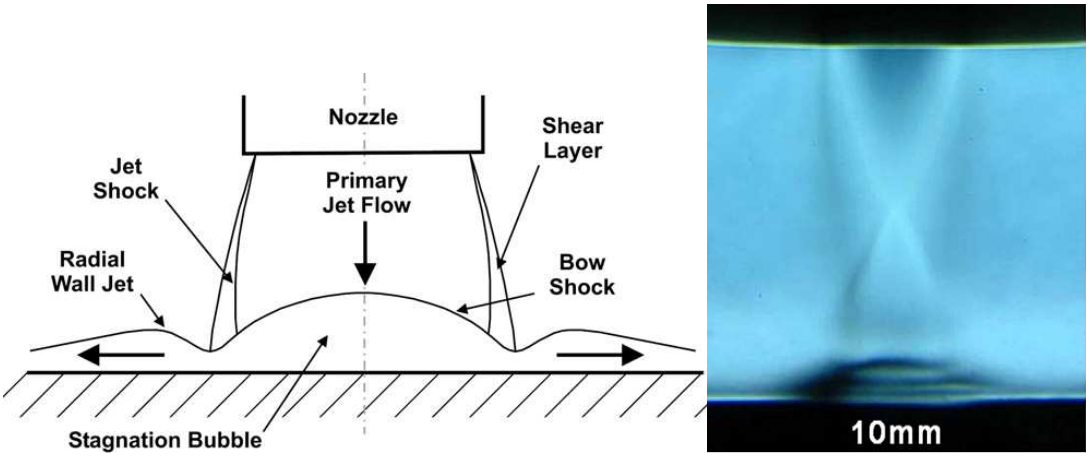

Figure 2-4 (a) Schematic diagram of the supersonic impingement zone at the substrate (b) Schlieren images of bow shock at 10 mm standoff distance from the nozzle [33]

Shockwaves occur as a result of the adjustment of a supersonic flow to downstream conditions; which in cold spraying is the substrate [33]. Figure 2-4 shows the schematic diagram of the interaction zone between the substrate and the supersonic flow. When the gas molecules impact the substrate, there is a change in energy and momentum, and the pressure waves form a normal shock wave. The subsonic flow downstream of shock wave adjusts by taking the form of

a radial jet of the primary jet flow. Since the substrate is perpendicular to the gas flow, the deflection angle is greater than maximum deflection angle for an oblique shockwave and as a result the shockwave is curved and detached- which is called a bow shock [33].

The pressure in the bow shock region is well confined which leads to a sharp increase of pressure and temperature in front of the substrate[36]. The bow shock formed at the interaction zone reduces the velocity of the gas and that of the entrained particles. If the particles are too large and heavy, they will not be accelerated enough within the nozzle, but the deceleration will be modest in the bow shock zone. However, if the particles are too small and light, they might acquire a high velocity but may be decelerated in the bow shock zone [26, 37]. Moreover, Samareh et al. [34] reported that copper particles with a size of <5 μm have a small chance to be deposited on the substrate since they lose their kinetic energy in going through the bow shock.

In addition, as the standoff distance is increased, the free gas jet shows a continual reduction in velocity away from the nozzle and viscous effects of the gas periphery cause the gas velocity to decrease and eventually turn into a subsonic stream [33]. The gas velocity is highest at the centre of the jet and can be imagined as a cone emanating from the nozzle exit. As the standoff distance is increased, the interaction area of this cone and substrate is decreased and the effect of bow shock is also decreased. With increasing standoff distance the bow shock disappears and deposition performance is increased. However, if the standoff is increased beyond an optimum distance the deposition efficiency is decreased due to a decrease of particle velocity [29].

2.3 Bonding mechanisms in cold spraying

The mechanism of bonding in cold spraying is a matter of some debate. A number of hypotheses have been proposed concerning the mechanism by which bonding takes place in cold spraying. The bonding studies undertaken by various researchers in the field can be divided into two categories: mathematical modelling of impact using numerical methods of investigations and experimental investigations using microstructural characterization techniques.

2.3.1 Mathematical modelling using numerical methods

A number of studies on numerical simulation of particle deformation during the cold spraying process have been reported by several researchers [1, 9, 11, 38-51]. The key findings of their studies will be outlined and the proposed bonding theories will be described here. The high strain rate material behaviour in the numerical simulations are described by the well known Johnson-Cook plasticity model which accounts for strain hardening, strain rate hardening and thermal softening of materials [52]. Finite element simulation software ABAQUS Explicit has been widely used in simulating the particle deformation in cold spraying. In addition, the CTH code developed at Sandia National Laboratories for multi-material, large deformation, strong shockwave, solid mechanics cases was also used to simulate the cold spraying process [40]. The first mathematical modelling of an impact of a copper particle onto a copper substrate was performed by Assadi et al. [1] in 2003. Following Assadi's work, using the same methodology Schmidt et al. [11] published a detailed study of critical velocity and critical diameter of a number of materials in 2005. Recently, a study by Bae et al. [39] reported a finite element modelling of 22 different materials using dissimilar particle-substrate combinations.

2.3.1.1 FE modelling of single particle impact in copper

Bond formation in cold spraying is now generally attributed to an adiabatic shear instability which occurs at the particle-substrate interface at or beyond a certain impact velocity called critical velocity. When a spherical particle, travelling at or above the critical velocity, impacts a substrate, a strong pressure field propagates spherically into the particle and substrate from the point of contact (Figure 2-5a). As a result of this pressure field, a shear load is generated which accelerates the material laterally and causes localized shear straining. The shear loading under critical conditions leads to what is termed as adiabatic shear instability where thermal softening is locally dominant over strain and strain rate hardening, which leads to a discontinuous jump in strain and temperature and breakdown of flow stresses [11]. This adiabatic shear instability phenomenon results in viscous flow of material in an outward flowing direction at temperatures close to the melting temperature of the material (Figure 2-5b). This material jetting is also a known phenomenon in explosive welding of materials. The evidence for this material jetting phenomenon is shown in Figure 2-5c which shows SEM images of a bonded particle with a ring of jet type morphology around the impact zone. The mean flattening ratio, defined as the diameter of splat to that of a spherical particle of same volume, was 1.31 for that copper particle.

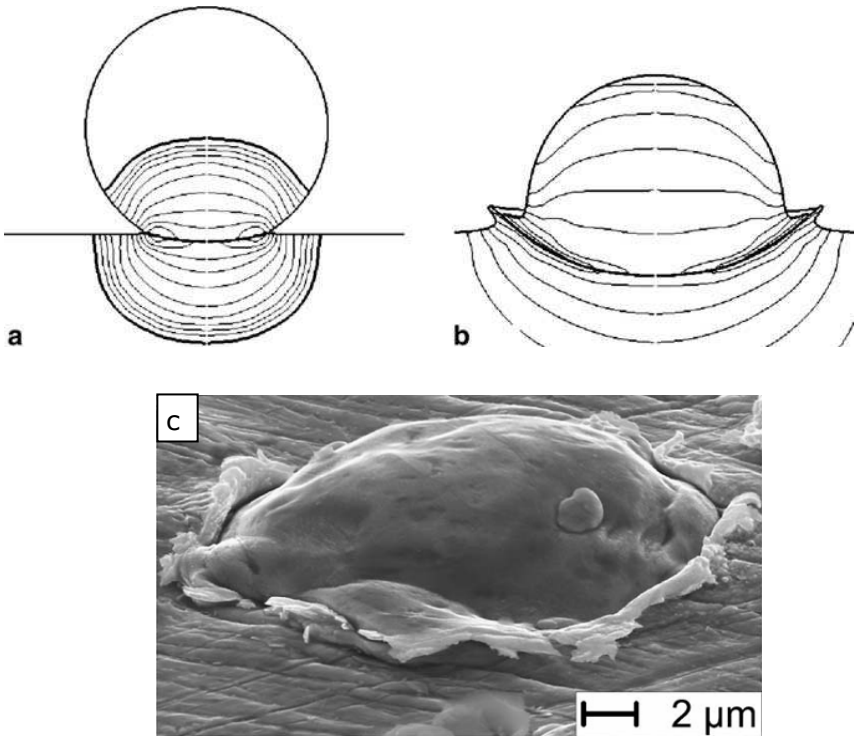

Figure 2-5 (a) Pressure field during impact (b) jetting [11] (c) SEM of a copper particle on a copper substrate [1]

Figure 2-6, from the work of Assadi et al.[1], shows the temporal development of plastic strain, temperature and flow stress at a point on copper particle which went through the highest amount of deformation (jetting) upon impacting a copper substrate for four different impact velocities. When the impacting velocity of the copper particle was 580 m/s there was a significant jump in strain up to a value of 10, which is different from the strain curves for other velocities. A material suitable for cold spray should withstand such severe conditions of plastic flow without fracturing[11]. The increase in velocity possibly changed the material deformation mechanism from plastic to viscous (Figure 2-6a). Similarly, for velocity of 580 m/s the temperature was significantly higher and approached the melting temperature of copper (Figure 2-6b). Figure 2-6c shows the temporal evolution of stress during the deformation of the particle. For the velocity of 580 m/s, after 0.03 µs there is a breakdown of stress which coincides with the increase of strain and temperature. This breakdown of stress could be due to

thermal softening of the material. When the material approaches the melting temperature, the shear strength is lost which results in excessive deformation (i.e. jetting) of the material. This jump in strain and temperature and breakdown of stress is defined as adiabatic shear instability phenomena [1]. Moreover, experimentally determined critical velocity of an inert gas atomized copper powder (-5 +22 μm) was 570 m/s [1].

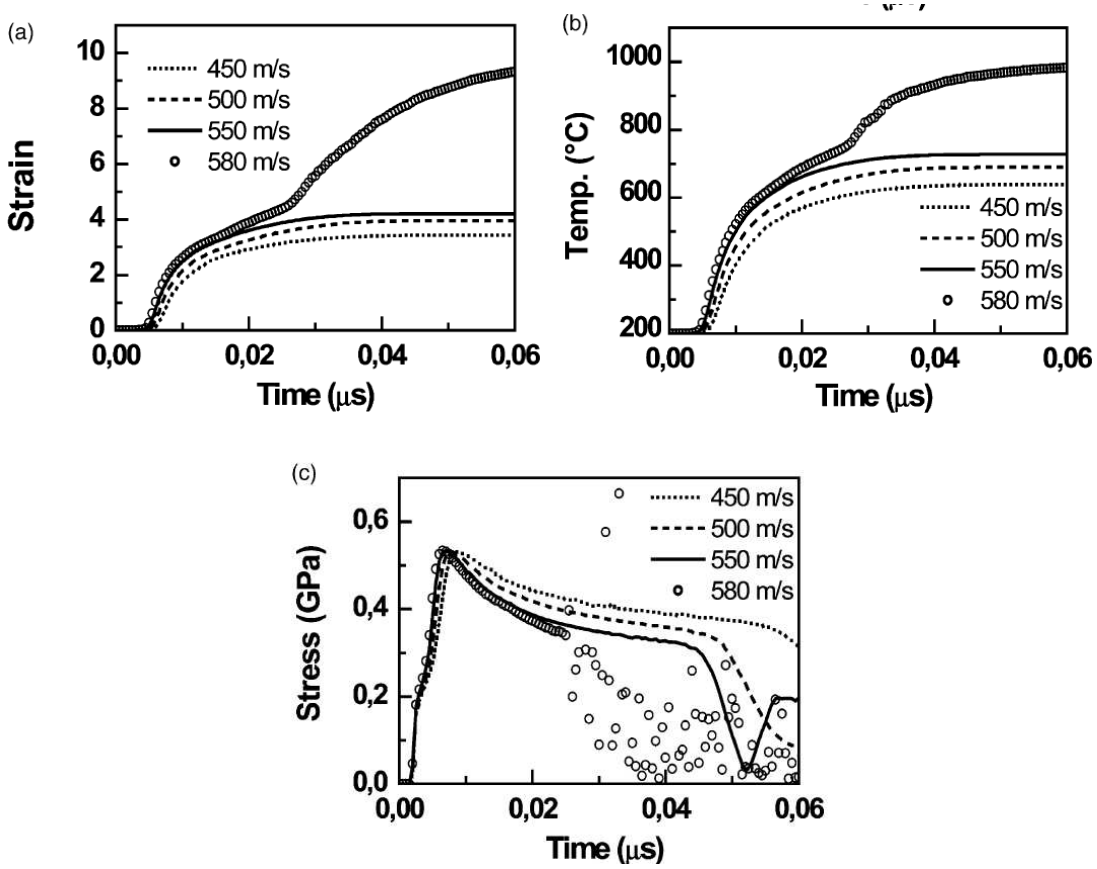

Figure 2-6 Calculated temporal development of (a) plastic strain (b) temperature and (c) flow stress at a critical node of sprayed Cu particle from FE on Cu substrate modelling of Assadi et al. [1]

Also, Grujicic et al. [9] argued that the particle substrate interaction is probably due to adiabatic shear instability not due to atomic diffusion. Due to very short contact time (~ 40ns), the atomic inter diffusion distance would be 0.004- 0.1 nm

which is only a fraction of inter atomic distance, hence atomic diffusion is unlikely to be the dominant mechanisms in cold spray.

2.3.1.2 Critical impact velocity and critical particle diameter

It would thus seem that successful bonding in cold spraying requires localized deformation and an adiabatic shear instability, which occurs when particles travel at a sufficiently high velocity called the critical velocity [1, 11, 26, 49]. Figure 2-7 shows the proposed schematic relationship between deposition efficiency and particle velocity. Deposition efficiency is the mass ratio of deposited to impacting particles. Particles travelling below a certain velocity will result in abrasion of the substrate upon impact. However, particles travelling at or above that certain velocity will result in deposition and coating formation. These relationships lead to the proposal of a cut-off velocity called critical velocity, below which abrasion occurs and above which deposition occurs [30].

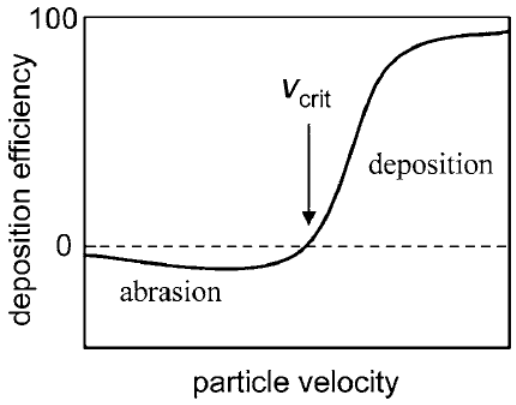

Figure 2-7 Schematic of relationship between particle velocity and deposition efficiency proposed by Gartner et al. [30]

An equation of the critical velocity taking into account of the material properties was proposed by Assadi et al. [1].

$$V_{cr} = 667 - 14\rho_p + 0.08T_m + 0.1\sigma_u - 0.4T_i \quad \text{equation 2.11}$$

Where, ρ_p is the density in g/cm^{3,} T_m is the melting temperature in °C, σ_u is the ultimate tensile strength in MPa and T_i is the initial particle temperature in °C. It can be seen from that equation that critical velocity increases with increasing yield strength and melting temperature and decreases with increasing density and particle temperature. [1].Later, Schmidt et al. [11] provided another equation to calculate the critical velocity of particles using energy balance theories.

$$V_{cr} = \sqrt{\frac{F_1 4\sigma_u \left(1 - \frac{T_i - T_R}{T_m - T_R}\right)}{\rho_p}} + F_2 c_p (T_m - T_i) \quad \text{equation 2.12}$$

Where F_1=1.2 and F_2=0.3 are calibration factors, T_R is reference temperature (293 K) and σ_u is the tensile strength of the material. Figure 2-8 shows the results for calculation of critical velocities for 25 µm particles for different materials. Schmidt's equation provides a better agreement with the experimentally determined critical velocities. This equation provides more accurate predication of critical velocity for materials like tin and tantalum over Assadi's equation.

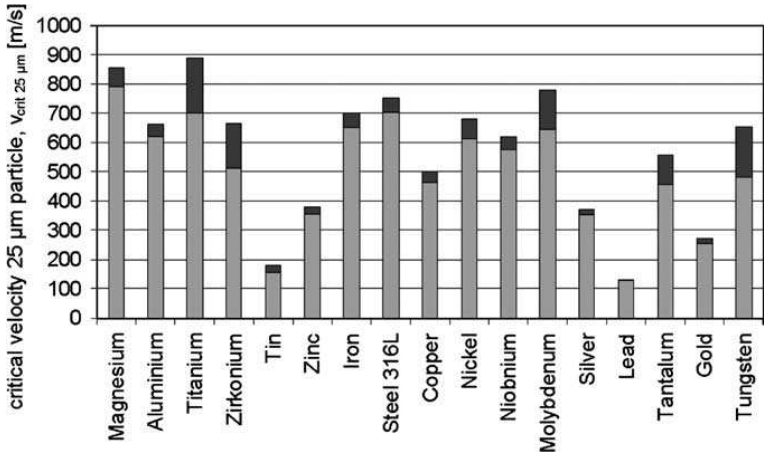

Figure 2-8 Critical impact velocity for a 25 µm particle calculated using Schmidt's equation [11]. The dark grey level indicates the range of uncertainity

Semi-empirical determination of critical velocity is performed by measuring the velocity distribution combined with the measured deposition efficiency and the particle size distribution to calculate the size and the velocity of the largest particle which would bond to the substrate. The corresponding velocity of this largest and slowest bonded particle is taken as the experimentally determined critical velocity [1, 11, 35].

The sizes of the particles also influence the critical velocity [11]. Following the adiabatic shear instability phenomenon, i.e., rapid increase in localized temperature at the bond zone, the rate at which the material loses heat plays an important role in bonding. The cooling rate of the material decreases with increasing particle size. The cooling rate has to be "low enough" to promote shear instability and on the other hand, "high enough" to let the interface solidify and finish the bonding process. Shear instability can be hindered in very small particles due to high temperature gradients and higher strain rate hardening due to a higher strain rate in the small particle. Moreover, smaller particles are exposed to higher quench rates during production which might result in a higher strength and due to higher surface to volume ratio smaller particles will have higher impurity. All these will hinder localized deformation at the onset of adiabatic shear instability and thus increase the critical velocity. Schmidt et al. proposed the following equation for critical dimension of particles

$$d_{crit} = 36\frac{\lambda_p}{c_p \cdot \rho_p \cdot V_p} \quad \text{equation 2.13}$$

where λ_p is the thermal conductivity and c_p is the specific heat of the particle. This equation signifies a critical dimension of particle above which thermal diffusion is slow enough for adiabatic shear instability to occur for an impacting particle. Figure 2-9 shows the critical diameter of different particles measured using the

equation and particle sizes smaller than the critical dimension will not reach adiabatic shear instability criterion.

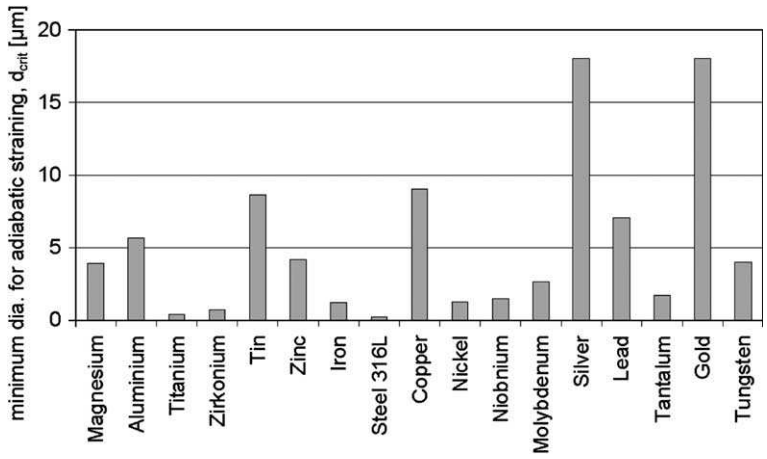

Figure 2-9 Minimum particle diameter for localized adiabatic shear instability for different materials [11]

2.3.1.3 Window of deposition in cold spraying

Figure 2-10 shows the proposed variation in deposition efficiency with particle velocity at a certain temperature [48, 49]. It is argued that at 50% deposition efficiency the corresponding velocity should be defined as the critical velocity [48]. For a ductile spraying material, deposition efficiency increases sharply following increase of the velocity beyond critical velocity reaching a saturation 100% deposition efficiency [48]. Optimum coating conditions can be expected at a region where deposition efficiency is nearly 100%. Beyond the saturation point, increase in particle velocity results in a decrease in deposition efficiency due to hydrodynamic erosion of particles [48, 53]. Cross-sectional images of large scale impact of a 20 mm copper ball impacting a low carbon steel are also shown in Figure 2-10 to illustrate the effect of this phenomenon. The velocity of the particles beyond which no deposition occurs (0% DE) and only results in erosion is defined as erosion velocity. In addition, erosion velocities of different materials can be calculated using Schmidt's equation with factors, F_1=4.8 and F_2= 1.2. The range of velocities between critical velocity and erosion velocity is a window

where material deposition can occur in cold spraying. Brittle materials, like ceramic will result in erosion at any velocity which makes it difficult to deposit using cold spraying.

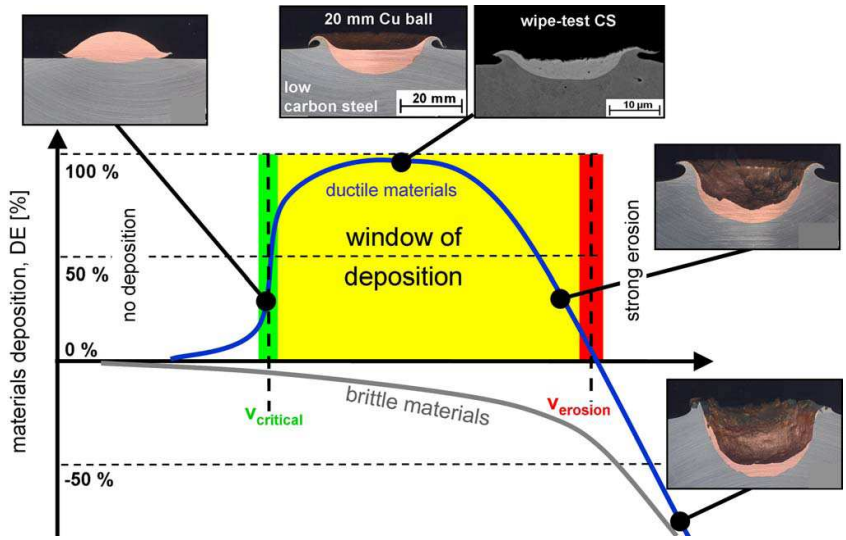

Figure 2-10 Schematic correlation between particle velocity, deposition efficiency and impact effects at constant temperature [48, 49]

Figure 2-11 shows the critical velocity and erosion velocity of particles as a function of temperature proposed by Schmidt et al. [10, 11, 54]. The window of deposition lies between the critical and erosion velocities for any material. Higher particle impact temperature decreases the critical velocity due to thermal softening [35].

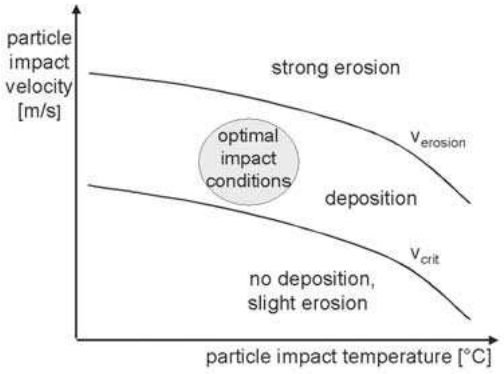

Figure 2-11 Critical velocity and erosion velocity as a function of particle temperature [10, 11]

2.3.1.4 FE modelling of single particle impacts in dissimilar materials

A recent study by Bae et al. [38, 39, 55], which extended the numerical modelling studies of Assadi et al., proposed the existence of a thermal boost up zone (TBZ) induced by adiabatic shear instability to be the dominant mechanism in particle-substrate bonding. Bae et al. suggested that after some incubation time during impact a thermal boost up zone is formed, as shown in Figure 2-12, when the particle is undergoing localized adiabatic shear instability. There is a transition point after which thermal boost up zone is formed. The following equation defines the thermal boostup zone.

$$TBZ\ (Z_{tb}) = H_{tb}.W_{tb} = [(T_{max}-T_r)/T_m][(t_c-t_i)/t_c] \qquad \text{equation 2.14}$$

Where T_{max} is the maximum temperature, T_r is the temperature of transition point, Tm is the melting temperature, t_i is the incubation time and t_c is the total contact time.

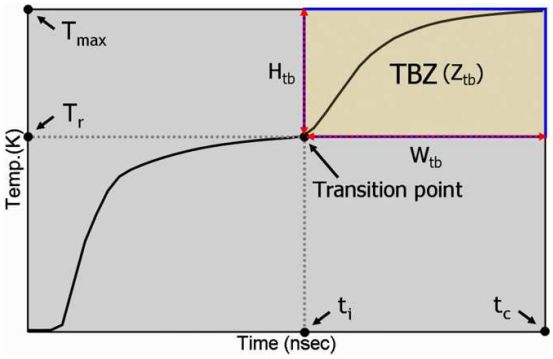

Figure 2-12 Schematics of thermal boost up zone (TBZ) [39]

This thermal boost up zone was used to differentiate different bonding behaviour of materials during impact. In Cu particle impacting a Cu substrate there was a large thermal boost up zone. However, in Al on Al and Ti on Ti both had a smaller thermal boost up zone compared to Cu-Cu, i.e., the thermal boost up zone height and width were both smaller than the Cu-Cu case. The delay in the onset of thermal boost up zone depends on thermal softening and strain, strain rate hardening of the materials. In Al particle impacting mild steel and Ti particle

impacting Al, the reported heating up rate was very high and no "transition point" prior to the thermal boost up zone was observed. In addition, the flow stresses collapsed to zero sharply. Whereas in Cu-Cu case, the flow stress fluctuated due to a competition between thermal softening and work hardening. The authors argued that the highly saturated temperature and low flow stress contributed to high adhesion and low rebound energy [56].

2.3.1.5 Particle-substrate impact behaviour

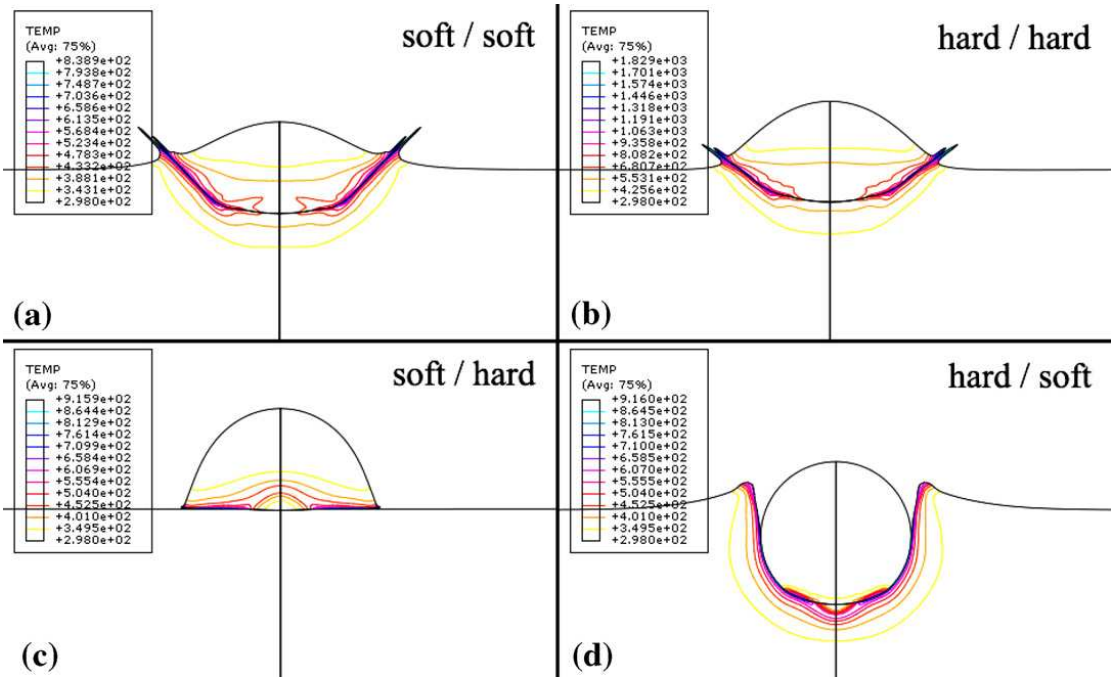

Figure 2-13Four cases of particle impact onto substrate (a) soft/soft (Al onto Al at 775 m/s) (b) hard/hard (Ti onto Ti at 865 m/s) (c) soft/hard (Al onto mild steel at 365 m/s) (d) hard/soft (Ti onto Al at 655 m/s) [39]

Deformation behaviour of four categories of particle-substrate combinations in cold spraying has been reported by be Bae et al [39]. In the case of soft particle /soft substrate (Al/Al), large deformation was observed as compared to hard particle /hard substrate (Ti/Ti) due to low material strengths in the former case. In both cases, the authors found higher temperature at the substrate side as

compared to the particle side. In the other two cases of soft particle /hard substrate (Al/mild steel) and hard particle /soft substrate (Ti/Al), the deformation occurred in the relative soft counterpart. In addition, a much higher temperature was achieved in the softer side. The authors classified 22 materials combination into the above four different categories and reported a detailed study on critical velocities, critical sizes, contact areas and contact time in reference [39].

2.3.1.6 Multiple particle impact

Recently a number of numerical simulations on multiple particle impact behaviour in coating formation in cold spraying have been reported in literature [36, 38, 57]. A study by Yin et al. [36] concluded that the interaction between copper particles during deposition plays an important role in particle deformation and coating formation. In another study, Yin et al.[57] examined the role of different simulation methods in multiple particle impact including Eulerian method, Lagrangian method and smoother particle hydrodynamics methods (SPH). It was suggested that the Eulerian method provided results comparable to the experimental investigations. In addition, multiple particle impact of titanium particles in cold spraying was also studied by Bae et al. [38, 55].

2.3.1.7 Rebound energy

Wu et al. [56] proposed a model based on experimental results to explain the bonding in cold spraying. It was proposed that bonding in cold spraying is a result of a competition of adhesion energy and rebound energy. The researchers experimentally observed the effect of velocities in deposition over a wide range (i.e., below critical velocity and above erosion velocity). Adhesion energy (Ad) is defined as the energy required to detach a bonded particle from the substrate. $Ad=a\%\ Ad_{max}$, where Ad_{max} is the maximum adhesion energy and a% is the fraction of bonded atoms per unit of adhesive interface. Kurochkin et al. proposed the following formula to calculate a% [58]

$$a\% = 1 - \exp\left\{ - \upsilon t_c \exp\left[\frac{-E_a}{kT_c + (1 - e_r) M_a V_p^2 / 2} \right] \right\} \quad \text{equation 2.15}$$

Where υ is the natural frequency of Eigen-oscillations of atoms in lattice, t_c is contact time, E_a is activation energy, T_c is contact temperature, k is Boltzman constant, e_r is recoil coefficient, M_a is the atomic mass and V_p is the velocity of the impacting particle.

$$Ad_{max} = S_c N_a E_1 \quad \text{equation 2.16}$$

Where S_c is the contact area of a single particle to substrate, N_a is the total number of atoms in unit plane and E_1 is the energy of a single bond between two atoms.

Rebound energy is defined as the energy required to bounce the particle from the substrate during the unloading moment during deposition. Rebound energy (Re) is expressed as

$$R = \frac{1}{2} e_r m_p V_p^2 \quad \text{equation 2.17}$$

Where m_p and V_p are mass and velocity of the particles and e_r is the recoil coefficient. Figure 2-14 shows the calculated adhesion energy and rebound energy of three sizes (25 μm, 30 μm & 50 μm) of Al-Si particles at different velocity. The particle will only attach to the substrate when the adhesion energy is higher than the rebound energy. When the particle velocity is below the critical velocity and above the erosion velocity, the rebound energy is above the adhesion energy and no deposition can occur.

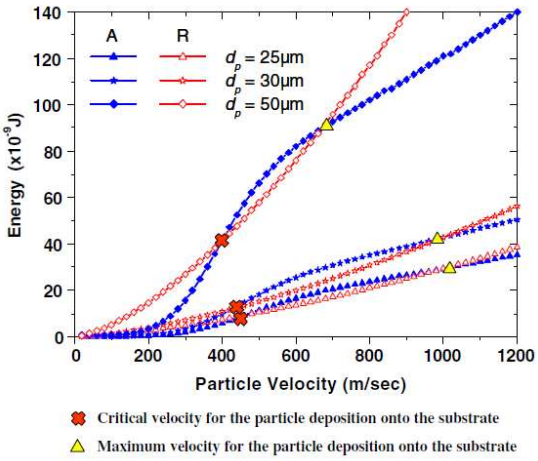

Figure 2-14 Calculated adhesion energy and rebound energy for various sized Al-Si feedstock impacting onto mild steel [56]

2.3.2 Experimental investigations

A number of experimental studies to explore the particle-substrate interaction in cold spraying to understand the bonding phenomena have been reported [4, 31, 35, 50, 51, 59-72]. This section summarizes the experimental findings on bonding behaviour in cold spraying and the factors which influence bonding.

2.3.2.1 Shear lip formation and cratering of substrates

Early observations of particle-substrate interactions in cold spraying showed shear lips formation at the interface of deposited particles and crater formation of the substrate from the rebounded particles. Papyrin et al. [5] studied the interaction of individual aluminium particles with the copper substrate at different velocities to investigate the transition from rebound to adhesion of particles. At a lower particle velocity there were individual craters formed by the particle impact and there were no deposited particles. With increasing the particle velocity, particles started adhering to the substrate. These experiments showed that beyond a threshold velocity of the particles, critical velocity, a transition from substrate erosion to deposition occurs. The jet type morphology of shear lips

around the deposited copper particles onto copper substrate was reported by Assadi et al. [1]. This jet type morphology was not noticed on the craters at the substrate left by non-adhering particles. Moreover, in a study of cold spraying of copper particle onto steel substrate, Dykhuizen et al. [64] reported that the crater formation is dependent on the particle velocity, i.e. with increasing the velocity the depth of the crater also increases.

2.3.2.2 Role of surface deformation and surface oxide

It has been proposed that the first layer of coating buildup (i.e., deposition of particles onto the substrate) involves, substrate surface cratering and activation of the surface by removing any surface contamination [5, 70, 71, 73]. Papyrin et al. argued that the first impinging particles increase the chemical activity of the surface by elevating the dislocation concentrations on the very top layer [73]. During the particle deformation phenomena, the oxide shells on the interacting surfaces are broken and clean surfaces are pressed together and thus bonded. It has also been proposed that the interfacial material jet produced from adiabatic shear instability phenomena helps in removing the oxide films from the surface and thus enable an intimate metal-to-metal contact to be established [1, 11, 64, 71]. In addition, Grujicic et al. [9] argued that adhesion might also be a mechanism for particle bonding. Adhesion on the nano scale involves atomic interactions between the contacting clean interface and high contact pressures to make the surfaces mutually conforming. The removal of surface oxides by a material jet produced by adiabatic shear instability can in principle, provide clean surface for adhesion between two mutually conforming regions.

Kang et al. [65] and Li et al. [66] studied the role of oxide content of the powder on critical velocity for deposition. It was argued that the critical velocity of material does not only depend on material properties but also on oxidation condition. It was found that increasing the oxide content of the copper powder

from 0.02 wt.% to 0.38 wt.%, the critical velocity increased from 300 m /s to 610 m /s [66]. In addition, Kang et al. [65] studied the role of oxide content of aluminium feedstock powder on critical velocity. It was reported that increasing the oxide content of the same powder size distribution from 0.001 wt.% to 0.045 wt.% increased the critical velocity from 742 m /s to 867 m /s. It was suggested that the critical velocity also depended on the oxide scale thickness. The thicker the oxide scale is, the more energy is required to remove the oxide and less plastic deformation energy is dissipated into the particle. Moreover, an increase in oxide content resulted in a decrease in particle flatting ratio. It is believed that the adiabatic shear instability at the particle-substrate interface can disrupt the oxide film; however, some part of the oxide remains at the interface which hinders particle-substrate adhesion. Figure 2-15 shows the presence of aluminium oxide at the interface of aluminium particle and substrate in a TEM image [65]. It was argued that the deformation of the particle was unable to remove the surface oxide layer.

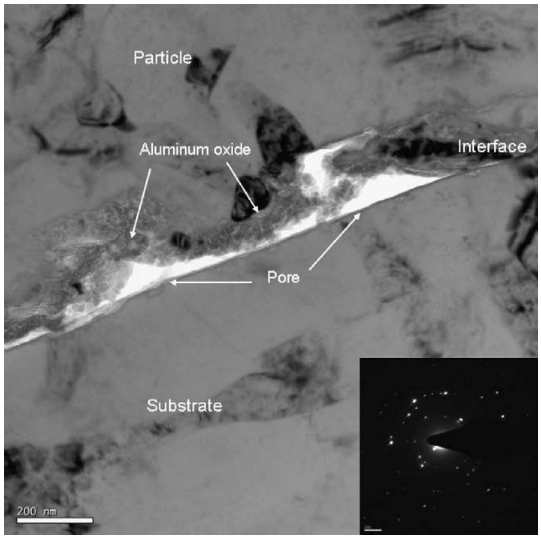

Figure 2-15 FE-TEM micrographs: bright field image of interface between aluminium powder and substrate showing aluminium oxide layer [65]

In recent years, a number of TEM investigations of the interface of cold sprayed copper particles onto aluminium substrates have been published [51, 60, 61, 74].

In one study, it was argued that the bonding occurred between cold sprayed copper splats because of the two oxide films, which were on two separate particle surfaces, fused together to form one continuous layer. In addition, the particle surface could reach a very high temperature resulting in releasing of oxygen which could get trapped in the liquid film. At the copper particle-aluminium substrate interface a number of different phases including nano-crystallized phases and intermetallics were present within a thickness of ~20 nm, except the bottom of the splat. The authors argued that the thickness of the intermediate phases suggest that diffusion occurred in a liquid state than in a solid state [51, 60, 61]. It was hypothesized that transient melting might act as a mechanism in Cu-Al interaction. King et al. [74] also reported melting of aluminium substrate at the crater wall where the copper particle slid past aluminium. It was suggested that adhesion was promoted from the solid material jetting and molten material jetting, which also contributed to mechanical interlocking [51].

2.3.2.3 Characterization of bond formation

Price et al. [4, 24] proposed a method to characterize the bonding between aluminium and copper particles following deposition by cold spraying. A blended copper-aluminium powder was cold sprayed and subsequently heat treated at 400 °C to form a layer of intermetallic where the true metal-to-metal contact had occurred. Figure 2-16 shows the BSE image of a heat treated copper-aluminium cold sprayed deposit showing formation of intermetallic where the metal-to-metal bond had established. In other regions, metal-to-metal contact was inhibited by a thin layer of surface oxide film. It was reported that by increasing the particle in-flight velocity, a greater degree of particle deformation and hence a greater metal-to-metal contact between particles was established.

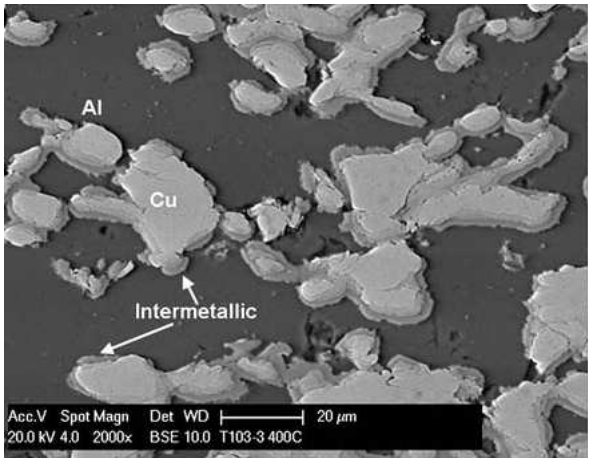

Figure 2-16 BSE image of heat-treated Cu-Al deposits showing intermetallic layer as an indicator of metal-to-metal bond formation [4]

2.3.2.4 Interfacial curvature and instability phenomena

The nano-micro scale mechanical material mixing at the cold sprayed coating substrate interface was observed by several researchers [40, 53, 62, 75]. They attributed this mixing phenomenon to Kelvin- Helmholtz instability mechanism. In the Kelvin-Helmholtz instability phenomenon, when two fluids in contact are moving at different velocities parallel to each other, instability can occur (due to non-zero curvature of the interface) and one fluid flows around the other, a centrifugal force is generated. This centrifugal force might also promote amplification of the interfacial perturbation.

Champagne et al. [62] provided the following equation to estimate particle velocity required for interfacial material mixing

$$V_p = \left[(7.5\times10^4)\left(\frac{B'}{\rho_p}\right)\right]^{0.5} \qquad \text{equation 2.18}$$

Where V_p is the particle velocity, B' is the Brinell hardness number of the substrate and ρ_p is the density of the coating material. This equation shows that the interfacial material mixing depends on substrate hardness and coating

material density. This interfacial material mixing may also be responsible for mechanical interlocking of the coating and substrate [53]. In addition, Klinkov et al.[53] proposed a mechanism called-"sticking" to explain the bonding in cold spraying. In "sticking", the particle first sticks to the substrate due to Van Der Waals or electrostatic forces, and strong adhesion is only formed when incoming particles impact onto sticking particles.

2.3.2.5 Coating build up mechanisms

Van Steenkiste et al. [71] studied the formation of cold sprayed aluminium coating with a relatively large powder particles (>50μm) and proposed a model to explain the coating build up process. The model was composed of four basic stages: in stage 1 the substrate surface is activated by substrate cratering and a first layer of coating is built up by fracturing the surface oxide layer, in stage 2 the particles deform and realign as a result of successive particle impact, in stage 3 metallic bond is formed which also results in a reduction of porosity and in the final stage the coating is further densified and work hardened. The four stages of coating build up is schematically shown in Figure 2-17.

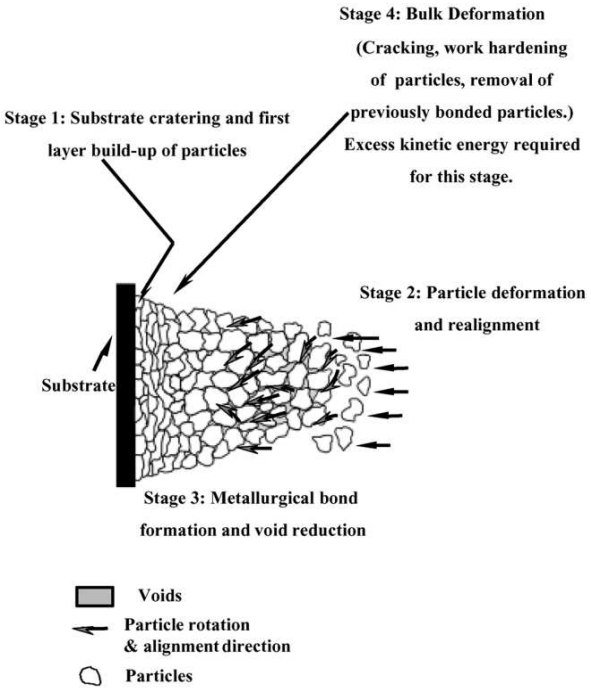

Figure 2-17 Stages in coating formation in kinetic spray process [71]

2.3.2.6 Role of surface preparations

To date, the effect of substrate surface preparation in bond formation has not been investigated widely. Marrocco et al. [76] explored the effect of different surface preparation techniques in controlling the bond strength of a cold sprayed titanium coating on Ti6Al4V. They proposed that grit-blasting of the Ti6Al4V substrate caused work hardening, which subsequently limited its deformation by impact of a titanium particle during cold spraying; it was argued that this restriction of substrate deformation resulted in less effective removal of surface oxide and thus led to lower bond strengths being observed. Wu et al. [77] studied an Al-Si coating, cold sprayed onto both polished and grit-blasted mild steel. Micro-pores and defects were found in the grit-blasted surface while an "intimate" interface was found following deposition onto a polished substrate; it was argued that the micro-pores on the grit-blasted surface resulted in lower bond strengths being observed. They also reported higher bond strength with increasing particle incident velocity. In contrast to the work of Marrocco et al. [76] and Wu et al. [77], Makinen et al. [78] found higher bond strengths for a copper deposit cold sprayed onto a grit-blasted copper surface compared to that observed for deposition onto an as-received surface.

The effect of substrate surface preparation on the deposition efficiency of the process has also been assessed. Sakaki et al. [79] reported a slight increase in the deposition efficiency of cold spraying copper and titanium by increasing substrate surface roughness (grit-blasted substrate compared to polished substrate). Richer et al. [80] also reported an increase in deposition efficiency in spraying an aluminium alloy particle onto a coarser grit-blasted surface when compared to a finer grit-blasted surface. However, the substrate surface roughness has an effect only on the first few layers of coating deposited, and as such, the effect on deposition efficiency may be small, depending upon the

significance of the coating initiation stage in the total time for coating development.

2.3.3 Summary of bonding mechanisms

It is generally accepted that upon impact of a particle under certain conditions onto the substrate, the material goes through adiabatic shear instability phenomenon where thermal softening dominates over strain hardening and strain rate hardening and a material jet is produced. This material jet removes any surface oxide layer or contamination from the metal surface, so that freshly exposed metal surfaces come together to form a bond. A number of TEM studies have also showed evidence of ruptured oxide layer at the particle-substrate interface. In addition, adiabatic shear instability phenomenon to occur at the particle-substrate interface, the particle has to travel at a velocity higher than critical velocity and has a diameter larger than critical diameter. Moreover, there exists a window of particle velocities, within which deposition of particle can occur without erosion. It was also argued that bonding in cold spraying depends on a competition between plastic adhesion energy and elastic rebound energy.

In summary, the localized deformation and adiabatic shear instability play an important role in particle-substrate deformation. However, the actual mechanism by which this thermal softening and adiabatic heating promote bonding is not yet clear. In addition, numerical simulations of particle impact in cold-spraying provide valuable information about the high stain rate deformation behaviour of materials, but are unable to provide a clear indication of the conditions under which intimate metallic bonding is established.

2.4 Cold spraying of copper

The microstructure of cold sprayed copper coatings has been extensively studied over a decade using optical microscope, scanning electron microscope, focused ion beam (FIB) lift out, transmission electron microscope and a number of other techniques [18, 74, 81-90]. The microstructure of the cold sprayed copper coating is made up of highly deformed "pancake shaped" splats with near zero porosity, as measured by electrochemical tests [91]. The properties of this face centred cubic (fcc) copper make it an ideal candidate for cold spraying [83]. TEM analysis of copper coatings revealed high dislocation densities and dynamic re-crystallization with grain refinement down to submicron levels, even in some cases static re-crystallization [18, 83]. King et al. [90] investigated the microstructure of individual copper particle using FIB and reported microstructure refinement at the particle-substrate interface due to severe plastic deformation. At the side of the copper particle the average strain of the metal reached around fifty percent. In addition, the dislocation density of copper coatings measured using XRD diffraction was reported to be in the range of ~3-4 $\times 10^{15}$ /m^2 [85], which indicates severe plastic deformation of the particles. Also the oxide content of the copper coatings following cold spraying was comparable to the bulk material.

Heat treatment to modify the microstructure of copper coatings and improve mechanical properties has been widely used [86, 87, 92]. In cold sprayed coatings, mainly recovery and re-crystallization during annealing determine the microstructural development of the coatings. Cold sprayed copper shows similar performance as highly deformed bulk material when sprayed with helium. However, following annealing of the sprayed deposit, strength and elongation to failure develop in a similar manner to cold rolled bulk material [87, 92]. The diffusion during annealing closes the interparticle pores and reduces the number

of crack propagation sites. Moreover, it was reported that cold sprayed copper can achieve 90% of the bulk electrical conductivity following annealing, which is significantly higher than HVOF or arc sprayed copper coatings [86].

2.5 Cold spraying of aluminium

After copper, aluminium is the most widely used material for cold spraying because of the availability of the suitable powder sizes and ductile properties [21, 37, 71, 75, 93-95]. However, the role of a stable oxide film of aluminium in bond formation in cold spraying has been a matter of much debate. It was argued that the oxide shell fracture is consistent with the threshold velocity of coating formation [71]. Critical velocity of an inert gas atomized aluminium powder with particle size below 45 μm was reported to be 660 m/s [1]. It was reported that aluminium coating showed anistropic behaviour in bond formation and particle deformation. Zhang et al. [93] investigated the role of different substrates on bond formation in cold spraying of aluminium and concluded that metallic substrates harder than aluminium particles generally promoted deposition. TEM investigations of aluminium coating showed presence of oxide layer at the interface of splats, but it was argued that multiple non depositing particles contributed in breaking down oxides from the surface of aluminium splats during cold spraying [75]. Dislocation pile-up was observed in the microstructure, in absence of any substrate, resulting in higher hardness of the aluminium coating than the bulk. Hall et al. [96] demonstrated that it was possible to create homogenous nanocrystalline microstructure from an ultra fine grained aluminium powder. A recent study by King et al. [97] showed that the flattening ratio of aluminium particle onto ceramic substrate decreases with a decrease in particle size, particle deformation is significantly limited for particles smaller than 5 μm.

Mechanical properties of cold-sprayed aluminium coatings were reported in a number of studies [71, 94, 98]. It was reported that the coating elastic modulus was half of the bulk aluminium due to incomplete bonding between particles [71, 94]. The residual stresses in aluminium coating were virtually non-existent [94] compared to thermal sprayed coating due to an absence of quenching and thermal stresses. In addition, depth profiling of coatings prepared from multiple passes showed tensile peaks at the interface between two tracks [98]. Moreover, the ultimate tensile strength was higher than that of the bulk material due to work hardening from plastic deformation. However, annealing treatment of aluminium coatings promoted ductile behaviour due to softening of the particles.

2.6 Interdiffusion of Cu-Al and Ti-Fe

Formation of intermetallic can be used to investigate the level of bonding between a substrate and coating if two dissimilar metals are known to form intermetallic at elevated temperature. In light of this, copper and aluminium form a number of intermetallics phases at various temperatures under equilibrium conditions, as can be seen from Figure 2-18. A number of studies on diffusion bonding of commercially pure copper and aluminium have documented this phenomenon from a thermodynamics view point in literature [99-101]. It was reported that five different intermetallic phases: θ ($CuAl_2$), η_2 (CuAl), ζ_2 (Cu_4Al_3), δ (Cu_3Al_2) and γ_1 (Cu_9Al_4) exist at the interdiffusion zone of the copper-aluminium couple when heat treated to 400°C [100]. The intermetallic development at elevated temperature follows solute diffusion controlled process. In addition, the growth kinetics of intermetallic layers and diffusion coefficients were calculated by Manna et al. [101] and Funamizu et al. [100]. It was reported that aluminium diffuses more rapidly than copper. Moreover, growth kinetics was found to increase with increasing cold work due to crystal defects increasing solute diffusivity. The dissolution process of surface oxide film during diffusion bonding on copper was theoretically and experimentally studied by Takahashi et al. [102]. Dissolution of

copper oxide occurs at temperature above >700 K for a prolonged heat treatment time (10^8 seconds). Dissolution time of copper oxide increases with increasing oxide thickness on the surface. In contrast to copper, aluminium has a high oxide stability and low oxygen solubility which does not dissolve during the diffusion bonding process.

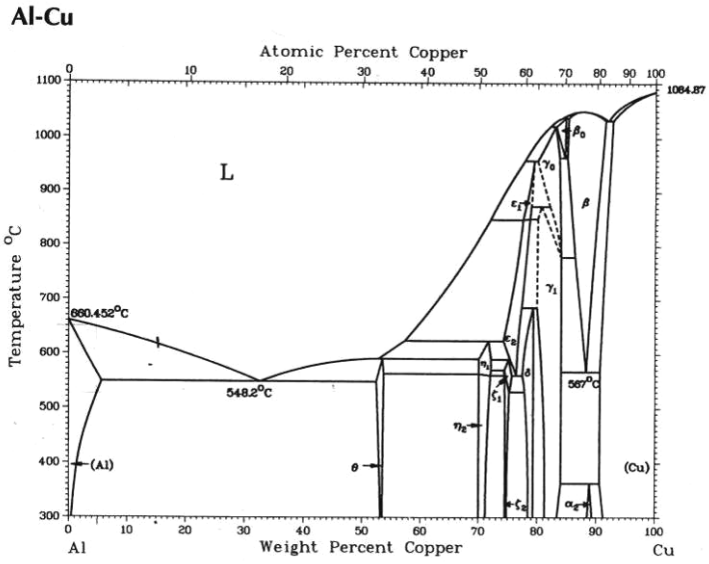

Figure 2-18 Al-Cu phase diagram [103]

Binary iron-titanium phase diagram in Figure 2-19 shows two intermetallics phases: TiFe (51.3 - 54.1 wt.% of iron), and $TiFe_2$ (68.2-75.4 wt.%) of iron; both of those form at temperatures above 400°C. Previous studies in diffusion bonding of commercially pure titanium to austenitic stainless steel showed formation of solid solutions and intermetallics at 700- 950°C [2, 3] and annealing heat treatment of explosively bonded commercially pure titanium to carbon steel showed formation of various intermetallic compounds at 750°C [104]. In addition, Momono et al. [105] observed a discontinuous dark layer consisting of TiC on diffusion bonded joint of commercially pure titanium with mild steel at 880 °C. It was argued that TiC suppresses the diffusion of titanium and iron. However, in the diffusion bonded joints of commercially pure titanium with low carbon steel

(0.01% C), there was no formation of TiC. The formation of different phases across the diffusion bonded titanium-iron couple depends on the carbon content [105]. In addition, titanium has a very high solubility of oxygen, i.e. the dissolution time for a <10 nm thick titanium oxide is less than a minute at temperatures higher than 1000 K [102].

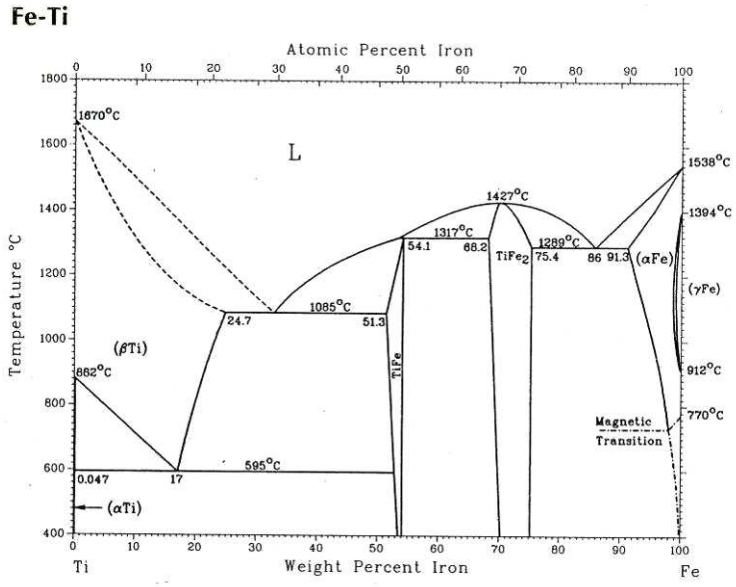

Figure 2-19 Ti-Fe phase diagram [103]

2.7 Cold spraying of titanium

Cold spraying of copper and aluminium has been widely explored in the last decade, now it is of growing interest to the scientific and engineering communities to explore the potential of titanium and its alloys. Titanium as a barrier layer has a great potential for corrosion resistant applications and as a material for near net shaped manufacturing for the aerospace industry where reducing the machining cost is a key factor [106]. Moreover, titanium has found many applications due to its bio-inertness [107]. A recent study on cold sprayed titanium for medical engineering showed that a titanium coating can be successfully used in the acetabular cup of a femoral component and vertebral prosthesis [108].

The potential difficulties in cold spraying of titanium are due to its high critical velocity, high reactivity with oxygen and crystal structure. The critical velocity of a 25 μm titanium particle is ~750 m/s, as calculated by numerical simulation, which is significantly higher compared to copper and aluminium [11]. Moreover, the high reactivity of titanium with oxygen at high temperature makes it challenging to spray titanium at higher process gas temperatures [109]. Furthermore, the hexagonal closed packed (hcp) crystal structure of titanium makes it difficult to deform the particles sufficiently to achieve a pore free coating [76].

2.7.1 Powder feedstock for titanium

Cold sprayed titanium coatings have been prepared from both angular feedstock powder and spherical feedstock powder [16, 76, 110-113]. Angular feedstock titanium powder is produced from hydride- dehydride process and spherical titanium powder is produced via inert gas atomization or plasma atomization process. In hydride-dehydride process, titanium is first hydrated by heating in a hydrogen atmosphere, the brittle titanium hydride compound is then easily crushed to desired size ranges which is then dehydried by heating in a vacuum [114]. In gas atomization process, a molten bath of titanium metal is levitated in a water cooled titanium shell (skull) to avoid contamination, and the molten metal flows through a nozzle which is then broken up using an inter gas into discrete particles. In plasma atomization process, there is no molten bath, titanium is fed in a wire form and plasma torches melt and atomize the powder in a vacuum [114-116]. The flowability of the spherical powder shows superior behaviour over angular titanium powder, which is desirable for uninterrupted powder feeding in various spraying process. However, the processing route for spherical titanium powder makes the end product quite expensive, i.e., a kilogram of spherical

titanium powder with size ranges suitable for cold spraying is five times more expensive than that of angular powder.

2.7.2 Deposition efficiency and critical velocity for titanium powders

2.7.2.1 Deposition efficiency of titanium powders

Deposition efficiency of a material is calculated as a ratio of mass of bonded particles to the mass of the sprayed particles. Deposition efficiency of a material depends on process parameters and properties of the particle and substrate. Blose et al [117-119] reported that deposition efficiency of angular titanium powder with mean particle size of 21 μm onto titanium substrate is 85%, which means 85% weight of the sprayed particles deposited on the substrate. The coating was prepared using helium as a propellant gas at 2.1-2.8 MPa and 400-500°C. Bae et al. [38] showed that an increase in particle velocity and temperature results in an increase in deposition efficiency of cold sprayed titanium onto mild steel. Increasing the particle velocity from 650 m/s to 950 m/s resulted in an increase in deposition efficiency from 85 % to 98 %. Moreover, increased particle temperature, using a powder preheating system, resulted in a higher deposition efficiency of titanium when the particle velocity was kept constant. Higher particle temperature could enhance the adiabatic shear instability zone and due to low thermal conductivity of titanium result in a higher plastic deformation zone. Wong et al. [16, 111, 112] reported a deposition efficiency up to 100% using both angular and spherical titanium powder sprayed onto mild steel substrate. The authors reported that above an average velocity of 688 m /s the deposition efficiency reaches 100% [111, 112].

2.7.2.2 Critical velocity of titanium powders

Cold spray coating deposition is significantly influenced by the velocity of the particles and there exists a velocity called critical velocity, beyond which successful deposition can occur. A number of particle velocity measurement studies of titanium powders have been reported by several researchers [16, 112, 120-122]**.** In the particle image measurement technique, velocity is measured by determining particle displacement over a short period of time using pulsed laser. Several methods exist in the ways critical velocities are measured. In numerical modelling, critical velocity is the velocity at which adiabatic shear instability occurs. In particle velocity measurements, critical velocity is the velocity when the transition from erosion to deposition occurs. Critical velocity can also be estimated from a knowledge of deposition efficiency, particle velocity and particle size distribution. Marrocco et al. [76] estimated the critical velocity by this method to be ~690 m/s for angular titanium powder. Schmidt et al. [11] numerically modelled the particle impact deformation behaviour using a finite element model and reported a critical velocity of around 750 m/s for a 25 μm titanium particle. Wong et al. [112] measured the critical velocity of spherical titanium powder (mean diameter 29 μm) using particle image velocimetry to be between 505 -610 m /s. It was also reported that a higher particle temperature leads to a lower critical velocity of titanium due to thermal softening of the particles.

2.7.2.3 Effect of particle velocity and temperature

Particle velocity and temperature are the two most important factors in coating formation. Beyond the limit of critical velocity, a further increase in particle velocity results in decrease in coating porosity. A recent study by Wong et al. [16] using optimized process parameters and nozzle design achieved an average velocity of 1173 m/s using helium as a accelerant gas. As a result of this high velocity, the coating produced was less porous. It was also reported that an

increase in particle velocity results in a smoother coating surface due to better packing and contact between splats [123]. In wipe tests of spherical titanium particles onto titanium substrates, it was seen that with increasing particle velocity and temperature, the degree of splat formation and jetting was increased [121].

The morphology of the powder also influences the velocity of the particles in the gas stream. It was observed that the velocity of angular titanium particle was always higher than the velocity of spherical titanium particles for the exact same conditions. It was argued that the drag coefficient of angular powder is higher than spherical powder with the same mass, hence acceleration for angular powder is higher [111].

Zahiri et al. [122, 124] measured the velocity distribution of the supersonic plume at various process gas pressures and temperatures. An increase in the process gas temperature contributed to an acceleration of in-flight particles at the vicinity of nozzle exit. However, an increase in process gas pressure expanded the region of the high velocity particles within the gas stream outside the nozzle. The particles at the centre of the nozzle had a higher particle velocity compared to the particles at the edge showing a bell shaped particle distribution. Moreover, it was reported that using helium as an accelerant gas significantly increases the high velocity plume outside the nozzle compared to heated nitrogen gas as an accelerant.

2.7.3 Bond strength

Bond strength values of cold sprayed commercially pure titanium coatings onto mild steel and Ti6Al4V alloy substrates have been reported by several researchers [38, 76, 125-127]. The bond strength tests of the coatings were normally carried

out according to the ASTM C633 standard. The deposit was glued to a counterpart using thermal curing epoxy and then pulled apart. A low bond strength value of cold sprayed titanium coating onto mild steel substrate has typically been reported in the literature (i.e., ~20 MPa). This should be compared with typical HVOF sprayed WC-Co coating where pull-off strength is >80 MPa. However, improvement of cold spraying apparatus, gun design and optimizing process conditions has resulted in an increase in bond strength values. Bond strength value of cold sprayed coating is a function of particle velocity and hence plastic deformation upon impact. A recent study by Bae et al. [38] reported a bond strength value of at least as high as 85 MPa (strength of the epoxy was 85 MPa) for cold sprayed titanium coating onto mild steel substrate. A commercially available CGT Kinetics cold spray system with helium as a propellant gas was used to reach a particle velocity of 950 m/s. It should also be noted that the surface of the mild steel substrate was prepared in a grit blasted finish with a coarse grit (350 μm) which also contributed to mechanical interlocking of the coating with the substrate. Wong et al. [111] also reported that grit blasting of mild steel with size 24 (~764 μm) alumina as a method of surface preparation produced strong bonding with a titanium deposit. However, the role of surface preparation in cold spraying of titanium coatings has not been explored intensively. Marrocco et al. [76] and Price et al. [127] both reported a decrease in bond strength values of cold sprayed titanium coatings when the substrate was grit blasted. It was argued that the work hardening phenomena associated with grit blasting might have made it difficult for the sprayed particle to bond to the substrate.

References	Bond Strength (MPa)	Substrate	Substrate preparation	Process conditions
Wang et al. [125]	8-16	Mild steel	Grit blasted (24 mesh alumina)	Xi'an Jiaotong University, N_2/Air and angular Ti
Li et al. [126]	15 ± 4	Mild steel	Grit blasted	CGT system, air and angular Ti
Bae et al. [38]	50-85	Mild Steel	Grit blasted (350 μm alumina)	CGT 3000, using N_2/ He and spherical Ti
Marrocco et al. [76]	7- 22	Ti6Al4V	Polished, ground and grit blasted	University of Nottingham system, room temp He and angular Ti
Price et al. [127]	32-37	Ti6Al4V	As received and grit blasted	University of Nottingham, room temperature He and angular Ti

Table 2-1 Pull-off bond strength values of Ti coatings

A new method; a modified ball bond shear test method, to measure the adhesion strength of the cold sprayed splats has been recently reported by Chromik et al. [121]. The adhesion strengths of titanium splats onto bulk titanium substrate was observed on the order of 240 MPa, which is approximately 63% of the bulk shear strength of titanium, for velocities above 770 m/s. However, it is not clear how this relates to traditional pull-off test values.

2.7.4 Porosity of the coating

Porosity in cold sprayed titanium deposit depends on a number of factors, such as particle velocity and particle temperature hence particle deformation. Therefore, minimization of porosity can be achieved by process parameter optimization. Table 2-2 shows the volume fraction of porosity values reported in literature. Compared to cold sprayed materials like copper, nickel and aluminium, titanium typically shows a higher degree of porosity. The porosity of cold sprayed titanium coatings varied from 20- 0.1% depending on process conditions. Earlier investigations in cold spraying of titanium using coarser angular powder and customized spraying systems resulted in a porosity level of around ~20% [76]. Modern cold spraying equipment is reportedly capable of producing cold spray coating with 0.1% porosity using heated nitrogen or helium gas. It is generally agreed that the critical velocity of titanium powder is around 700 m /s. It is noticed that increasing the velocity of the particle by increasing gas temperature and pressure results in a lower porosity coating, as can be seen from Table 2-2 [16, 111-113, 120]. Higher particle velocity also gives reduced porosity. In addition, Zahiri et al. [128] reported a coating porosity of 0.5 % by increasing the particle velocity to 1380 m/s. In general, the porosity decreased further when the particle velocity was increased using helium as accelerant gas. However, the role of particle morphology in cold sprayed titanium coating is not yet clear. Porosity of less than 1% has been achieved both from hydride de-hydride angular powder and gas atomized spherical powder. Although, it is hypothesised that the angular shape of the particle might be beneficial in getting rid of interparticle pores through plastic deformation [111], the experimental results are still not conclusive.

Temperature of the impacting powder particle also contributes significantly in reducing the porosity. Bae et al. [38] reported a decrease in porosity from 9.5%

to 1% by preheating the powder to 600 °C, thus enhancing thermal softening. In addition, Zahiri et al.[128] reported that with increasing the standoff distance in cold spraying the volume fraction of porosity increases. This is due to a longer travelling distance outside the nozzle which leads to a deceleration of particles. Moreover, a small particle size and narrow particle size distribution was reported to lead to reduced porosity, for example using a mean particle diameter of 16 μm instead of 22 μm led to a decrease in porosity value by 1.5%. Furthermore, X-ray microscopy and microtomography was utilized to visualize the pores in cold sprayed titanium deposit [129].

Porosity measurements on cross-section images from optical microscope and scanning electron microscope are sensitive to sample preparation. Smearing of titanium coating surface could occur if special care is not taken. In imaging techniques, a 2D representation of the surface of the sample with some contrast mechanism is used to distinguish pores. Moreover, in an ideally prepared sample surface the measurement of porosity is limited by the resolution limit of the microscope [130]. Futhermore, automated image analysis requires careful selection of pore boundaries.

Ref.	Gas pressure	Gas temperature	Particle velocity	Porosity measurement technique	Porosity	Process conditions
Marrocco et al. [76]	2.9 MPa He	Room temp	690 m/s (numerical model)	Image analysis of optical method	~20 %	University Nottingham, angular powder
Zahiri et al. [128]	2.4 MPa N_2 & 1.5 MPa He	600 °C	720 m/s & 1380 m/s	Water displacement ASTM C 20: 2000	9.5 % & 0.5 %	CGT 3000, angular powder
Wong et al. [16, 111, 112]	3.0 MPa & 4.0 MPa N_2	300 °C & 800 °C	610 m/s & 805 m/s	Image analysis	20 % & 2%	CGT 4000, spherical powder
Bae et al. [38]	2.5 MPa N_2 and 1.5 MPa He	600 °C	650 m/s & 950 m/s	Image analysis	9.5 & 0.1 %	CGT 3000, spherical powder
Gulizia et al. [113]	2.0 MPa N_2 & 3.5 MPa N_2	400 °C & 800 °C	-	Image analysis	11 % & 1 %	CGT 4000, spherical powder
Chromik et al. [121]	3 MPa & 4 MPa N_2	500 °C & 800 °C	695 m/s & 825 m/s	Image analysis (LOM)	1.6 % & 1.0 %	CGT 4000, spherical powder

Table 2-2 Porosity of cold sprayed titanium coatings reported in literature

2.7.5 Microhardness of the coating

Table 2-3 shows the average hardness values of cold sprayed titanium coatings reported in literature. Typical microhardness of a commercially pure grade 1 bulk titanium is ~145 kgf/ mm^2 and that of a gas atomized spherical titanium powder is ~141 kgf/ mm^2 [111]. In cold spraying, an increase in particle velocity results in an increase in coating hardness [120]. A higher particle velocity will lead to greater amount of bonding between splats, compaction within the splats and higher dislocation density. Gulizia et al. [113] reported an average increase of hardness of cold sprayed titanium coating by 16% compared to bulk materials. However, in cold spraying of copper and aluminium, an increase of 50% to 100% in hardness was reported [113]. The hexagonal closed packed (hcp) structure of titanium makes it more resistant to deformation. An increase in hardness values compared to the bulk of any material can be attributed to fine grain structure and/ or a high dislocation density.

Zahiri et al. [128] showed that the hardness of titanium coating varies as a function of porosity; as the porosity decreases the hardness increases. Porosity and hardness, both are directly related to the particle deformation in cold spraying; the higher deformation results in work hardening which may be related to twinning, dislocation pile ups and imperfections during deformation. It was reported that higher gas temperature results in higher hardness due to greater work hardening [111, 112]. It was found that microhardness at the bottom of the coating was always greater than the top of the coating in cold sprayed titanium. This was attributed to a greater degree of deformation of the particles at the bottom layer. Moreover, nanoindentation hardness measurements on cold sprayed titanium coatings, prepared from angular feed stock, was carried out by Moy et al. [131]. Nanoindentation tests also showed occasional lower values due

to imperfections or porosity within the titanium coating with a typical microhardness value of 350- 460 kgf /mm^2.

Ref.	Gas pressure	Gas temp.	Powder type	Spraying system	Vickers microhardness (kgf /mm^2)	Comments
Zahiri et al. [128]	2.4 MPa N_2 & 1.5 MPa He	600 °C	Angular	CGT 3000	150 & 320	Particle velocity 720 m/s & 1380 m/s
Zahiri et al. [132]	1.5 MPa He	600 °C	Angular	CGT 3000	320	Measured on ground cross section
Wong et al. [16, 111, 112]	3.0 MPa & 4.0 MPa N_2	300 °C & 800 °C	Spherical	CGT 4000	190 & 220	Powder hardness 141 kgf/ mm^2
Bae et al. [38]	2.5 MPa N_2 and 1.5 MPa He	600 °C	Spherical	CGT 3000	180 & 260	
Gulizia et al. [113]	2.0 MPa & 3.5 MPa N_2	400 °C & 600 °C	Spherical	CGT 4000	275 & 300	Powder hardness 244 kgf/ mm^2 and indentation load 5g

Table 2-3 Hardness of titanium coatings reported in the literature

2.7.6 Constituents of cold sprayed titanium

2.7.6.1 Composition: oxygen nitrogen levels

The oxygen and nitrogen contents of the commercially pure titanium powder and titanium coating prepared using cold spraying have been reported by Li et al. [109, 133] and Gulizia et al. [134]. Table 2-4 shows the measurements of oxygen and nitrogen in starting feedstock powder and in the coatings by different researchers. Nitrogen and oxygen levels increased in cold sprayed deposits compared to the starting powder. However, the oxygen and nitrogen contents of the coatings are well below the level of any thermal sprayed titanium coatings. It was also reported that [134] an increase in oxygen content occurs with increasing the process gas temperature of the cold spraying. The increase in process gas temperature results in an increase in particle temperature and hence, higher tendency to oxidation.

Ref.	Powder		Coating		Process conditions
	O (wt.%)	N (wt.%)	O (wt.%)	N (wt.%)	
Li et al. [109, 133]	0.31	0.07	0.6	0.1	
Gulizia et al. [134]	0.437	0.011	0.517	0.026	Using N_2 at 400°C
			0.539	0.024	Using N_2 at 600°C
			0.588	0.035	Using N_2 at 800 °C

Table 2-4 Oxygen-nitrogen contents of titanium powder and cold sprayed coatings

2.7.6.2 Phases: XPS & TEM

X-ray photoelectron spectroscopy (XPS) is a technique that measures the elemental composition of the material [135]. In XPS, a beam of X-rays with fixed wavelength are focused on the surface and photoelectrons are released from the atoms at the top few nanometres on the material surface. The kinetic energy of the released electrons can be related to the binding energy of the electrons in the atoms. Moy et al. [131] and Gulizia et al. [134] investigated the surface of cold sprayed titanium deposits using XPS. Gulizia et al. [134] reported a complex structure of several phases, i.e., titanium metal, titanium nitrides, oxides and oxi-nitrides in a range of stoichiometries on the coating surface. Moy et al. [131] argued that nitrogen was picked up during the spray in form of N and TiN. Also, the amount of N shows a slight increase closer to the interface. Gulizia et al. [134] reported that an increase in Ti 2p signal associated with lower oxidation states occurs with increasing process gas temperature. The high reactivity of titanium with nitrogen and the occurrence of flashing jet during the deposition of titanium were thought to be responsible for this phenomenon [126].

TEM was used to investigate the interparticle microstructure of the coatings and coating-substrate interface [131, 136]. The interface of the titanium coating onto aluminium substrate showed a sharp interface, indicating both coating and substrate remained solid during impact and hence a metal-to-metal bond was established [131]. Although a number of other TEM studies reported formation of intermetallics in cold spraying of copper, aluminium and nickel, no such phenomena were noticed in titanium. It was argued that the high melting point of titanium makes it difficult to form secondary phase along the interface.

2.7.6.3 Microstructural features

Cold sprayed titanium coatings show two distinctive regions: a porous top layer and a less porous bottom layer. Coatings prepared from both angular powder and spherical powder resulted in these two distinct regions of porosity [76, 110, 111]. It was observed that the size of the pores reduced towards the bottom of the coating. Moreover, the deformation of the particles and the flattening ratio were also increased towards the interface [131]. The tamping effect on the particles at the bottom layer by successive impacts of the following particles resulted in this less porous microstructure at the bottom. During the spraying of titanium, a flashing jet outside the nozzle was observed which is thought to be due to the reaction with oxygen in the air [109]. It was argued that the oxide layer on the surface of titanium powder is broken up due to friction and the porous structure of the coatings was attributed to this surface activity during spraying [133].

Metal-to-metal bond formation within the titanium coating was reported in literature in etched titanium coating [109, 126]. Probably, the high particle surface temperature during the impact contributed to this scenario. It is also debated in the literature that the local surface melting of titanium can occur due to low thermal conductivity and resulting thermal diffusivity of titanium [38, 126]. Titanium also has a higher adiabacity compared to copper, aluminium and nickel for the same particle size range and velocity. Adiabacity is defined as the level of localized thermal build up during the high strain rate deformation process [38]. Moreover, Bae et al. [38] reported nano sized, spheroidical particles on the coating surface when titanium was sprayed using helium as an accelerant gas at 950 m/s particle velocity. These small spherical particles were thought to be a sign of melting which was also supported by numerical simulations.

2.7.6.3.1 Microstrain, texture and residual stress

Rafaja et al. and Moi et al. [131, 137] studied the microstrain of commercially pure titanium particle and cold sprayed deposits using X-ray diffraction peak broadening. Williamson-Hall method [138] of peak broadening was utilized in both the cases to measure microstrain. Table 2-5 shows the microstrain of angular titanium powder and the cold sprayed coating prepared from that powder. Rafaja et al. [137] reported an increase in microstrain from 6.4×10^{-4} to 2.2×10^{-3} following cold spraying. The increase in microstrain in the coating is due to severe plastic deformation of the powder during the deposition process. It was also reported that a steep increase in microstrain in titanium coatings occur from the top of the coating to the interface [137]. This suggests that the titanium is mostly deformed at the particle-substrate interface.

Ref.	Microstrain in powder	Microstrain in coating	Powder type
Rafaja et al. [137]	6.4×10^{-4}	2.2×10^{-3}	Angular
Moy et al. [131]	7.0×10^{-4}	4.5×10^{-3}	Angular

Table 2-5 Microstrain determination of Ti powder and coatings

X-ray diffraction technique was also used by Zahiri et al. [132] to study texture formation in cold sprayed titanium coating prepared from angular powder. Cold spraying of titanium resulted in preferred orientation of crystallographic planes; a significant increase in intensity of α titanium peak at 38.4 ° (0002) compared with titanium powder was reported. However, formation of any TiO or TiO_2 was not detected in cold sprayed titanium coatings within the detectable range of XRD [133, 137].

Residual stress of titanium deposits produced by cold spraying were investigated by Gulizia et al. [113] and Price et al. [127]. Residual stress in cold sprayed coating is usually compressive in nature and tensile in the substrate. This tensile residual stress in the substrate has a detrimental effect on fatigue endurance limit of the substrate. It was noticed that increasing the process gas temperature and pressure resulted in an increase in residual stress within the titanium deposit. A process gas temperature of 800 °C and 3.5 MPa resulted in a compressive residual stress as much as 250 MPa, measured by X-ray diffraction method. Residual stress in cold sprayed titanium deposit was higher than cold sprayed ductile materials, like aluminium, due to different crystal lattice structures.

2.7.6.3.2 TEM analysis

Transmission electron microscopy (TEM) images of cold sprayed titanium coatings revealed a number of interesting features in the cold sprayed titanium coatings [131, 136, 139]. Bae et al. [139] observed two regions in titanium coating: a region of larger grains (>250nm) with high dislocation density and a region of smaller nanocrystalline grains (<100nm) with dislocation free grain boundaries. The authors argued that the dislocation free grains were mostly attributed to the relatively high temperature generated during strain accumulation, due to successive impact of particles, along with low thermal conductivity of titanium [139]. It was also believed that thermally activated static recovery process contributed in annealing out of dislocations in the smaller grains. The high density dislocations in the grains can provide strain hardening and increased ductility of the material. Also, the fine grained nano structure can promote grain boundary sliding and consequently enhance ductility.

2.7.7 Mechanical properties of free standing deposits and coatings

Cold sprayed titanium deposit has a high potential to build up ultra thick coatings and net shaped manufacturing product for rapid prototyping for automotive and aerospace industry. Machining high strength materials i.e., titanium is difficult and time intensive so there is a great interest in producing thick titanium deposit with desirable mechanical properties. Blose et al. [117] and Zahiri et al. [132] measured the typical tensile stress-strain relationship of titanium deposit produced from angular powder feedstock. Blose et al. [117] reported that the tensile strength of the as-sprayed titanium deposit was 100 MPa and the as sprayed deposit showed limited ductility due to interparticle defect and porosity. However, Zahiri et al. [132] used a commercially available cold spray system with higher pressure of helium gas and reported a tensile strength of 800 MPa for as-sprayed deposit, which was higher than that of commercially pure bulk titanium. A significant reduction in porosity of the deposit contributed to this high tensile strength value. However, the ductility of the as-sprayed deposit was limited to plastic deformation of 0.02%. Moreover, this ductility of the as sprayed material was improved following annealing.

The elastic modulus of the cold sprayed titanium deposit was measured by various techniques (i.e. knoop indentation, four point bending and nanoindentation) [24, 123, 131]. Young's modulus of titanium deposit using indentation and four point bending tests were ~20 GPa, which is significantly lower than the young's modulus of a bulk material which is 120 GPa. Limited bonding between interparticle splats due to porosity resulted in the lower Young's modulus. In addition, a recent study in 2010 by Moy et al. [131] reported a

Young's modulus of the titanium deposit between 92 GPa and 120 GPa measured using nanoindentation technique.

Tubular coating tensile (TCT) test is a fast and cost-efficient way of providing tensile strength of the deposits [10, 140]. The ultimate tensile strength of the TCT samples prepared from commercially pure titanium feedstock showed an increase in strength with reducing porosity. It was reported that when the porosity of the titanium deposit increased from 0.13 to 1%, the tensile strength of the deposit reduced to half. In addition, the tensile strength of the coating increased linearly with increasing process gas temperature; the tensile strength of titanium deposit reached a value of ~450 MPa at a pressure of 4.0 MPa and 1000 °C using nitrogen as an accelerant. The tubular coating tensile strength data was verified using micro flat tensile (MFT) test. In MFT test, tensile test samples are produced using electro discharge machining and typical stress-strain properties are investigated under one dimensional condition. It was shown that the TCT tensile strength values correlated in a linear way with the MFT tensile strength values.

2.7.8 Effect of heat treatment on free standing deposits and coatings

Post deposition heat treatment was used to reduce porosity and internal defects and to improve mechanical properties of the sprayed titanium and titanium alloys [141]. A number of post spray techniques to alter the microstructure and hence optimize the cold sprayed titanium coating have been reported in literature [117, 118, 132, 133, 142]. Zahiri et al. [132] reported the effect of annealing of cold sprayed titanium deposit at 350-550 °C. The annealing treatment resulted in ultrafine grains (<5 μm) formation in 25% of the area with an average grain size of 7μm. The ultrafine grains provide the mechanical strength to the deposits and

larger grains provide the ductility to the material. In addition, annealing of cold sprayed titanium resulted in an elongation of 8%, which was a significant improvement in the ductility compared to the as-sprayed condition. However, the strength of the material decreased from 800 MPa to 600 MPa following annealing.

Heat treatment of titanium coatings results in recovery, recrystallization and grain growth, although it was difficult to identify the recovery stage in the isothermal annealing experiments [132]. Annealing of cold sprayed titanium deposit resulted in metallurgical bond formation and removal of particle-particle interface due to recrystallization and grain growth [133]. It was also noticed that micro-pores are generated in the annealing process in the healing of the interface through atom diffusion. Fracture surface analysis of the annealing deposit showed evidence of ductile failure.

Blose et al. [117, 118] also studied the properties of cold sprayed titanium and titanium alloys with post spray heat treatment and hot isostatic pressing (HIP). Heat treatment at 840 °C for four hours of commercially pure titanium deposits, which was prepared from angular powder, improved in yield strength and ultimate tensile strength by a factor of 2.5 but the elongation to failure was still very low (<1%). However, HIPing resulted in an increase in yield strength and ultimate tensile strength by a factor of 3.5 over the heat treated sample and elongation of the sample increased to 4%. Moreover, after HIPing the porosity of the deposits was reduced to zero.

2.7.9 An overview of warm sprayed titanium

Warm spraying is a modified form of high velocity oxy-fuel (HVOF) spraying technique in which nitrogen gas is mixed with the HVOF flame jet to lower the temperature of the powder particles [143]. A number of studies of high strain

rate deformation behaviour of warm sprayed titanium have been published recently [143-150]. During warm spraying, titanium powders are heated to approximately half of the melting temperature. Oxidation of the particles occurs during the flight due to high temperature. The oxygen level in the warm sprayed titanium coatings sprayed using optimized parameters were ~1.5 wt.%, which was produced from a powder with 0.14 wt.% oxygen content [151]. The oxygen content of the warm sprayed titanium coatings is 2.5- 3% higher than cold sprayed titanium coatings reported in the literature. However, the particles had very high deposition efficiency and bonded well due to thermal softening. In addition, fully nanocrystalline particles were formed by dynamic recrystallization [146]. Moreover, the warm spraying is reportedly capable of producing titanium coatings with porosity levels less than 1%.

2.7.10 Summary of literature review of cold sprayed titanium

The summary of the literature review on cold sprayed titanium coatings are as follows

- The microstructure of the cold sprayed titanium coating shows a porous top layer and a less porous layer closer to the coating-substrate interface. The hammering and compaction of the cold sprayed particles result in this less porous bottom layer.
- The process parameters (velocity and temperature) play a critical role in coating formation. Increasing the process gas pressure and temperature results in a higher velocity of the particles. In addition, helium as an accelerant gas provides higher particle velocity compared to nitrogen as an accelerant.

- Typical deposition efficiency of titanium particles was 85– 100 % for both angular and spherical powder. Typical critical velocity for deposition of titanium particle was 505- 750 m/s.
- Bond strengths of the titanium coatings onto different substrates show a wide range of values from 7 to 85 MPa. It was reported that the grit blasting using coarser alumina improved the bond strength value.
- Image analysis technique to measure the porosity of the cold sprayed titanium coating has been widely used. A wide range of values ranging from 20 % to 0.1 % has been reported.
- The microhardness of the titanium coating was always higher than that of the bulk material. Typical values of the coatings were in the range of 150 to 300 kgf/ mm^2. However, the interparticle porosity within the coating contributed to occasional variation in hardness.
- Both oxygen and nitrogen levels in the coatings showed an increase following deposition. Typical values of oxygen content in the coatings were ~0.5- 0.6 wt. %, which were prepared from powders containing 0.3- 0.4 % oxygen. However, the oxygen contents in the cold sprayed titanium coatings are three times lower than that of warm sprayed titanium coatings.
- Typical microstrain of the coating was 2- 4 × 10^{-3} ,which is an increase of an order of magnitude form the microstrain of the feedstock powder.
- Tensile strength of the titanium deposits showed a wide range of values from 100 to 800 MPa depending on the porosity level. However, the elongation to failure for all the deposits was very small. In addition, a new method called tubular coating tensile test (TCT) was used to measure the tensile strength of titanium deposit (value of 450 MPa), the values

correlated well with the microflat tensile tests. The ranges of Young's modulus of the titanium deposits were 20- 120 GPa.

- Heat treatment of the sprayed deposits showed an improvement in porosity level and mechanical properties. However, there exists a gap in understanding the change in porosity of the cold sprayed titanium deposit following heat treatment.

2.8 Corrosion

This section will provide a summary of the corrosion principles of metal in aqueous solution and methods of electrochemical corrosion measurements. In addition, corrosion performance of bulk titanium and sprayed titanium coatings prepared by various methods will be discussed. The corrosion principles described in this section are extracted from standard corrosion text books [152-156].

2.8.1 Thermodynamics of corrosion

The tendency of metals to recombine with environmental components and thus transforming to a lower energy state is called corrosion [155]. In other words, *corrosion is defined as the destruction or deterioration of a material because of a reaction with its environment* [153]. However, there exists an energy barrier between the metal and its corrosion product. Metal atoms have to surmount the energy barrier before it can start corroding; hence more energy has to be supplied. The amount of energy required to overcome this barrier is called free energy of activation.

2.8.2 Electrochemical corrosion

Wet corrosion occurs in an aqueous medium and the predominant mechanism is electrochemical. When a metal is immersed in an electrolyte (an electrically conducting solution), the following oxidation or anodic reaction (a loss of electron) occurs

$$M \rightarrow M^{Z+} + ze^{-}$$

in which, M is a metal atom and z is the number of electrons donated by each atom, which is governed by the valency of the metal. The site at which oxidation takes place is called anode [152]. The electrons released from the metal atoms must be consumed by other species to balance the reactions. The corrosion balancing reactions depend on the type of the electrolyte. The electron consuming reactions are called cathodic reaction or reduction and the site at which cathodic reaction takes place is called a cathode. The corrosion balancing reactions for acid solution is

$$2H^{+} + 2e^{-} \rightarrow H_2$$

in which hydrogen gas is evolved. However, an acid solution with dissolved oxygen will reduce as follows

$$O_2 + 4H^{+} + 4e^{-} \rightarrow 2H_2O$$

In a neutral or basic aqueous solution, the following corrosion balancing reaction may occur if dissolved oxygen is present

$$O_2 + 2H_2O \ + 4e^{-} \rightarrow 4(OH^{-})$$

Without any external influence, the system reaches a dynamic equilibrium in which metal ions are continually entering and leaving the electrolyte at the same rate. When a state of equilibrium of anodic and cathodic reactions is reached, there is no net current flowing. In fact, there is still current flowing, but it is equal and opposite; hence, cannot be measured.

2.8.2.1 Electric double layer

When a metal is immersed in an electrolyte, it forms an ionic form by losing electrons which is used up at the cathode. As dissolution proceeds the metal acquires a negative charge and a non-homogeneous distribution of ions at the

metal surface occurs which is referred to as electric double layer. Electric double layer has also a potential difference across it. In addition, work must be done on the metal ions to cross this double layer. An electric double layer consists of two layers: a compact layer or Helmholtz layer and a diffuse outer layer or Gouy-Chapman layer. The equilibrium condition in electric double layer can be destroyed by an increase in either anodic or cathodic reactions and a new condition can be established in which a flow of anions and cations performs the bulk current carrying role of the electrodes. The open circuit potential changes when the electrical double layer composition is changed [156].

2.8.2.2 Polarization

When a metal is not at equilibrium with its ions in an electrolyte, the deviation of electrode potential form equilibrium potential is known as polarization or overpotential. If the anodic reaction is faster than the cathodic reaction, then an overall corrosion reaction will occur and the equilibrium will be destroyed. If the change in potential occurs by using an external power source, the electrical double layer composition will be altered and will produce an electrical current. Applying an overpotential in the anodic direction will cause the metal to corrode and produce current which can be measured [157]. Nernst equation mathematically states the relationship between electric double layer and electric potential.

$$E = E_o - (RT/nF)\ln\{(a_{products})/(a_{reactants})\} \quad \text{equation 2.19}$$

Where E is the measured potential, E_o is the open circuit potential when all activities in the equation are equal to 1, R is the ideal gas constant and T is the temperature, n is the number of electrons in anodic half reaction, F is the Faraday constant and a is the chemical activity. However, Nernst equation does not provide any relationship with electrical current. According to Ohm's law, applying a potential to an electrode in an electrolyte will produce electric current, because

electric double layer has both resistance and voltage. Butler- Volmer equation relates electrical current to metal potential caused by an external power source.

$$i = i_o (e^{\frac{\alpha \eta n F}{RT}} - e^{\frac{(1-\alpha)\eta n F}{RT}}) \qquad \text{equation 2.20}$$

in which, i is the external current density, i_o is the corrosion current density, η is the total overpotential, αη is the anodic polarization and (1- α)η is the cathodic polarization. According to Butler-Volmer equation, an electrode is essentially an anode when overpotential is ≥ 50mV and conversely, the electrode becomes essentially a cathode when overpotential decreases below -50mV.

The measured current values can be related to corrosion rate by Faraday's law of electrolysis. Following integration with time on Faraday's law of electrolysis, the following expression can be achieved

$$i = zFJ \qquad \text{equation 2.21}$$

in which, i is the current density, z is the number of electrons in the corrosion reaction, F is the Faraday constant and J is the flux of the substrate dM/dt, which is equivalent to corrosion rate. This equation is very important as this allows to measure the corrosion rate by measuring current density [155]. The relationship of current density to overpotential can be expressed by Tafel equations

$$\eta_a = \beta_a \log i_a - \beta_a \log i_o$$
$$\eta_c = \beta_c \log i_c - \beta_c \log i_o \qquad \text{equation 2.22}$$

in which, β_a and β_c are called anodic and cathodic Tafel constants, i_a and i_c are anodic and cathodic current density, η is overpotential and i_o is the current density at equilibrium. A graph of overpotential (η) against log i for either of anodic or cathodic processes gives a straight line with a slope equivalent to the β constants and the intercept values equivalent to -β log i_o.

2.8.2.3 Mixed potential theory

Mixed potential theory forms the basis of modern electrochemisty of corrosion science. The first hypothesis of mixed potential theory states that any electrochemical reaction can be divided into two or more partial oxidation and reduction reactions. The second hypothesis states that during corrosion of an electrically isolated metal sample, the total rate of oxidation must be equal to the total rate of reduction. Given these hypotheses, it is relatively simple to calculate the corrosion currents and potentials for a variety of corrosion conditions. This is most easily done graphically using what is called the Evans diagram. Evans diagram is a plot of potential versus current density for both electrodes in a corrosion cell. The point at the intersection where the total rates of oxidation and reduction are equal is called corrosion potential E_{corr} and the current density corresponding to this point is called corrosion current density, i_{corr}. This corrosion current density is directly proportional to corrosion rate of the metal.

2.8.2.4 Active-passive behaviour of metal

Passivity is a phenomenon observed during the corrosion of certain metals and alloys. Passivity can be defined as a loss of chemical reactivity under certain environmental conditions. This is due to a surface film which is approximately 30 angstroms in thickness on the metal surface and very delicate in nature. Iron, chromium, nickel, titanium and their alloys demonstrate this active-passive behaviour (Figure 2-20). Generally all metals follow typical Tafel behaviour, i.e., the dissolution rate increases with increasing electrode potential, this is called active region. Active-passive metals also show this behaviour, however, at more noble potential, dissolution rate decreases to a very small value and remains essentially independent of the potential over a considerable potential region. This region is called passive zone where the surface film of the metal is stopping further metal dissolution. Finally, at very high potential dissolution rate again increases with an increase in potential which is called transpassive region [153].

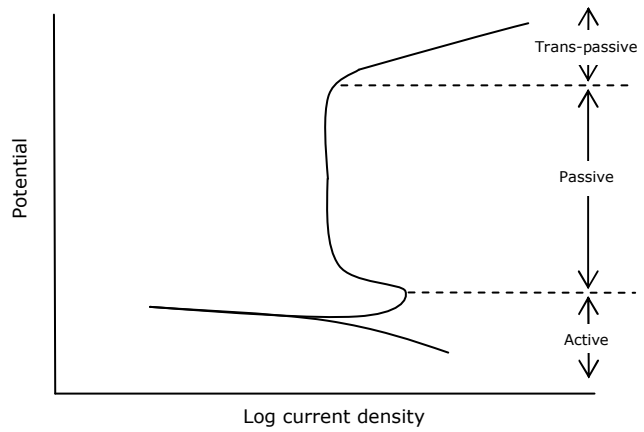

Figure 2-20 Typical active-passive behaviour of a metal

2.8.2.5 Electrochemical series and galvanic series

Standard electrode potential, E^o is measured for various metals using hydrogen standard reference electrode [154]. The electrode potential of hydrogen gives exactly zero volt. Thus the values in this series lists the absolute electrochemical data needed for precise calculations. The series is called electrochemical series and compares the reduction potentials of metals. The series is measured under standard conditions and thus independent of other species in the environment. The standard electrode potential of titanium, iron, platinum and hydrogen are shown below.

Electrode reaction	E^o/V
$Pt^{2+} + 2e^- = Pt$	+1.2
$2H^+ + 2e^- = H_2$	0.00
$Fe^{2+} + 2e^- = Fe$	-0.44
$Ti^{2+} + 2e^- = Ti$	-1.63

The galvanic series yields a more accurate predication of galvanic relationships than the electrochemical series. Galvanic series enables a rapid prediction of corrosion resistance of a dissimilar metal couple. The galvanic series is a relative qualitative series of both metals and alloys listing an experimental order of

nobility. The galvanic series of titanium, mild steel and stainless steel at 25°C in sea water with respect to standard calomel electrode (SCE) are showed below [155]. The potential listed below are actually free corrosion potentials in that environment.

Materials	Free corrosion potential (SCE)/ V
Platinum	+0.25 to +0.22
Titanium	+0.05 to -0.05
Stainless steel (304)	-0.05 to -0.1 (passive)
	-0.45 to -0.55 (active)
Mild steel	-0.6 to -0.72

2.8.3 Corrosion behaviour of bulk titanium

Titanium is a reactive metal and depends on a protective film of TiO_2 for corrosion resistance. Titanium has excellent corrosion resistance to (1) sea water and other chloride solutions (b) hypochlorites and wet chloride, and (3) nitric acid including fuming acids. In addition, $FeCl_3$ and $CuCl_2$ salts that tend to pit most metals actually inhibit corrosion of titanium. Titanium also has a very good pitting corrosion resistance as compared to stainless steel in sea water. However, titanium is not resistant to relatively pure sulphuric and hydrochloric acids [153, 158]. In reducing acid, the oxide film on titanium can deteriorate or dissolve, and the unprotected metal is oxidized as follows: $Ti \rightarrow Ti^{3+} + 3e^{-}$. If dissolved oxygen is present in the reducing acid, then Ti^{3+} ion is oxidized to the less soluble Ti^{4+} ion.

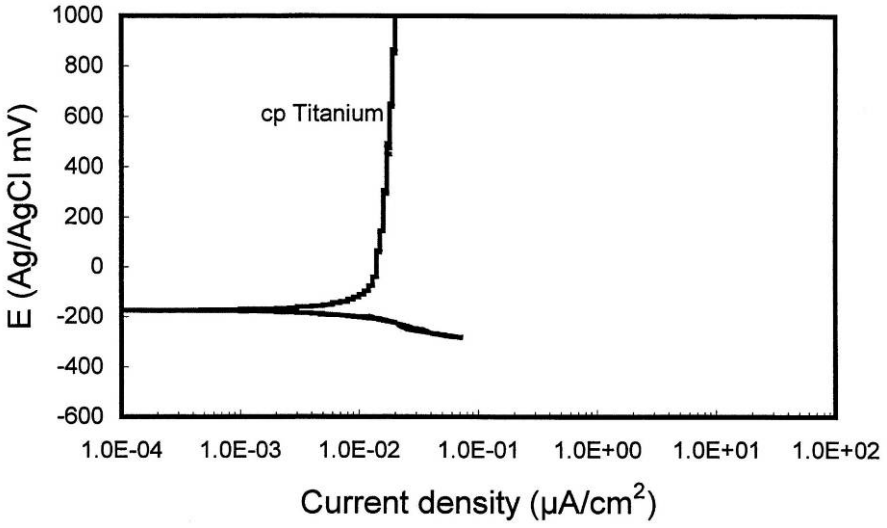

Figure 2-21 Polarization curve of cp titanium in 0.5 M NaCl [159]

A number of researchers have studied the corrosion behaviour of bulk titanium in salt solution using electrochemical polarization methods [160-164]. Figure 2-21 shows a typical polarization curve of a cp titanium in 0.5 M NaCl. Hackerman et al. [161] and Bomberger et al. [163] studied the cathodic and anodic polarization curve of titanium in aerated salt solution. The anodic polarization observed was believed to be due to an adherent insoluble film. In addition, after five years exposure of titanium in sea water, Bomberger et al. [165] concluded that there was no detrimental effect (no weight loss) on commercially pure titanium. Similar results of completely resistant properties of titanium in 3% NaCl solution have been reported by Golden et al. [166]. However, titanium and its alloys are subjected to localized attacks in crevices which are exposed to hot (> 70°C) chloride solution [167, 168]. Crevice corrosion of titanium is similar to the crevice corrosion in stainless steel where oxygen depleted reducing acid conditions develop in tight crevices [158]. Usually, titanium chloride is formed within a tight crevice which is unstable and tends to form hydrochloric acid (HCl) and titanium oxide / hydroxide corrosion products. In addition, crevice corrosion of titanium also occurs in bromide, iodide and sulphate solutions.

2.8.4 Corrosion of sprayed titanium coatings

Titanium coatings produced from different thermal spraying methods produce a wide variation in microstructure and hence their performance in corrosion tests also varies significantly. A barrier layer of titanium coating applied onto a less noble metal substrate should protect the substrate from corrosion attack. However, the presence of pores, oxides and nitrides play a critical role in corrosion behaviour of the spraying titanium coatings.

2.8.4.1 Corrosion behaviour of plasma sprayed titanium

Plasma spraying has been widely used to produce titanium coatings for corrosion protection purposes [159, 164, 169-172]. Plasma spraying of titanium in air (APS) results in severely oxidized, inhomogeneous and porous coatings due to the high reactivity of titanium with oxygen and nitrogen. However, shrouded plasma spraying (APS/S) or low pressure plasma spraying (LPPS) can produce coatings with reduced oxidation and porosity. The potentiodynamic scans of free standing APS and APS/S titanium coatings showed increasing corrosion current density with increasing potential (Figure 2-22a). In addition, the free standing deposits did not show any passivation behaviour like bulk titanium and the corrosion current density was a decade of magnitude higher than bulk titanium. Nevertheless, the polarization scans of APS-S coatings on carbon steel (Figure 2-22b) resulted in higher corrosion current density compared to bulk titanium due to interconnected porosity and oxides. APS/S coatings were unable to provide suitable protection to the underlying substrates [164, 169].

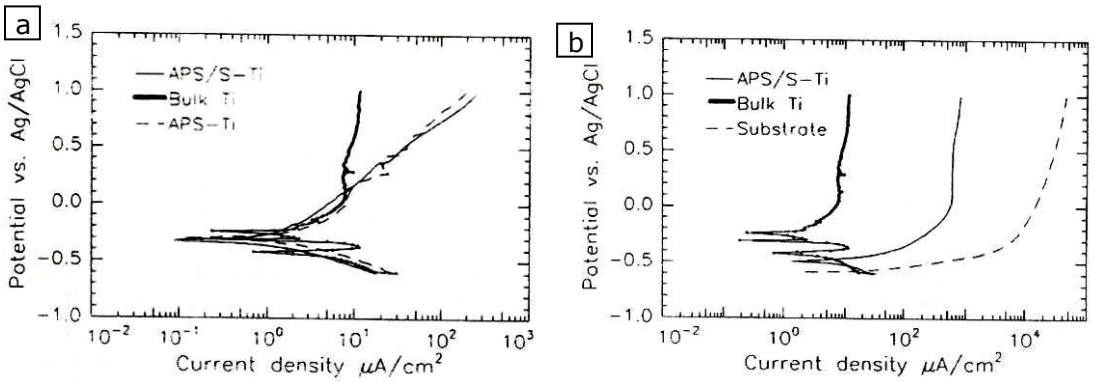

Figure 2-22 (a) Polarization curves of free standing atmospheric plasma sprayed (APS) Ti, APS-shrouded Ti and bulk Ti in 3% NaCl (b) Polarization curves of APS/S Ti on carbon steel, Bulk Ti and carbon steel [169]

2.8.4.2 Corrosion behaviour of flame sprayed titanium

Ishikawa et al. [173] investigated the corrosion behaviour of flame sprayed titanium coatings in 3.5 wt.% NaCl solution. It was observed that almost half of the titanium coating had changed to oxides, nitrides and carbides during the wire flame spraying. Figure 2-23 shows the anodic polarization scans of detached (free standing) flame sprayed titanium and as-sprayed titanium onto carbon steel substrate in NaCl solution. The rest potential of the detached coating is below the rest potential of bulk titanium due to presence of oxides, nitrides and carbides. In addition, the potentiodynamic scans of as-sprayed titanium onto carbon steel shows a large increase in the corrosion current density compared to the bulk titanium indicating no resistance to chloride solution. However, a post-spray epoxy and silicon resin sealing treatment of the flame sprayed coating showed improved resistance to chloride solution.

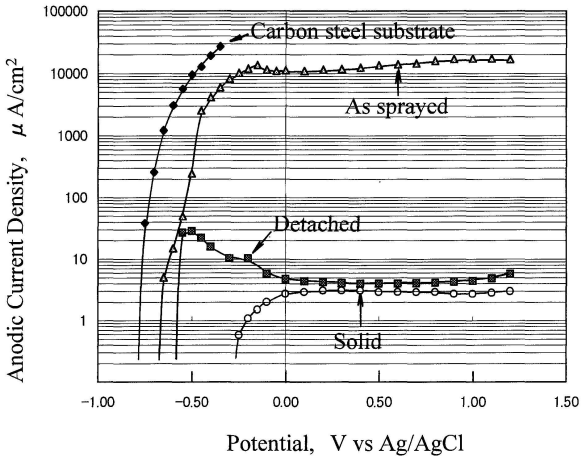

Figure 2-23 Anodic polarization scans of flame sprayed Ti on steel (as-sprayed), free standing Ti (detached), bulk Ti (solid) and carbon steel substrate in de-aerated 3.5% NaCl.

2.8.4.3 Corrosion behaviour of arc sprayed titanium

To improve the corrosion resistance of carbon steel substrate, Zhao et al. [174] sprayed titanium onto a steel substrate using arc spray technique. The arc sprayed coating was entirely composed of TiN and Ti_2O due to reactions of titanium with air during the atomization process. XRD analysis of the coating showed a complete absence of α titanium peaks because all the titanium had changed to TiN and Ti_2O. Tafel polarization curves of various coatings were tested in 3.5 wt.% NaCl solution. The oxides in the coatings resulted in a more negative open circuit potential and a higher corrosion current density. However, the corrosion resistance of the coating was improved by decreasing the amount of oxide. It was also showed that the corrosion current density is very sensitive to spray process parameters which can decrease from 1000 μA/ cm^2 to 5 μA/ cm^2 by optimizing spraying current, voltage and stand-off distance.

2.8.4.4 Corrosion behaviour of warm sprayed titanium

More recently a modified high velocity oxy-fuel (HVOF) process termed warm spraying is reportedly capable of producing titanium coatings with porosity levels less than 1% measured by mercury intrusion porosimetry [151, 175]. However,

the corrosion rates of these warm sprayed coatings were also higher than bulk titanium because of the presence of interconnected porosity. Figure 2-24 shows the potentiodynamic scans of warm sprayed titanium coatings of two different porosity values on carbon steel substrate in seawater. Both the coatings show higher corrosion current densities compared to bulk titanium, but with a decrease in porosity value the corrosion current density also decreases.

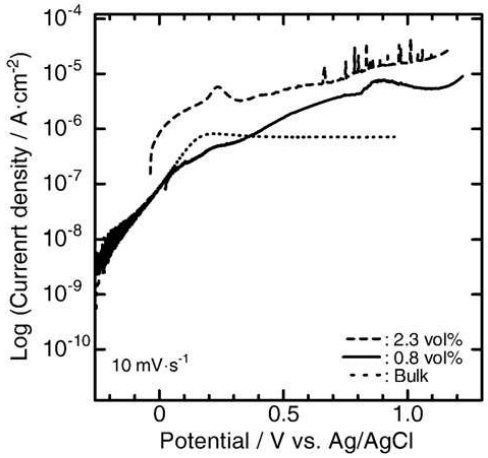

Figure 2-24 Anodic polarization curves of warm sprayed Ti coatings on carbon steel substrate and bulk Ti in de-aerated artificial seawater [175]

However, a post-spray grinding and polishing treatment of these warm sprayed coatings resulted in higher corrosion resistance in immersion tests over three days. There was no evidence of rusting on the coatings surface following this test. The mechanical grinding and polishing of the coating surface enhanced the barrier characteristics by bridging the interparticle gaps [151, 176]. Microstructural investigations of the warm sprayed titanium coatings showed presence of some oxides; however, by increasing the flow rate of the nitrogen cooling gas the level of oxidation in the coatings was reduced [151, 175].

2.8.4.5 Corrosion behaviour of cold sprayed titanium

The corrosion studies of cold sprayed titanium coatings are limited. Wang et al. [125, 177] studied the behaviour of cold sprayed titanium coatings using open

circuit potential measurements and potentiodynamic polarization. Figure 2-25 shows the open circuit potential measurements of cold sprayed titanium coating on carbon steel and bulk titanium in natural seawater. The open circuit potential of cold sprayed titanium is more negative than the bulk titanium due to interconnected porosity. Interconnected porosity and limited bonding between intermediate particles in cold sprayed titanium coatings is a major issue in producing corrosion resistant barrier layer.

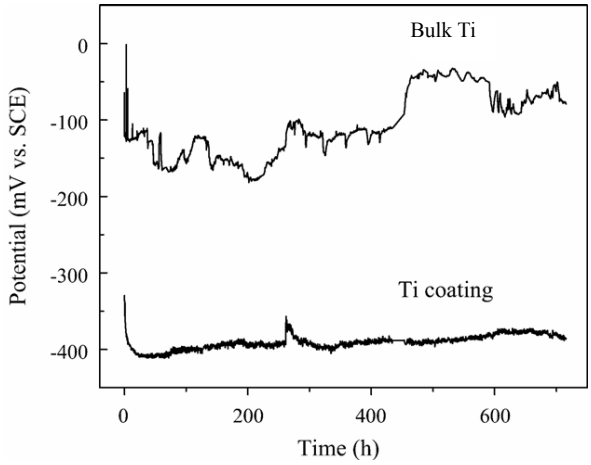

Figure 2-25 Open circuit potential measurements of bulk Ti and cold sprayed Ti in natural seawater [177]

Figure 2-26 shows the potentiodynamic polarization scans of cold sprayed titanium coatings onto carbon steel substrates sprayed at three different process gas pressures, which were all scanned in as sprayed and after a polishing treatment. The polarization curves of cold sprayed coatings show influence of substrate, which is evident from the increased corrosion current density compared to bulk titanium. However, increasing the process gas pressure improved the corrosion current density by a decade in potentiodynamic polarization scans. Similar effect was seen by increasing the process gas temperature. Increasing the process gas pressure and temperature results in a reduction of porosity which provides a better resistance to corrosion. Similar to the warm sprayed titanium coatings, polishing surface treatment of the cold

sprayed titanium coatings also led to an improvement in corrosion resistance as can be seen in Figure 2-26 by a decrease in corrosion current density. However, a barrier coating like properties of cold sprayed titanium has not been reported.

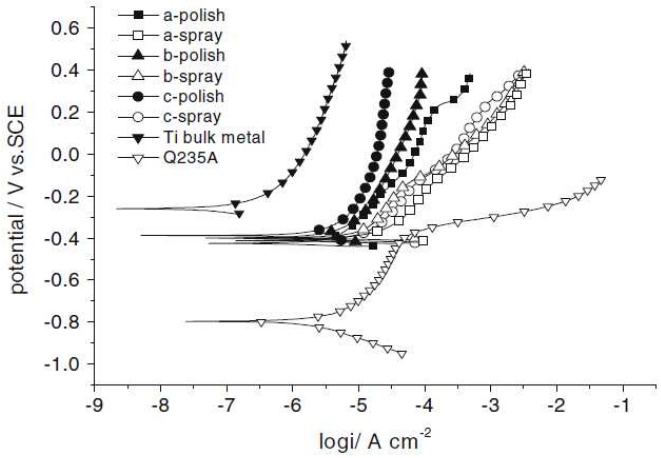

Figure 2-26 Polarization curves of cold sprayed Ti at different process conditions of (a)1.5 MPa (b) 1.8 MPa (c) 2.0 MPa in 3.5wt.% NaCl [125]

2.8.4.6 Laser surface melting of titanium coatings

Laser is widely used in surface engineering, i.e., melting, cladding, alloying, hardening of materials [178]. In a laser surface treatment the electronic energy derived from the beam of incident photons of laser are converted to heat. Due to the very high energy density of laser beam ($\sim 10^{10\text{-}12}$ W/m^2), the effect of this heat is confined to the surface while the bulk materials can remain virtually unaffected. In laser surface melting, the heat energy from the laser beam is sufficient enough to melt the surface without vaporizing the material. A melt pool is formed at the material surface which is governed by the forces of buoyancy due to density difference and convections due to surface tension gradients. The substrate acts a heat sink and as soon as the laser beam traverses past, the solidification process starts from the solid-liquid interface towards the surface [179]. Laser surface melting is characterized by very high heating/cooling rate, thermal gradient and a rapid solidification velocity [157].

Laser melting promotes a homogeneous and refined microstructure as a result of rapid melting and solidification which potentially can improve corrosion properties. A number of post-spray treatments (i.e., laser surface melting and electron beam diffusion) have been reported to improve the corrosion behaviour of the plasma sprayed titanium coatings [164, 169, 170, 172]. Figure 2-27 shows the open circuit potential of plasma sprayed titanium and laser consolidated titanium coating onto steel for the 15 day immersion in natural sea water. OCP of the plasma sprayed titanium coating at the end of the test was -0.56 V, which was much closer to the steel substrate than to the pure titanium. However, the OCP of laser consolidated titanium was -0.28 V, which is about 440 mV more noble than the base metal and 130 mV less noble that the pure titanium. The laser consolidated coating showed no evidence of corrosion after 15 days of immersion, but the as sprayed coating showed pitting corrosion of the steel at the coating-substrate interface.

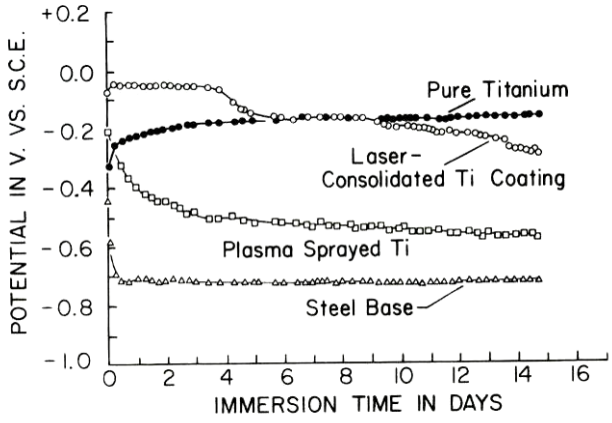

Figure 2-27 Open circuit potential of plasma sprayed Ti and laser treated plasma sprayed Ti in flowing natural sea water [164]

Kinos et al. [169, 170] modified the microstructure of shrouded plasma sprayed (APS/S) titanium coatings using electron beam welding apparatus to improve the corrosion properties. Potentiodynamic polarization scans of as-sprayed and electron beam diffused titanium coatings were conducted in 3% NaCl and 1N

sulphuric acid solution. In both medium, the corrosion current densities of the electron beam diffused titanium coating onto steel were lower than that of the bulk titanium. Moreover, it was reported that electron beam post-treatments were found less suitable to APS titanium coating than APS/S titanium coatings because of the more heterogeneous structure of APS titanium.

2.8.5 Summary of the literature review of corrosion

The summary of the literature review of corrosion are as follows.

- Titanium metal has an excellent corrosion resistance in seawater because of an adherent oxide film on its surface. Titanium metal can be used as a barrier layer to provide protection to a less noble metal substrate in corrosive environment.
- Atmospheric plasma spraying of titanium resulted in severely oxidized, porous and inhomogeneous coatings which showed two orders of magnitude higher corrosion current density than bulk titanium. In addition, the free standing deposits also did not show passivation behaviour like bulk titanium.
- Flame sprayed titanium coatings showed no protection to the carbon steel substrate in NaCl solution due to a significant amount of oxides, nitrides and carbides in the coatings.
- Arc spraying of titanium changed the composition of titanium to TiN and Ti_2O and resulted in higher corrosion current density and lower open circuit potential compared to bulk titanium. The corrosion current density was improved by 200 times using optimized process parameters.
- Warm spraying produced titanium coatings with less than 1 vol.% porosity with 1.5 wt.% oxygen content. However, due to the presence of interconnected porosity the corrosion current density of the coatings was higher than that of bulk titanium.

- Cold sprayed titanium coatings had a more negative open circuit potential than bulk titanium by 300 mV in NaCl solution. The corrosion current densities of the coatings were 1-2 orders of magnitude higher than bulk titanium.
- Post-spray laser surface melting has been reported to improve the performance of plasma sprayed coatings measured by open circuit potential test in sea water. After 15 days of exposure, the OCP of the laser treated coating showed a shift of 280 mV towards the bulk titanium.

2.9 Aims and objectives of the research

Based on the literature review, the following aims and objectives are set for this research work.

- To study the particle impact and deformation behaviour in cold spraying and to understand the bonding mechanisms taking place during this high strain rate deformation. In addition, to investigate the existence of a metal-to-metal bonding at the cold sprayed coating-substrate interface.
- To investigate the role of process parameters on microstructural and mechanical properties of cold sprayed titanium coatings. To find a method to characterize the porosity of the cold sprayed coatings reliably.
- To evaluate the role of porosity in corrosion performance of the cold sprayed titanium coatings and methods of eliminating porosity in the coatings.
- To investigate the possibility of post-spray treatments to improve the corrosion resistance of the cold sprayed titanium coatings so that the coatings can provide suitable protection to the less noble substrate in corrosion reactions.

In addition, detailed aims and objectives of each chapter are provided at the beginning of each chapter.

3 Experimental

3.1 Introduction

This chapter provides an overview of the cold spray apparatus used in depositing the coatings and a description of the experimental equipment utilized to characterize the coatings. This covers all the coating experiments for copper, aluminium and titanium including wipe tests. A brief overview of the working principles of the equipment used in the experiments is included in this chapter. Moreover, the methodology used for the experiments is justified.

3.2 Overview of cold spray equipment

3.2.1 Cold spraying with room temperature helium

The University of Nottingham cold spraying apparatus is an in-house built rig designed to spray using room temperature helium [93, 180]. A schematic illustration of the cold spray system is shown in Figure 3-1. The system utilizes room temperature helium at 2.9 MPa for the primary accelerating gas and room temperature nitrogen as the powder carrier gas. The pressure of the carrier gas was normally set approximately 0.1 MPa higher (~ 3.0 MPa) than the primary gas pressure to ensure powder feeding into the primary gas flow. The nozzle was fixed vertically to a frame and the samples moved below the nozzle on a computer controlled X-Y traverse table. The convergent-divergent nozzle had a throat diameter of 1.35 mm, with an area expansion ratio of ~8.8 and divergent section was 100 mm in length. A high pressure powder feeder (Praxair 1264HP, Indianapolis, IN, USA) was used with either a 120 hole or a 12 slot feeding wheel. Copper and titanium metals were sprayed using a feed wheel of 120 holes and only aluminium was sprayed using a 12 slotted feeding wheel. The nozzle-substrate standoff distance for all the spray runs was fixed at 20 mm. The

samples were rinsed with methanol and dried using compressed air immediately prior to spraying. Substrates were then clamped side-by-side on an X-Y traverse table which controlled the relative motion between the nozzle and the sample. A relative motion of 100 mm/s of the traverse unit at 2-3 rpm of the powder feeding wheel was used for coating deposition and a relative motion of 500 mm/s at 0.5 rpm was used for single particle impact test, wipe tests.

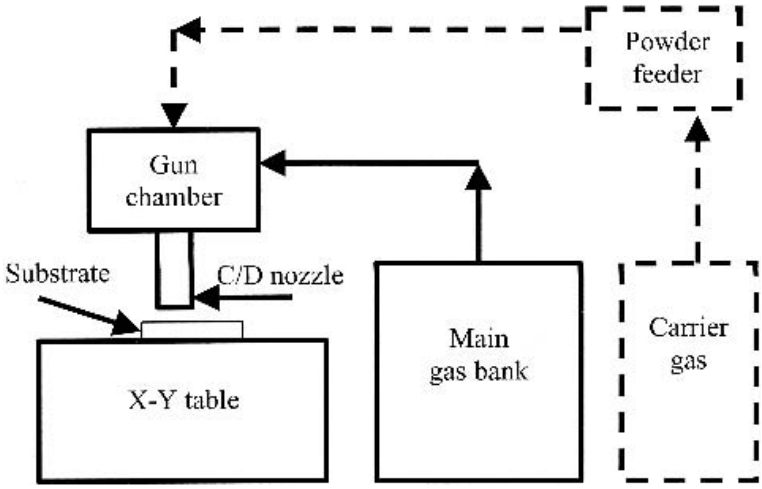

Figure 3-1 Schematic of room temperature helium cold spray system [93]

3.2.2 Cold spraying with the CGT™ Kinetiks® system

CGT Kinetiks 4000/ 47 system was used to deposit titanium onto iron and titanium based alloys at TWI Ltd (Sheffield, UK). The cold spray system with the robot and powder feeder at TWI is shown in Figure 3-2. A schematic of the CGT cold spray system is shown in Figure 3-3. The system utilizes nitrogen gas, both for the primary accelerating gas and the powder carrier gas. The primary gas flows from the gas bank to a primary gas heater and then to a secondary gas heater before it is fed through the nozzle pre-chamber, where the powder is introduced in the primary flow by the carrier gas. The combined flow then passes through the nozzle, accelerates and a coating is built up onto the substrate. The upper limit of the CGT Kinetiks system is 800 °C process gas temperature at 4.0 MPa. There were two heaters in the system: a primary gas heater which heats gas up to 450 °C and a secondary gun heater which increases the gas

temperature up to 800 °C. The de Laval nozzle (WC- type 24) had a throat diameter of 2.7 mm with an area expansion ratio of ~6.5. The convergent section of the nozzle was 50 mm long and the divergent section was 120 mm long. The nozzle-substrate standoff distance was always fixed at 40 mm. The cold spray gun was mounted on a six axis robotic manipulator (ABB, Zurich, Switzerland). A high pressure powder feeder- Kinetiks 4000 Comfort, capable of working with cold spraying with pressures up to 4.0 MPa was used. For coating deposition, a powder feeding wheel speed of 3.5 rpm was used and for wipe tests a speed of 0.5 rpm was used. The flow rate of carrier gas in both coating deposition and wipe test experiments was 3.7 m^3/h. There are no tools needed to disassemble the powder feeder and refilling can be done within few minutes. The powder feeder can load up to 4 dm^3 of powder which enables production period over 4 hours.

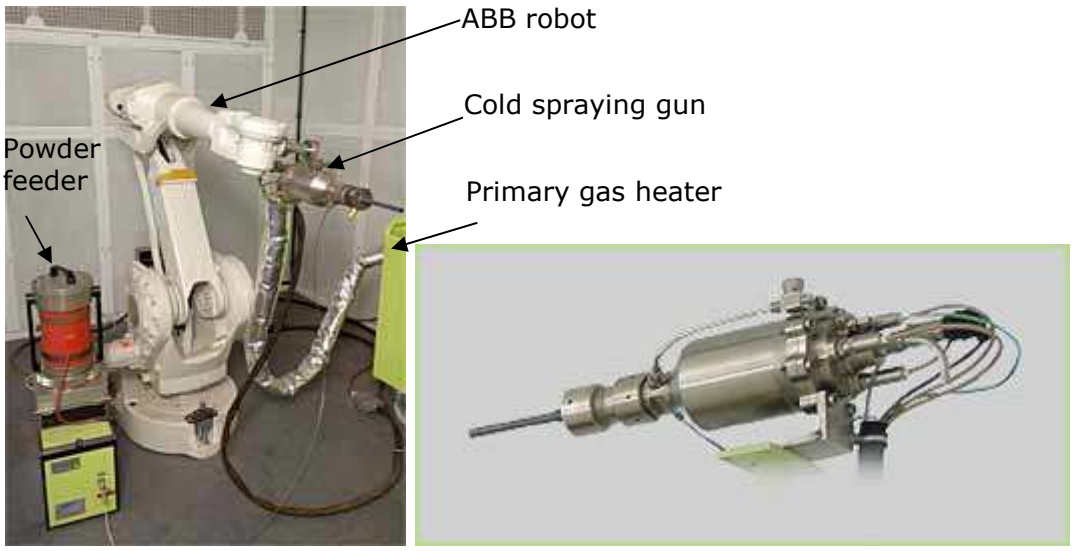

Figure 3-2 CGT Kinetiks 4000/47 system mounted on a robot at TWI, Sheffield and a close up view of the cold spraying gun

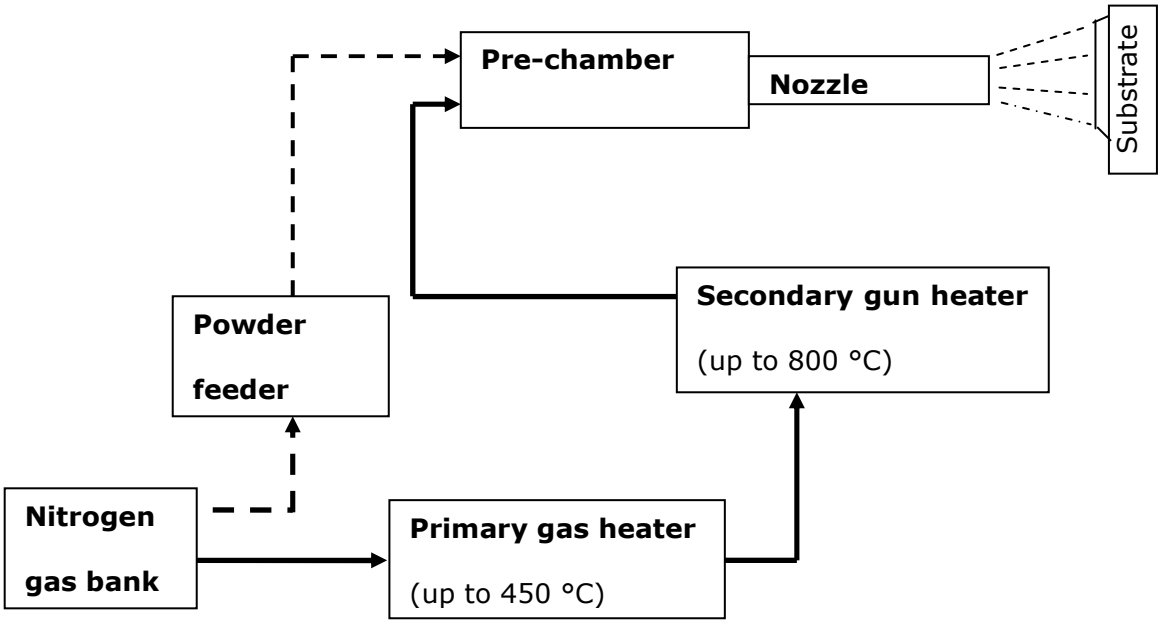

Figure 3-3 Schematic of heated nitrogen rig cold spray system

Figure 3-4 shows the assembly view of the CGT Kinetiks 4000 cold spray gun. After leaving the primary gas heater, the gas is fed to the cold spray gun at the back of the gun assembly. A pressure sensor housed in the gun assembly measures the pressure of the primary gas. The gas is then passed through a gun pre-heater which can heat the gas using three heating cartridges. The heated gas flows through a flow straightener before entering the pre-chamber (not seen in the assembly image). The powder is fed axially to the flow of the gas stream at the nozzle pre-chamber, which is made of Inconel and 120 mm in length. A temperature sensor measures the temperature of the gas before entering the pre-chamber. The gas is then fed through the convergent-divergent nozzle which accelerates the powder particles to a velocity required for cold spray deposition. Compressed air is fed to the nozzle shroud, which covers the nozzle, to cool the material of the nozzle.

There were two substrate holding techniques used in this study. In one setup, the substrate was clamped on a stationary fixture and the cold spray gun scanned the

surface of the samples in a predetermined increment. In the other setup, the samples were mounted on a rotary turntable and the gun was scanned in the vertical direction. The relative scanning speed of the cold spray gun with respect to the substrate was ~600 mm/s for coating deposition and 1700 mm/s for wipe test.

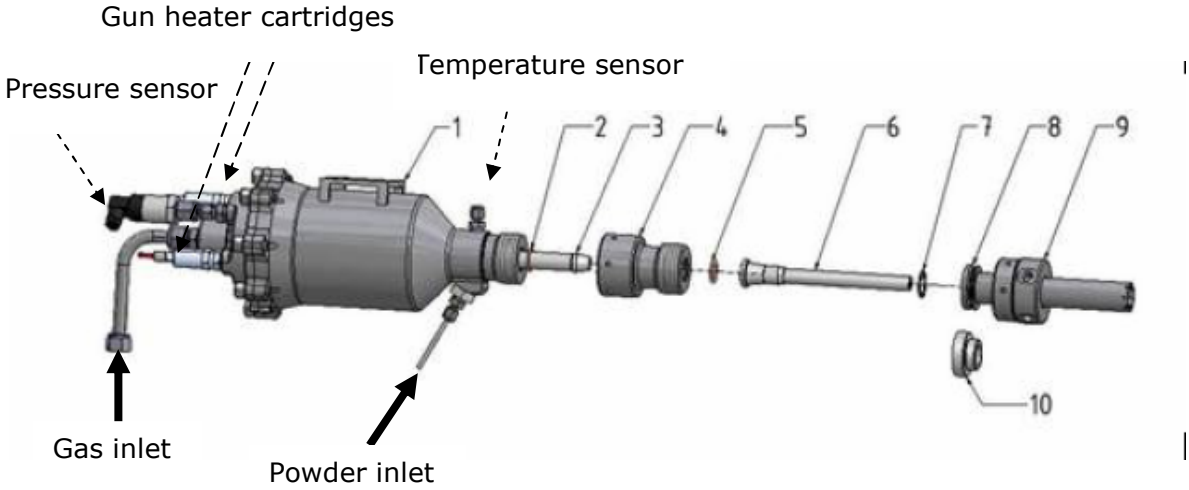

Figure 3-4 Assembly view of CGT cold spray gun showing all the components and location of sensors

1. CGT Kinetiks 4000 gun
2. Pre-chamber o-ring
3. Pre-chamber
4. Pre-chamber sleeve
5. O-ring
6. Convergent-divergent nozzle
7. O-ring
8. Nozzle shroud
9. Nozzle sleeve
10. Spacer

3.3 Particle size measurements

Particle size analysis of the powders was measured by laser diffractometry using Malvern Mastersizer S (Malvern Instruments, Worchestershire, UK). The process is based on the principle that particles passing through a laser beam will scatter light at an angle that is directly related to their size. Large particles scatter light at narrow angles with high intensity, whereas small particles scatter light at wider angles with low intensity. The scattered light produced over a wide range of

angles is captured in a series of detectors. The system software then uses Mie light scattering theory to obtain the energy distribution of the particles and produce a particle size analysis based on a equivalent spherical diameter. The analysis produced by Malvern Mastersizer is a volume based measurement and is therefore sensitive to small changes in the number of larger particles in the sample. A helium-neon light source with a wavelength of 632.8 nm was used for measuring the particle sizes, which limits the measurable particle size to 1 μm. For each powder, three measurements were taken and the mean calculated. To prevent particle agglomeration a representative sample was suspended in water in a wet dispersion magnetically stirred cell. When the size range of the titanium powder was measured, few drops of surfactant (nonidet) was used to achieve a good dispersion of powder in the liquid.

3.4 Substrate composition analysis

The chemical composition of the substrates was measured using an optical emission spectroscopy (OES) (Foundry-Master UV, Oxford instruments, Bucks, UK). Emission spectroscopy examines the wavelengths of photons emitted by atoms during the transition from an excited state to a low energy state. Every element has a characteristic set of discrete wavelengths according to its structure. In optical emission spectroscopy, the elemental composition of the sample can be determined by analyzing these wavelengths. The sample surface was ground using a belt grinder to remove any oxide layer before the test.

3.5 Microstructural characterization

Cross-sections of copper and aluminium coatings were prepared by cutting samples with a diamond slitting wheel; sections were mounted in conducting epoxy resin and sequentially ground using SiC paper to P 1200 grit finish and then polished to 1 μm diamond surface finish. However, titanium coating cross-sections were prepared by sequentially grinding using SiC paper to P 4000 finish

and polished with 10:1 colloidal (0.1 μm) silica suspension and H_2O_2 on a MD-Chem cloth (Struers, Rotherham, UK). This polishing method was previously used by Marrocco [6] and Price [24] to polish cold sprayed titanium coatings and proven to avoid smearing of the coating and embedding of diamond during preparations.

To analyze the morphology of the powder, a representative sample of powder was dispersed on a carbon stub and the excess was blown over using compressed gas before examining in a scanning electron microscope. For microstructural investigations, the samples were etched and observed in optical microscope. Titanium coating was etched in Kroll's etchant (2% hydrofluoric acid, 5% HNO_3 and 95% H_2O solution), low carbon steel and Armco iron were etched using 5% nital, and austenitic stainless steel was etched using Aqua Regia (a ratio of 1:3 parts nitric and hydrochloric acid) solution.

A FEI XL30 (FEI Europe, Eindhoven, The Netherlands) scanning electron microscope (SEM) operated at 20 kV was employed to examine the microstructure of the materials using secondary electron (SE) and backscattered electron (BSE) imaging. In the latter, contrast results from differences in the mean atomic number of the phases being imaged. Energy dispersive X-ray (EDX) analysis was carried out in the SEM to identify the phases present.

3.6 Surface profilometry

The surface roughness (Ra) following spray deposition was measured using a vertical scanning interferometer (Fogale Nanotech Photomap 3D, Ville Active, Nimes, France), with a typical ~ 1 mm × 1 mm measurement area. From this area a line scan of 1 mm in length was extracted and the Ra value measured. Vertical scanning interferometry has the highest resolution among all the optical

measurement techniques (up to 0.1 nm). The system utilizes phase-shifting interferometry principles to scan the surface. Interferometry is a technique of diagnosing two or more phases of waves by studying the pattern of interference created by the superposition. A 5x objective lens was used to scan the prepared surfaces. The interferometer was used in white light mode to scan the surface and then linear interpolation mode was used to calculate the surface profile. Moreover, a four point levelling technique was used to level the scanned surface profile before surface roughness measurements. Furthermore, all the substrate surfaces following grit blasting were cleaned in an ultrasonic bath in acetone for 15 minutes and blown using compressed air to get rid of any loose grit, which might affect the profilometry results.

3.7 X-ray diffraction analysis

X-ray diffraction (XRD) analysis (Siemens D500, Siemens Analytics, Munich, Germany) with monochromatic Cu K_α radiation (0.15406 nm) was used for phase identification and peak broadening measurements in titanium powder, as-sprayed and heat-treated deposits. In an XRD apparatus, a beam of X-ray strikes a crystal and constructively diffracts according to the Bragg's Law

$$n\lambda = 2d \sin\theta \quad \text{equation 3.1}$$

where n is an integer, λ is the wavelength of incident wave, d is the spacing between the planes and θ is angle between the incident ray and scattering plane. Analyzing the angles and intensities of these diffracted beams, the crystal structure of the material can be determined. XRD scans were performed with a step size of 0.05° and a dwell time of 5 s per step in the 2θ range from 30° to 90°. The dimension of the samples was 1 cm × 1cm and the surface condition was as-sprayed. Phases present in the spectra were identified using with the aid of Joint Committee on Powder Diffraction Standards (JCPDS) diffraction files.

3.8 Microhardness measurements

Hardness of the substrates was measured using a Leco M400 microhardness tester (Cheshire, UK). All the hardnesses were measured on the cross-sectional polished surface of the substrates. An indentation load of 25 gf was used for copper and aluminium substrates, and a load of 100 gf was used for ferrous alloys and Ti6Al4V substrates. For the bulk hardness of the substrates, ten measurements were made at the centre of the substrates (typically >3mm from the prepared surface) and ten hardness measurements made at the same load within 10 μm of the prepared surface, referred to as near-surface hardness.

Microhardness of titanium coatings was measured in a layer by layer method to determine variations. The coating was divided into four sections according to four passes of the spraying gun. A number of 10 indentation sets, 100 μm apart, along a line were made using a 100 gf load. Figure 3-5 shows the schematic of hardness measurements of the coatings. The measurements were taken in a way that the top 150 μm porous layer was avoided from the measurements.

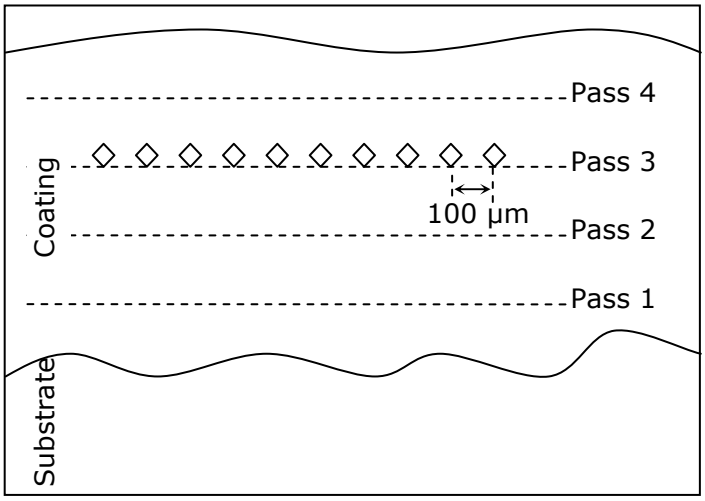

Figure 3-5 Schematic profiles of hardness measurements across the coating cross section. Ten indentations were made along every pass.

3.9 Post spray heat treatment of titanium deposits

Free standing titanium deposits were heat treated in vacuum to alter the microstructure. Following deposition onto the substrates, the deposits were delaminated by carefully bending the substrate on a vice by clamping the edge of the substrates. The deposits were sealed in a quartz tube under a vacuum of 10^{-4} Torr to avoid oxidation during the heat treatment. The heat treatment was performed at 1050 °C for 60 minutes in a rapid heating furnace (Carbolite, Sheffield, UK) at a heating rate of 50 °C/min. The heat treatment temperature was chosen to be approximately 150 °C above the β-transus temperature of commercially pure titanium with 0.25 wt.% oxygen. Following the heat treatment, the quartz tube was air cooled to room temperature.

3.10 Laser surface melting

3.10.1 Materials

Trials to optimize the laser process parameters were performed on the cold sprayed titanium coating onto carbon steel substrate (40 ×25 ×2 mm) sprayed at process gas temperature of 800 °C.

3.10.2 Equipment and process parameters

Laser surface melting was performed using a Trumpf DMD 505 (Trumpf GmbH, Ditzingen, Germany) 2 kW CO_2 laser. The laser was used to melt only the top layer of the material in a protective helium atmosphere to avoid oxidation of titanium. The samples were clamped on a copper block to dissipate the heat produced from the laser heating and to avoid distortion of the coatings and hence delamination. The trials were carried out at laser power ranges from 440 W to 1000 W, traverse speed of 15 mm/s to 48.3 mm/s, and a spot diameter of 0.3 to

1.08 mm. Prometec beam profiler (Prometec GmbH, Aachen, Germany) was used to measure the spot sizes.

3.10.3 Primary trials to optimize settings

A number of trials were conducted onto cold sprayed titanium coating to study the shape and depth of melt pool. Table 3-1 shows the process parameters used in the trials on the titanium coatings. Run no 1 and 2 were conducted at a lower laser power, whereas run no 3 to 6 were conducted at higher laser power of 1000 W. In run no 3-6, the spot diameter was fixed at 1.08 mm but the scanning speed was varied from 15 to 48.3 mm/s.

Run No	Power, P' (W)	Speed, U (mm/s)	Spot diameter, D (mm)
1	**440**	25	0.3
2	**540**	25	0.408
3	1000	**15**	1.08
4	1000	**21.6**	1.08
5	1000	**31.6**	1.08
6	1000	**48.3**	1.08

Table 3-1 Preliminary trials to optimize settings on a titanium coating deposited onto carbon steel using process gas temperature 800°C

3.10.4 Production of melted areas

Laser surface melted areas were prepared on cold sprayed titanium coatings deposited onto carbon steel substrates at a process gas temperature of 800° C. The coatings had dimensions 40 ×25 mm. Two rectangular areas of dimensions 16 mm × 16mm were laser melted using overlapping tracks. The process parameters used in run no 4 (Table 3-1) were used to produce the laser melted

areas. The laser tracks were 1.2 mm in width and the tracks were overlapped by 0.2 mm to produce a continuously melted area. These melted areas were used for microstructural investigations and corrosion tests.

3.11 Mercury intrusion porosimetry (MIP)

The porosity of free standing titanium deposits was measured using a mercury intrusion porosimeter (Autopore IV, Micromeritics, Norcross, GA, USA). To measure porosity, delaminated samples were placed in a penetrometer, which consists of a glass sample holder attached to a silver coated capillary tube (Figure 3-6). When mercury penetrates the sample it results in a change in capacitance of the capillary tube, which is then used to measure the intrusion of mercury.

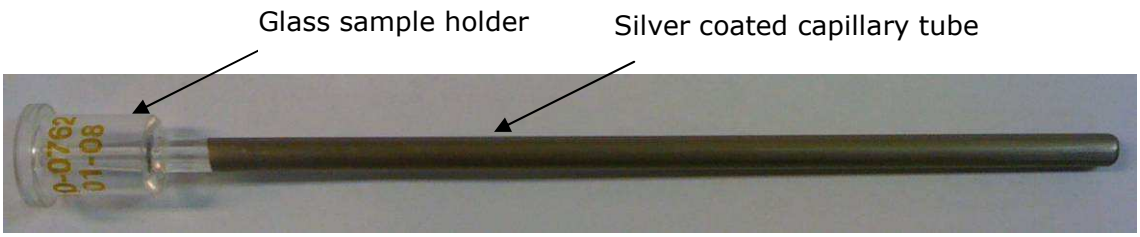

Figure 3-6 Penetrometer of the mercury intrusion test

Results are presented in the form of intrusion volume of mercury per gram of sample versus pressure where pore diameter is then calculated by the operating software from the pressure values using Washburn's equation.

$$D = -\left(\frac{1}{P_a}\right) 4\gamma \cos\varphi \qquad \text{equation 3.2}$$

Where D is the pore diameter, P_a is the applied pressure, γ is the surface tension, and φ is the contact angle. There are two ports in the mercury porosimeter: a low pressure port and a high pressure port. The low pressure port evacuates any air trapped inside the sample and then fills it with mercury at 0.14 MPa. The sample

is then transferred to the high pressure port where the mercury infiltrates the sample at pressures up to 415 MPa. Free standing deposits of dimension 10× 8× 1 mm were used for the mercury intrusion tests. Mercury intrusion porosimetry can only be used to measure the porosity which is connected to the surface of the deposits, where mercury can penetrate. Total mercury intrusion (mL/g) values were converted to volume percentages of porosity of the deposits assuming that the density of titanium is 4500 kg/m^3.

3.12 Bond strength pull-off tests

The pull-off strength of the as-sprayed copper and aluminium deposits was measured using a portable pull-off precision adhesion test (PAT) machine from DFD instruments (Woking, Surrey, UK) according to ASTM D4541- 09e1. Figure 3-7 shows a schematic illustration of the precision adhesion test (PAT) setup. The diameter of the coating for pull-off tests was 8.16 mm, which was deposited using a mask. The specimen holder is designed to be self aligning in such a way that it applies uniform stress distribution over the area under test. The load was applied using a hand operated hydraulic pump. A thermal cure resin, E1100S supplied by DFD instruments (Woking, Surrey, UK) was used, which itself had a tensile strength of around 80 MPa. A steel pull rod (the dolly) was bonded to the top surface of the coating; the dollies were ground using a coarse SiC abrasive paper and cleaned using methanol prior to application of the adhesive. After applying the adhesive, samples were put in a vacuum desiccators to remove any air bubbles trapped in the adhesive and then cured in a fan-assisted oven at 120°C for 90 min. Five pull-off tests were performed for each substrate type, with the mean and standard error in the mean of these five measurements being quoted. Following pull-off testing, the fractured surfaces were examined in the SEM.

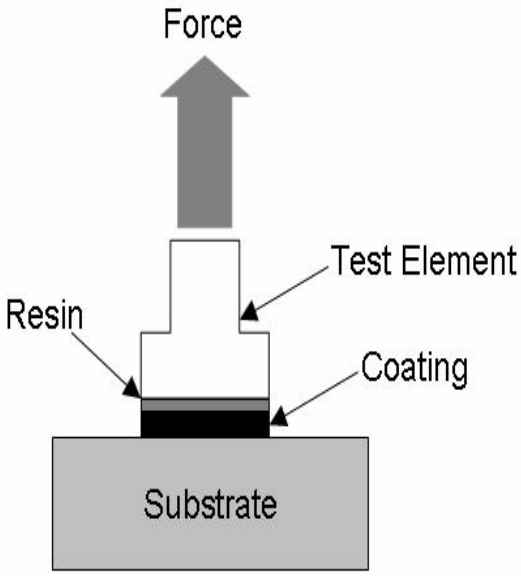

Figure 3-7 Schematic of pull-off PAT tests [24]

Bond strength of the titanium coatings onto steel and titanium alloy substrates was measured according to ASTM standard C633-01(2008) with a universal tensile testing machine (Instron 8500, Massachusetts, USA). Figure 3-8 shows a schematic diagram of the bond strength test according the ASTM C633. During the tests, the universal joints on both ends ensured that the applied load was distributed evenly across the entire cross-section of the coating. The coating diameter was 1" which was deposited onto a 1" diameter cylindrical substrate. Single part thermal curing epoxy adhesive, Araldite AV 119 (Huntsman Advanced Materials, Cambridge, England), was used to measure the bond strength of the deposits. The tensile strength of the adhesive itself was 88 ± 2 MPa. The steel pull rod was grit blasted and ultrasonically cleaned in acetone before attaching to the top surface of the coating. The samples were cured in an oven at 140 °C for 45 minutes. Three pull-off tests were performed for each substrate type and following the test, the fractured surfaces were examined in the SEM.

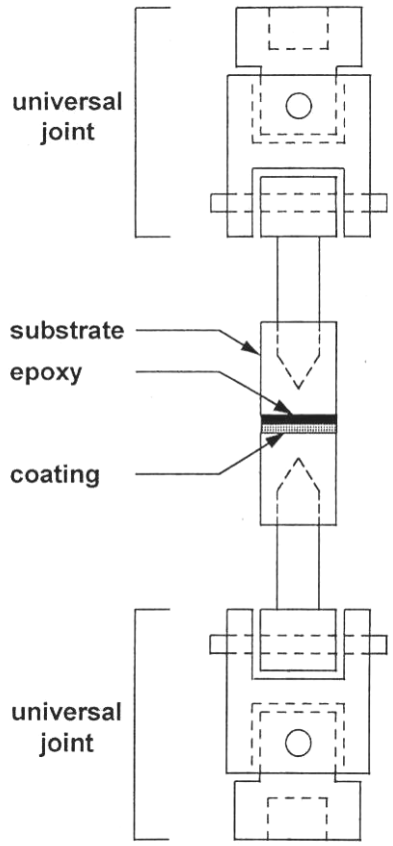

Figure 3-8 Schematic of tensile adhesion test according to ASTM C633 [181]

3.13 Tubular coating tensile (TCT) test

In order to determine the tensile strength (UTS) of the titanium deposits, the tubular coating tensile (TCT) test was performed [10, 11, 182]. To prepare tubular coating tensile test samples, two 1"φ screwable cylindrical substrates (similar to the substrates used for ASTM C633 bond strength test) were placed face to face on a lathe machine, no gap was allowed in between the two samples. The substrates were made of carbon steel and the surface of the substrate was prepared by grit blasting using the cold spray gun. The coating was deposited on the circumference of the substrate while the substrate was rotating on the lathe building up to a thickness of ~ 900 µm. A universal tensile testing machine was used to measure the maximum load before failure. The load was divided by cross

section area to find the tensile strength of the deposit. Three tubular coating tensile tests were performed and the fracture surfaces were examined by SEM. Figure 3-9a shows the plan view and Figure 3-9b shows the cross-section of tubular coating tensile test samples after tensile tests.

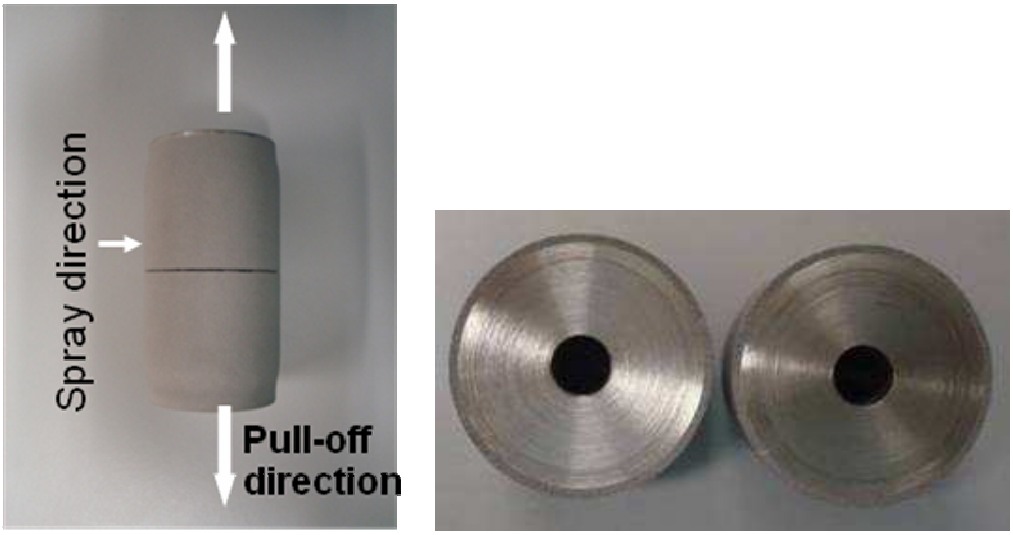

Figure 3-9 Tubular coating tensile (TCT) test samples after failure. (a) Plan view of the sample showing spray direction and pull-off direction in the tensile testing machine, (b) Cross-section of the samples.

The geometrical design of the substrate introduces a stress concentration in the coating [10]. Therefore, the stress concentration in the gap of the two substrates increases the Von Mises stress by a factor of 1.5 – 1.7, as can be seen in the finite element analysis of the TCT test in Figure 3-10. To calculate the ultimate tensile strength of the coating, the failure stress has to be multiplied by the factor to compensate for the stress concentration [11].

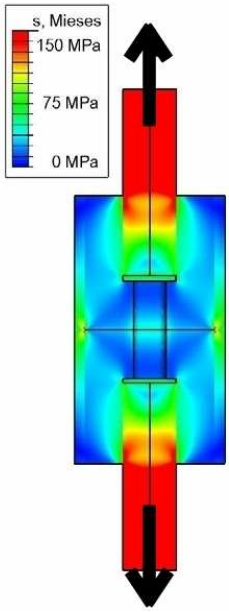

Figure 3-10 Axi-symmetric finite element stress analysis of tubular coating tensile (TCT) test [182]

3.14 Electrochemical tests

Potentiodynamic electrochemical tests of free standing titanium deposits and coatings were carried out using an ACM Gill 8 sequencer (ACM Instruments, Cumbria, UK) in a standard three electrode cell. The three electrode cell contains a working electrode, reference electrode and an auxiliary electrode. These are connected together to a potentiostat as shown in Figure 3-11. A working electrode is the material being investigated. Potential measurements are made between the working and reference electrode and current measurements are made between the working and auxiliary electrode. Auxiliary electrode is used to carry the current created in the circuit by the investigations. A platinum metal strip of 100 mm^2 was used as an auxiliary electrode. The reference electrode provides a datum against which the potential of the working electrode can be measured. Reference electrode carries negligible current, so it does not participate in the cell reactions and the potential remains constant. In the potentiodynamic experiments, all the potentials were measured with respect to an Ag/AgCl secondary electrode.

The cell temperature was maintained at 30±1°C using a water bath. The samples were tested in a solution of 3.5 wt. % NaCl in de-ionized water and a flow of nitrogen gas was maintained at 0.1 L/min during the full duration of the experiments. Nitrogen flowed through the solution for 30 minutes before the start of the test to stabilize the cell.

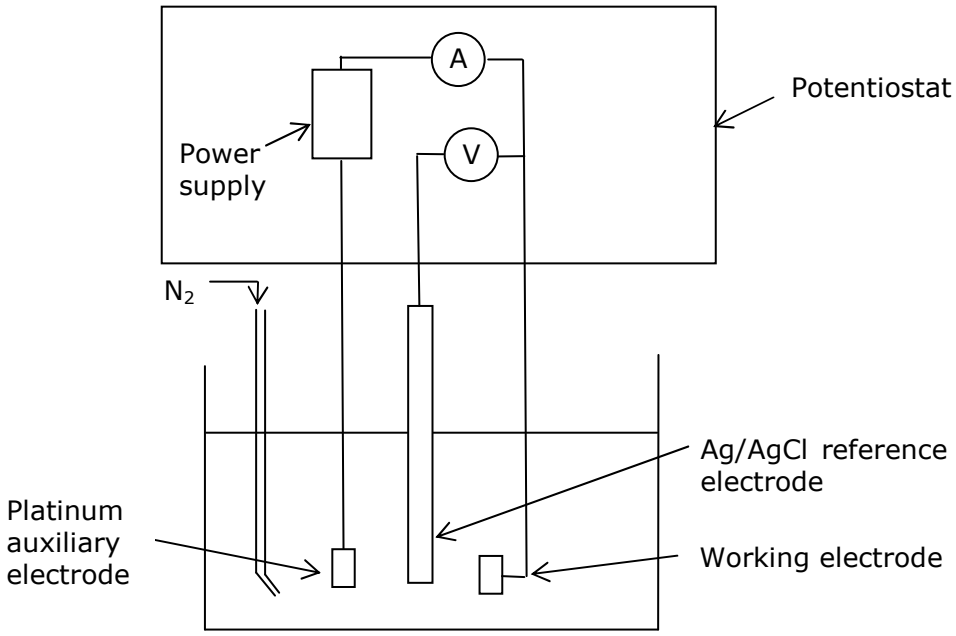

Figure 3-11 A schematic diagram of three electrode cell used in potentiodynamic tests

The open circuit potential (OCP) of the specimens was measured during the first 60 minutes of immersion before starting the potentiodynamic scans. To conduct the polarization scans the samples were first lowered to a potential of 200 mV below the open circuit potential and then scanned at a rate of 20 mV/ min in the anodic direction. The scans were stopped when the potential of the samples reached an upper limit of 1800 mV above the rest potential, Ecorr. The intersection of the anodic and cathodic linear extrapolations at the rest potential of potentiodynamic polarization scans (Tafel extrapolation) was taken as the

corrosion current density, Icorr. The passive current density, Ipp was taken as the current density of the passive region from the potentiodynamic polarization scans. ASTM G5- 94(2004) guidelines were followed for the potentiodynamic polarization tests.

Reproducibility of the corrosion measurements was evaluated by running repeat tests on both free standing deposits and coatings. Three separate samples of free standing deposit sprayed at 600 °C gas temperature and three samples of coating deposited onto carbon steel using a gas temperature of 800 °C were tested under the same conditions. The variations in measured values of the three free standing deposits were as follows: OCP ± 30 mV; Ecorr ± 2.5 mV; Ipp ± 0.005 mA/cm^2 and Icorr ± 0.0005 mA/cm^2. The variations in measured values of the three coatings were as follows: OCP ± 13 mV; Ecorr ± 30 mV; Ipp ± 0.025 mA/cm^2 and Icorr ± 0.0005 mA/cm^2. These values are well within the typical range of experimental in electrochemical studies of this type. Therefore graphs of typical open circuit potential changes with time and potentiodynamic polarization scans for each sample are presented in this thesis.

3.14.1 Sample preparation for electrochemical tests

Free standing samples were spot welded at the back to provide electrical connections and then cold mounted in the epoxy resin for the electrochemical tests. The substrate side of the free standing samples was lightly ground to remove any residual steel. Coatings onto carbon steel samples were only spot welded at the back to provide electrical connections and all the exposed sides were covered with stopping off lacquer. The as-sprayed surface of each sample was ground to P1200 grit finish to remove the top porous layer. The samples were painted with a stopping off lacquer to expose an area of 100 mm^2 for

testing. Finally, the sample surfaces were degreased using methanol, cleaned with de-ionized water and dried immediately before immersion.

3.15 Salt spray (fog) tests

In the salt spray test, a 5 wt.% NaCl solution is atomized to create a fog within an enclosed chamber holding the coated fixtures. The temperature of the salt spray cabinet was maintained at 35 ^{o}C. The position of the coatings was such that they were supported 15 to 30^{o} from the vertical and parallel to the principle direction of flow of the fog through the chamber. Changes to the coating surface during the exposure were recorded at regular intervals. The salt spray tests were conducted according to ASTM B117-09 standard.

3.15.1 Sample preparation for salt spray

Salt spray (fog) tests of titanium coatings sprayed onto carbon steel substrates (dimensions of 25 × 20 × 2.5 mm) using process gas temperatures of 600 and 800 °C were performed for 24 hours. The back and the sides of the samples were covered with a red stopping off lacquer to avoid any galvanic corrosion and only the top of the coating surface was exposed. High resolution digital images were taken at regular intervals to characterize the extent of corrosion attack. In addition, a cold sprayed titanium onto carbon steel substrate (15 × 10 × 2.5 mm), which was sprayed at 600 °C process gas temperature, was prepared with a P1200 ground surface finish and exposed in salt spray for 3500 hours to investigate the effect of surface preparation on the corrosion behaviour. Moreover, salt spray test of laser treated coating was performed by exposing an area of 100 mm^2 for a total of 100 hours. For reference purposes, a 100 mm^2 area of the as-sprayed coating from the same sample, which had not been laser treated, was exposed in the salt spray for 24 hours and then covered with red stopping of lacquer.

3.16 Immersion tests

The immersion tests were performed on titanium coatings sprayed onto stainless steel substrates (304) using process gas temperatures of 600 and 800 °C in 1 litre of 3.5 wt.% NaCl solution at 80° C. The solution temperature was maintained within ±2 °C of the set temperature using a fan assisted oven. Only the titanium coating surface was exposed to the solution and the back and the sides of the samples were painted with a stopping off lacquer. The concentration of the salt solution was maintained by topping up with de-ionized water every 24 hours to compensate for any loss of solution due to evaporation. The immersion tests were conducted for 165 hours after which the samples were cross-sectioned and analyzed in SEM. The surface finish of the samples was in as-sprayed condition.

4 Impact behaviour and bonding mechanisms in cold spraying

4.1 Introduction

The mechanism of bonding in cold spraying is still a matter of some debate. A number of hypotheses have been proposed concerning the mechanism by which bonding takes place in cold spraying. The bonding mechanism is believed to be the result of an adiabatic shear instability at the interface during impact which occurs as a result of high strain rate deformation processes and creates a metal jet [9, 40, 42, 64]. It is the formation of this metal jet which, it is proposed, results in the removal of the surface oxide layer and allows true metal to metal contact to be established. Numerical simulations of particle impact in cold-spraying provide valuable information about the high strain rate deformation behaviour of materials, but are unable to provide a clear indication of the conditions under which intimate metallic bonding is established. High resolution transmission electron microscopy (TEM) provides valuable information of the interfacial features but only a small fraction of the interface can be analysed at a time. The time consuming sample preparation makes it difficult to look at few mm of the coating- substrate interface.

Price et al. [4] proposed a method to characterize the interparticle bond formation in cold spraying; here, a blended powder of copper and aluminium particles was cold sprayed and subsequently annealed at 400°C. It is known [99-101] that the formation of intermetallic phases during annealing of aluminium-copper diffusion couples indicates that the surfaces in contact are free of oxide layers, and Price et al. [4] thus utilized the formation of such intermetallics between copper and aluminium particles within the coating as an indicator of

metal-to-metal bonding where surface oxide films had been removed during spraying. The study reported by Price et al. investigated the metal-to-metal bond formation within the coating, not at the coating-substrate interface. The methodology proposed by Price et al. [4] formed an important part of this chapter. This method of using a short heat treatment to promote interdiffusion and intermetallic formation was utilized at the coating- substrate interface to identify the formation of metal-to-metal bonding. Three different coating-substrate systems were studied in this chapter, namely: copper coatings onto aluminium substrates, aluminium coatings onto copper substrates and titanium particles onto three steel substrates. Cold sprayed copper deposit is the most popular type of cold sprayed deposit because of the ease in spraying. A number of studies were available on cold spraying of copper deposits at the beginning of this project. Aluminium deposits were sprayed onto copper substrates using the same process parameters to investigate how the change in particle momentum/ kinetic energy affects bonding. In addition, titanium particles were deposited onto three different steel substrates: Armco iron, low carbon steel and stainless steel to investigate the bonding mechanisms. The cold-spraying of titanium has received much attention in the literature, driven primarily by the possibility of surface engineering of components with a material with such desirable corrosion resistance [76, 110, 124, 125, 129, 132, 183]. Specifically, a barrier layer of titanium coating deposited onto a low carbon steel substrate has been shown to have the potential to prevent corrosion attacks in sea water [125] and titanium clad stainless steel is a desirable component for various applications in nuclear industry [2, 3].

The aims and objective of the work reported in this chapter were as follows

- To investigate the interfacial bonding mechanisms between a cold-sprayed copper deposit and an aluminium substrate.

- To compare the interfacial bonding mechanisms of an aluminium deposit-copper substrate system to a copper deposit-aluminium substrate system.
- To explore the role of surface preparation of copper and aluminium substrates and how it affects the bonding behaviour.
- To study the interfacial bonding mechanisms of titanium particles onto steel substrates.
- To identify the role of particle shapes of titanium powder (i.e. spherical and angular) in bond formation onto steel substrates.

4.2 Experimental

4.2.1 Materials

4.2.1.1 Powder

Commercial purity (>99 wt.%) copper powder (Sandvik Osprey, Neath, UK) with a size range of -25 +5 μm was used to produce the copper coatings. In addition, commercial purity aluminium powder (The Aluminium Powder Company, Sutton Coldfield, UK) with a size range of -45 +15 μm was used to produce the aluminium coatings. Two types of titanium powders with different morphology were used for the single particle impact tests. Commercial purity gas atomized titanium powder (Pyrogenesis, Canada) with a size range of <25 μm and commercially pure hydride dehydride titanium powder (Active Metals, UK) with a size range of <45 μm were used as the feedstock. The gas atomized titanium powder was of rounded morphology and the hydride-dedydride powder was of angular shape.

4.2.1.2 Substrates

The copper powder was deposited onto samples cut from a single 6082 aluminium plate (1.00 wt.% Si, 0.7 wt.% Mn, 0.9 wt.% Mg, 0.2 wt.% Fe, balance Al),

sample dimensions being 38 ×15 × 7 mm. The aluminium powder was deposited onto samples prepared from a commercially pure copper plate (0.01 wt.% Pb, 0.03 wt.% P, 0.01 wt.% Mn, 0.004 wt.% Ag, 0.02 wt.% Co, balance Cu) with dimensions of 40 ×15 × 2 mm. The dimensions of the aluminium substrate for bond strength testing were 20 ×15 × 7 mm and dimensions of the copper substrate for bond strength testing were 20 ×15 × 2 mm. Moreover, titanium powders were deposited onto three different substrates: Armco iron, low carbon steel, and austenitic stainless steel (304). The chemical compositions of the substrates were measured using optical emission spectroscopy (Foundry-Master UV, Oxford Instruments, Bucks, UK) and are shown in Table 4-1. The dimensions of the steel substrates were 40 ×15 × 2 mm.

Substrate types	Element (wt %)										
	C	Cr	Ni	Mo	P	S	Mn	Si	Al	V	Fe
Low carbon steel	.04	.03	.01	-	.01	.02	.17	-	.03	-	bal.
Armco iron	<.005	.01	.02	-	-	.01	.04	-	.01	-	bal.
Stainless steel, 304	.05	17.8	8.31	.18	.04	-	1.24	.34	-	.08	bal.

Table 4-1 Chemical compositions of the low carbon steel, Armco iron, and stainless steel (304) measured using optical emission spectroscopy

4.2.2 Substrate preparations

The aluminium and copper substrates were prepared with three different procedures as follows (termed ground, polished and grit-blasted respectively):

a) ground with 58.5 μm SiC paper;

b) ground with 58.5 µm, 35 µm, 21.8 µm and 15.3 µm SiC paper. Polished with 6 µm and 1 µm diamond paste on soft cloth wheels. Polished with 0.1 µm colloidal silica final polishing suspension;

c) cabinet grit-blasted with Al_2O_3 with grit size of ~500 µm.

It was recognised that the surface preparation of the substrates would not only change the profile of the surfaces, but could also result in different levels of cold work. As such, following surface preparation by each of the three routes described, a number of aluminium substrates were annealed at 450 °C for 1 hour in protective argon atmosphere and copper substrates were annealed at 800 °C for 20 minutes in 75% hydrogen and 25% nitrogen environment. All the three steel substrates were prepared with a polished surface finish using 1 µm diamond paste on soft cloth.

4.2.3 Cold spray deposition conditions

Cold spraying was performed with an in-house built cold gas spraying system at the University of Nottingham. A schematic diagram and the description of the rig are given in chapter 3 section 3.2.1. Coatings were built up with copper and aluminium powders and wipe tests were performed with all three powders i.e. copper, aluminium and titanium. Previous studies on the interdiffusion of titanium coatings onto steel substrates resulted in coating debonding due to mismatch in thermal expansion co-efficient; therefore, only wipe test samples of titanium was used to study bonding in this chapter. Room temperature helium at 2.9 MPa was used as the primary accelerating gas and nitrogen as the powder carrier gas. The pressure of the carrier gas was set approximately 0.1 MPa higher (~3.0 MPa). A high pressure powder feeder with a 120 hole feeding wheel rotating at 4 rpm was used during the deposition of copper coating and a 12 slot feeding wheel rotating at 2 rpm was during the deposition of aluminium coating. However, during the particle impact tests (wipe tests), the lowest powder feed rate at 0.5 rpm was

used for both copper and aluminium power to achieve the lowest impacting particle flux onto the substrate. In a similar manner, wipe tests of titanium was performed using a 120 hole feeding wheel rotation at 0.5 rpm. The nozzle-substrate standoff distance for all the spray runs was fixed at 20 mm.

All substrates were rinsed with methanol and dried using compressed air immediately prior to spraying. Aluminium (one of each of the different surface preparation routes), copper (one of each of the different surface preparation routes) and steel substrates (three different types) were clamped side-by-side on an X-Y traverse table which controlled the relative motion between the nozzle and the sample. Each type of the substrates was sprayed under the same spray run to ensure that all the substrates were exposed to the same particle flux. For coating deposition, the table moved the samples at 100 mm /s relative to the nozzle. However, for the single particle impact tests, the highest scan rate of 500 mm/s was used to achieve the lowest impacting particle flux onto the substrate. Copper and aluminium coatings were deposited using a series of linear passes over an area of 20 × 15 mm on each sample type; to achieve uniform coverage, the table was indexed 2 mm between adjacent tracks. The deposit was built up using a number of passes to create a deposit thickness of around 400 μm. In order to manufacture samples for bond strength pull-off tests, coating was sprayed onto all the different types of aluminium and copper substrates using a mask with circular cut-outs of 8.16 mm diameter.

Spherical titanium was also sprayed onto the austenitic stainless steel substrates using heated nitrogen gas utilizing a commercial system, namely a CGT Kinetiks 4000/ 47. The description and a schematic diagram of the system are shown in section 3.2.2. The primary gas pressure was set at 4.0 MPa, the temperature at 800 °C and the flow rate at 80 m^3/h. A high pressure powder feeder (CGT) was

used at carrier gas flow-rate of 3.7 m^3/h with a powder feeder wheel speed of 0.5 rpm. The nozzle-substrate standoff distance was fixed at 40 mm. The austenitic stainless steel substrate was clamped on a stationary fixture and cold-spray gun mounted on a six axis robot manipulator scanned the surface of the samples at 1700 mm/s.

4.2.4 Post spray heat treatment

Heat treatment was performed in a tube furnace (Lenton Furnaces, Sheffield, UK) with a protective argon atmosphere. Commercial purity argon with rare gas purifier filter was used at a gas flow rate of 100 cm^3 /min. Following coating deposition (copper, aluminium) onto the substrates (aluminium, copper), samples were heat treated to allow formation of copper- aluminium intermetallics at the interfacial regions where the oxide layers had been disrupted during the spraying process. The heat treatment was performed at 400°C for 15 min in the tube furnace. The samples were heated at 20° C/min to the desired temperature and furnace cooled to room temperature. Following deposition of titanium onto steels, samples were heated at 20° C/min to 750 °C for 60 minutes to allow formation of titanium- iron intermetallics at the interfacial regions and then furnace cooled to room temperature.

To quantify the extent of the coverage of the intermetallic phase formed during annealing at the coating-substrate interface, image analysis software (ImageJ, U.S. National Institute of Health, MD) was employed. For each condition in copper-aluminium study, eight representative BSE images of the coating substrate interface microstructure were selected for measurement; each image had a field of view of approximately 300 × 225 μm. In titanium-steels study, five representation BSE images of the particle-substrate interface microstructure for each materials combination were selected for measurement.

Results

4.3 Bonding mechanisms of copper onto aluminium

4.3.1 Characterization of copper powder

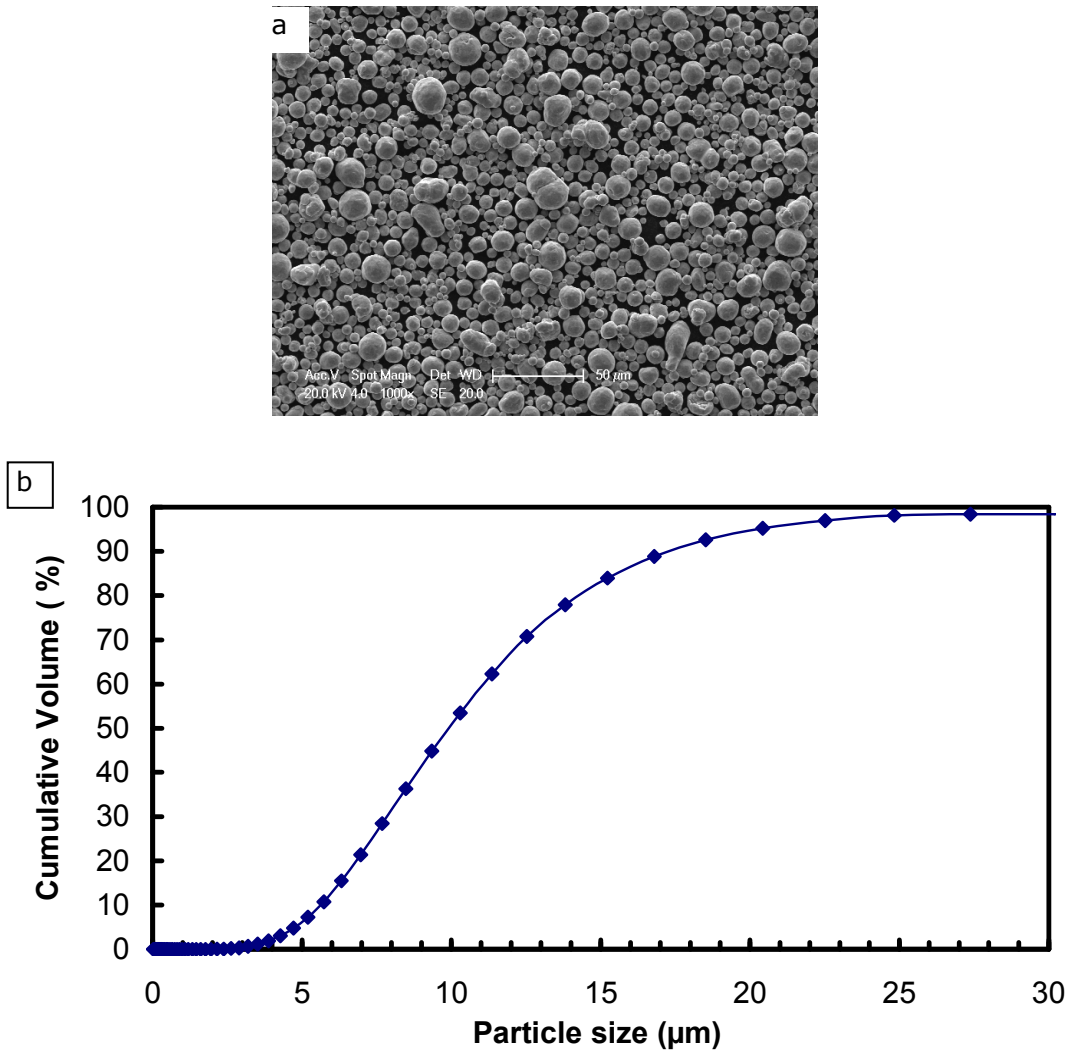

Figure 4-1 (a) SE image of gas atomized copper showing its morphology (b) Cumulative size distribution of copper powder measured by laser diffractometry

Figure 4-1 shows the morphology of the feedstock copper powder. It can be seen that the particles have a rounded morphology. The particle size analysis (Figure

4-1b) measured by laser diffractometry (Laser Mastersizer, Malvern Instruments, Malvern, U.K.) indicates that 92% of the particles are in the specified size range of -25 +5 μm with approximately 6 vol.% below 5 μm and 2 vol.% above 25 μm.

4.3.2 Single particle impact of copper onto aluminium

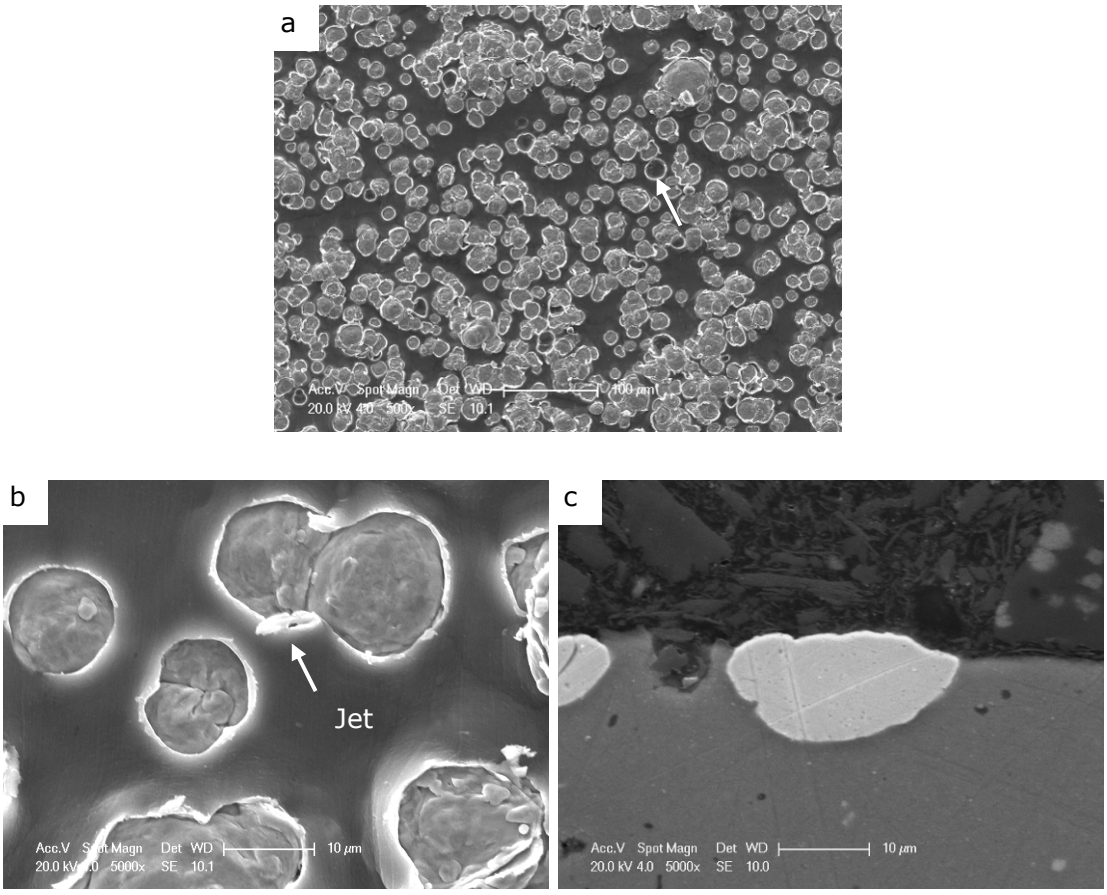

Figure 4-2 (a) SE image of copper particles on aluminium substrate. Higher magnification images of (b) copper particles on aluminium substrate (c) cross-section of a copper particle on aluminium substrate.

Figure 4-2(a) shows the surface of the aluminium substrate following wipe test. A large number of copper particles deposited onto the aluminium substrate and very few craters were formed. The craters are marked with an arrow in the image (Figure 4-2a). The craters left by the impacting copper particles indicate

significant substrate deformation. Figure 4-2 (b) shows the jet formation of aluminium substrate around the particle following deposition of copper (marked with an arrow). The cross section image in Figure 4-2(c) shows the particle was embedded in the aluminium substrate which went through significant deformation. In addition, the bottom of the particle retained a parabolic shape which is typical of an impact of a harder material on a softer substrate [184]. Moreover, Grujicic et al. [40] modelled the impact of copper particle onto aluminium substrate and noticed that the embedded particle will be flattened at the bottom compared to the top. This flattening of the particle creates a feature which is wider at the bottom and narrower at the top, essentially a rivet like assembly.

4.3.3 Characterization of different substrate surfaces

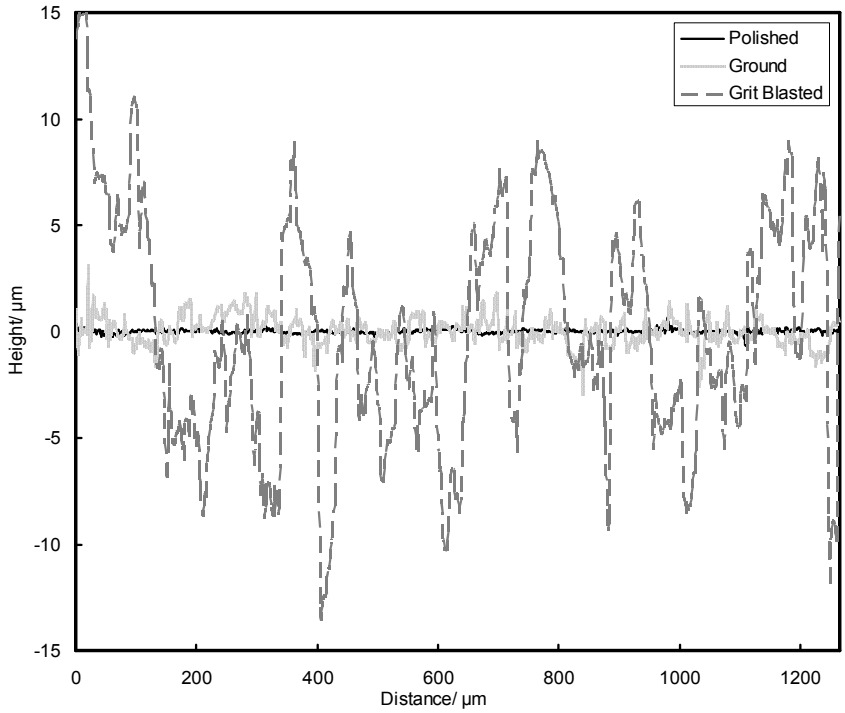

Figure 4-3 Typical line profiles extracted from the polished, ground and grit blasted surfaces

The roughness of polished, ground and grit-blasted aluminium substrates was 0.05 μm, 0.4 μm and 3.9 μm respectively. Observations of the substrate following grit-blasting showed the presence of embedded alumina grit in some cases. Figure 4-3 shows the typical surface profiles of the substrate following the three surface preparation methods. The typical peak-to-trough height of the grit-blasted surface was ~20 μm whereas the peak-to-trough height of the polished surface was less than 1 μm. The surface profile of the ground surface shows uniformly distributed peaks and valleys with a typical peak-to-trough height of 3 μm. Figure 4-4 shows the magnified profiles of the three surfaces in relation to a 15 μm spherical particle.

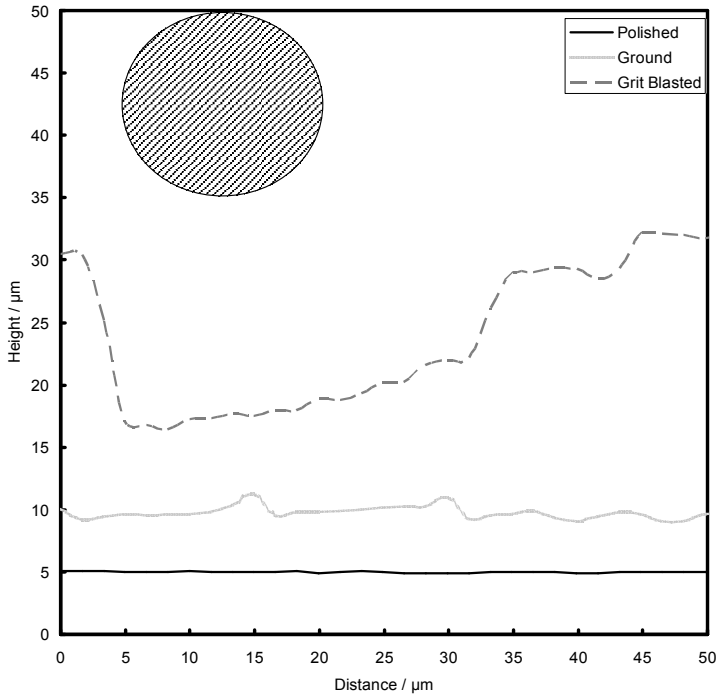

Figure 4-4 Surface profiles of polished, ground and grit blasted surfaces (with identical horizontal and vertical scaling) in comparison with a disk representing a section through a 15μm diameter spherical particle.

To identify any surface hardening during the surface preparation of the samples, microhardness indentations were made on a finally polished cross section. Ten

hardness measurements were taken within 10 μm of the prepared surface (referred to as near-surface hardness) and ten measurements made at the same load in the centre of the substrate (typically >3mm from the prepared surface). In a similar manner, the hardnesses of the bulk and surface regions following the annealing heat treatment were measured. The annealing treatment reduced the hardness of the bulk material from 115 kgf /mm^2 to 40 kgf /mm^2. The measured near-surface hardnesses are shown in Table 4-2. It can be seen that in the case of the as-prepared material, the hardnesses of both the ground and polished surface regions were very similar to that of the bulk material. However, grit-blasting resulted in significant hardening of the surface. To compare with these, a sample of 6082 alloy was cold rolled to a strain of ~ 360%; the hardness of this cold rolled material was 132 kgf /mm^2. It can be seen that this value is significantly lower than that of 179 kgf /mm^2 measured for the grit-blasted sample. Following annealing, the hardness of the polished and ground surface regions were similar to that of the bulk but the hardness of the annealed, grit-blasted surface was significantly higher than that of the bulk (50 kgf /mm^2 as opposed to 40 kgf /mm^2). Nevertheless, it was greatly reduced compared to that before annealing.

Preparation method	Surface roughness (Ra) / μm	Vickers microhardness (25gf load) / kgf /mm^2	
		As prepared	Annealed
Polished surface	0.05	114.5 ± 1.0	38.9 ± 0.3
Ground surface	0.4	105.9 ± 2.4	35.4 ±0 .5
Grit-blasted surface	3.9	179.1 ± 12.3	50 ± 1.2

Table 4-2 Near-surface hardness and surface roughness of the aluminium substrates as-prepared and following annealing. The hardness values of the bulk aluminium were 115 ± 1 kgf /mm^2 and 40 ± 1 kgf /mm^2 in the as-prepared and annealed conditions respectively.

4.3.4 Bond strength tests and fracture surface analysis

4.3.4.1 Bond strength tests

Values for the pull-off bond strength for the copper sprayed onto the aluminium substrate, as a function of the preparation method of the substrate are presented in Table 4-3. The values of the bond strength of cold sprayed copper on aluminium reported in Table 4-3 are in reasonable agreement with the values reported by other researchers [18, 86, 185]. For the as-prepared substrates (i.e. without an annealing treatment following the surface preparation), the bond strength was greatest with the polished surface and lowest with the grit-blasted surface. Similar behaviour of reduced bond strength with grit-blasting has been reported for the deposition of titanium by cold spraying [76].

Substrate surface preparation	Bond strength (as-prepared substrate) / MPa	Bond strength (annealed substrate) / MPa
Polished surface	57.4 ± 5.3	>69.2
Ground surface	55.9 ± 4.0	59.4 ± 4.5
Grit-blasted surface	35.5 ± 4.7	56.6 ± 2.9

Table 4-3 Bond strength values for the copper deposited onto aluminium substrates for as-prepared surfaces and following annealing treatment.

Table 4-3 also shows that for polishing or grit-blasting, the bond strength was significantly increased by annealing of the substrate prior to copper deposition. In the pull-off tests for copper deposited onto polished and annealed substrates, the failure was always in the adhesive between the copper and the dolly (rather than between the copper and aluminium); as such, the values recorded simply indicate a lower bound of the bond-strength of the copper-aluminium interface. However,

for the ground surface little change occurred when the substrate was annealed prior to deposition.

4.3.4.2 Fracture surfaces

The fracture surfaces following the pull-off tests were examined, and are shown in Figure 4-5 for the as-prepared surfaces, and in Figure 4-6 for the annealed substrates. In each case, both the aluminium substrate and copper deposit surfaces are shown. In addition, the fractional area of aluminium on the fracture surface of the copper deposit along with the complimentary measure of copper on the aluminium substrate fracture surface are shown in Table 4-4. Looking at the aluminium substrates, it is clear that copper particles (regions of high brightness) are observed to adhere both as single particles and as groups of particles (Figure 4-5a-c and Figure 4-6a-b); no significant differences were noted in the amount of copper particles retained as a function of the methods of preparation of the aluminium substrate (Table 4-4). On the surfaces of the copper deposits, aluminium is clearly observed (regions of low brightness). For the polished and ground samples, aluminium is observed primarily in between the copper particles (Figure 4-5d-e and Figure 4-6c). The aluminium has the appearance of being extruded between the copper particles as shown by the higher magnification image of Figure 4-7. In contrast to this, the observations for the grit-blasted surfaces show that the aluminium is found more widely dispersed on the copper deposit fracture surface and in larger areas (Figure 4-5f and Figure 4-6d). It is notable that for the grit-blasted substrates, the fraction of aluminium visible on the deposit surface is significantly greater than for polished or ground surfaces. Also, it has a different morphology of flat irregular particles as opposed to the solely interparticle presence in polished or ground substrates. This is the case irrespective of whether or not the substrate was annealed before copper deposition.

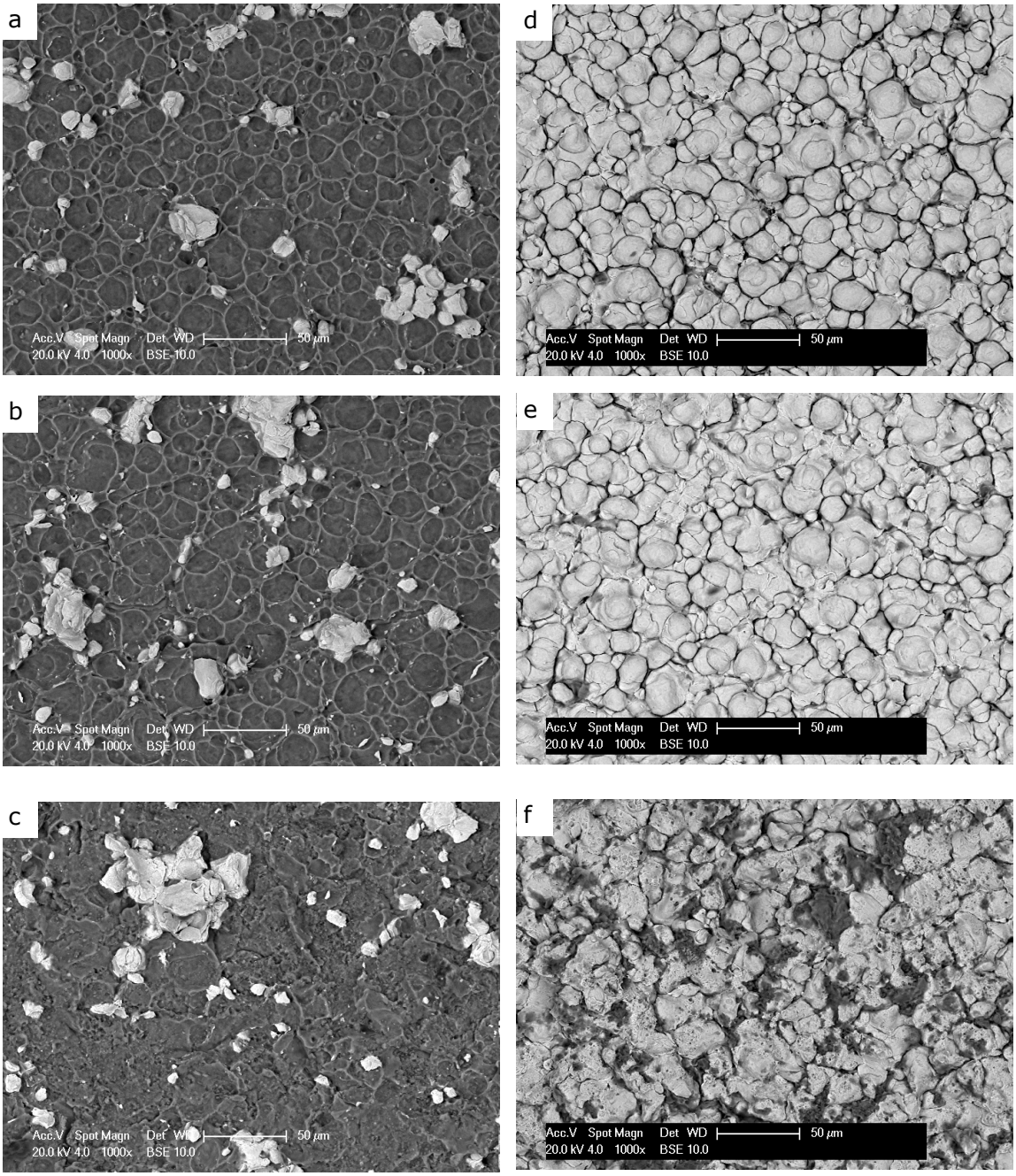

Figure 4-5 Fracture surfaces, after pull off test, of as prepared Al substrate (a-c) and corresponding copper coating (d-f) with different substrate surface preparations: (a, d) polished; (b, e) ground; and (c, f) grit blasted. The bright phase is Cu and the darker one Al. The Al substrate shows the presence of individual Cu particles adhered to it and the Cu coating shows Al trapped in between Cu particles.

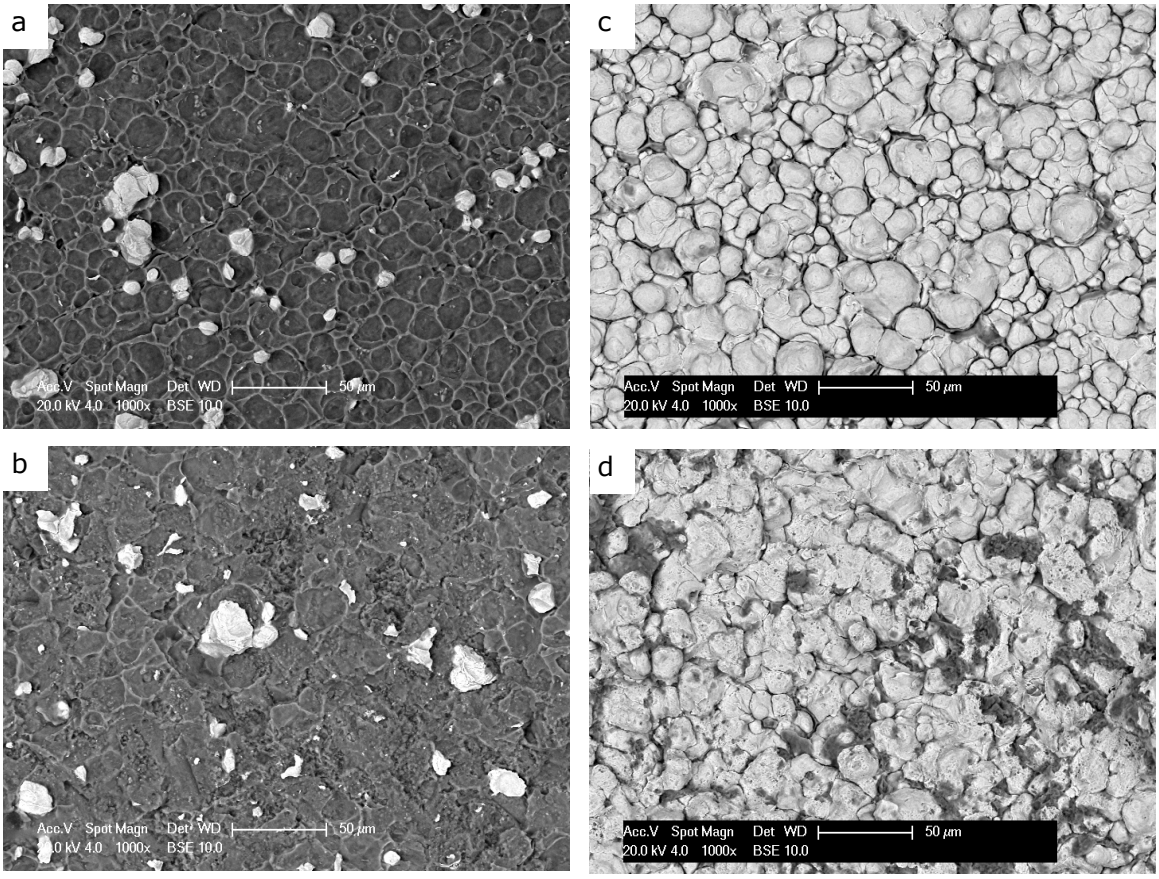

Figure 4-6 Fracture surfaces, after pull off test, of annealed Al substrate (a-b) and corresponding copper coating (c-d) with different substrate surface preparations: (a, c) ground; (b, d) grit blasted.

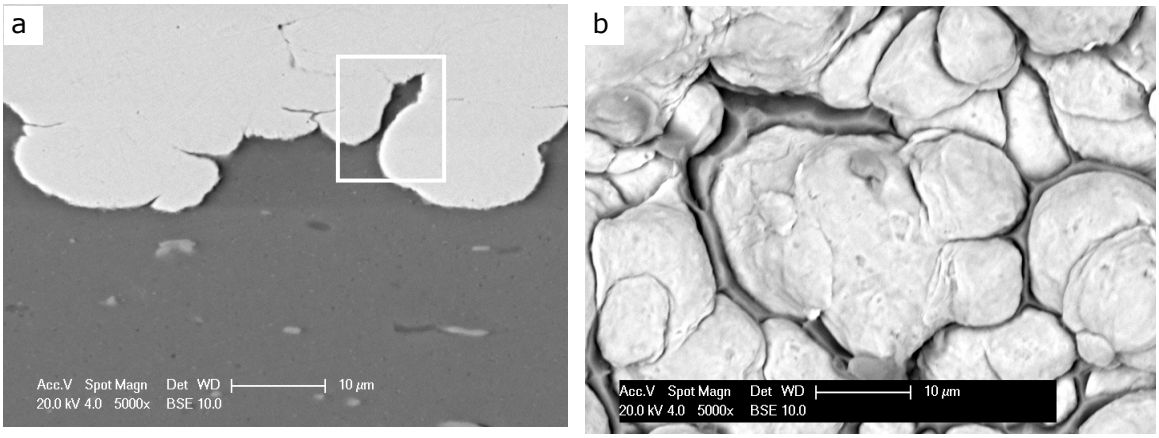

Figure 4-7 (a) High magnification image of copper coating on ground and annealed aluminium substrate showing aluminium extruded in between copper particles. (b) Fracture surface (coating side) after pull off test on

the same coating-substrate combination showing rim of Al (dark) around Cu particles (bright).

It is also notable that the fracture surfaces of both the copper deposits and the aluminium substrates show the clear rounded morphology of the copper particles for both the polished and ground surfaces (Figure 4-5a, b, d, e and Figure 4-6a, c), indicating that plastic deformation upon impact was primarily within the aluminium substrate. In contrast, following spraying onto grit-blasted aluminium, the fracture surfaces of both the copper deposits and the aluminium substrates indicate significant deformation (flattening) of the copper particles on impact, irrespective of whether the aluminium substrate was hard (~ 179 kgf /mm^2 in the as-grit-blasted state) or soft (~ 50 kgf /mm^2 in the annealed state) (Figure 4-5 c, f and Figure 4-6 b, d).

Substrate surface preparation	Fraction of counter-element present			
	As-prepared substrate		Annealed substrate	
	Copper on substrate	Aluminium on coating	Copper on substrate	Aluminium on coating
Polished	0.09	0.11	N/A	N/A
Ground	0.10	0.09	0.06	0.14
Grit-blasted	0.12	0.25	0.07	0.21

Table 4-4 Microscopic analysis of the material present on the substrate and on the coating after bond strength pull-off tests (All measurements were taken on BSE images with a field size of 300 ×225 µm). The polished substrate which was annealed failed in the adhesive not at the interface.

Table 4-4 shows the area fractions of aluminium retained on the copper deposit fracture surface and copper retained on the aluminium substrate fracture surface. It is clear that when fracture occurs, the fraction of copper that is retained on the substrate surface is low (around 10%) and generally independent of substrate preparation method or whether or not it had been annealed. The amount of aluminium retained on the surface of the copper deposit depended upon the surface preparation route (although not significantly on whether the substrate had been annealed or not following its preparation). For the polished and ground substrates, around 12% of the area was retained aluminium (primarily retained between copper particles are outlined previously in Figure 4-5d, e and Figure 4-6c). Around 23% of the surface was retained aluminium in the case of deposition onto the grit-blasted surfaces and this aluminium was widely distributed across the fracture surface (Figure 4-5 f and Figure 4-6 d).

4.3.5 Microstructural analysis of bond formation

Figure 4-8 (a, b, c) show cross-sections of the interface regions following deposition of the copper coating onto the as-prepared polished, ground and grit-blasted aluminium substrates. The copper particles give brighter contrast in the BSE images due to the higher atomic number of copper. In all cases, the coating showed very little porosity with good inter-particle contact. Deformation of the aluminium substrate by cold sprayed copper particles is evident at the interface. In the case of the deposits onto both the polished and ground substrates (Figure 4-8 a, b), significant deformation of the substrate is observed with the rounded shapes of the copper particles being preserved (in line with the fractographs presented earlier) However, following spraying onto the grit-blasted substrates (Figure 4-8c), the general profile of the grit-blasted surface can be observed (with undulations on the length scale of ~100 μm, but local deformation of the substrate due to particle impact is not as clear, indicating that the particles

themselves underwent significant deformation (in preference to substrate deformation) on impact.

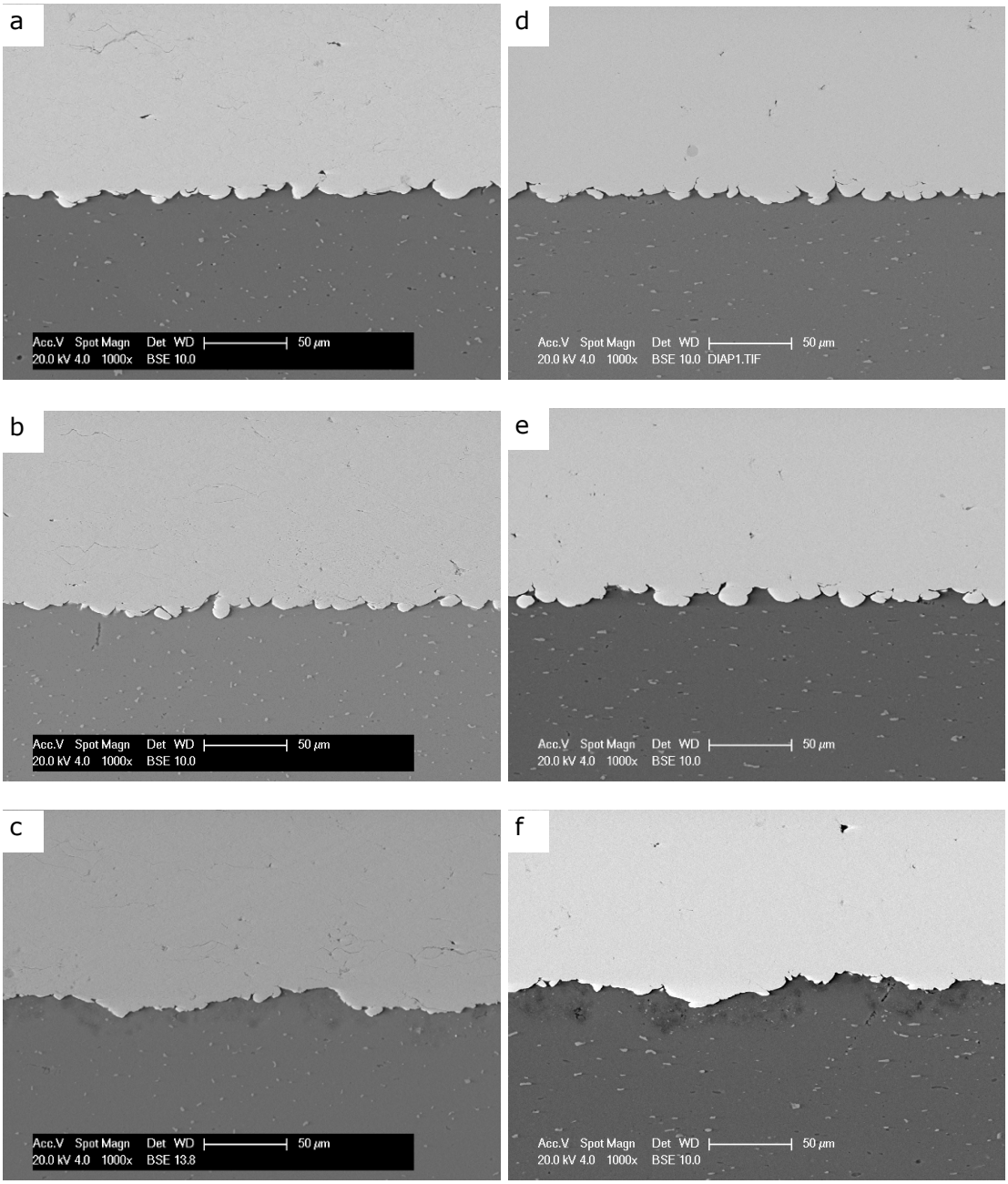

Figure 4-8 BSE images of Cu (bright) on as-prepared Al substrate (dark) with (a) polished (b) ground (c) grit blasted surfaces. BSE images of Cu (bright) on annealed Al substrate (dark) with (d) polished (e) ground (f) grit blasted surfaces in the as-sprayed condition. Micron sized bright particles within the Al substrate are constituent intermetallics in the 6082 alloy.

Figure 4-8 (d, e, f) show cross-sections of the interface regions following deposition of copper coating onto the substrates which had been annealed following surface preparation, as a function of surface preparation method. In all cases, more significant deformation of the aluminium substrate close to the interface is observed, associated with the softening of the substrate due to annealing (see Table 4-2). However, it is still notable that the shape of the particles close to the interface cannot be clearly observed following deposition onto the grit-blasted and annealed surface, indicating preferential deformation of the particle in this case.

Heat treatment to form Cu-Al intermetallics has been used previously as a means to identify regions where intimate aluminium-copper contact exists (where the intermetallic grows readily) and regions where the metals are separated by oxide films (where intermetallic growth is restricted) [4]. Thus, the coated substrates were heat treated at 400 °C to investigate the degree of intermetallic phase formation.

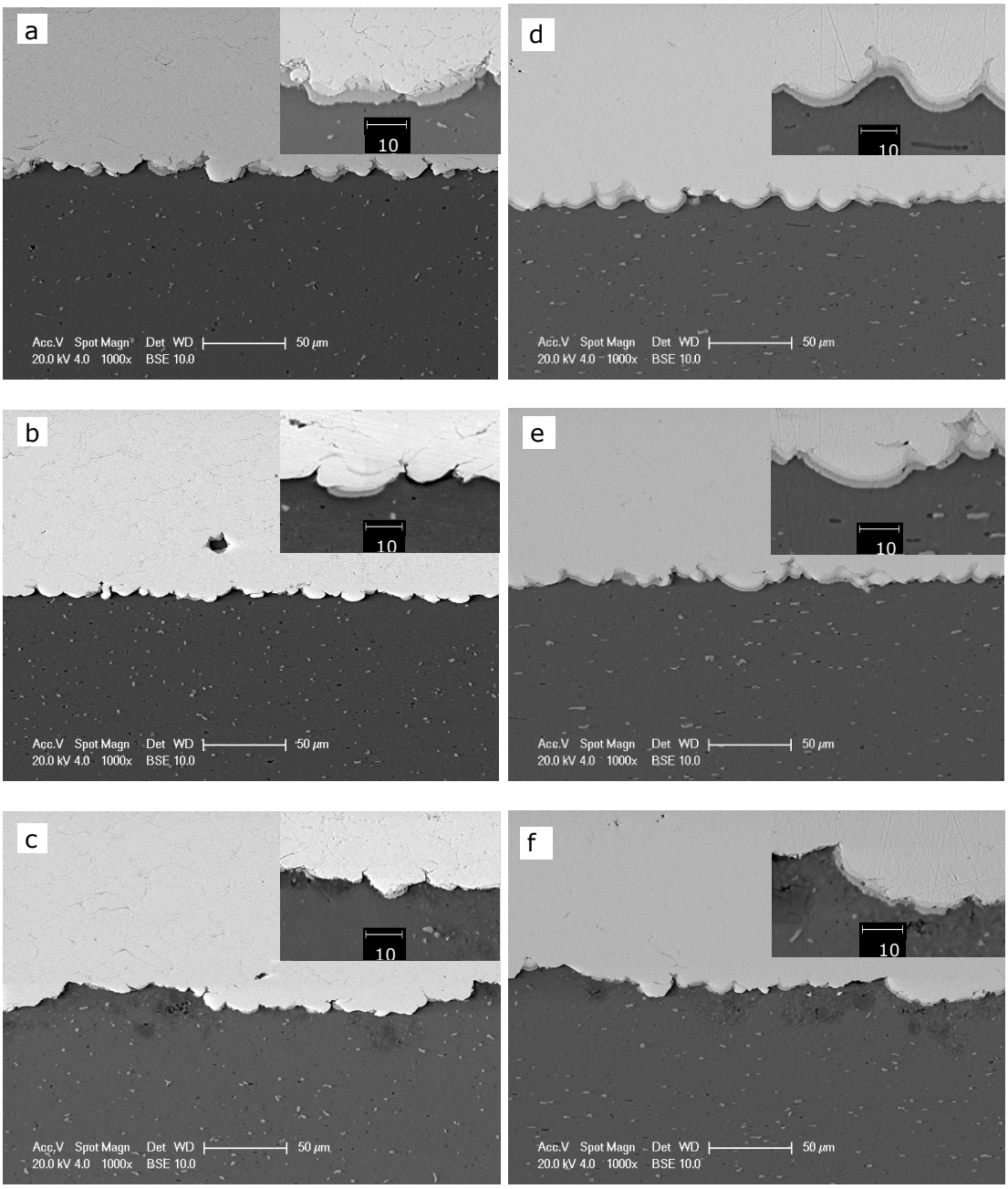

Figure 4-9 BSE images of Cu (bright) on as-prepared Al substrate (dark) with (a) polished, (b) ground, (c) grit blasted surfaces. BSE images of Cu (bright) on annealed Al substrate (dark) with (d) polished, (e) ground, (f) grit blasted surfaces. Samples annealed at 400 °C for 15 min following deposition. Grey contrast levels in the higher magnification insets show intermetallic that formed during annealing.

Figure 4-9 (a, b, c) show cross-sections of the interface regions following heat treatment for copper deposited onto the as-prepared polished, ground and grit-blasted aluminium substrates. Cu-Al intermetallics are identified as the regions with mid-grey contrast between the substrate and the deposit. The intermetallics at the interface grew to a few microns thick in some places, but the coverage of the interface by intermetallics is seen to be limited. Figure 4-9 (d, e, f) show cross-sections of the interface regions (following heat treatment) for copper deposited onto the aluminium substrates which had been annealed after surface preparation. The intermetallic coverage of the interface is evidently more extensive compared to the equivalent surface preparation (but without an annealing step before copper deposition), see Figure 4-9 (a, b, c). The intermetallic layer at the polished surface in the annealed sample is almost continuous (see Figure 4-9 d). Intermetallic coverage is lower following deposition onto the ground substrate (Figure 4-9e), although here again, there is a significant increase associated with the annealing treatment following grinding. The intermetallic coverage for the grit-blasted surface is lower again, with any intermetallic being formed having a low thickness, Figure 4-9 (c).

Substrate surface preparation	Fraction of the interface covered with intermetallics	
	As-prepared substrate	Annealed substrate
Polished	0.46 ± 0.05	0.94 ± 0.01
Ground	0.27 ± 0.03	0.77 ± 0.02
Grit-blasted	0.34 ± 0.03	0.50 ± 0.05

Table 4-5 Measurements of the fraction of the copper-aluminium interface covered with intermetallic phases after a short heat treatment of 15 min at 400°C (All measurements taken on eight BSE images of the interface cross-section comprising approximately a 2.5 mm length of the interface).

Table 4-5 presents the fraction of the interface covered with intermetallics for both as-prepared and annealed substrates for all three surface preparation methods. For the as-prepared substrates, the fraction of interface covered by intermetallics for the polished substrate was the highest. The coverage of intermetallics on the substrates which had been either ground or grit-blasted was significantly lower (and close to each other). The intermetallics formed on the grit-blasted surface showed an irregular pattern which is different from the other two surfaces.

For the substrates that were annealed after surface preparation, the fraction of interface covered with intermetallics increased significantly. Table 4-5 shows that the fraction of intermetallics was highest for the polished substrate, followed by the ground and then the grit-blasted surfaces. The significantly greater degree of coverage by intermetallic phases is indicative of a greater area of metal-to-metal contact (i.e. interface free from oxide) in the samples annealed following their surface preparation, as has been demonstrated previously.

4.4 Bonding mechanisms of aluminium onto copper

4.4.1 Characterization of aluminium powder

Figure 4-10 shows the morphology of the feedstock aluminium powder. It can be seen that the particles have a mixture of rounded and globular (elongated) morphology with a small fraction exhibiting satellite particles. The supplier specified size range of the powder was -45 +15 μm; with 0.8 % above 45 μm and 0.1% below 15 micron. Moreover, the D50 value of the powder was 34.6 μm.

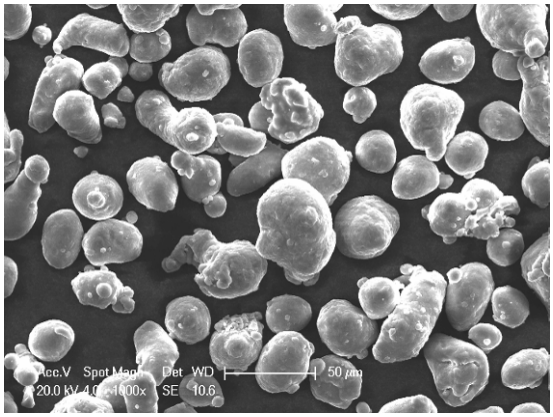

Figure 4-10 SE image of gas atomized aluminium powder showing its morphology

4.4.2 Single particle impact of aluminium onto copper

Figure 4-11(a) shows the surface of the copper substrate following wipe test of aluminium particles. The copper substrate shows a number of deposited aluminium particle along with a large number of craters. The craters left on the substrate indicate that the impacting particles did not achieve the critical conditions necessary for successful deposition and bounced back from the substrate. In addition, the size range of the craters was from 10 to 60 µm. Higher magnification image of a bonded aluminium particle onto copper substrate shows formation of jet composed of aluminium (Figure 4-11b). The cross section image of a bonded aluminium particle onto copper substrate shows deformation of the substrate following impact (Figure 4-11c).

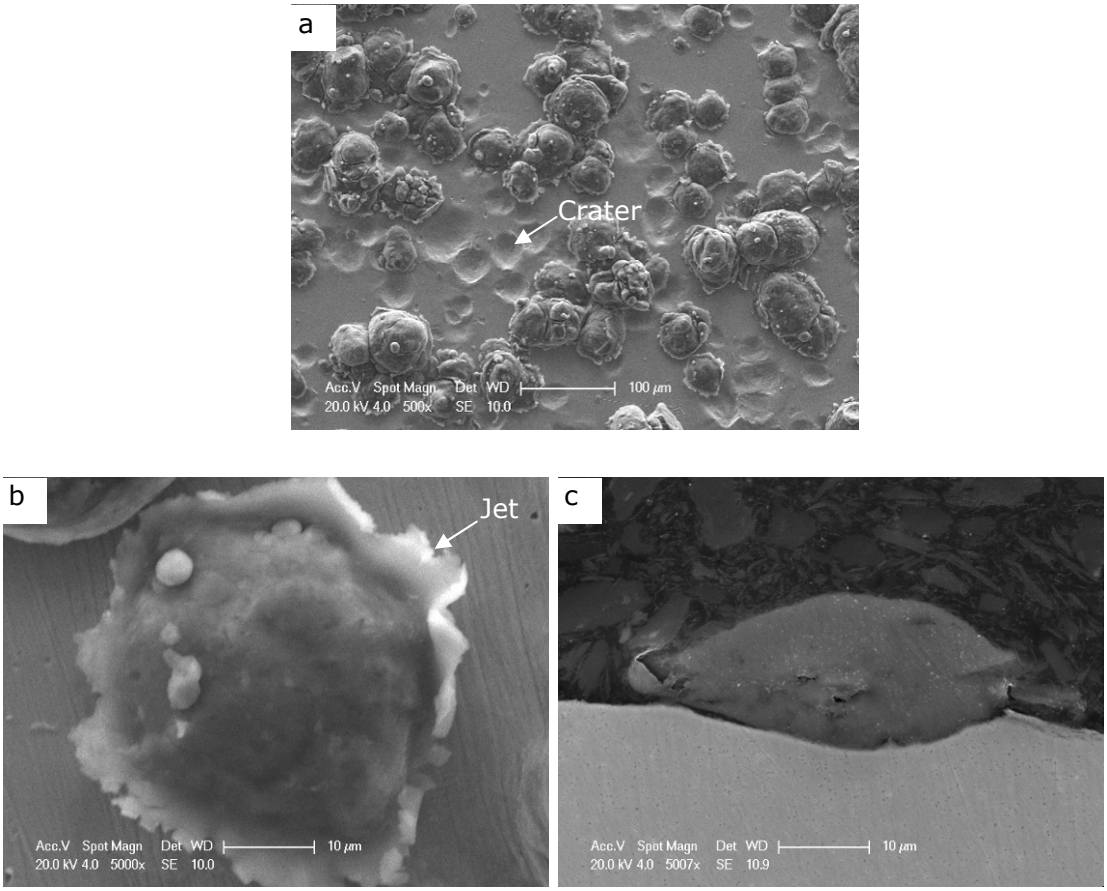

Figure 4-11 SE image of (a) aluminium particles on copper substrate. Higher magnification image of (b) an aluminium particle on copper substrate (c) cross-section of an aluminium particle on copper substrate.

4.4.3 Characterization of different substrate surfaces

The roughness of polished, ground, and grit-blasted copper substrates was 0.07, 0.4, and 3.3 μm, respectively. Observation of the grit-blasted substrate showed the presence of embedded alumina grit in some cases. Figure 4-12 shows the typical surface profiles of the substrate following the three surface preparation methods. The typical peak-to-trough height of the grit-blasted surface was 20 μm, whereas the peak-to-through height of the polished surface was less than 1 μm. The surface profile of the ground surface shows uniformly distributed peaks and valleys with a typical peak-to-trough height of 3 μm. Figure 4-13 shows the magnified profiles of three surfaces in relation to a 35 μm spherical particle.

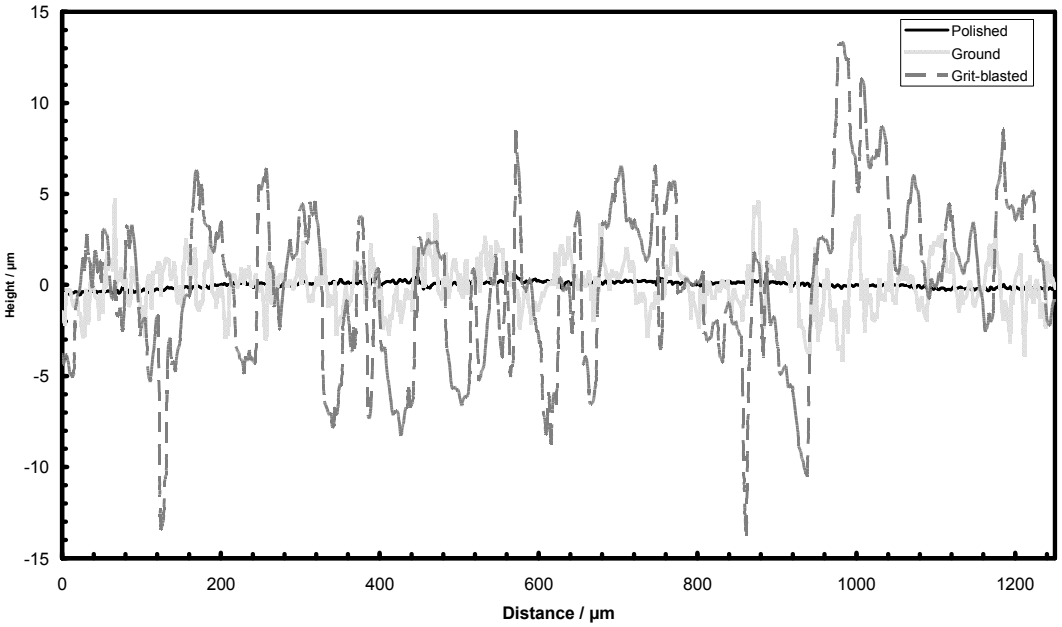

Figure 4-12 Typical line profiles extracted from the polished, ground, and grit-blasted surfaces

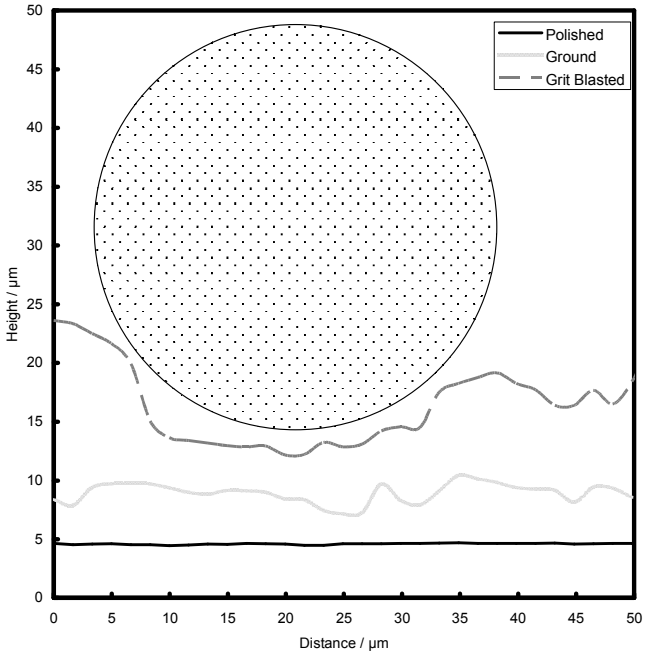

Figure 4-13 Surface profiles of polished, ground, and grit-blasted surfaces (with identical horizontal and vertical scaling) in comparison with a disk representing a section through a 35 µm diameter spherical particle

To identify surface hardening during the surface preparation of the samples, microhardness indentations were made on a finally polished cross section. Ten hardness measurements were taken within 10 μm of the prepared surface (referred to as near –surface hardness) and ten measurements made at the same load in the centre of the substrate. In a similar manner, the hardness of the bulk and surface regions following annealing heat treatment were measured. The annealing treatment reduced the bulk hardness of copper from 91 to 56 kgf /mm^2. The measured near surface hardnesses are shown in Table 4-6. It can be seen that in the case of the as-prepared material, the hardnesses of both polished and ground surface regions were very similar to the bulk material. However, grit blasting resulted in significant hardening of the substrate. In the annealed case, the hardness of the polished surface region was very similar to that of the bulk annealed sample.

Preparation method	Surface roughness (Ra) / μm	Vickers microhardness (25gf load) / kgf mm^{-2}	
		As prepared	Annealed
Polished surface	0.07	89.2±4.9	51±2
Ground surface	1.0	100.7±3.1	-
Grit-blasted surface	3.3	152.9±4.1	-

Table 4-6 Near-surface hardness and surface roughness of the copper substrates. As-received copper substrate hardness 90.7±0.9 and annealed copper substrate hardness 55.9±1.2 .

4.4.4 Bond strength tests and fracture surface analysis

4.4.4.1 Bond strength tests

Pull-off bond strength test values for the aluminium sprayed onto copper substrate, as a function of the preparation method of the substrate, are presented in Table 4-7. There was very little variation of the bond strength values following different substrate preparation methods. The bond strength values of the aluminium coating onto the copper substrates are significantly low compared to that of copper coatings onto aluminium substrates. In all the pull-off tests, the failure was always at the coating-substrate interface. In addition, it has been reported that the bond strength value on grit blasted substrate (i.e., aluminium and titanium alloys) is usually lower than polished and ground substrates [76, 186]. However, no such decrease in bond strength value onto grit-blasted copper substrate compared to other two surface preparation techniques was observed in this study.

Substrate surface preparation	Bond strength (as-prepared substrate) / MPa
Polished surface	1.1 ± 0.2
Ground surface	3.2 ± 0.5
Grit-blasted surface	1.8 ± 0.6

Table 4-7 Bond strength values for the aluminium deposited onto copper substrates for as-sprayed surfaces

4.4.4.2 Fracture surfaces

The fracture surfaces following the pull-off bond strength tests were examined, and are shown in Figure 4-14. In each case, both the copper substrate and the

corresponding aluminium deposit surfaces are shown. In addition, the fractional area of aluminium remaining on the copper fracture surface along with the complimentary measure of copper on the aluminium fracture surface are shown in Table 4-8. Looking at the copper substrate, it is clear that the aluminium particles are observed to adhere as single particle (Figure 4-14 a-c, Figure 4-15 a-c); no significant differences were noted in the amount of aluminium particles retained as a function of the methods of preparation of the copper substrate. On the fracture surfaces of the aluminium deposits in Figure 4-15(d-f), copper is visible as the region of high brightness. For the polished sample, copper is barely visible at the fracture surface of the aluminium deposit (Figure 4-15d); in ground substrate, the fracture surface of the aluminium deposit contained copper (region of high brightness) along the ground marks of the surface preparation. In contrast to this, the grit-blasted surfaces show that the copper is found more widely dispersed on the aluminium deposit fracture surface (Figure 4-15f). It is notable that for the grit blasted substrates, the fraction of copper visible on the deposit surface is significantly greater than for polished and ground surfaces.

It is also notable that the fracture surfaces of both the copper substrates and aluminium deposits show the rounded morphology of the aluminium particles for both the polished and ground surfaces (Figure 4-14a-b, d-e), indicating the plastic deformation upon impact was primarily within the copper substrate. This type of deformation is quite different from the deformation of the aluminium substrate following deposition of copper particles, in which copper particles create deep impacts onto the aluminium substrate. Careful examination of the fracture surface of the copper substrate following ground surface preparation showed that the ground mark left by the SiC particles are still visible following deposition of copper particles (Figure 4-14b), which indicates shallow craters on the copper surface following impacts of aluminium particles. In contrast, following spraying onto grit blasted copper substrate, the fracture surfaces of both the aluminium

deposits and copper substrates indicate significant deformation of the aluminium particles on impact.

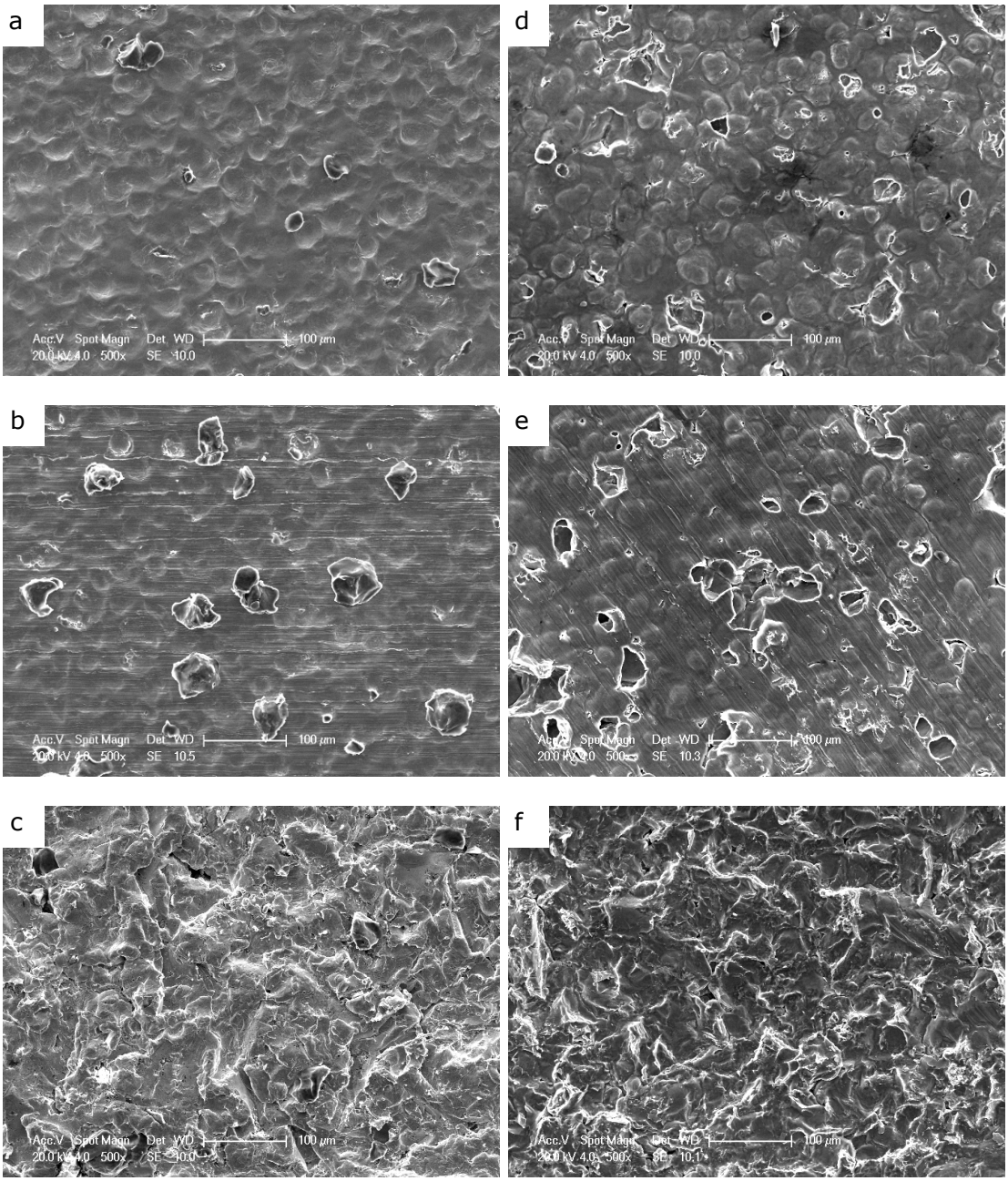

Figure 4-14 SE images of fracture surfaces, after pull-off test, of as-prepared Cu substrate (a-c) and corresponding aluminium coating (d-f) with different substrate surface preparations: (a, d) polished; (b, c) ground; and (c, f) grit-blasted.

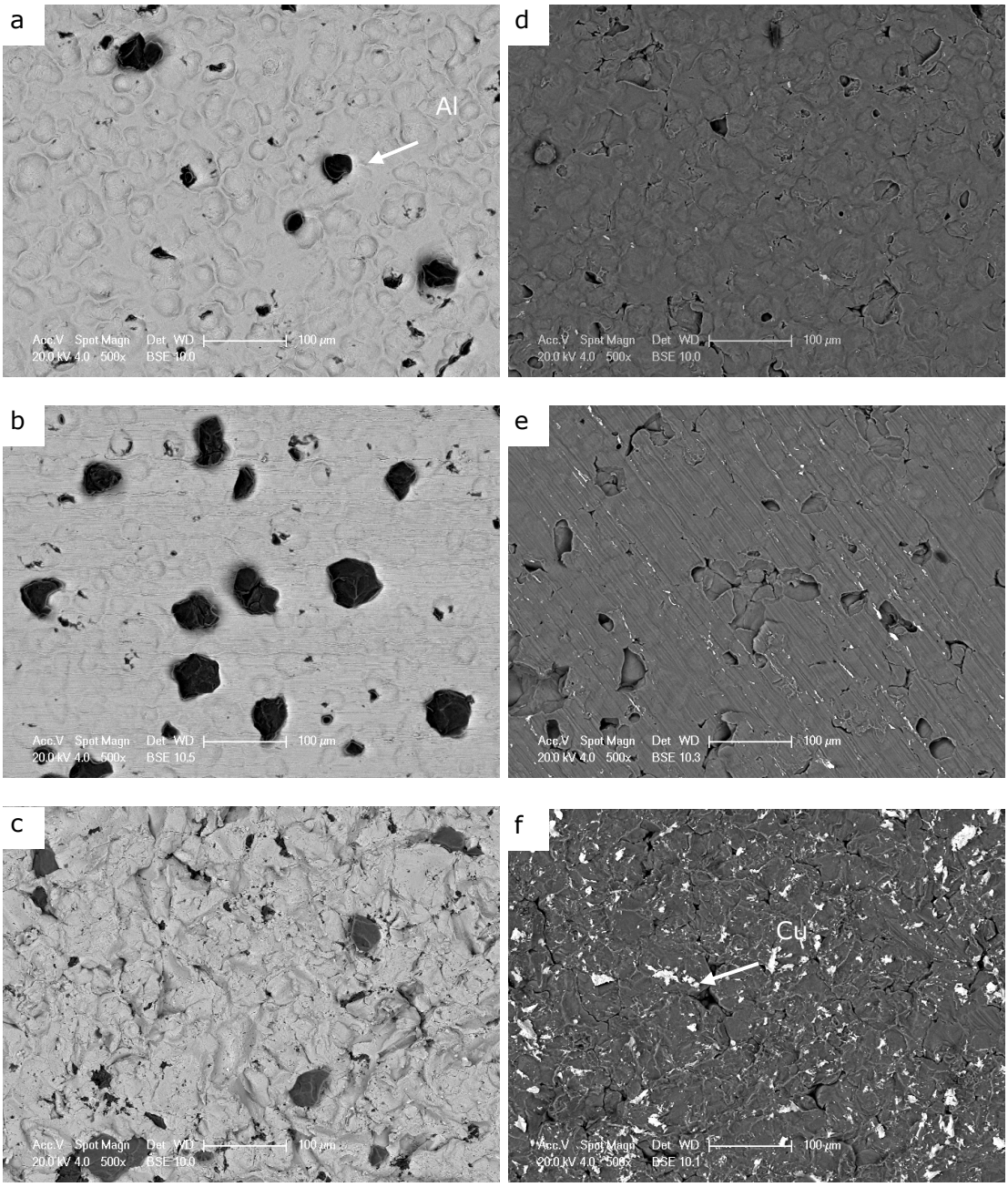

Figure 4-15 BSE images of fracture surfaces, after pull-off test, of as prepared Cu substrate (a-c) and corresponding aluminium coating (d-f) with different substrate surface preparations: (a, d) polished; (b, c) ground; and (c, f) grit-blasted. Arrow indicates retained Al particle.

Table 4-8 shows the area fractions of aluminium retained on the copper substrate fracture surfaces and copper retained on the aluminium deposit fracture surfaces. It is obvious when the fracture occurs, the fraction of aluminium that is retained

on the substrate surface is greater and irrespective of the substrate preparation method. The amount of copper retained on the aluminium deposit depended on the surface preparation route (although not significantly on whether the substrate had been polished or ground). For the polished and ground substrates, less than 1% of the area was retained copper; whereas 7% of the surface retained copper in the case of deposition onto the grit blasted surfaces.

Substrate surface preparation	Fraction of counter-element present	
	Aluminium on Substrate	Copper on Coating
Polished	0.04	<0.01
Ground	0.09	0.01
Grit-blasted	0.09	0.07

Table 4-8 Microscopic analysis of the material present on the substrate and on the coating after bond strength pull-off tests (all measurements were taken on BSE images with a field size of 300 × 225 µm)

Figure 4-16 shows the high magnification fracture surface of as-prepared polished copper substrate and corresponding fracture surface of aluminium deposit. SE image of the fracture surface of the copper substrate shows a distinctive feature present at the surface (marked with a circle in Figure 4-16a). High magnification images of the aluminium deposit fracture surface in Figure 4-16(b) shows the counterpart fracture feature, where metallic contact with the copper substrate might have occurred.

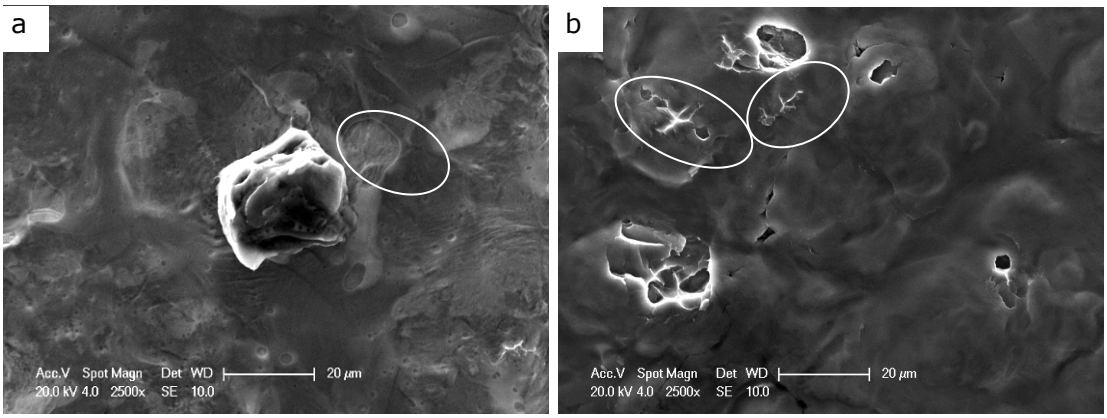

Figure 4-16 High magnification SE images of fracture surfaces, after pull-off test, of (a) as-prepared polished Cu substrate (b) corresponding aluminium deposit. Circles indicate the regions of metallurgical bonding.

4.4.5 Microstructural analysis of bond formation

Figure 4-17(a-c) show cross-sections of the interface regions following deposition of the aluminium coating onto the as prepared polished, ground and grit-blasted copper substrates. The aluminium deposits give a darker contrast due to the lower atomic weight of aluminium. Deformation of copper substrate by cold sprayed aluminium particles is evident at few places marked with arrows in the polished and ground substrates (Figure 4-17a-b). This substrate deformation of copper is very shallow compared to the aluminium substrate deformation following impact of copper particles in cold spraying (Figure 4-8). In the case of deposits following spraying onto the grit-blasted substrates (Figure 4-17c), the general profile of the grit-blasted surface can be observed with undulations on the length scale of 50 μm, but the local deformation of the substrate due to particle impact is not as clear.

To investigate the effect of substrate characteristics on aluminium deposition, a polished copper substrate was heat treated before deposition. Figure 4-18(a) shows the cross section of the interface regions following deposition of aluminium coating onto the substrate which had been annealed following surface

preparation. A higher degree of deformation of the copper substrate near the interface is observed, associated with the softening of the substrate due to annealing (marked with an arrow in Figure 4-18a).

Heat treatment to form Al-Cu intermetallics has been previously used as a means to identify regions where intimate contact between aluminium-copper exists (where the intermetallic grows readily) and regions where the metals are separated by oxide films (intermetallic growth is restricted). The deposited substrates were heat treated at 400°C to investigate the degree of intermetallic phase formation.

Figure 4-17(d-f) show cross-sections of the interface regions following heat treatment for aluminium deposited onto the as-prepared polished, ground, and grit-blasted copper substrates. Al-Cu intermetallics are identified as the regions of mid-grey contrast between the substrate and the deposit. The intermetallics at the interface grew to 2-3 μm thick in few places, but the coverage of the interface by intermetallics is seen to be limited. The intermetallics only grew to the places where the copper substrate showed some degree of deformation upon impact of aluminium particles (marked with arrows in Figure 4-17d-e).

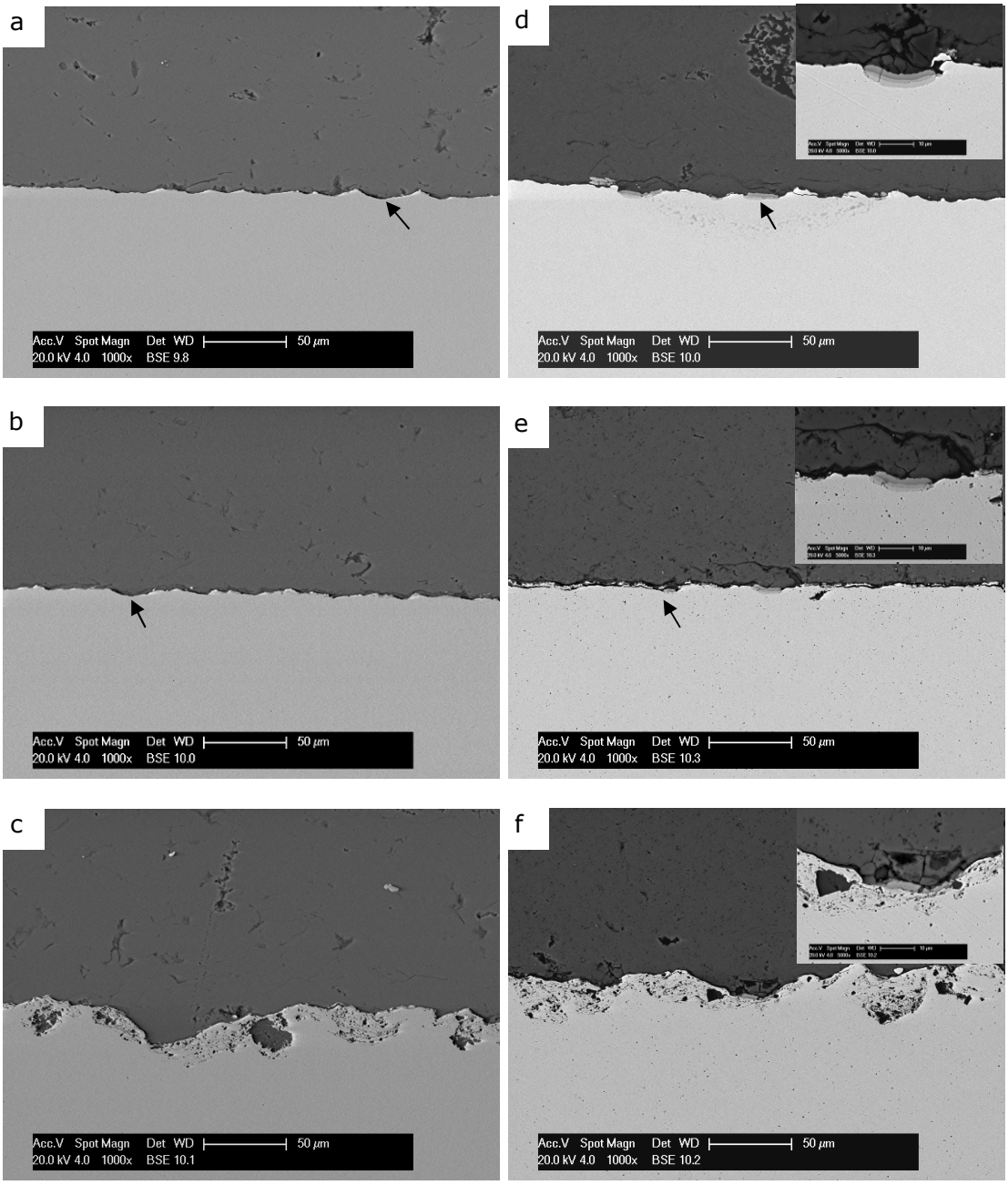

Figure 4-17 BSE images of Al(dark) on as-sprayed Cu substrate (bright) with (a) polished (b) ground (c) grit blasted surface. BSE images of the samples annealed at 400°C for 15 min following deposition (d) polished (e) ground (f) grit blasted surface. Arrows showing substrate deformation

Figure 4-18(b) shows the cross section of the interface regions (following heat treatment) of aluminium deposited onto the copper substrates which had been annealed after substrate preparation. The intermetallics coverage of the interface

is similar to the samples compared to the polished surface preparation without any annealing step (Figure 4-17d). The coverage of the interface covered by the intermetallics is confined to the areas where copper substrate showed some degree of substrate deformation (marked with arrow in the Figure 4-18b).

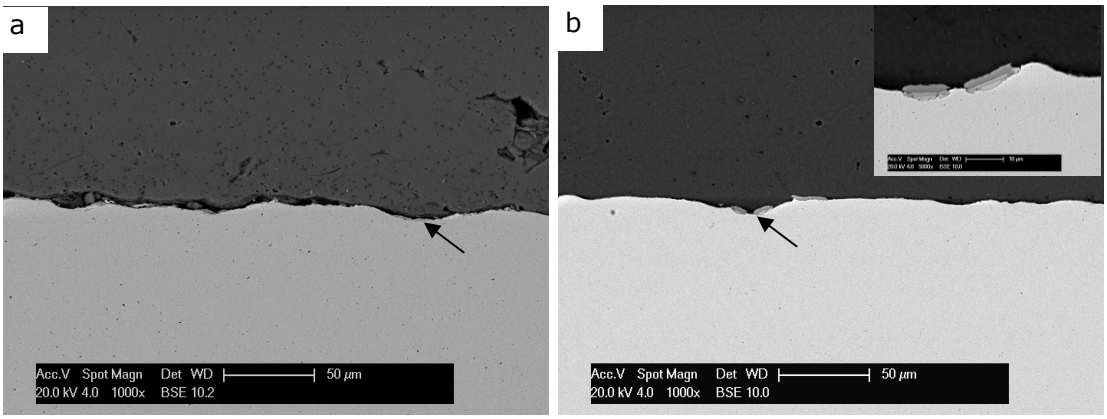

Figure 4-18 BSE images of (a) Al(dark) on softened Cu substrate (bright) with polished surface (b) the same coating annealed at 800°C for 20 min following deposition. Arrows showing substrate deformation

Table 4-9 presents the fraction of the interface covered with intermetallics for three as-prepared surface preparation methods and polished annealed substrate preparation methods. For the as-prepared substrates, the fraction of interface covered by intermetallics was the highest for the polished substrate, which was twice the coverage of intermetallics on the substrates which had been either ground or grit-blasted. For the substrate that was annealed after surface preparation, the fraction of interface covered with intermetallics remained the same as the as-prepared polished surface (Table 4-9). However, it should be mentioned here that in copper deposited onto aluminium substrate, the fraction of interface covered with intermetallics increased significantly following annealing after surface preparation.

Substrate surface preparation	Fraction of the interface covered with intermetallics	
	As-prepared substrate	Annealed substrate
Polished	0.13±0.03	0.13±0.02
Ground	0.07±0.01	-
Grit-blasted	0.06±0.01	-

Table 4-9 Measurements of the fraction of the aluminium-copper interface covered with intermetallic phases after a short heat treatment of 15 min at 400°C (all measurements taken on eight BSE images of the interface cross-section comprising approximately a 2.5mm length of the interface)

4.5 Bonding mechanisms of titanium onto steels

The methodology used in understanding the bonding mechanisms of copper-aluminium and aluminium-copper coating-substrate systems was also used in titanium–steel system. Previous studies on titanium-iron diffusion couples and explosively bonded commercially pure titanium- low-carbon/ austenitic stainless steel have found various intermetallics at the interfaces following annealing heat treatment [2, 3, 104, 105]. In light of the fact that the titanium-iron system is known to form various intermetallics at elevated temperature [187], the method of formation of intermetallic phases on heat treatment as a means to identify regions of intimate metal-to-metal bonding was used. However, unlike Cu-Al and Al-Cu systems, interfacial interdiffusion experiments on Ti-steel system were conducted on wipe test samples. The heat treatment of titanium coating-steel substrate results in coating delamination because of a mismatch in co-efficient of thermal expansion.

In this section, titanium was sprayed onto three types of steel substrates. Low-carbon steel (containing a small amount of carbon which alters its strain hardening properties) and Armco iron (a commercially-pure grade of pure iron with very low carbon content) were selected to investigate the role of carbon during the deformation between a steel and an impacting titanium particle. In addition, it is known that austenitic stainless steel has a very different oxide layer structure from that observed on Armco-iron and low carbon steel, and as such, a 304 stainless steel was also used as a substrate. However, it is known that for higher carbon steels, interdiffusion between titanium and the steel during elevated temperature heat treatments is stifled by the formation of a TiC layer at the interface [105]; as such, the method of using intermediate phase formation between steel and titanium as a method for detecting intimate bonding is not suitable for higher carbon steels, and thus the steels chosen for this study all had carbon levels of 0.05 wt% or lower. Previous studies in diffusion bonding of commercially pure titanium to austenitic stainless steel showed formation of solid solutions and intermetallics at 700-800 °C [3] and annealing heat treatment of explosively bonded commercially pure titanium to carbon steel (0.2%) formed various intermetallic compounds at 750 °C [104]. Thus, in this work, the deposited samples were heat treated at 750 °C to use intermediate phase formation as an indicator of the distribution of regions of intimate bonding.

Titanium powders for cold-spraying are readily available; spherical powders are generally produced by inert gas atomization, and more angular powders can be produced by the hydride de-hydride process, the latter powders costing approximately a fifth of those produced by inert gas atomization. Two different shapes of titanium particle (spherical and angular) were also used to understand the disruption of the oxide layer following deposition and formation of metal-to-metal bonding. The differences between room temperature cold-spraying with a helium accelerant and elevated temperature cold-spraying with a nitrogen

accelerant on metal-to-metal bond formation in the titanium-stainless steel system were also investigated.

4.5.1 Characterization of titanium powder

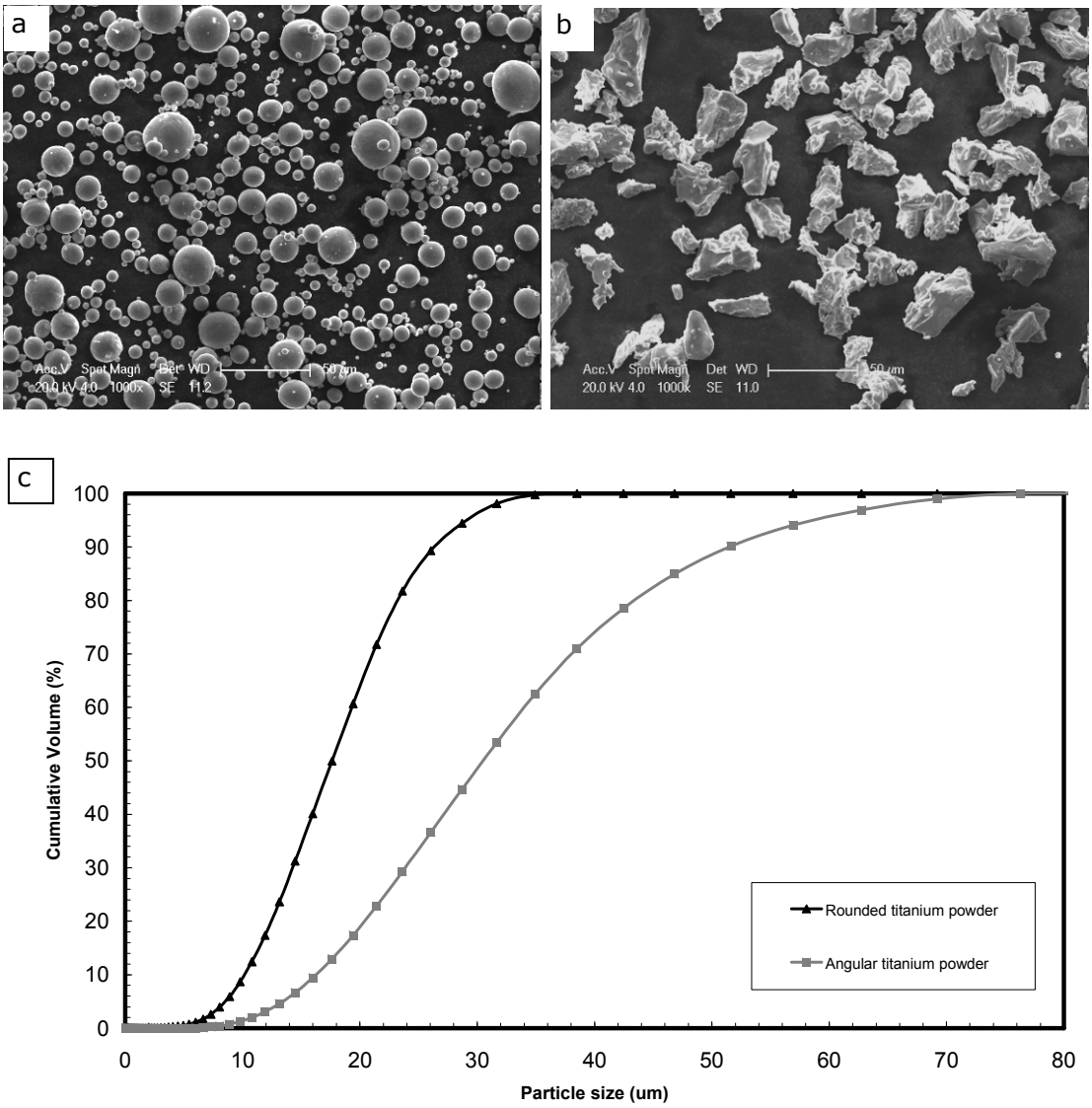

Figure 4-19 (a) Secondary electron (SE) image of spherical titanium powder (b) SE image of angular titanium powder showing their morphology (c) Cumulative vol.% size distribution of both spherical and angular powder

Figure 4-19(a) shows the morphology of the feedstock gas atomized powder (supplier specified size range of <25μm). It can be seen that the particles have a spherical morphology with very few satellite particles. Particle size analysis shows approximately 10 vol.% of particles are above 25μm (Figure 4-19c). Figure 4-19(b) shows the morphology of the hydride de-hydride powder (supplier specified size range of <45μm). It can be seen that the particle shapes are angular and irregular. Particle size analysis (Figure 4-19c) indicates that approximately 15 vol.% of particles are above 45 μm.

4.5.2 Characterization of substrates

The etched microstructures of all three substrates are shown in Figure 4-20. Low carbon steel contains 0.04% carbon and is composed of α-Fe and pearlite. Figure 4-20(a) shows equiaxed grains of α-Fe with an average grain size of ~10 μm and pearlite (the darker contrast in the optical microscopy image). Armco iron is an ultra low carbon commercially pure ingot iron which also has a body centred cubic (bcc) structure. Figure 4-20(b) shows that the microstructure of Armco iron is composed of α-Fe grains in the order of hundred of microns in size. The austenitic stainless steel has a γ-Fe face centred cubic (fcc) structure. Figure 4-20(c) shows etched microstructure of austenitic stainless steel with uniform grain sizes of ~50 μm and a few twin boundaries.

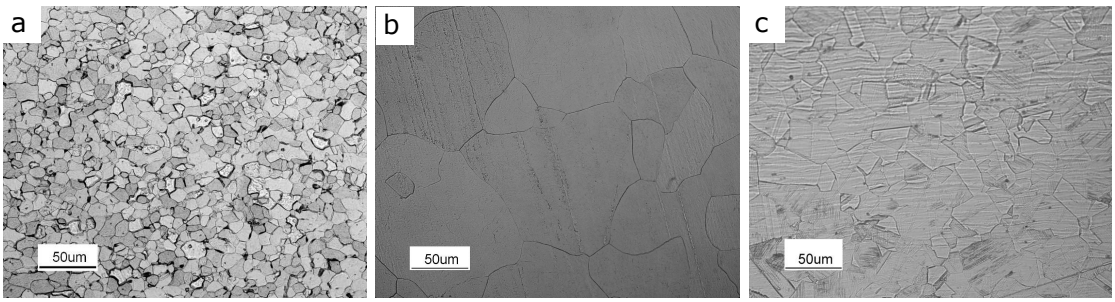

Figure 4-20 Optical microscope images of etched microstructure of (a) low carbon steel, (b) Armco iron, and (c) austenitic stainless steel

The microhardness of the three iron based alloys are shown in Table 4-10. The austenitic stainless steel is the hardest of all the materials with a hardness of

222±2 kgf/ mm^2 and Armco iron is the softest with a hardness of 123±1 kgf/ mm^2. Low carbon steel has a hardness of 167±1 kgf/ mm^2, which is higher than Armco iron due to presence of higher amount of carbon and heat treatment procedures. For comparison, a piece of commercially pure grade 1 titanium (chosen as an analogue of the powder particles) exhibited a hardness of 145±3 kgf/ mm^2.

Substrate	Vickers microhardness (100 gf load) / kgf /mm^2
Low carbon steel	167±1
Armco iron	123±1
Stainless steel, 304	222±2

Table 4-10 Bulk substrate microhardness of the low carbon steel, Armco iron, and stainless steel (304). The hardness value of bulk commercially pure grade 1 titanium was 145±3 kgf/ mm^2

4.5.3 Microstructural analysis of bond formation

4.5.3.1 Spherical titanium powder onto ferrous alloys using room temperature helium

4.5.3.1.1 As sprayed deposits

Cold-sprayed spherical titanium particles following deposition onto low carbon steel, Armco iron, and austenitic stainless steel substrates are shown in Figure 4-21. The substrate surface of low carbon steel (Figure 4-21a) shows a large number of craters following cold-spraying. In cold-spraying, the craters are formed on the substrate when the impacting particles rebound from the substrate; as such, they are deemed to have been travelling at a velocity lower than the critical velocity required for the bonding to occur [10, 11, 56]. In contrast, Figure 4-21 (b, c) show a much wider size range of particles which have

deposited onto the Armco iron and stainless steel substrates, which by definition must have exceeded the critical velocity for bonding onto the substrates. Moreover, in Figure 4-21 (b1, c1), a significant reduction in the incidence of crater formation is observed compared to low carbon steel substrate. In comparing between the three material types, there are no changes in the nature of the spray plume characteristics (as there would be if the powder type or spraying conditions were changed); as such, all three materials were exposed to the same particle flux but image analysis of Figure 4-21 (a, b, c) indicate that the area fraction of titanium bonded to the steel surface is ~0.25, 0.50 and 0.40 (all ± 0.05) for the low carbon steel, Armco iron and 304 stainless substrates respectively.

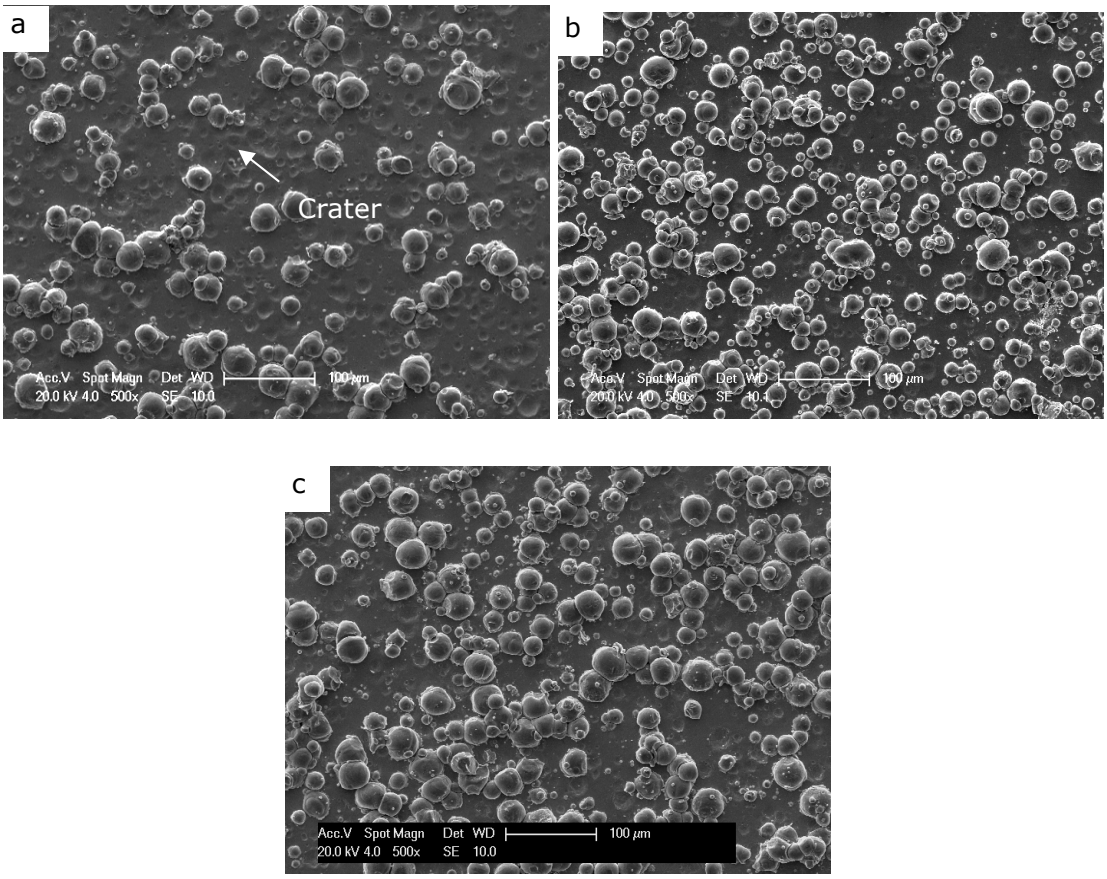

Figure 4-21 Low-magnification SE images of spherical titanium particles as-sprayed using room temperature helium onto (a) low carbon steel, (b) Armco iron, (c) austenitic stainless steel

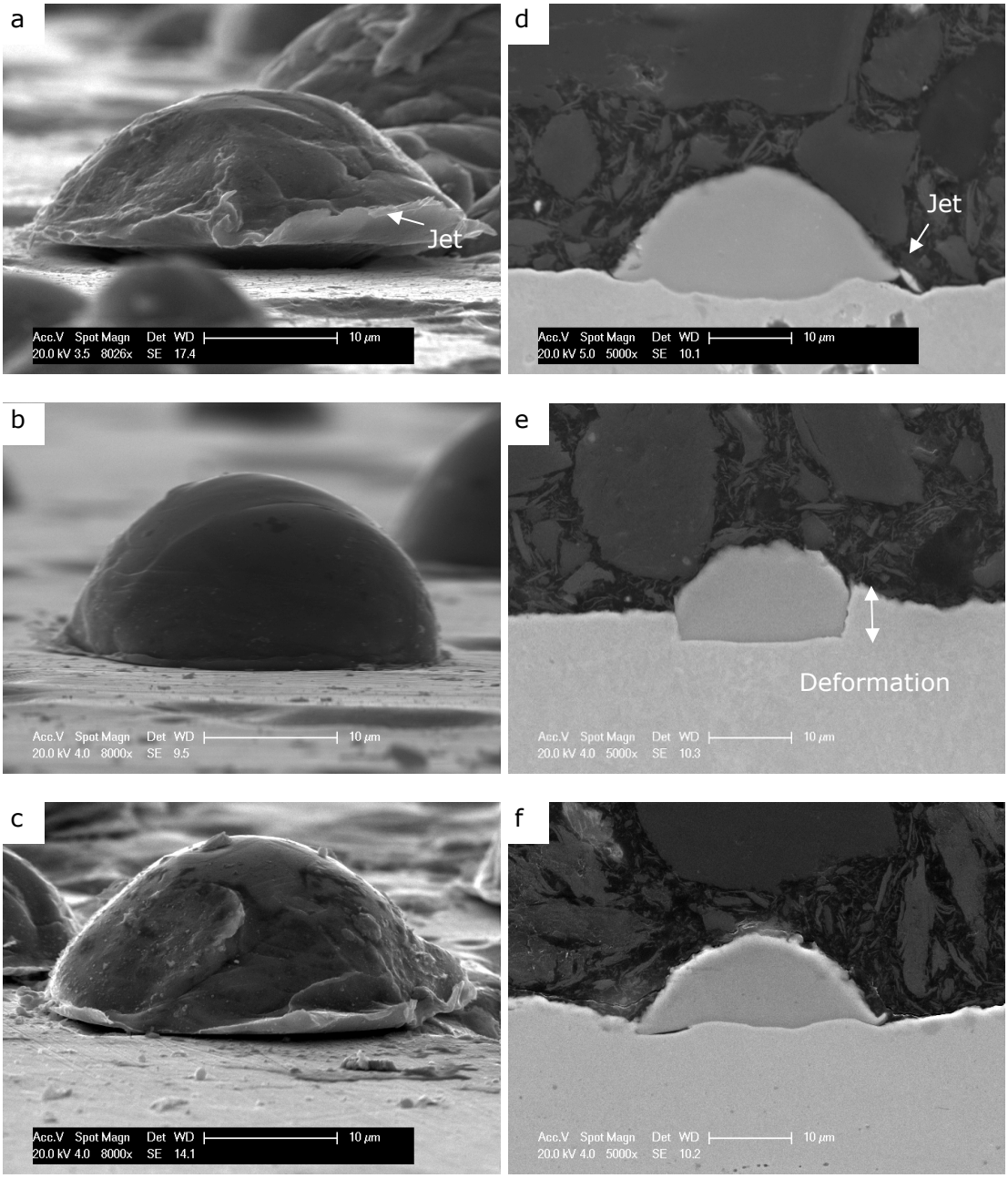

Figure 4-22 Higher magnification SE images of 86 ° tilted view of as sprayed titanium particles onto (a) low carbon steel, (b) Armco iron, (c) austenitic stainless steel, and cross-section of as sprayed titanium particles onto (d) low carbon steel, (e) Armco iron, (f) austenitic stainless steel

Tilted view images of titanium particles onto low carbon steel, Armco iron, and austenitic stainless steel are shown in Figure 4-22 (a, b, c). Titanium particles deposited onto low carbon steel substrate show formation of metallic jet, marked with an arrow in Figure 4-22 (a); the metal jet is moving away from the centre of the particle and the particle is attached to the substrate only in the central region. Figure 4-22 (d) shows the cross-section of a titanium particle deposited onto low carbon steel, where it is clearly visible that the particle is attached to the substrate in the central region and the particle shows formation of a metal jet on both sides with limited substrate deformation. In contrast, a different mode of particle-substrate interaction is observed following cold-spay impact of a titanium particle onto an Armco iron substrate (Figure 4-22b), where little particle flattening was observed. The cross-section of a deposited particle onto Armco iron in Figure 4-22 (e) shows the particle is embedded into the Armco iron substrate which deformed significantly following deposition; in contrast to the behaviour observed for low carbon steel substrates, no material jetting upon impact is observed in this system. The shape of the material jet upon impacting onto different substrates was consistently observed in the SEM images; ten images of each particle-substrate combination were studied.

Figure 4-22 (c) shows a titanium particle deposited onto austenitic stainless steel; the jet from the particle is facing upward and no evidence of jetting of austenitic stainless steel is present. Figure 4-22 (f) shows the cross-section of a titanium particle onto austenitic stainless steel substrate; the particle is well attached to the inner rim region and the material jet is detached from the substrate.

4.5.3.1.2 Heat treated deposits

Heat treatment to form intermediate phases between dissimilar substrate-deposit combinations has been used previously as a means to identify regions where intimate contact exists (where the intermediate phase grows readily) and regions

where metals are separated by oxide films or surface debris (where intermediate phase growth is restricted) [4, 186].

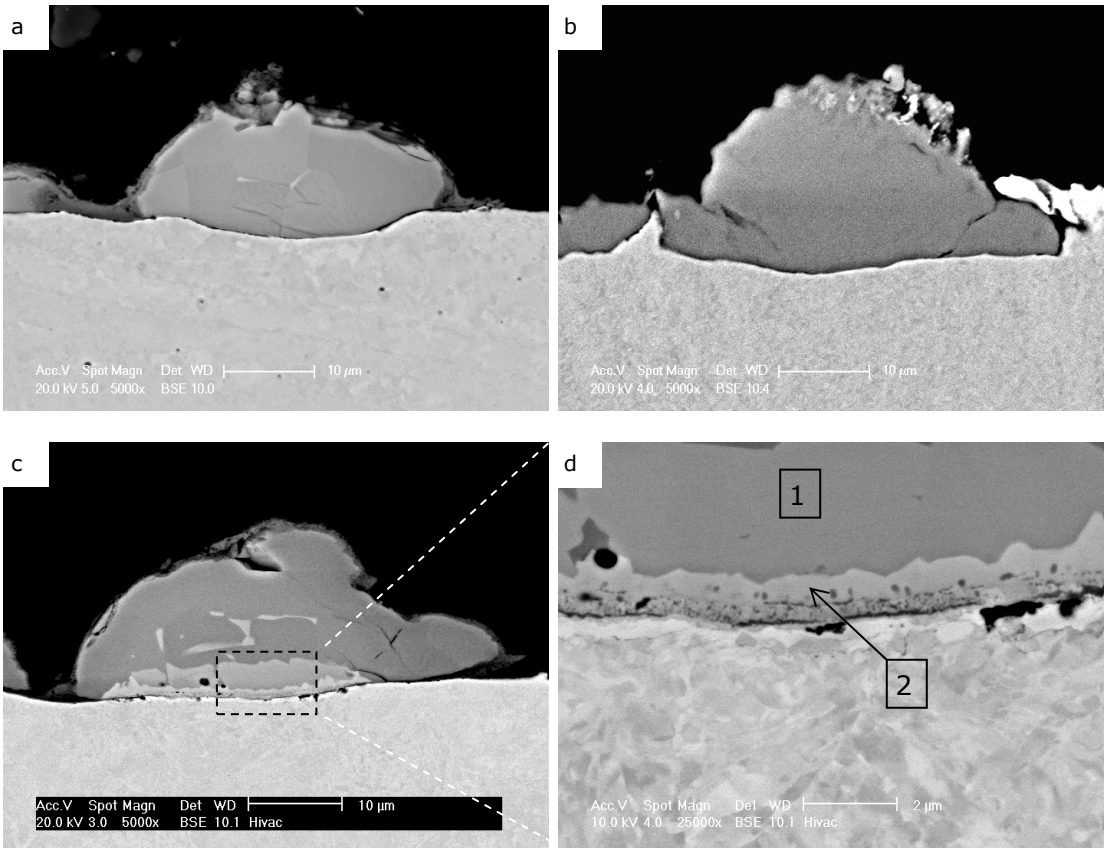

Figure 4-23 BSE images of spherical titanium particles sprayed using room temperature helium followed by heat treatment, for substrates as follows: (a) low carbon steel, (b) Armco iron, (c) austenitic stainless steel. (d) Higher magnification images of the intermediate phases shown in (c) (mid-grey contrast levels)

Figure 4-23 (a, b, c) shows the cross-sections of the spherical titanium particles onto the low carbon steel, Armco iron, and austenitic stainless steel substrates following heat treatment. Titanium-iron intermediate phases are identified as the regions with an intermediate contrast level between the iron substrate and titanium particles in the back scattered images. Figure 4-23 (a) shows a cross-section of a titanium particle on a low carbon steel substrate following heat treatment; no intermediate phases were formed at the particle-substrate

interface. A thin layer with a darker contrast level was found to be covering the particle; this was identified as titanium oxide, which has formed in spite of the samples being heat treated in a protective argon atmosphere with a noble gas purifier. In an attempt to promote formation of intermediate phases, a further sample with spherical titanium particles deposited onto low carbon steel was heat treated at 900 °C in a vacuum-sealed quartz tube for 30 minutes (not shown here), but, even at these temperatures, no intermediate phase formation was found at the interface. Figure 4-23 (b) shows a cross-section of a titanium particle deposited onto Armco iron following heat treatment. Again, there was no new intermediate phase formation following heat treatment at the particle-substrate interface or inside the particle.

Figure 4-23 (c) shows the cross-section of a titanium particle deposited onto an austenitic stainless substrate following heat treatment. A region of intermediate phases composed of two distinctive layers was identified at the particle-substrate interface (mid-grey contrast level). The new phases at the interface grew to a few microns thick at the centre region of the particle-substrate interface. A higher magnification image of the intermediate phases (boxed region) is shown in Figure 4-23 (d); spot analysis using EDX was performed to identify the phases. It can be seen from Figure 4-23 (d) that the two distinct intermediate phases were formed on the titanium particle side. EDX analysis of the phases on the titanium side (indicated as point 1 in Figure 4-23d) shows that it is composed of ~85 wt% titanium, ~13 wt% iron with small amount of nickel and chromium. The phase closer to the iron substrate (indicated as point 2 in Figure 4-23d) was found to contain 22-31 wt% Fe, 58-66 wt% Ti, 2-5 wt% Cr, 6-10 wt% Ni.

4.5.3.2 Angular titanium powder onto the austenitic stainless steel using room temperature helium

To investigate the effect of different feedstock powder morphologies in metal-to-metal bond formation, angular hydride de-hydride titanium powder was sprayed under the same conditions as utilized for the spherical titanium powder using room temperature helium. The angular titanium was only sprayed onto austenitic stainless steel substrates since intermediate phases had been observed only with this substrate material following spherical particle deposition and annealing. Figure 4-24(a) shows the plan-view of the stainless steel substrate following deposition of angular titanium particles. The surface exhibits reasonable coverage with titanium particles and a significantly reduced number of craters compared to that following deposition with spherical powders (Figure 4-21c). Figure 4-24 (b) shows the cross-section of an angular titanium particle deposited onto an austenitic stainless steel substrate. The irregular shape of the particle resulted in localized deformation of the austenitic stainless substrate (marked with an arrow). Figure 4-24(c) shows the cross-section of a substrate following deposition of an angular titanium particle and subsequent heat treatment. Titanium-iron intermediate phases are identified as the regions with mid-grey contrast between the substrate and the particle. The intermediate phases grew to a few microns thick in some places, but the coverage of the interface by intermediate phases is limited (Figure 4-23c). The intermediate phases are composed of two different contrast levels, indicating two different phases similar to those observed following heat treatment of the spherical titanium particles deposited onto the austenitic stainless steel substrates. The intermediate phases only grew in regions where the substrate went through a greater degree of deformation following deposition compared to the rest of the surface (marked with arrows in Figure 4-24 b, c).

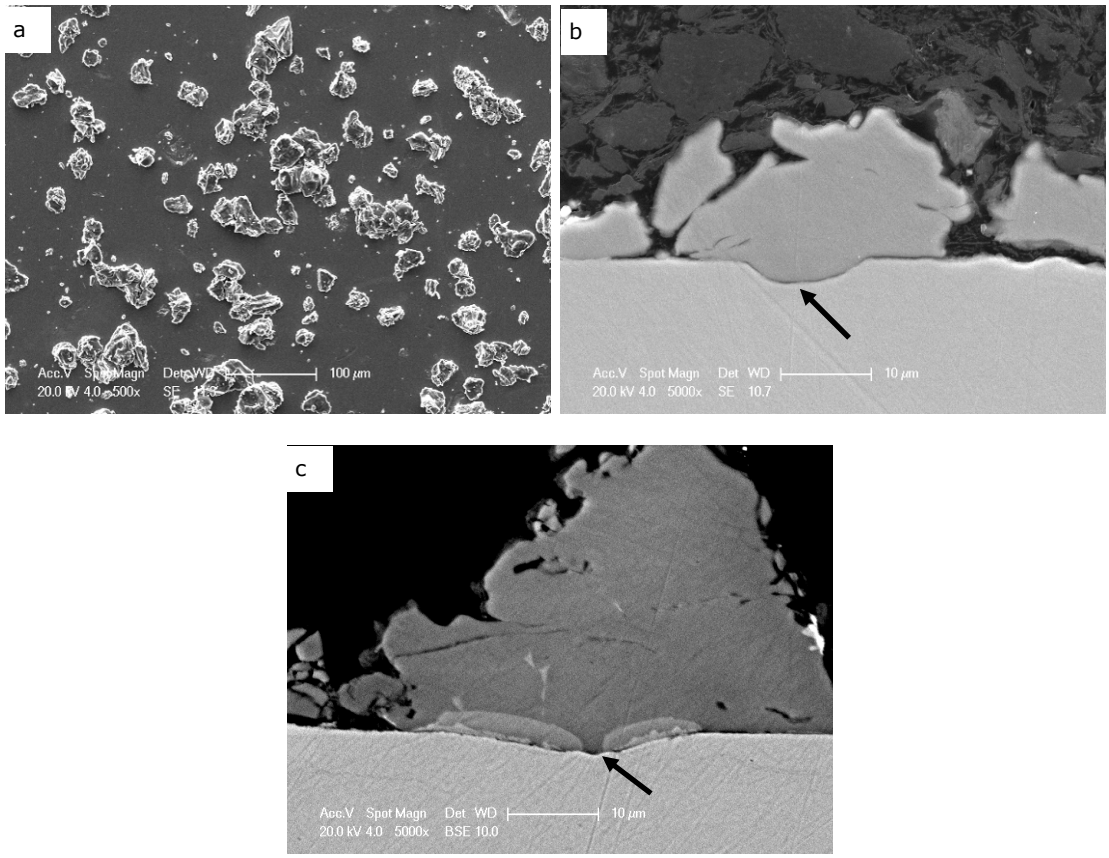

Figure 4-24 SEM images of angular titanium particles sprayed onto austenitic stainless steel using room temperature helium gas: (a) SE plan view; (b) SE cross–sectional image; (c) BSE cross-sectional image following heat treatment showing intermediate phase. Arrows indicate point of maximum deformation

4.5.3.3 Spherical titanium powder onto stainless steel using heated nitrogen

The previous experiments with titanium particles being sprayed onto austenitic stainless steel using room temperature helium resulted in intermediate phase formation following heat treatment (Figure 4-23c, Figure 4-24c). To investigate the effect of using heated nitrogen gas as the accelerant (in place of room temperature helium), spherical titanium particles were deposited onto austenitic stainless steel. Figure 4-25(a) shows the plan view of the substrate following deposition of the particles; a large number of particles with a wide size distribution are seen on the surface. It should be noted that the substrate was

exposed to a particle flux which was different to that experienced during spraying using room temperature helium gas due to change in spray apparatus, making direct comparison of the area fractions of particle deposition invalid. Nevertheless, a reduced number of craters on the stainless steel substrate was seen when heated nitrogen was used as the accelerant in comparison to when room temperature helium was used as the accelerant (Figure 4-21c), which suggests a higher fraction of particles were travelling above the so called critical velocity for deposition. Figure 4-25 (b) shows the cross-section through a spherical titanium particle following deposition onto austenitic stainless steel using heated nitrogen; the titanium particle is highly deformed compared to the particles sprayed using room temperature helium (Figure 4-22f). The jetting phenomenon is clearly observed at both sides of the particle deposited onto the substrate in Figure 4-25 (b), and the austenitic stainless steel substrate shows a greater degree of deformation compared to that following deposition of particles using helium as accelerating gas. Figure 4-25(c) shows the cross-section of a titanium particle deposited onto austenitic steel following annealing; a thick layer of intermediate phases have formed across the particle-substrate interface identified by the mid-grey contrast regions. The coverage of the intermediate phases is seen to be continuous across the full length of particle-substrate interface; this is clearly more extensive compared to that observed in the samples sprayed using room temperature helium, see Figure 4-23(c). Two layers of intermediate phases were identified at the particle-substrate interface in Figure 4-25(c); the phase on the titanium side grew to ~ 3-4 μm thick and the phase closer to the austenitic steel side grew only to ~ 1 μm thick.

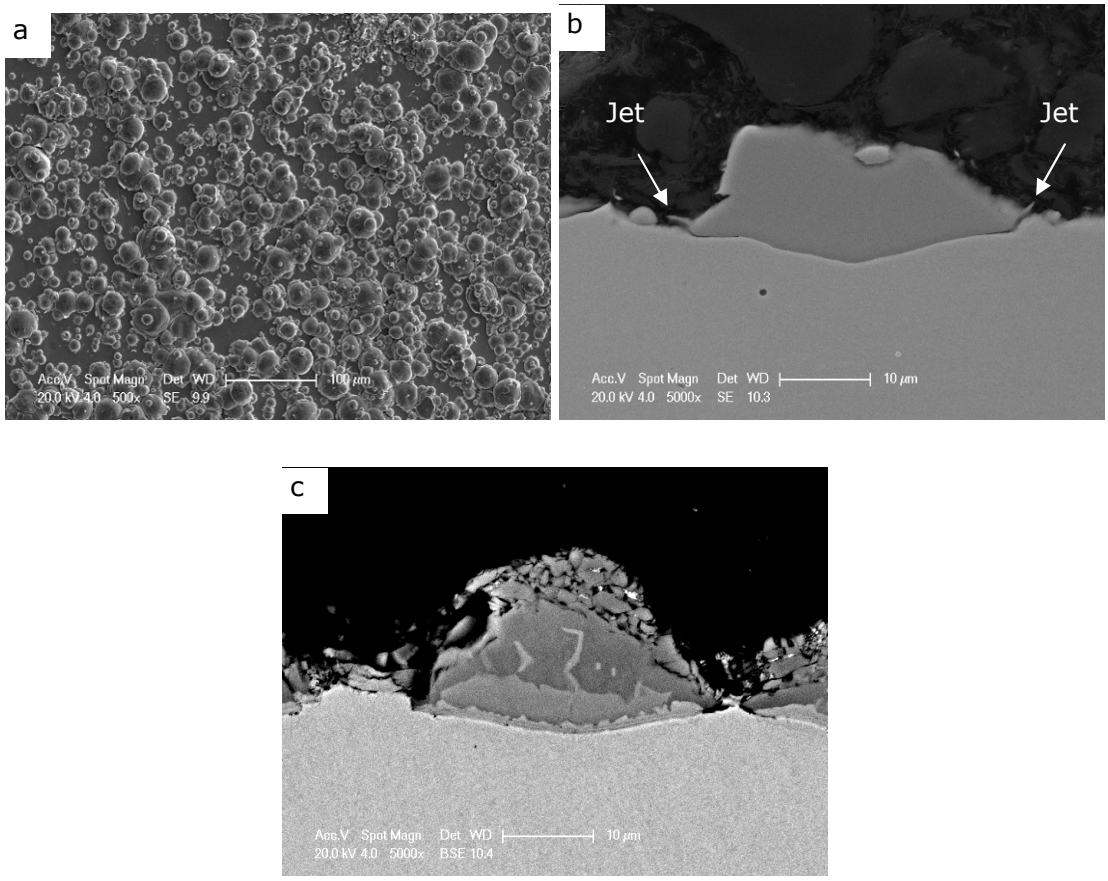

Figure 4-25 SEM images of spherical titanium particles sprayed onto austenitic stainless steel using heated nitrogen gas at 800 °C and 4.0 MPa: (a) SE plan view; (b) SE cross–sectional image; (c) BSE cross-sectional heat treated image showing formation of intermediate phases (mid-grey contrast levels)

4.6 Discussion

The discussion of this chapter is divided into three main sections. The bonding mechanisms of copper deposit onto aluminium substrate will be discussed first in relation to a newly proposed bonding model. Then, the bonding mechanisms of aluminium deposit onto copper substrate will be compared and contrasted to the bonding mechanisms in copper deposit onto aluminium substrate. Moreover, the impact and deformation behaviour of titanium particles onto three different steel substrates will also be discussed.

4.6.1 Bonding mechanisms of copper coatings onto aluminium substrates

The discussion proceeds by treating the grit-blasted substrates separately from the other forms of preparation, since it is argued that very different phenomena are observed in the two situations.

4.6.1.1 Bond formation – ground and polished aluminium substrates

4.6.1.1.1 Experimental observations on bonding and failure mechanisms

The differences between the ground and the polished aluminium substrates are primarily in their hardness and their roughness characteristics. Table 4-2 shows that the near-surface hardness of the ground material is slightly less than that of the polished material (and indeed slightly less than the bulk of the sample), and that this lower hardness is retained even after annealing. However, the reasons for this reduced hardness are not clear at present. The surface roughness of the polished surface (Ra = 0.05 μm) is significantly less than that of the ground surface (Ra = 0.4 μm) (Table 4-2). To visualize the significance of the difference in surface profiles, line traces of both the polished and the ground surfaces (with the same magnifications in the horizontal and vertical directions) are shown in Figure 4-4. In the same figure is a representation of a 15 μm copper particle on the same scale. It can be seen that the polished surface may be approximated as a flat plane whereas the ground surface profile may provide some small perturbations which could affect the deformations experienced during impact.

Figure 4-5 and Figure 4-6 show the fracture surfaces of the aluminium substrates and copper deposits (both as-prepared and annealed substrate conditions) after they have failed in the pull-off test whilst Figure 4-8 shows cross-sections of the same deposit-substrate interfaces before testing. Deformation takes place principally in the aluminium substrate (little flattening of the copper particles is

evident). Moreover, there is little evidence in these images for a significant difference between copper deposited onto a polished or a ground surface. Furthermore, ground surfaces behave in a similar manner in both as-prepared and annealed conditions despite the significant decrease in hardness brought about by annealing (106 to 35 kgf /mm^2). Fracture surfaces from substrates that were polished prior to application of the deposit could not be compared with and without annealing because in the latter condition glue failure occurred in the pull-off test. Whilst the small differences in surface profile compared to the particle size (as seen in Figure 4-4) may explain why surface morphology is insensitive to the surface preparation method (ground versus polished), its insensitivity to initial surface hardness is more surprising. This insensitivity to hardness (within the range examined) suggests that during the impact process, high strain rate deformation causes significant work hardening at the interface so that the initial condition of the material before impact does not significantly affect its subsequent deformation characteristics.

The mechanism of deposit-substrate bonding in cold spraying has commonly been perceived to be primarily via the formation of metallic bonds following removal of surface oxides and creation of clean interfaces; an impacting particle causes jetting of the material which removes the surface oxide layer and a true metallurgical bond is created [9, 40, 42, 64, 70, 71]. However, the present observations lead to propose an additional contribution which is termed "interlocking". It is proposed that the metal jetting due to the impact of incoming copper particles causes lips of aluminium to form which partially envelop the copper particles as shown schematically in Figure 4-26. This creates mechanical interlocking of the substrate with the powder particle. Experimental evidence for this is clearly seen in the cross-sectional images of Figure 4-8 (a, b, d, e). Moreover, the fracture surfaces of the copper deposit following pull-off testing show regions of failed aluminium substrate outlining many of the particle

boundaries (Figure 4-5d, e and Figure 4-6c). A higher magnification image of such extruded lips of aluminium are shown in Figure 4-7. It should be noted that whilst this mechanical interlocking of the aluminium substrate into the copper deposit is seen to be widespread, it does not exist between a significant number of the particles that can be seen on the fracture surface. Table 4-4 shows that when fracture surfaces are assessed the fractional area coverage of the copper coating side by these extruded lips is of the order of 0.1 and varies little with surface preparation.

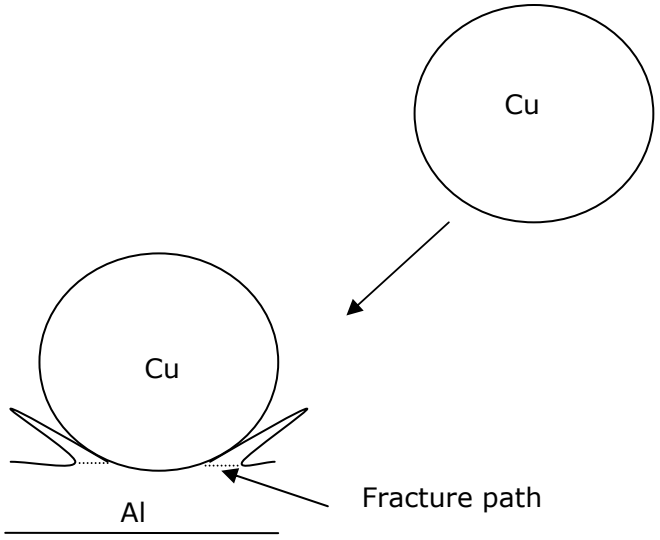

Figure 4-26 Schematic illustration of jet formation on an aluminium substrate by an impinging copper particle. The jet is subsequently trapped in the copper coating by incoming copper particles. During the bond strength test fracture occurs in the aluminium jet shown by the dotted line.

In summary, it is clear that in the case of polished substrates and ground substrates there are very few morphological differences in the nature of the substrate-deposit interface as a function of whether the substrate surface is ground or polished, or whether it is hard or soft.

Turning now to a consideration of deposits that were annealed at 400 °C for 15 min, the results show some very marked differences in intermetallic formation depending on substrate preparation. It is important to recollect that this annealing leads to intermetallic formation only when interdiffusion is possible, i.e. intermetallic formation acts as a marker for metallurgically clean interface regions. Figure 4-9 shows the formation of the intermetallics, with the fractions of the interface covered with intermetallic phase presented in Table 4-5. On the as-prepared (polished) substrate it can be seen (Figure 4-9a) that, despite significant substrate deformation (with evidence of interlocked jets of aluminium in the deposit structure), the intermetallic area fraction was only 0.46 (see Table 4-5). The intermetallic formation on the as-prepared ground sample (Figure 4-9b) was even lower at only 0.27 (Table 4-5). The values for the fraction of the interface covered with intermetallics were increased to 0.94 and 0.77 respectively for polished and ground substrates that were annealed before cold spraying.

In summary, intermetallics grow more readily on polished surfaces than on ground surfaces, and annealing of the substrate at 450 °C for 1 hour prior to spraying promotes intermetallic formation in both of the surface preparation conditions. It is believed that increases in intermetallic formation must be associated with more extensive removal of oxide during the jetting process that occurs on impact. Further research is needed here but one could speculate that by annealing the substrates before cold spraying, the surface oxide is being modified; possibly being transformed from a hydrated layer to one which is corundum (α-Al_2O_3). The effect of polishing compared to grinding is less easy to rationalise at this stage.

4.6.1.1.2 Bonding model

For the polished and ground substrates (i.e. where the adverse effects associated with the grit-blasting do not come into play), it has been demonstrated that the

bonding of the coating to the substrate depends upon two primary components: (i) metallurgical bonding associated with the formation of oxide-free surfaces during jetting; and (ii) mechanical interlocking of jetted material between the powder particles making up the coating structure. During bond strength testing of such coatings, decohesion of the coating from the substrate must result in failure of both the metallurgically bonded regions and the mechanically interlocked material.

To model this situation in a semi-quantitative manner, it is proposed to treat the region across the interface as a simple unidirectional composite. The composite components are the jetted material regions and the metallurgically bonded regions as shown schematically in Figure 4-27.

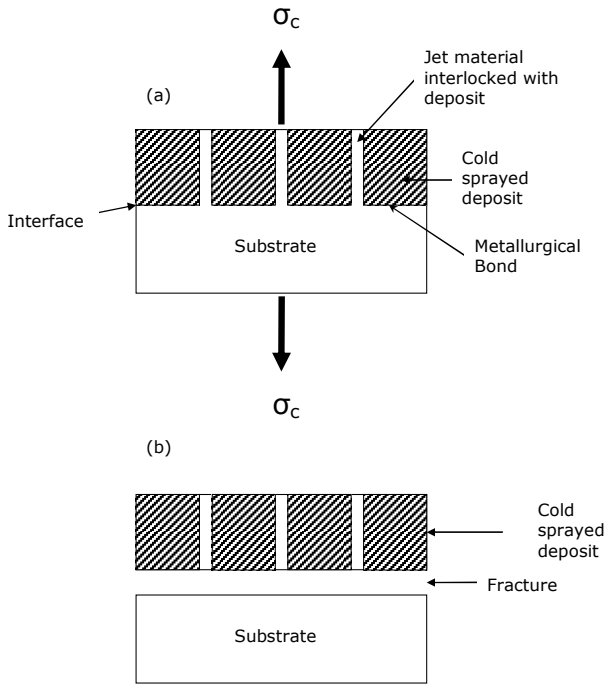

Figure 4-27 Schematic diagram of deposit-substrate debonding at the interface, indicating failure of both the interlocked substrate and the regions of deposit-substrate metallurgical bonding; (a) prior to failure; (b) post failure.

The jetted material is regarded as an elastic solid which exhibits ductile behaviour and is continuous across the interface region. The areas where the cold sprayed deposit and the substrate come into contact are treated as elastically brittle regions. The stress-strain behaviour of each component is shown schematically in Figure 4-28 where σ_m is the stress in the metallurgically bonded areas and σ_i the stress in the interlocked regions. σ_{mf} is the failure stress of the former and σ_i' is the stress in the interlocked regions when the metallurgical bond fails.

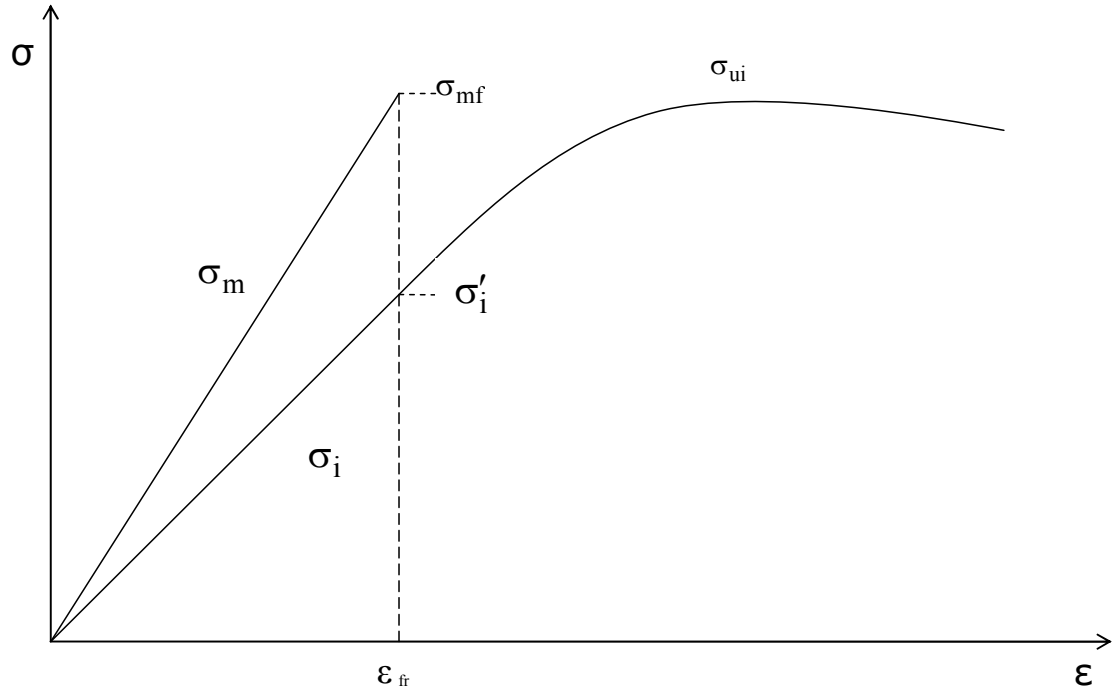

Figure 4-28 Stress strain behaviour of metallurgically bonded area and mechanically interlocked area assuming that the metallurgically bonded area exhibits brittle behaviour and that the mechanically interlocked area exhibits ductile behaviour

Using this approach, the standard theory for longitudinal tensile strength of a long fibre reinforced composite can be applied.

The stress in the composite, σ_c, is given by

$$\sigma_c = \sigma_m f_m + \sigma_i f_i \qquad \text{equation 4.1}$$

where f_m and f_i are the area fraction of the interface corresponding to metallurgical bond and interlocked material respectively.

If we assume that the interlocked material is ductile but the metallurgical bond fails in a brittle manner at a critical stress σ_{mf} (see Figure 4-28) then the stress in the composite, σ_c' when this failure occurs is given by

$$\sigma_c' = \sigma_{mf} f_m + \sigma_i' f_i \qquad \text{equation 4.2}$$

Assuming that $f_m + f_i = 1$, then

$$\sigma_c' = (\sigma_{mf} - \sigma_i')\, f_m + \sigma_i' \qquad \text{equation 4.3}$$

When the metallurgical bonded region fails, all the load is transferred to the interlocked material. The maximum composite stress that can be transferred to interlocked material is given by

$$\sigma_c' = \sigma_{ui} f_i = \sigma_{ui}(1 - f_m) \qquad \text{equation 4.4}$$

where σ_{ui} is the tensile strength of the interlocked material (Figure 4-28).

Classically, equations 4.3 and 4.4 are represented by plotting stress as a function of f_m as shown by the schematic diagram in Figure 4-29.

However, in the present situation the equations need to be modified to take account of the fact that the true metallurgically bonded area fraction, f_m^T, differs from the apparent contact area fraction, f_m .

We define f_m as the apparent metallurgically bonded area such that $f_m + f_i = 1$ and take the true metallurgically bonded area to be given by

$$f_m^T = f_m \times f_{int} \quad \text{equation 4.5}$$

where f_{int} is the measured area fraction of intermetallic coverage as presented in Table 4-5.

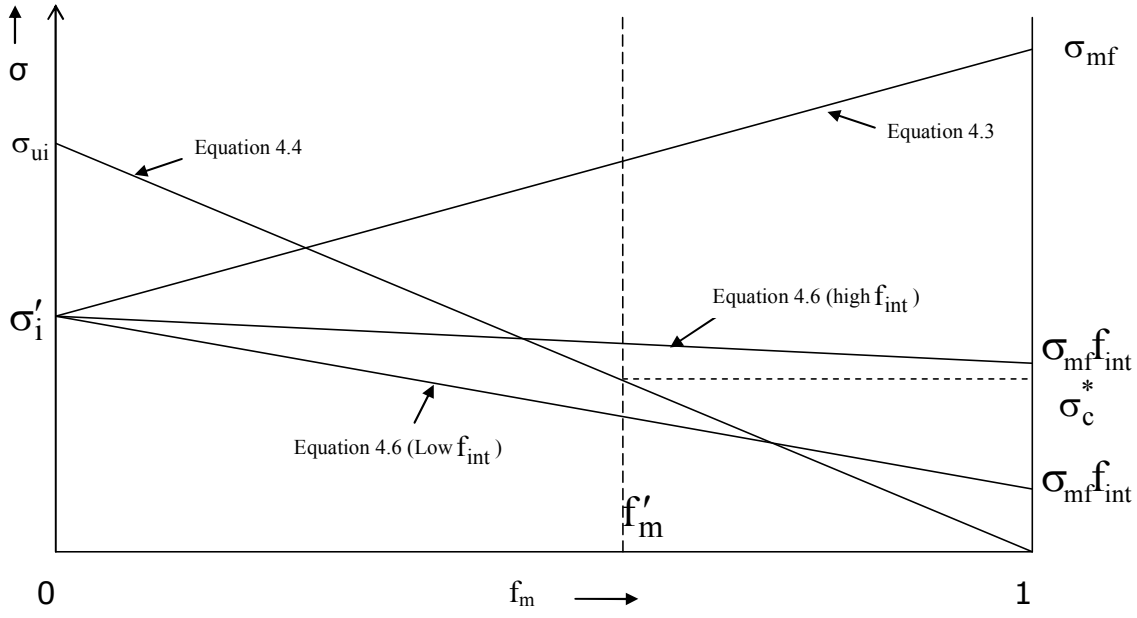

Figure 4-29 Failure stresses associated with the different failure modes as indicated in equation 4.3, 4.4 and 4.6 as a function of the fraction of the metallurgically bonded material

So for metallurgical bond failure equation 4.2 is modified to become

$$\sigma'_c = \sigma_{mf} f_m f_{int} + \sigma'_i(1 - f_m) = (\sigma_{mf} f_{int} - \sigma'_i) f_m + \sigma'_i \qquad \text{equation 4.6}$$

Clearly for a given value of f_m, changes in f_{int} will affect the position of the composite failure strength line in relation to the line for composite strength that can be supported by interlocked material (equation 4.4). The behaviours of equations 4.3, 4.4 and 4.6 are illustrated schematically in Figure 4-29. It is evident that for a chosen value of f_m (shown as f'_m in Fig. 14) there are two possible types of behaviour.

Case 1

Below a critical value for f_{int}, the composite failure strength will be controlled by failure of the interlocked material and will be constant at the value σ_c^* shown on Figure 4-29.

Case 2

Above a critical value for f_{int}, the composite failure strength will be governed by equation 4.6.

It is now possible to apply this model to the experimental data reported in Table 4-3, Table 4-4 and Table 4-5. The bond strength is almost constant for as-prepared polished, as-prepared ground and annealed ground substrates (Table 4-3). For these conditions the fraction of interlocked material, f_i, also remains constant at about 0.12 (this is the fraction of aluminium on the copper coating). For these three conditions, the f_{int} value varies from 0.27 to 0.77 but with no apparent effect on the bond strength. Therefore we can explain this on the basis that these values of f_{int} are such that failure strength is controlled as in case 1 above. Taking the fraction of interlocked material, f_i, to be 0.11 and estimating

the value of σ_{ui} to be 432 MPa (1/3 of the hardness of the 6082 alloy cold rolled to a strain of 360%), we find that σ_c' is of the order of 48 MPa from equation 4.4. This is in good agreement with the observed values, given the approximate nature of the analysis.

In the case of the polished sample which was annealed before deposition of copper, it is argued that f_{int} had increased to such an extent that failure occurred according to the behaviour ascribed to case 2 above. The bond strength could not be measured since the fracture occurred in the adhesive at an applied stress of 69 MPa. Young's moduli of both the interlocked and metallurgically bonded regions need to be known in order to determine how the stress is distributed between the two components of the composite. If they are taken to be equal, and if f_{int} is taken to be 1, then a lower bound value for σ_{mf} is 69 MPa. In practice, f_{int} is less than 1 and the metallurgically bonded regions are likely to be of higher stiffness (being composed of aluminium and copper) than the interlocked regions (which are composed of aluminium), and so the actual value for σ_{mf} will probably be in excess of this value.

4.6.1.2 Bond formation - grit-blasted aluminium substrates

In considering the behaviour of grit-blasted surfaces, the morphology of fracture surfaces following the pull-off test will be examined first of all and this will be followed by a consideration of how this might modify bonding during cold spraying.

4.6.1.2.1 Morphological features arising from impact

The principal features due to impact on a grit-blasted surface seen in Figure 4-5(c) and Figure 4-8(c) appear very similar to those observed following impact on the grit-blasted and annealed surface (Figure 4-6b and Figure 4-8f), despite

the fact that the annealed surface is significantly less hard, namely 50 kgf /mm^2, compared with 180 kgf /mm^2. It is evident that a very large proportion of the copper particles that impacted on the grit-blasted surfaces developed a rough and pitted appearance which is mirrored by the appearance of the substrate (i.e. the aluminium side of the fracture surfaces). These features are clearly attributable to the use of the Al_2O_3 grit in the preparation stage and it would appear that under the conditions used to prepare these substrates, the brittle Al_2O_3 fragmented and some of these fine fragments became embedded in the soft aluminium substrate. In the cross-sectional BSE images of deposits on grit-blasted substrates (Figure 4-8c, f and Figure 4-9c, f), evidence of a slightly lower contrast material just below the substrate surface can be seen, along with some porosity in that zone. This material is believed to be embedded Al_2O_3 fines, a hypothesis which is consistent with EDX measurements which indicated no other elements than aluminium and oxygen in this region. The porosity observed was typically less than 5 μm in size, which is much less than the size of the original blast-media particle size, but similar to that of the embedded fines.

The similar behaviour of as-prepared and annealed substrates in terms of deformation characteristics confirms the previous observation on ground/polished surfaces that very low strain rate hardness measurements cannot adequately predict the behaviour of surfaces under the high rates of strain associated with impact. The hardness reduction that does take place is probably due to the high temperature annealing treatment allowing classical recovery or recrystallisation processes to occur in the aluminium alloy. The Al_2O_3 fines contribute to the near-surface hardness of the aluminium since they act as a dispersion strengthening phase. This contribution is of course not affected by annealing and is presumably responsible for the higher near-surface hardness (Table 4-2) of the annealed, grit-blasted substrate compared to other surface preparations.

4.6.1.2.2 Influence of grit-blasting on jetting and bond strength measurements

A key question for bond formation during cold spraying is how the surface morphology, near-surface hardness and microstructure will affect jetting phenomena during impact. The grit-blasting changes the profile of the substrate surface with a significant increase in Ra compared to the other two preparation processes (Table 4-2). Figure 4-3 shows the surface profile with Figure 4-4 showing the profile with the same magnifications in horizontal and vertical directions, along with a typical powder particle size. In this latter image, it can be seen therefore that the local conditions during impact of powder particles onto a grit-blasted substrate will be very variable. The flattening of the copper particles seen in Figure 4-8 indicates that the surface material in the grit-blasted substrate is more resistant to deformation under impact conditions, and that jetting during impact will be restricted. There is significantly less evidence of jetted substrate material forming a mechanical interlock with the deposit for the grit-blasted substrate than for the other two surface preparation methods. This limitation of jetting during impact also affects the efficacy of removal of surface oxide layers during impact (and thus the efficacy of any metallurgical bonding between the copper and aluminium). Figure 4-9 (c, f) show the interfaces between the aluminium and copper following intermetallic growth. It can be seen that the intermetallic growth is limited in both cases. In the non-annealed samples (Figure 4-9a-c), the intermetallic growth is similar to that observed on the ground sample and slightly lower than that on the polished sample (see Table 4-5). However, whilst the coverage of intermetallic increased for the grit-blasted samples with annealing (from approximately 34 to 50%), this was much less significant that the effect that the annealing had on the other two sample preparation types (see Table 4-5).

The bond strength in pull-off testing of the samples with as-prepared grit-blasted substrates was significantly lower than those observed with the other two

preparation types (around 35 MPa as compared to around 56 MPa). Figure 4-5(f) shows that, unlike the deposit surfaces from the other two types (Figure 4-5d, e), significant regions of the aluminium substrate were retained on the surface. This indicates that fracture is occurring in the aluminium substrate, and it is proposed that fracture is being promoted in the zone which contains the embedded grit-blasting fines, it being weakened by the presence of these fines. The same effect is observed following fracture of the deposit from the grit-blasted surface that had been annealed before spraying (Figure 4-6d), but to a lesser degree. However, it is observed that the bond strength for the grit-blasted samples was significantly increased from around 35 MPa to around 57 MPa by the annealing process (see Table 4-3). The fraction of intermetallics has also increased significantly with annealing of the substrate, from 34% to 50% (see Table 4-5). Thus, although the substrate surface is roughened by the blasting process, the embedment of grit fines in the surface results in a surface which is much more resistant to high strain rate deformation (even if the effects of work hardening are eliminated). This results in less jetting of the aluminium during impact and thus to a restriction in the formation of metallurgical bonds between the deposit and substrate. The embedded grit results in fracture actually within the substrate following pull-off testing.

In summary, grit-blasting has been seen to be detrimental to the bonding process in the system comprising copper particles and an aluminium substrate examined in the present study. It must be recognised, however, that due to the low hardness of the substrate, the tendency for grit fines to embed during blasting will be relatively high compared to materials such as steel or titanium alloys. Grit-blasting of other, harder substrates may not result in such significant embedment of fines, and thus the adverse effects of the blasting process observed in this work may not be universal.

4.6.2 Bonding mechanisms of aluminium coatings onto copper substrates

4.6.2.1 Bond formation: ground and polished copper substrate

4.6.2.1.1 Experimental observations on bonding and failure mechanisms

The differences between the polished and ground copper substrates are primarily in their near surface hardness and the roughness characteristics. Table 4-6 shows that the near surface hardness of the ground material is slightly higher than the polished material and the bulk of the sample. This slightly increased hardness is possibly due to mechanical removal of materials from the surface. The surface roughness of the polished surface (Ra= 0.07 μm) is significantly less than that of the ground substrate (Ra= 1 μm) (Table 4-6). To visualize the differences both the polished and ground surfaces with same magnification on the horizontal and vertical lines with respect to a 35 μm particle on the same scale are shown in Figure 4-13. It can be seen that the polished surface may be approximated as a flat plane whereas the ground surface profile may provide some perturbation which could affect the deformation experience during impact. In addition, similar surface profiles following polishing and grinding of aluminium substrates were observed.

Figure 4-14 and Figure 4-15 show the fracture surface of the copper substrate and aluminium deposits after they had failed in the pull-off bond strength test. The cross section of the deposit-substrate interfaces before the pull-off tests are shown in Figure 4-17. There is little evidence in these images of a significant difference between aluminium deposited onto a polished or ground surface. The small differences in surface profile compared to the particle size (Figure 4-13) may explain why interface morphology is insensitive to the surface preparation methods (polished vs. ground). Furthermore polished surface behave in a similar

manner in both as-prepared (Figure 4-17a) and annealed conditions (Figure 4-18a) despite the significant decrease in hardness brought about by annealing (89 to 51 kgf /mm^2). This insensitivity to hardness suggests during impact process, high-strain rate deformation causes significant work hardening at the interface so that the initial conditions of the material before the impact do not affect the subsequent deformation characteristics. In addition, this insensitivity to hardness was also observed in the cold sprayed copper coating onto as-prepared and annealed aluminium substrate.

The fracture surfaces of aluminium deposits and copper substrates do not show any evidence of "mechanical interlocking", which was previously observed in the fracture surfaces of copper deposits on aluminium substrates following pull-off tests. The lips of substrates which form following impact of incoming particle are completely absent in the case of aluminium deposits onto copper substrates. Figure 4-16 shows the aluminium deposits are adhering to the top layer of the copper substrate instead of "mechanical interlocking" and during pull-off testing, failure occurs at the top layer. The fracture surface of the aluminium deposits following pull-off testing show a limited fraction of failed copper substrates (Figure 4-15d, e). This phenomena was not enhanced by altering the copper substrate hardness significantly after annealing as can be seen from the cross section of aluminium deposits onto annealed copper substrate (Figure 4-18a).

In summary, it is clear that in the case of polished and ground substrates there are very few morphological differences in the nature of the substrate deposit interface as a function of whether the surface is ground or polished.

Turning now to a consideration of deposits that were annealed at 400°C for 15 minutes, the results does not show any significant difference in intermetallics formation of as-prepared polished substrate and annealed polished substrate (both ~ 0.13) (Table 4-9). There was a slight reduction in intermetallics formation following deposition onto ground surface (0.07) compared to polished surface (0.13). It is important to recollect that annealing leads to intermetallic formation only when interdiffusion is possible. Therefore, a decrease in intermetallic formation must be associated with less extensive removal of oxide during impact process.

4.6.2.1.2 Bonding model

The bonding model proposed in section 4.6.1.1.2 can be applied to the experimental data of aluminium deposits sprayed onto copper substrates. Table 4-7 shows the bond strength is almost constant for as-prepared polished and ground samples. This bond strength values are significantly lower compared to the copper deposits sprayed onto aluminium substrates (35-70 MPa). For both polished and ground surface preparation interlocked material f_i is very low and remains constant at 0.01 (this is fraction of copper on aluminium deposit), which is an order of magnitude lower compared to copper deposited onto aluminium substrates case. For these two conditions, fraction of metallurgically bonded area f_{int} value varies from 0.13 to 0.07 without any significant affect on bond strength values. Therefore it can be explained on the basis that these values of f_{int} are such that failure strength is controlled by case I. Case I states that below a critical value for $f_{int,}$ the composite failure strength will be controlled by failure of the interlocked material and will be constant at a σ_c* shown in Figure 4-29. In the case of polished sample which was annealed after the surface preparation methods, the f_{int} did not show any increase compared to as-prepared polished substrate. The bond strength test of aluminium deposit onto polished copper substrate, which was annealed following surface preparation, could not be

performed due to poor adhesion. If the bond strength testing of copper deposit onto annealed copper substrate were successfully performed, it would indicate that the bond strength values were similar to the values found in the case of as prepared polished copper substrate.

4.6.2.2 Bond formation: grit blasted copper substrate

4.6.2.2.1 Morphological features arising from impact

A large number of aluminium particles that impacted on the grit-blasted copper substrate developed a rough appearance which is mirrored by the appearance of the substrate (Figure 4-14c, f and Figure 4-15c, f). The use of alumina grit in the preparation resulted in fragmentation of the grit and some of these fine fragments became embedded in the copper substrate. This is also evident in the cross section of the BSE images of the deposits on grit-blasted surface in Figure 4-17c, which shows evidence of a slightly lower contrast material just below the substrate surface. EDX measurements indicated those are composed of aluminium and oxygen. These finely dispersed alumina fine contribute to the near surface hardness (152 kgf/ mm^2) which act as a dispersion strengthening phase.

4.6.2.2.2 Influence of grit-blasting on jetting and bond strength measurements

The grit blasting changes the profile of the substrate surface with a significant increase in Ra compared to polished and ground surface preparations (Table 4-6). Figure 4-12 shows the typical surface profile of grit-blasted surface and Figure 4-13 shows surface profile with respect to a 35μm particle with the same magnification in horizontal and vertical directions. The local conditions during impact onto grit blasting surface will be different from the other two surface preparation methods. The growth of intermetallic on grit-blasted surface is similar to the ground substrate and slightly lower than that of the polished sample (Table 4-9).

The pull-off bond strength tests of the samples with grit-blasted surface was similar to the other two surface preparation methods. Figure 4-15 (f) shows a slightly greater amount of copper retained on the coating surface after the pull-off tests (0.07 compared to 0.01 or less). This indicates some degree of the fracture is occurring in the copper substrate, and it may be promoted by the areas containing embedded fines.

4.6.2.3 Comparison of copper coatings onto aluminium and aluminium coatings onto copper

The deformation behaviour of aluminium particle on copper substrate and copper particle on aluminium substrate are different due to lower density of aluminium and thus less kinetic energy available up on impact [42]. In cold spray deformation mechanisms, the kinetic energy of the particle is converted into plastic dissipation energy upon impact [39]. As a result, aluminium particles need a higher velocity for deposition as that of the same sized copper particle. The so called- critical velocity for a 25 µm aluminium particle was reported 650 m/s and that of a 25 µm copper particle was 500 m/s [11]. Moreover, the aluminium particle used in this experiment had a larger size than the copper particles. According to the particle acceleration models, the particle velocity decreases with an increase in particle size [28-30].

In all the cases of aluminium sprayed onto copper substrate resulted in a lack of "mechanical interlocking" of the substrate and the particle, which resulted in a low bond strength value. On the other hand, copper particles sprayed onto aluminium substrate resulted in "mechanically interlocked" regions and consecutively a higher pull-off bond strength value. The differences in the deformation behaviour can be attributed to the higher kinetic energy of the copper particle in comparison to aluminium [40]. The fraction of metallurgically

bonded interface was also very low in aluminium deposited onto copper substrate. Aluminium particles have a tenacious oxide layer compared to the oxide surrounding copper particles. Due to incomplete oxide removal of the aluminium deposits, the metallurgically bonded interface was also limited. In addition, single particle impact test of aluminium particle onto copper substrate showed that the metal jet is composed of only aluminium and no evidence of jetting form the copper substrate occurs (Figure 4-11). On the other hand, single particle impact test of copper onto aluminium substrate showed deformation of both particle and substrate to a great extent (Figure 4-2). Apparently, this higher degree of substrate deformation behaviour was effective in removing the surface oxide from the aluminium and produce intimate contact.

In summary, copper particle sprayed onto aluminium substrate was effective in removing surface oxide and produce "mechanically interlocked" microstructure compared to aluminium particles sprayed onto copper substrate. This "mechanically interlocked" structure and metallurgically bonded region contributed to a higher bond strength value for cold-sprayed copper coatings onto aluminium substrate.

4.6.3 Impact and bonding behaviour of titanium particles onto steel substrates

4.6.3.1 Particle substrate deformation behaviour

Particle bonding in cold-spraying is dependent on plastic deformation of the impacting particles and the substrates. Adiabatic shear instability occurs at the particle-substrate interface, which results in abnormal temperature and strain histories and thus to the collapse of stresses; visco-plastic behaviour of the metals is generally postulated due to dominance of thermal softening over work hardening [1, 39]. When a harder material impacts with a softer material, the

plastic energy is primarily dissipated in the softer counterpart [39]. As such, when titanium impacts with the softer Armco iron, the plastic deformation is mostly in the Armco iron. The deformation of Armco iron is far greater than the deformation of low carbon steel following impact by titanium particles, an observation which may be explained as follows. Armco iron contains less than <0.005 wt% carbon and 0.04 wt% manganese; in contrast, the low carbon steel contains 0.04 wt% carbon and 0.17 wt% manganese (Table 4-1), resulting in a higher hardness for the carbon steel compared to the Armco iron. The amount of carbon and manganese present in the carbon steel changes the high strain rate behaviour [188] and therefore will affect the way in which particle and substrate deform upon impact. Moreover, the hardness of a piece of commercially pure titanium (judged to be a reasonable analogue to the titanium particle feedstock) (145 kgf/ mm^2) is lower than that of both the low carbon steel and the austenitic stainless steel, but higher than that of the Armco iron. Although very low strain rate hardness measurements cannot predict the high strain rate deformation behaviour associated with impact, the softest material (Armco iron) is also observed to be the material which deformed most significantly during particle impact.

Deposition of titanium onto low carbon steel resulted in a large number of craters on the surface. This rebounding phenomenon can be explained by the energy balance theory for cold-spraying [39, 56]. According to energy balance theory, adiabatic local heating induced by plastic dissipation energy and frictional dissipation energy contributes to adhesion energy, and only stored elastic energy contributes to rebound energy [56]. It is argued that in cold-spraying, the particle remains attached to the substrate when the adhesion energy is higher than the rebound energy. Below the critical adhesion velocity, the adhesion energy of a particle is lower than the rebound energy and no deposition can occur; similarly above the maximum velocity of particle deposition onto the substrate, the

rebound energy is higher than adhesive energy and again no deposition can occur. Moreover, Wu et al. [56] showed that the adhesion and rebound energy increase with increasing velocity for all materials. Specially, when softer materials impact onto the carbon steel substrate, the rate of rebound energy increases sharply, which makes the particles more prone to rebound [39]. It was suggested that the rebound energy is associated with the elastic modulus of the impacting particle and substrate. This higher rebound energy is responsible for the significant number of titanium particles which rebound from the low carbon steel substrate surface.

4.6.3.2 Johnson-Cook plasticity model of material behaviour

The impact behaviour of particles at high strain rate can be described by the Johnson-Cook model. The Johnson-Cook plasticity model [52], which includes strain hardening, strain-rate hardening and thermal softening effects, can be described by the following equation:

$$\sigma = [A + B\varepsilon_p^n]\left[1 + C\ln\left(\frac{\bar{\varepsilon}_p}{\bar{\varepsilon}_0}\right)\right]\left[1 - \left(T^*\right)^m\right] \quad \text{equation 4.7}$$

Where σ is the equivalent flow stress, ε_p is the equivalent plastic strain, $\overline{\varepsilon_p}$ is the equivalent plastic strain rate, $\overline{\varepsilon_0}$ is the reference strain rate and T* is the normalized temperature. A, B, C, m, and n are material specific properties; A is the yield stress in a simple quasi static tension/ compression test, B is the stain-hardening parameter, C is the dimensionless strain-rate hardening coefficient and n, m are exponents of strain-hardening and thermal-softening terms. The normalized temperature T* is described as follows

$$T^* = \begin{cases} 0; & T < T_{trans} \\ (T - T_{trans})/(T_{melt} - T_{trans}); & T_{trans} \leq T \leq T_{melt} \\ 1; & T_{melt} < T \end{cases} \quad \text{equation 4.8}$$

T_{melt} is the melting temperature above which the flow stress of the material is zero and T_{trans} is a reference temperature above which thermal softening is assumed to occur. The Johnson-Cook model parameters experimentally extracted at relatively low strain rates (typically 10^3- 10^5 /s) may not be adequate to describe the higher range of strain-rate estimated for cold-spray and warm-spray particle impact (typically 10^6 -10^9 /s [1, 11, 45]). Nevertheless, the Johnson-cook model will provide with a way to compare the flow stresses of different materials at elevated strain-rates.

To calculate the stress strain behaviour of a material using the Johnson-Cook model requires estimates of the appropriate temperature and strain rate to be made. These estimates were made as follows:

4.6.3.2.1 Estimate of strain rate

The strain rate of a perfectly plastic impact of a spherical particle onto metal substrate is given by Hutchings [189] :

$$\dot{\bar{\varepsilon}}_p \approx \frac{2^{\frac{3}{2}}}{5\pi} \frac{V_p^{\frac{1}{2}}}{r} \left(\frac{3P_a}{2\rho_p} \right)^{\frac{1}{4}} \quad \text{equation 4.9}$$

where, P_a is the mean pressure acting on the sphere during indentation, ρ_p is the density, r is the radius of the sphere and V_p is the velocity of the sphere. In computing the strain rate, a mean pressure P_a= 1422 MPa was taken corresponding to quasistatic indentation hardness of commercially pure titanium (hardness of titanium 145 kgf/ mm^2), ρ_p = 4500 kg/m and V_p = 600 m/s and r = 10 µm. The calculated strain rate under these conditions is ~ 10^7 /s.

4.6.3.2.2 Estimate of temperature

According to slip-line field theory, when a rigid punch deforms an ideally plastic material, the zone of plastic deformation is twice the diameter of the punch [190]. If we assume a 10 μm radius spherical titanium particle impacts the substrate, the radius of the plastic deformation zone on the substrate will be ~20 μm. The rigid punch assumptions will not be valid in cold-spraying due to plastic deformation of the particles upon impact; nevertheless this assumption will provide an approximate value to perform the necessary calculations. If the plastic zone on the substrate is assumed to be hemispherical in shape, then the volume of the plastic zone can be calculated using $v = \frac{2}{3}\pi.r'^3$, here r' = 20μm, which gives 1.67 × 10^{-14} m^3. The kinetic energy of a particle can be calculated using, $KE = \frac{1}{3}m.V_p^2$. Using this equation, a 10 μm radius titanium particle travelling at 600 m/s has a kinetic energy of ~3.4 × 10^{-6} J. Assuming that this kinetic energy is dissipated over the entire plastic zone volume following impact results in an energy density of 2 × 10^8 J/m^3. The temperature rise in the adiabatic shear bands (ASB) at high strain rates >10^3 /s is considered adiabatic, and the plastic deformation energy is converted to heat and leads to a rise in temperature which is given by Yang et al. [191]

$$T' - T_i = \frac{\beta}{C_v \rho_p}\int_0^{\varepsilon} \sigma d\varepsilon \quad \text{equation 4.10}$$

T' is temperature at the adiabatic shear band, T_i is initial temperature, C_v is heat capacity and β is a constant, which, for adiabatic processes, is taken as 0.9 (90% of the energy converted to heat). For titanium C_v= 528 J/kg/K, T_i = 293 K and kinetic energy dissipated = 2 ×10^8 J/m^3, then the temperature rise at the adiabatic shear band is only ~100 K.

	Material types (with references for data)			
Johnson-Cook parameters	Titanium [39]	Carbon steel [39]	Armco iron [52]	Stainless steel, 304 [192]
A, MPa	806.57	532.0	175	110
B, MPa	481.61	229.0	380	1500
n	0.319	0.3024	0.32	0.36
C	0.0194	0.0274	0.06	0.014
m	0.655	1.0	0.55	1
T_{melt}, K	1923	1793	1811	1694
T_{trans}, K	298	283	298	298
Ref strain rate, /s	1	1	1	10^3

Table 4-11 Johnson-Cook materials properties of titanium, carbon steel, Armco iron and stainless steel

Table 4-11 shows the Johnson-Cook parameters for titanium, carbon steel, Armco iron, and austenitic stainless steel collected from the literature. Figure 4-30 illustrates the flow stress of these materials at strain rate of 10^7 /s at 373 K. In comparison to titanium, carbon steel and Armco iron, the flow stress of the austenitic stainless steel rises sharply with increasing plastic strain. The strain hardening parameter (B) for austenitic stainless steel is very high compared to those of titanium, carbon steel and Armco iron (Table 4-11). Figure 4-30 shows the stress- strain curve of titanium is above the stress-strain curve of carbon steel and Armco iron. This implies that upon impact of titanium onto carbon steel or Armco iron, the deformation will predominantly take place in the substrate material. In contrast, the stress-stain curves (under these high strain rate, high

temperature conditions) for the austenitic stainless steel and titanium cross each other at a plastic strain of around 0.55. As such, the relative deformation behaviour of the titanium particles and the austenitic stainless steel substrate will vary as a function of plastic strain. At plastic strain strains of less than 0.55, the deformation will predominantly take place in the austenitic stainless steel and above that value, the deformation will predominantly take place in titanium.

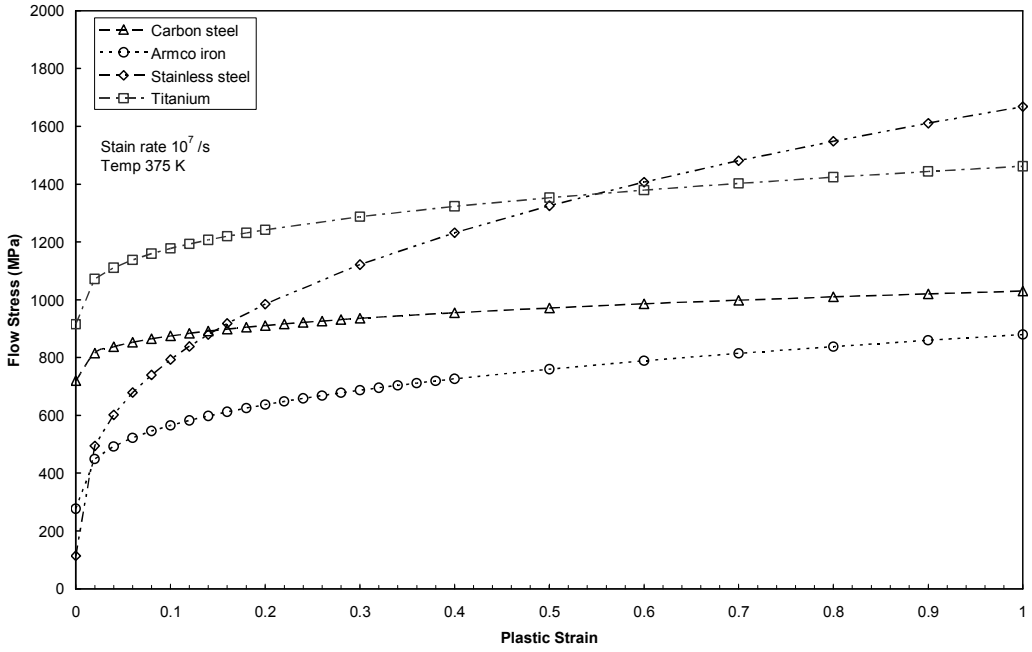

Figure 4-30 Flow stress of titanium, carbon steel, Armco iron and austenitic stainless steel as a function of plastic strains at strain rate 10^7 /s and 375K according to the J-C model with data from Table 4-11

The area under the flow stress and plastic strain curve represents the plastic energy density involved in the deformation. If there is no loss of energy during the high strain rate deformation process, then the 2×10^8 J /m^3 of kinetic energy per particle will result in an equivalent plastic strain of 0.23 in carbon steel, 0.34 in Armco iron and 0.25 in austenitic stainless steel. The area under the curves was calculated using trapezoidal rule. It is interesting to note that Armco iron is expected to exhibit a plastic strain of ~1.5 times than that of carbon steel.

Experimental evidence from the impact of titanium particle onto Armco iron also shows a greater degree of deformation of the Armco iron substrate compared to low carbon steel substrate (Figure 4-22 d, e).

4.6.3.3 Metal-to-Metal bond formation upon impact

In this current investigation, no intermediate phases formed at the titanium-low carbon steel and titanium-Armco iron interfaces following heat treatment at 750 °C. According to the Ti-Fe equilibrium phase diagram, several intermetallic phases (TiFe, $TiFe_2$) exist at 750 °C. Titanium has a tenacious TiO_2 layer of a couple of nanometres thick surrounding the particles at room temperature [193] and iron oxidised at room temperature will form a two layered scale of Fe_2O_3 and Fe_3O_4 on its surface [194-196]. An intermediate phase layer will only form at the interface following heat treatment, when both the titanium and iron can diffuse without the oxide barriers between them. In the impact of a titanium particle with a low carbon steel substrate discussed in section 4.6.3.2, it was argued that the deformation will be localized at the low carbon substrate. The Armco iron substrate deformed to a greater extent following deposition of titanium; despite this high degree of substrate deformation, no intermediate phases were formed at the titanium-Armco iron interface following heat treatment. Here, the titanium particle was deformed very little. In a similar manner, Kim et al. [197] examined warm-spraying of titanium particles onto an aluminium substrate and showed that although the aluminium substrate was heavily deformed upon impact of titanium particles, the oxide that originally existed on the titanium particle was not removed while the oxide on the aluminium substrate was removed by the shear instability phenomena producing the material jet. A similar phenomenon can be operating in cold spraying of titanium onto a softer substrate like Armco iron.

The heat treatment of the titanium-austenitic steel resulted in two distinctive layers of intermediate phases. Both the phases grew to a thickness of couple of microns at the titanium side. It has been reported that titanium diffuses only a small distance into the 304 stainless steel compared to the diffusion of iron, chromium and nickel into the titanium [198]. EDX analysis of the phases on the titanium side, which grew to thicknesses of 3-4 μm, suggests that it is β-titanium with iron, chromium and nickel in solid solution (Figure 4-23d). The phase in between this β-titanium and steel substrate is less than a micron thick and EDX analysis suggests this is possibly the TiFe intermetallic phase.

It is well known that titanium oxide films will dissolve into titanium upon heat treatment at elevated temperatures due to the high solubility of oxygen in titanium [102]. The oxide film thickness on the titanium particles has been estimated from the bulk measurements of the oxygen content in the powder (0.14 wt.%); making the assumption that all of this oxygen is in the form of a surface oxide. This calculation indicates that an oxide thickness of around ~20 nm may be expected. Takahashi et al. [102] have shown that at the annealing temperatures used in this work (750 °C) an oxide film of this thickness will be expected to dissolve in less than 100 seconds.

From the experiments, it is clear that in the case of the stainless steel substrate, intermetallics were able to form between this and the deposited titanium particles. However, with the Armco iron and the low carbon steel substrates, intermetallics did not form, contrary to expectations based on Takahashi's analysis [102]. Consequently, whilst the nature of the barrier between the impacting titanium particle and the low carbon steel or Armco iron substrates is not firmly established, it is evident that such a barrier does indeed exist which is not removed during either deposition or the post-deposition heat treatment

process. In contrast, in the case of the stainless steel/ Ti particle interfaces, the barrier is removed either during impact or during heat treatment. It can thus be concluded that metal-to-metal contact was not achieved in the case of low carbon steel or Armco iron. In the case of stainless steel, however, a definitive judgement cannot be made about the reasons for intimate metal-to-metal contact as revealed by intermetallic formation following annealing at 750 °C.

4.6.3.3.1 Effect of particle shape on metal-to-metal bond formation

Angular titanium particles which adhered to the stainless steel substrate showed localized deformation of the substrate (Figure 4-24b). In contrast, there are no such localized deformation features following impact of spherical particles onto stainless steel (Figure 4-22f, Figure 4-25b), with the deformation of the substrate being more or less uniform across the entire region where the particle is attached to the substrate. It is notable that following impact of the angular titanium, the intermediate phases were not necessarily formed in the regions where the substrate deformation was maximum. It might have been expected that impact of angular particles (with the associated regions of high contact stresses) would have resulted in more efficient removal of surface oxide layers and thus to better bonding; however, in making this direct comparison, it must be noted that the particle size distribution of the angular feedstock was much larger than that of the spherical feedstock which may have resulted in lower impact velocities; it may thus be the impact velocity rather than the particle shape which has the greatest influence on bond formation.

4.6.3.3.2 Effect of gas accelerant characteristics on metal-to-metal bond formation

The impact velocity of the particles is a critical parameter for cold-spray particle deposition, since only the particles which travel at or above the threshold velocity (known as the critical velocity) will contribute to coating buildup. The spherical

titanium particles sprayed onto stainless steel using room temperature helium were significantly less deformed (Figure 4-22f) than the particles sprayed using heated nitrogen gas (Figure 4-25b). Following heat treatment, the coverage of intermediate phases at the particle-substrate interface of the hot nitrogen gas sprayed particles was almost complete (Figure 4-25c) in contrast to the contact between the room-temperature helium sprayed particle and substrate, where a significant fraction of the interface exhibited no intermediate phase formation (Figure 4-23c).

Heating of a gas stream is known to generally increase particle impact velocities in cold-spraying and to increase the temperature of both the particles and the substrate. In this case, given that different cold-spray systems were employed and that different accelerant gases were used for the heated and room temperature spraying, no definitive statements can be made regarding the expected differences in particle velocities in the two cases. However, it is clear that the bonding in the particles sprayed with heated nitrogen (a low cost accelerating gas) is more efficient than that resulting from the deposition with room-temperature helium (a high cost accelerating gas).

Whilst the differences in velocity in the two cases are not clear, it is known that the particles and substrate will be at higher temperatures when sprayed with heated nitrogen. This will change the flow stress of both particle and substrate which will enhance the deformation of the contact; Bae et al. [38] reported that plastic dissipation energy upon impact increases with increasing particle temperature and the elastic recovery energy decreases.

4.7 Summary

The bonding mechanisms operating in cold spraying of copper coating onto aluminium alloy substrate have been investigated experimentally as a function of

the different surface preparation procedures for the substrate, namely polished, ground and grit- blasted substrate surfaces. In addition, some substrates were annealed following surface preparation to allow a separation of the effects of work hardening during preparation from those of changes in surface morphology. The bonding mechanisms operating in aluminium coating onto copper substrate has also been investigated experimentally and compared to the copper coating-aluminium substrate system. Moreover, the impact and bonding mechanisms operating in cold spraying of titanium particles onto three steel substrates was also investigated. The findings of this study are summarized here:

- A bonding mechanism has been proposed to explain the observations which utilizes two mechanisms of bonding, namely that of metallurgical bonding between the substrate and the coating and that of material extruded from the substrate during impact of the particles which is then interlocked within the coating structure (termed interlocked material). The contributions of these two mechanisms to the observed bond strength is rationalised in terms of a modified composite theory.
- The efficiency of metallurgical bonding was assessed via a relatively new intermetallic growth method. In copper coating-aluminium substrate, when the efficiency of metallurgical bonding was low, the coating-substrate adhesive strength was controlled by the strength of the interlocked material. Simple calculations based upon the area fraction of interlocked material at the interface along with the strength of that material show a good correlation with the observed bond strengths in these cases. However, when the efficiency of the metallurgical bonding was increased (when spraying aluminium onto a polished and annealed aluminium alloy substrate), the strength was then dictated by the metallurgically bonded material.

- Coating-substrate adhesion following spraying onto a grit-blasted aluminium surface (whether or not the effects of work hardening had been removed by annealing or not) was significantly reduced by grit embedment into the aluminium surface during blasting. It is postulated that the grit-blasted surface also restricted the jet formation upon impact of the copper particles which resulted in less successful removal of oxide from the interface and hence a weaker metallurgical bond. Also, the increased strength of the particulate strengthened substrate material resisted formation of interlocked material between the coating and substrate, and thus again resulted in a reduction in observed bond strength.
- The bond strengths of aluminium coatings onto copper substrate were lower than those of copper coating onto aluminium substrate. There was no evidence of substrate material interlocking within the aluminium coating because of a lower momentum of the particles and a lack of formation of substrate jets. Also, a lower fraction of the intermetallic formation at the interface indicates the efficiency of the metallurgical bonding was low.
- There exists a barrier to metal-to-metal contact at the interface of the titanium powder deposited onto the low carbon steel and Armco iron substrates which is not removed by the deposition or the consequent heat treatment process. The suggested reason for this is that the mechanical properties of the low carbon steel and Armco iron at high strain rates result in localized deformation of only the substrates.
- When titanium is deposited onto austenitic stainless steel substrates, the barrier is removed either during impact or possibly during heat treatment and thus intimate metal-to-metal contact at the interface is established for this material system. This efficient removal of the barrier could be associated with significant plastic deformation taking place in both the

particle and the substrate as revealed by analysis of the Johnson-Cook equations for these materials. However, the possibility of TiO_2 dissolution at high temperature cannot be discounted.

- When compared to spherical titanium powder, angular titanium particles create more localized surface deformation of the austenitic stainless steel substrate. However, the regions of localized deformation do not, surprisingly, result in formation of intermetallic compounds following heat treatment.
- Spraying of spherical titanium particles with heated nitrogen resulted in a higher degree of deformation of the particle and substrate as compared to the use of room temperature helium gas. This higher particle-substrate deformation results in a near-continuous layer of intermetallic phase formation following heat treatment.

5 Process- structure characteristics of cold sprayed and post-spray processed titanium deposits

5.1 Introduction

As reported in the literature review there is considerable interest in the manufacture of cold sprayed titanium for a wide range of applications such as corrosion barrier layers, coatings on biomedical implants and in the manufacture of free– standing components by direct metal deposition (DMD). However, in order to realise these potential applications certain crucial problems have to be overcome. First, in the manufacture of coatings adequate bond strength has to be achieved, typically 60- 80 MPa would be a necessary value. Secondly, in the production of barrier layers or DMD components coating porosity has to be eliminated.

The aims and objectives of this chapter were as follows

- To investigate the role of processing conditions on coating characteristics.
- To study the role of substrate type and surface preparations on coating deposition.
- To measure the bond strengths and tensile strengths of the sprayed titanium deposits.
- To examine the effect of post-spray processing on the porosity of cold sprayed deposits.

This chapter is divided into three main sections. The first deals with the materials and experiments procedures, the second addresses the effect of cold spray processing conditions on coating/ deposit characteristics whilst the third examines the effect of post-spray processing specifically on the porosity of deposits.

5.2 Materials and experimental procedures

This section summarizes experimental procedures relevant specifically to the work described in this chapter.

5.2.1 Feedstock powder

Commercially pure inert gas atomized titanium powder from LPW, Cheshire, UK with a nominal size range of +10 -30 μm were employed. The oxygen and nitrogen contents of the powder was 0.14 and <0.01 wt. % respectively. The powder particles were largely spherical and free from internal porosity.

5.2.2 Substrates and surface preparation

Three different substrate types were employed namely low carbon steel (BS 970), type 304 stainless steel and Ti6Al4V. The chemical composition of low carbon steel and type 304 stainless steel are given in Chapter 4 Table 4-1. The chemical composition (wt.%) of Ti6Al4V was 6.54 % Al, 4.13 % V, 0.02 % Si, 0.01 Mn, 0.03 Mo, 0.05 Fe, 0.04 Nb and balance Ti. The microhardness values of low carbon steel and type 304 stainless steel are given in Chapter 4 Table 4-10. Ti6Al4V had a hardness value of 387 ± 7 kgf/ mm^2. Substrates were normally 40 ×25 ×2 mm except for pull–off bond strength tests which had a diameter of 1 inch and were performed according to ASTM C633.

Initially, surface preparation involved conventional cabinet grit blasting (0.275 MPa with a Al_2O_3 grit size ~125 μm). However, modified grit blasting was also

investigated as a means of improving bond strength. The modified grit blasting, termed in-situ, involved using 45-90 μm Al_2O_3 grit fed through the cold spray system with the following parameters:

Parameters	In-situ grit blasting using rotary table
Gas pressure, MPa	2.5
Gas temperature, °C	400
Gas flow rate, m^3/h	60
Powder feed wheel, rpm	2
Carrier gas flow rate, m^3/h	5.5

Table 5-1 Process parameters of in-situ grit blasting using cold spraying gun

The samples were mounted on a rotary table travelling at 32 rpm and the robot mounted gun travelled in a vertical direction at 0.8 mm/s. The standoff distance was 30 mm and only 1 pass of the gun was used. The in-situ surface preparation was employed for all pull-off and tubular coating tensile tests except for Ti6Al4V which had a machined surface finish. Prior to spraying all substrates were cleaned ultrasonically in a bath of acetone for 15 minutes, rinsed with methanol and dried using compressed air immediately prior to spraying.

5.2.3 Cold spray parameters

Two nitrogen process gas temperatures were employed namely 600 and 800 °C. Powder was fed from a CGT powder feeder with a nitrogen carrier gas flow rate of 3.7 m^3/h and a powder wheel speed of 3.5 rpm (140 mm φ wheel) giving an approximate feed rate of 1.6 kg/ hr. The nozzle-substrate standoff distance for all the spray conditions was fixed at 40 mm. Spray parameters were as follows

Spray parameters	600 °C coatings	800 °C coatings
Gas pressure, MPa	4	4
Gas temperature, °C	600	800
Gas flow rate, m^3/h	86	80

Table 5-2 Process parameters of cold spraying of titanium at 600 and 800°C onto cabinet grit blasted samples

Cabinet grit blasted samples were held in a clamp and sprayed onto with the gun traversed at 600 mm/s across the face of the samples. A vertical scan increment of 0.75 mm with 4 complete gun passes over the entire surface was used.

However in later trials, the in-situ grit blasted carbon steel and stainless steel samples were sprayed onto only at 800 °C process gas temperature using a rotary table. The samples were held onto the sample holders of the rotating table while the cold spray gun mounted on the robot traversed along the vertical direction. The rpm of the rotation table was 35 (circumferential velocity 666 mm/s) and the vertical velocity of the gun was 0.44 mm/s. The remainder of the parameters were the same as the spraying conditions for the stationary substrate sprayed at 800 °C in Table 5-2**.** In addition, the same spraying parameters were used for pull-off bond strength test samples except the number of passes was limited to only two instead of four to achieve a coating thickness of only ~380 µm.

Tubular coating tensile test (TCT) samples was sprayed using a lathe. The samples were clamped in a lathe chuck rotating at 500 rpm (circumferential velocity 666 mm/s) and the horizontal velocity of the spraying gun was 6.23

mm/s. The rest of the spraying parameters were the same as 800 °C coating in Table 5-2**.** The coatings were built up using four passes to a thickness of ~890 µm.

Results

5.3 Characterization of feedstock powder

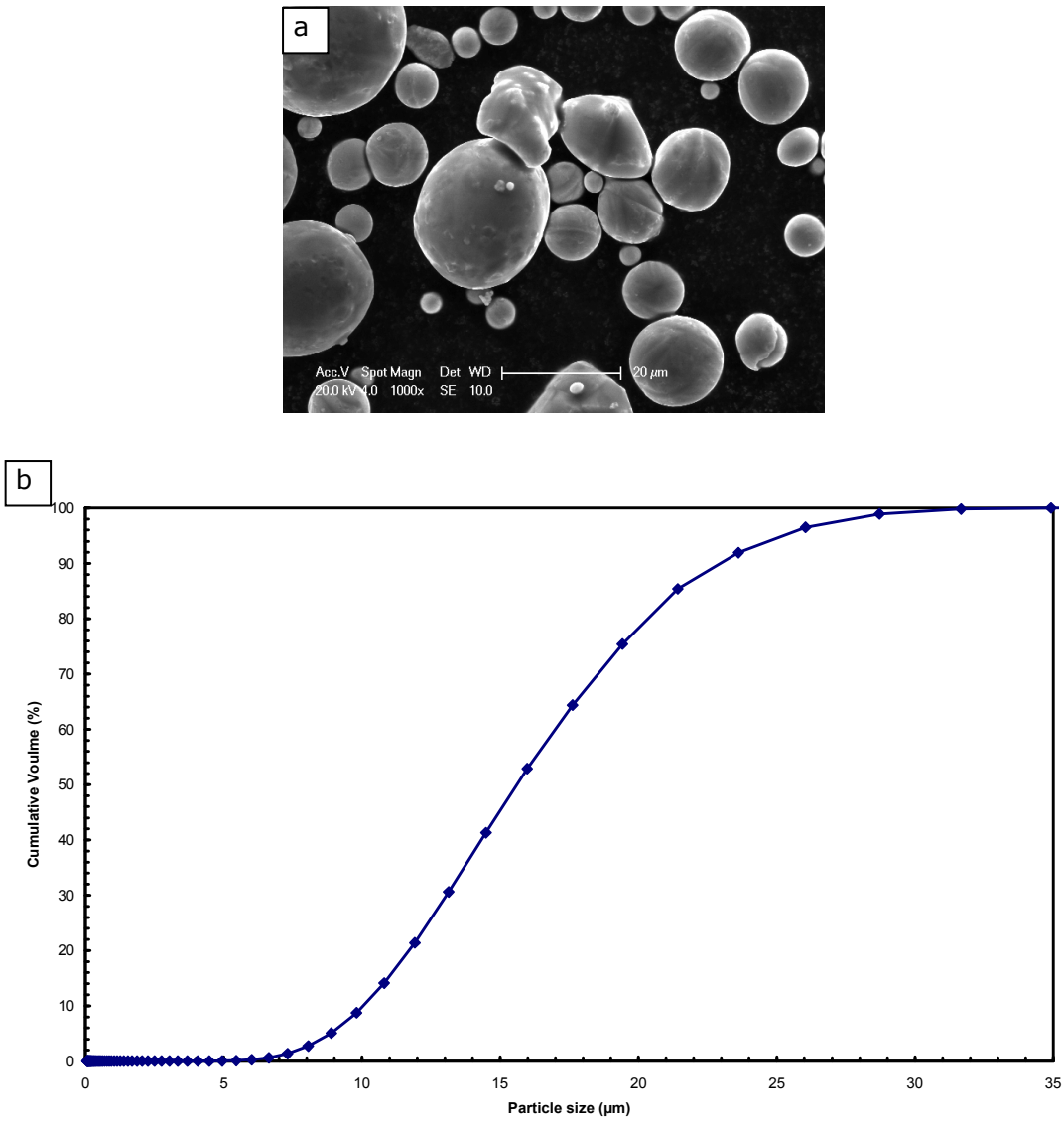

Figure 5-1 (a) SEM image of gas atomized titanium feedstock powder showing its near-spherical morphology. (b) Cumulative size distribution of the powder measured by laser diffractrometry

Low magnification view of the powder showing its morphology and powder size measurements using Malvern Mastersizer are reported in Figure 5-1. The feedstock powder was spherical in shape with only a very small fraction exhibiting satellite particles and the powder had a nominal size range of +10 -30 μm with approximately 10 vol. % below 10 μm. The SEM image of the cross section of an un-etched powder particle is shown in Figure 5-2 (a) and Figure 5-2 (b) shows the cross-section of the powder after etching. There is no porosity visible in the un-etched powder and the etched powder particle shows an acicular structure (martensitic) as a result of the rapid cooling in the gas atomization process [139].

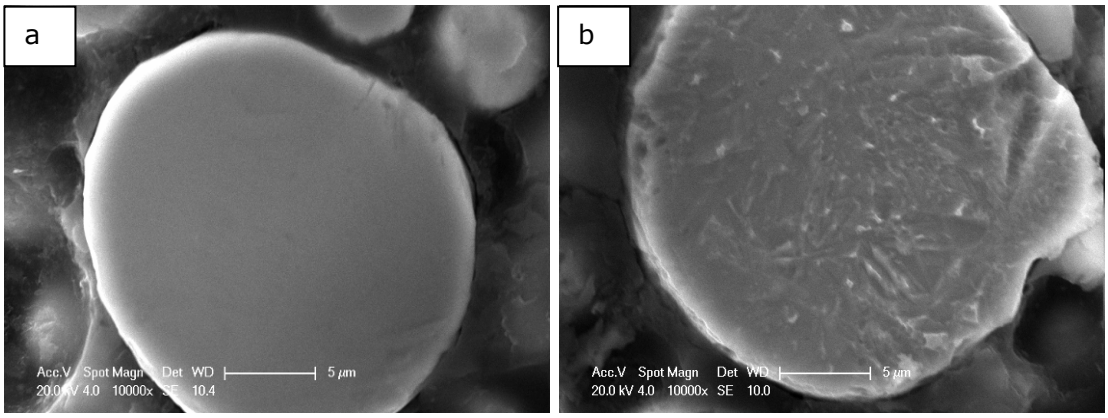

Figure 5-2 SEM images showing (a) un-etched cross section of the powder (c) etched cross section of the powder showing acicular microstructure

5.4 Effect of processing conditions on coating characteristics

5.4.1 Effect of process gas temperature on microstructure and microhardness

These experiments were performed only on cabinet grit blasted type 304 stainless steel substrate. First, it was confirmed, using XRD that process gas temperature did not have a detectable effect on phase formation. At both temperatures only α-

titanium was found in the coating. Figure 5-3 shows XRD pattern of the original powder and coatings sprayed with the two different gas temperatures. Oxide phases were not detected in any of the samples. Peak height ratios of the coating differ somewhat for the powder – especially the 100, 002 and 101 peaks, which indicates that a preferred texture developed in the coating. Also line broadening is apparent in the two coatings samples which are due to a combination of microstrain and sub-micron coherent diffracting domain size.

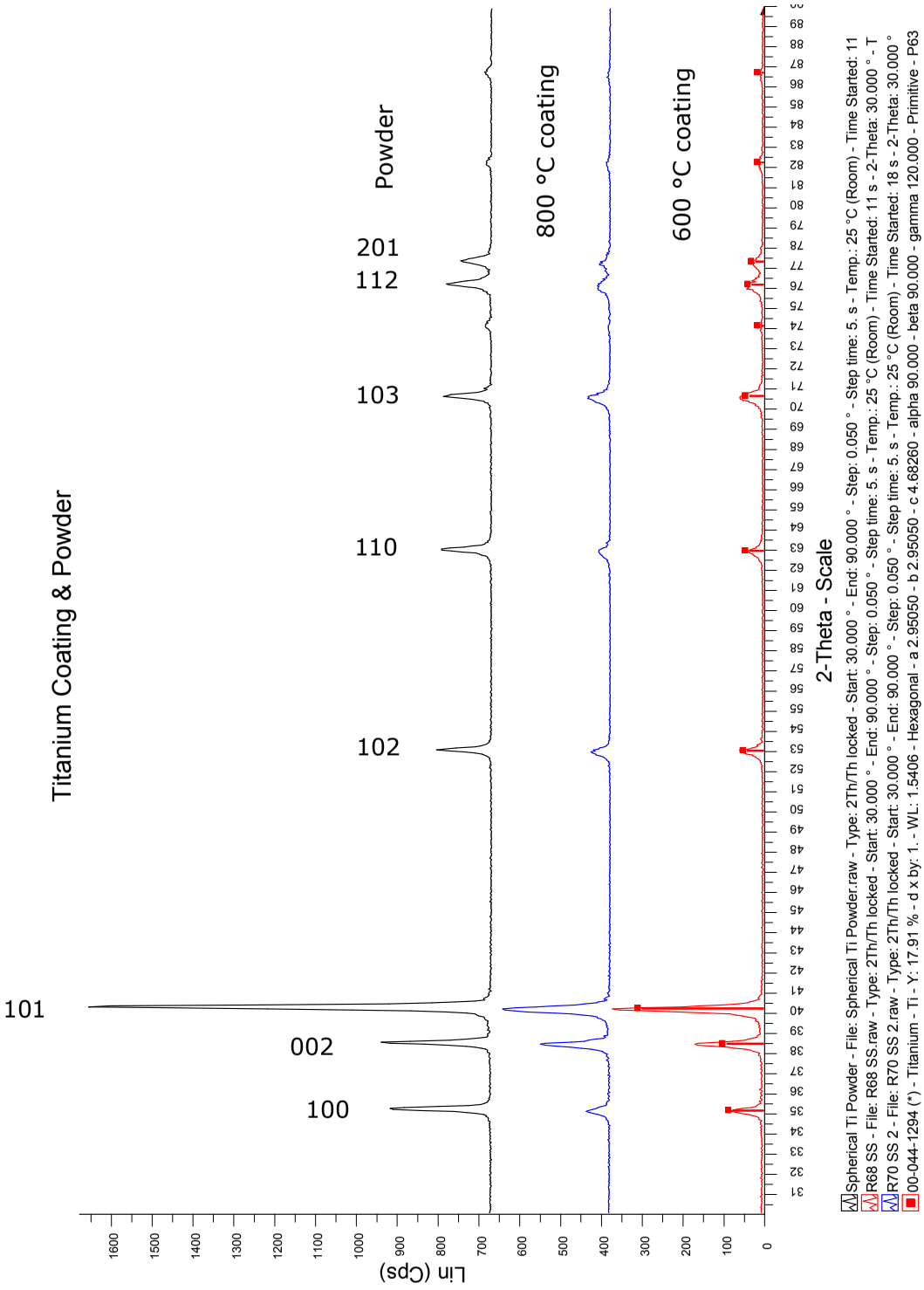

Figure 5-3 XRD profiles of titanium powder, coatings sprayed at 600 and 800°C process gas temperatures

Process gas temperature did, however, have a very significant effect on the macro features of the coating as seen from the optical micrograph montages of

Figure 5-4. The approximate boundaries of the four passes are marked. The most significant feature is the top porous layer in the coating sprayed at 600 °C which is much reduced in the 800 °C coating. It is clear that despite having the same number of passes the 800 °C coating has a thickness of only 900 μm compared to 1400 μm for the 600 °C coating. This difference in coating thickness is due to irregularities in powder feeding, although the nominal powder feed rate and gun traverse speed in both cases were the same. There are also significant differences in the microstructure following etching in Kroll's reagent for 15 seconds as shown in Figure 5-5. The etch is known to attack the grain boundaries or particle boundaries so the features seen in Figure 5-5 are probably due to chemical removal of particles by the etching process. It is significant that there are many more near circular features seen in the coating sprayed at 600 °C than that sprayed at 800 °C (see circular areas) suggesting a greater degree of particle deformation in the latter.

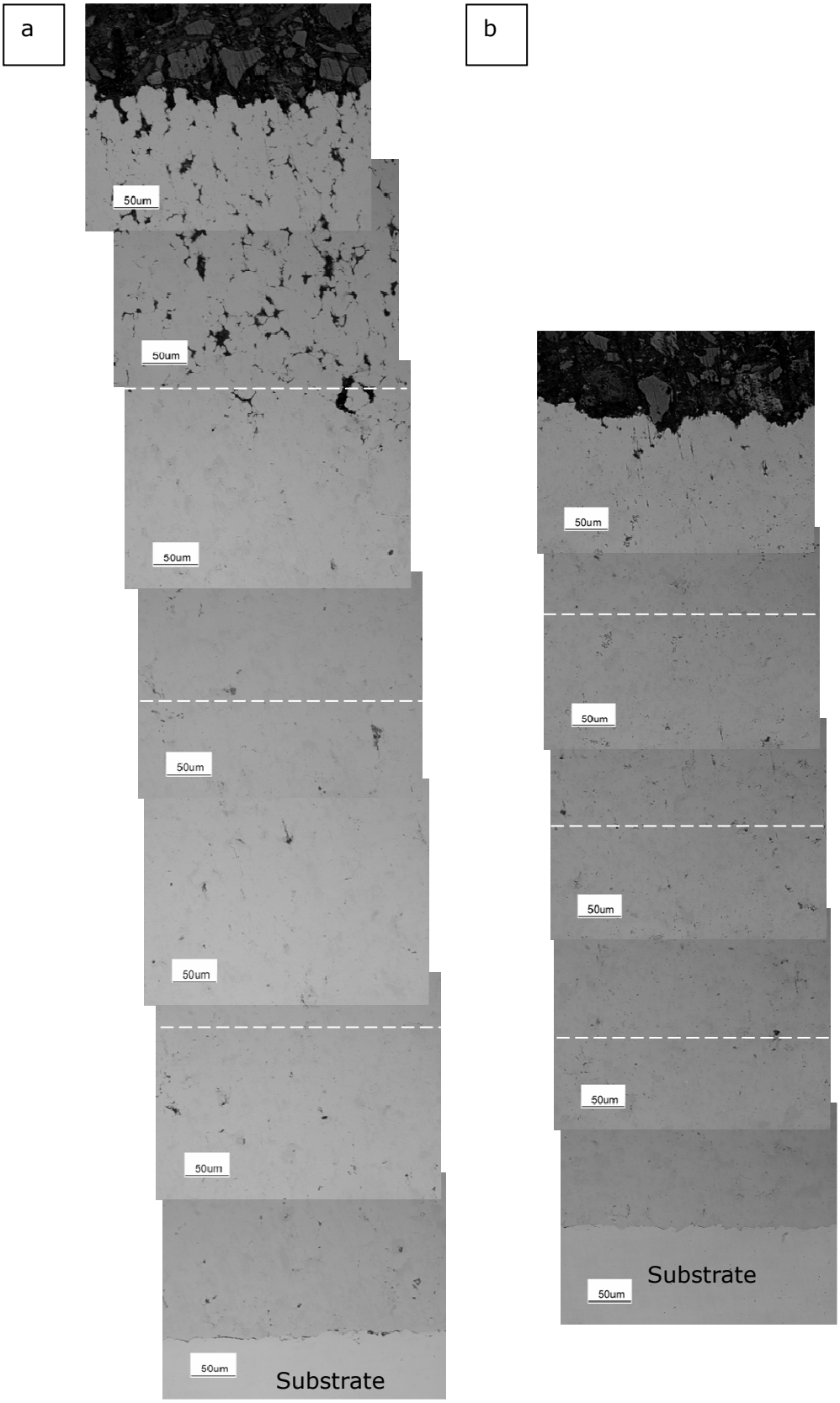

Figure 5-4 OM images of un-etched titanium coatings onto stainless steel substrates at process gas temperatures of (a) 600 & (b) 800˚C. Broken lines indicate the approximate locations of the inter-pass boundaries.

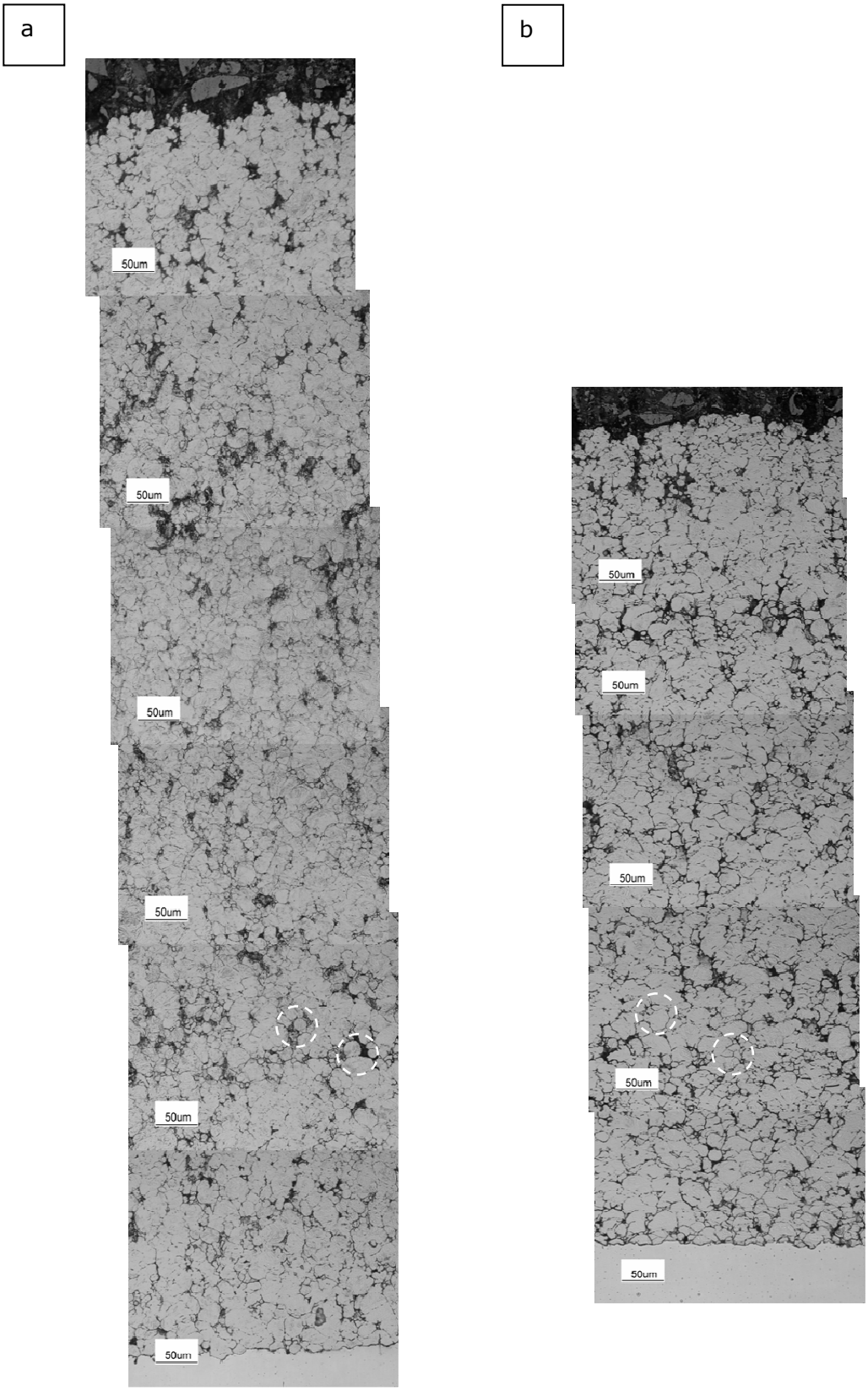

Figure 5-5 OM images of etched (15 s in Kroll's solution) titanium coatings sprayed at (c) 600 & (d) 800°C

The progressive etching effect of Kroll's reagent was extended up to an etching time of 50 seconds and the results for the coatings sprayed at 600 and 800°C are shown in Figure 5-6. Here it is even more apparent that a higher proportion of near-circular particle sections are visible in the coating sprayed at 600 °C, which underwent decreased deformation.

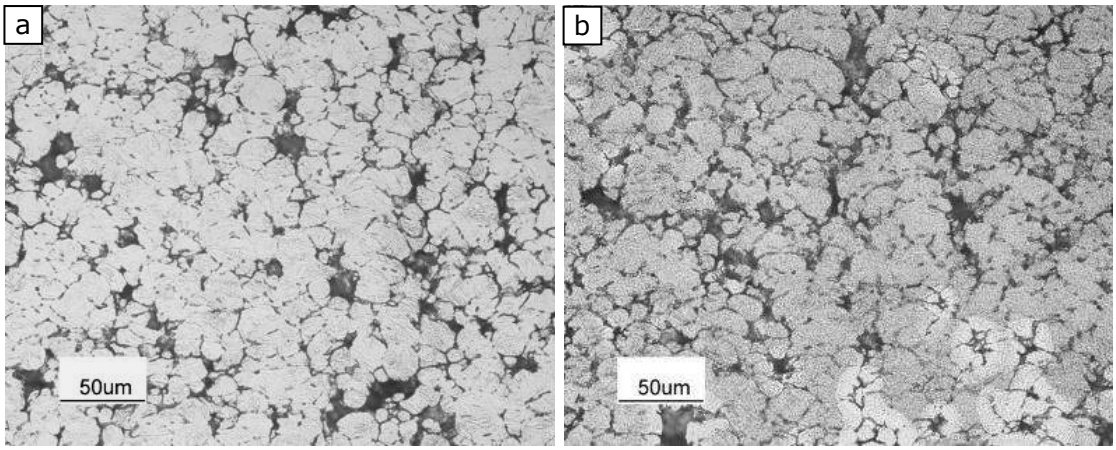

Figure 5-6 Cross section of (a) 600 & (b) 800 °C coatings etched in Kroll's agent for a duration of 50 seconds

As well as there being a variation in microstructure through the coating thickness there was also a variation in microhardness. Hardness of the coatings deposited at process gas conditions of 600 and 800 °C are shown in Table 5-3 with standard error of mean. In both coatings, the bottom layer (1st pass) is the hardest of all layers and the hardness value decreases from the bottom of the coating to the top. This high microhardness of the bottom layer of titanium coating prepared from gas atomized spherical powder was previously reported by other researchers [112, 199]. The particles at the bottom of the coating possibly went through a greater degree of plastic deformation because of incoming particles. It is noticeable that the top layer (4th pass) of the 600 °C coating has a hardness value similar to a piece of rolled commercially pure bulk titanium sheet (145 HV). One of the key factors which influence the microhardness of the coatings is porosity. Porosity within the coating leads to a reduction in microhardness values.

In all four layers, hardness of the coating sprayed at 800 °C showed higher hardness values compared to the coating sprayed at 600 °C. Moreover, the microhardness value of the bottom layer (1st pass) of the 800 °C coating was 281 HV, which is approximately twice the hardness of cp titanium sheet.

Coating	No of passes of the gun	Hardness $HV_{0.1}$
600°C coating	4th layer (top)	145 ± 8
	3rd layer	183 ± 13
	2nd layer	184 ± 11
	1st layer (bottom)	217 ± 12
800°C coating	4th layer (top)	239 ± 9
	3rd layer	240 ± 13
	2nd layer	209 ± 7
	1st layer (bottom)	281 ± 2

Table 5-3 Microhardness values with standard error of mean measured on the polished cross-section of the coatings sprayed at 600 and 800°C temperatures

5.4.2 Effect of process gas temperature on surface morphology

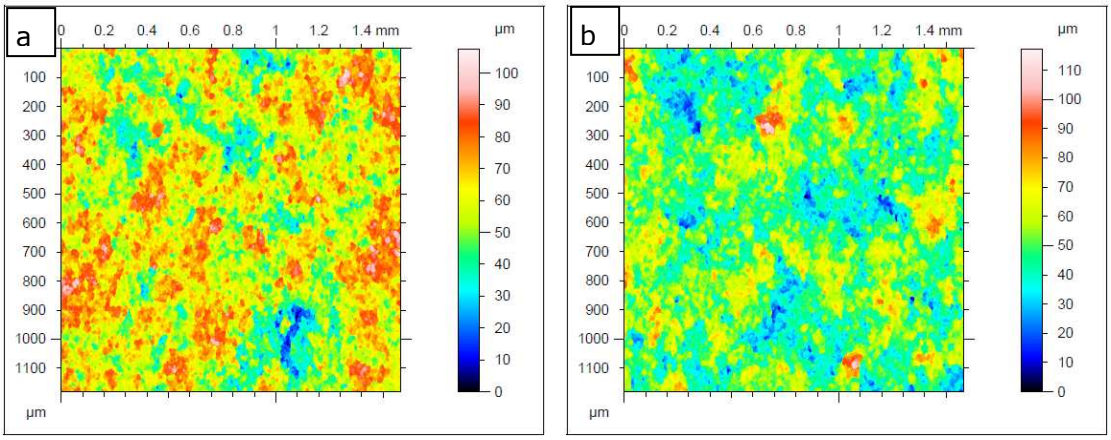

Figure 5-7 Topography of titanium coatings using surface profilometry: (a) 600 & (b) 800°C

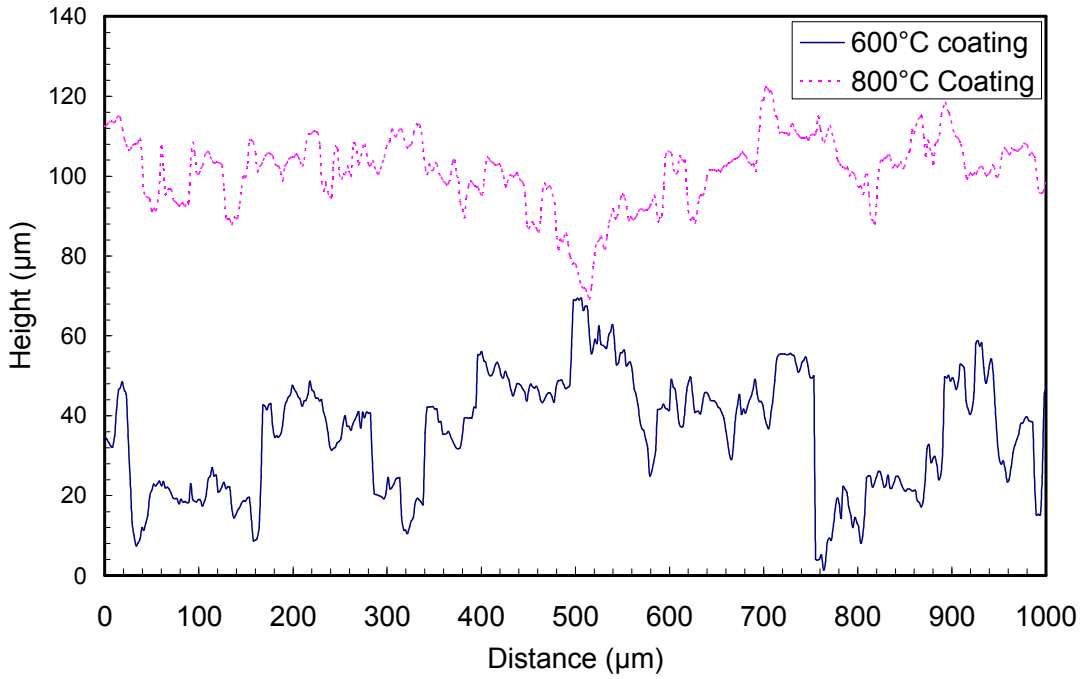

Figure 5-8 Typical line profiles extracted from the top surface of 600 and 800°C coatings

Figure 5-7 shows the topography of the 600 and 800 °C coatings measured using surface profilometry. It can be seen that 600 °C coating top surface shows scattered regions of high surface roughness (red in colour), whilst those regions are noticeably less in 800 °C coating. Typical line profiles extracted from the top surface of 600 and 800 °C coatings are shown in Figure 5-8. Typical peak-trough height of the former was ~70 µm, whereas peak-trough height of the latter was ~50 µm with surface roughness (Ra) values of 7.9 µm and 4.1 µm for the 600 and 800 °C coatings respectively. The surface roughness of the substrates, onto which the coatings were deposited, was 1.6 µm.

SEM backscattered micrographs of 600 and 800 °C coatings onto stainless steel are shown in Figure 5-9 (a, b). The top porous layer is marked with a dotted line in Figure 5-9 (a). The coating-substrate boundary does not show any cracks or de-lamination. Higher magnification SEM images of the top porous layer are

shown in Figure 5-9 (b, c). The image shows presence of interparticle pores due to insufficient deformation of the particles in the 600°C coating. However, the fraction of porosity in the top layer of 800°C coating has reduced significantly.

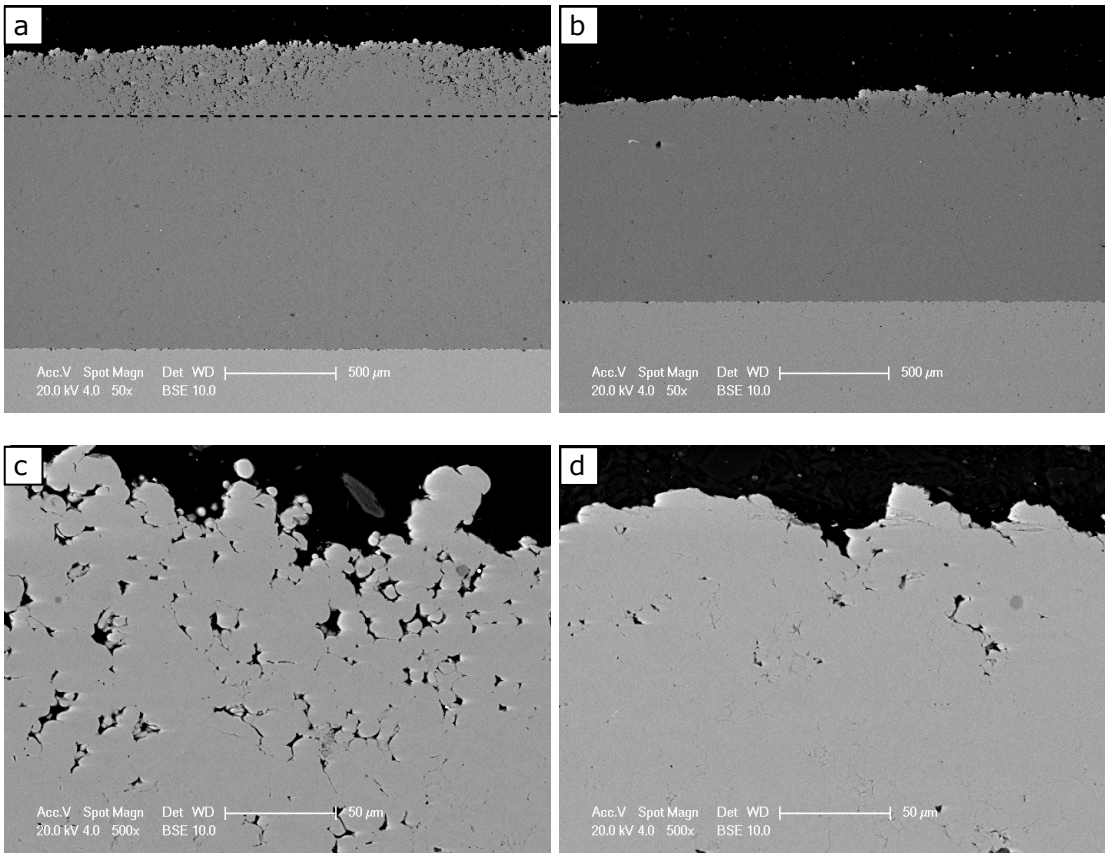

Figure 5-9 Lower magnification BSE images of coatings sprayed at (a) 600 & (b) 800°C. Higher magnification BSE images of coating top layer sprayed at (c) 600 & (d) 800°C

Figure 5-10 shows the top surface view of coatings sprayed at 600 and 800 °C. The top surface of 600 °C coating appears to show a higher surface roughness which corresponds to the top porous layer in the cross-sectional image in Figure 5-9 (a). Figure 5-10 (c, d) shows higher magnification images of 600 and 800 °C coatings. The 600 °C coating shows smaller titanium particles deposited onto larger titanium particles, and in some places larger particles show craters and evidence of sliding and rebounding after impact. Rupture of some interparticle bonds is also observed in the image, marked with a box in the Figure 5-10 (c).

Figure 5-10 (d) in contrast, shows the shear lips of titanium particles upon impact, marked with arrows, where the plastic flow of titanium occurred following presumably an adiabatic shear instability phenomena [38].

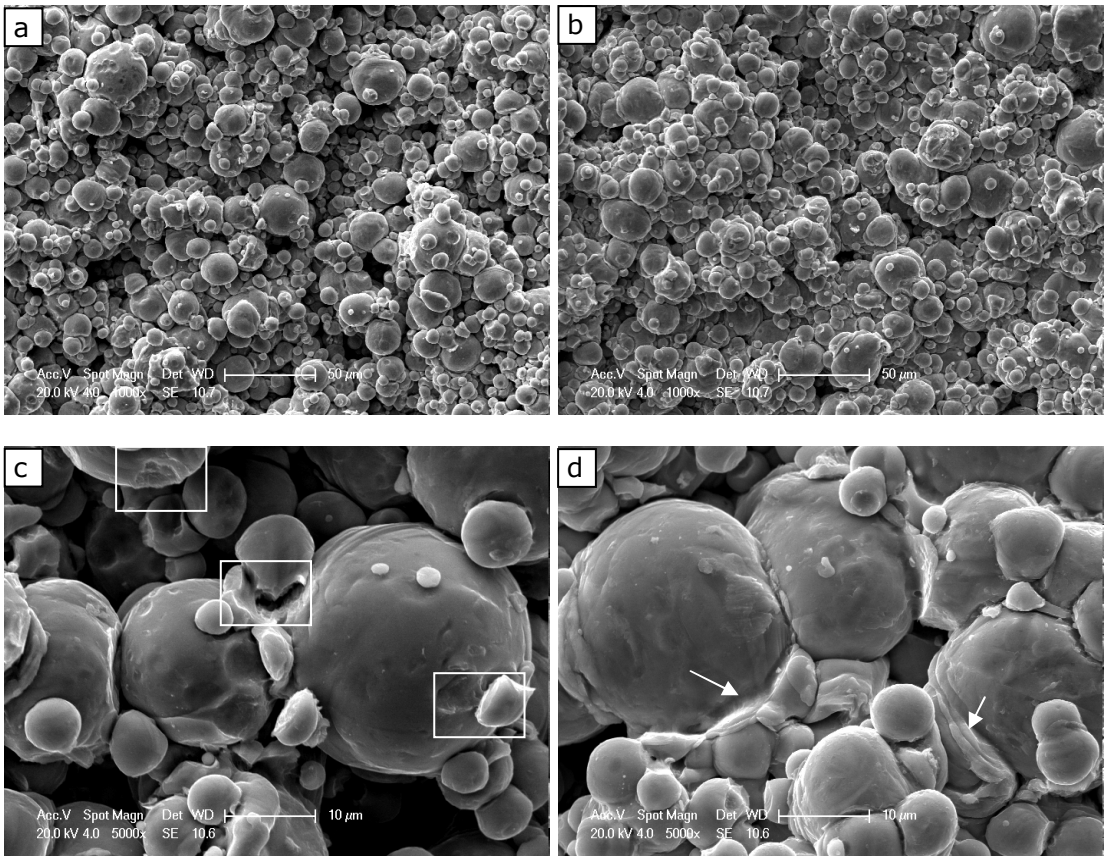

Figure 5-10 Lower magnification images of (a) 600 & (b) 800°C coatings. Higher magnification images of (c) 600 & (b) 800°C coatings. (boxed area showing rupture of bonds, arrows showing viscous flow of material)

5.4.3 Effect of substrate types and surface preparations on coating deposition

The deposition trials reported in section 5.4.1 (different process gas temperatures) were reported using grit blasted Ti6Al4V and type 304 stainless steel substrates. With the former similar effects were observed as with stainless steel- namely a top porous layer with 600 °gas but a more uniform coating with 800 °C gas. The thickness buildup was similar to that in stainless steel. In the case of carbon steel a similar thickness build up and top porous layer formed with

gas at 600 °C but when 800 °C gas was used debonding occurred after only two passes. This debonding suggested that the interfacial bond strength was low with conventional grit blasting and for this reason the alternative in-situ technique was investigated for both carbon steel and stainless steel. Using the surface preparation conditions listed in section 5.2.2 the surfaces of the substrates were examined by profilometry and SEM. Typical line profiles are shown in Figure 5-11 and Ra values are given in Table 5-4.

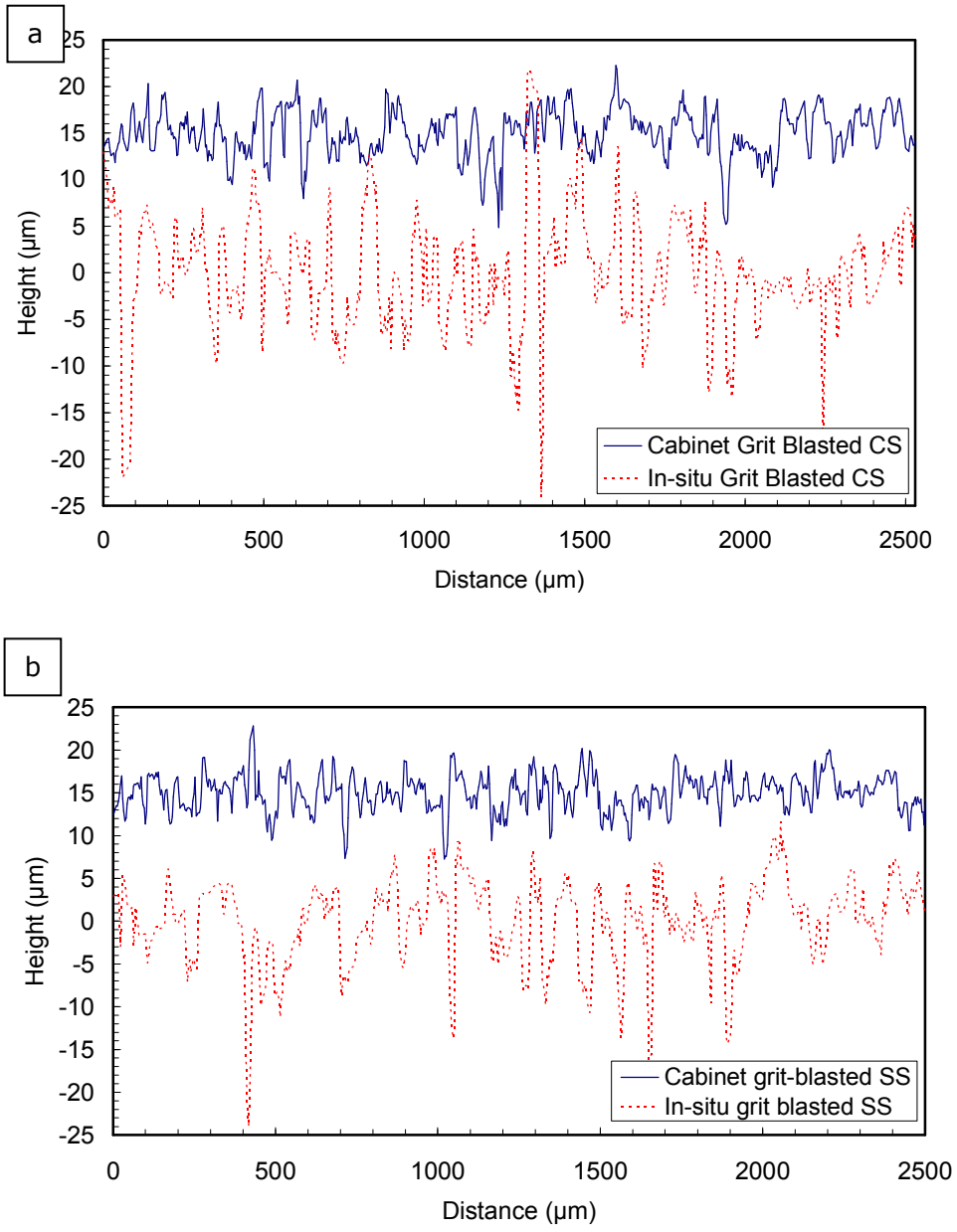

Figure 5-11 Typical line profiles extracted from conventional cabinet grit-blasted and in-situ grit blasted (a) carbon steel (b) stainless steel

Preparation method	Surface roughness, Ra (μm)
Cabinet grit blasted carbon steel	1.9
In-situ grit-blasted carbon steel	3.5
Cabinet grit-blasted stainless steel	1.6
In-situ grit-blasted stainless steel	2.8

Table 5-4 Surface roughness of the cabinet grit-blasted and in-situ grit blasted carbon steel and stainless steel

Clearly in-situ grit blasting significantly increases Ra with some very large peak-to-trough values. SEM images taken in both SE and BSE modes of the surfaces of carbon steel and stainless steel following conventional cabinet grit blasting and in-situ grit blasted methods are shown in Figure 5-12. Secondary electron image of the conventional cabinet grit-blasted surface (Figure 5-12a) shows shallow craters formed by the alumina. The surface of the in-situ grit blasted surface shows deep craters (marked with circles in Figure 5-12b) made by the alumina and also a large number of alumina grits present at the surface. BSE images of both the conventional grit blasted and in-situ grit blasted surface (Figure 5-12c, d) show alumina (darker in contrast), with its angular morphology at the prepared substrate surface. Looking at surface of the cabinet grit blasted surface, the fragmented alumina on the surface is noticed. It should be noted that the mean size of the alumina used in conventional grit blasting was ~129 μm and that of in-situ grit blasting was ~69 μm. The alumina on the in-situ grit blasted carbon steel surface are embedded which probably had a higher velocity than that of the cabinet grit blasting process. In the case of stainless steel (Figure 5-12e, f), the preparation methods had similar effect to carbon steel substrates. However, the BSE images of stainless steel surface (Figure 5-12g, h) show a lower amount of alumina embedment following the preparation methods, possibly due to high hardness of the stainless steel. Table 5-5 shows the fraction of alumina present at the surfaces prepared in both preparation methods. In both

carbon steel and stainless steel, the fraction of the surface covered by alumina which was prepared in-situ grit blasting method was over two times to the conventional cabinet blasting method.

Conventional cabinet grit-blasted surface

In-situ grit-blasted surface

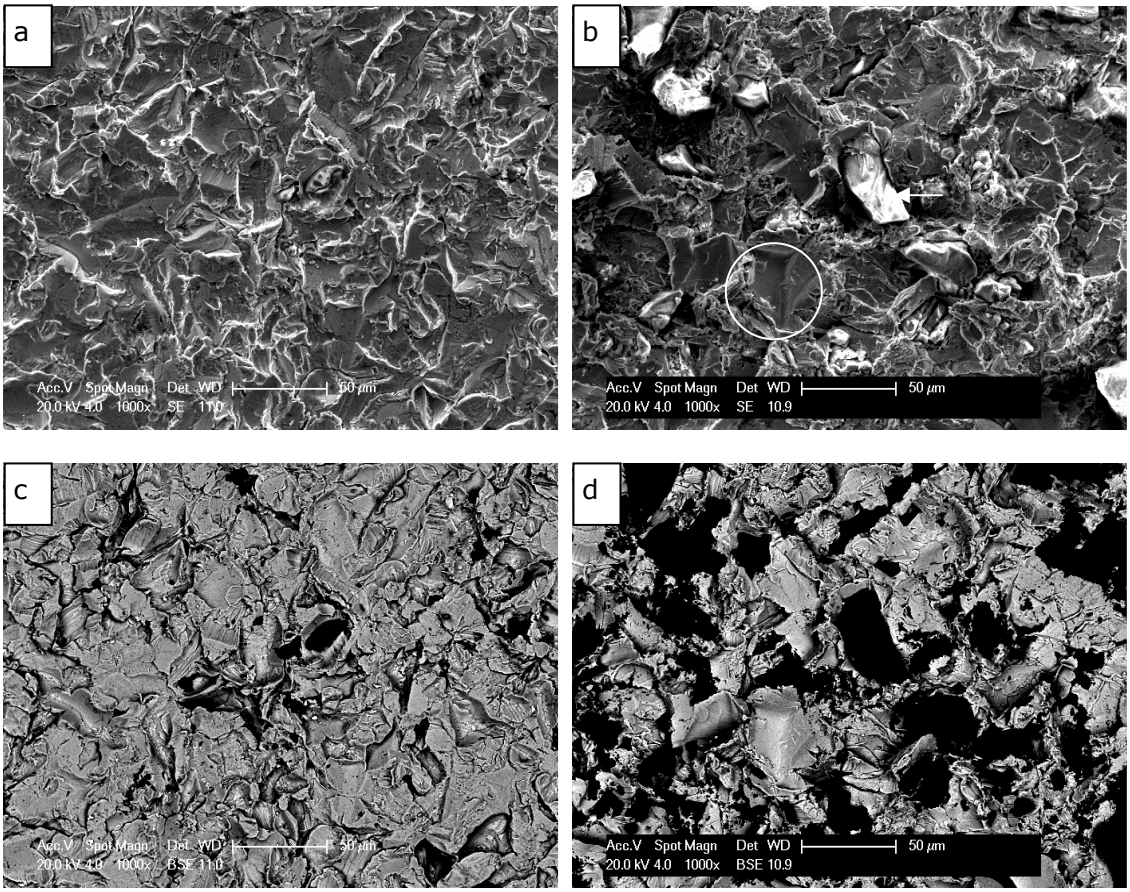

Carbon steel

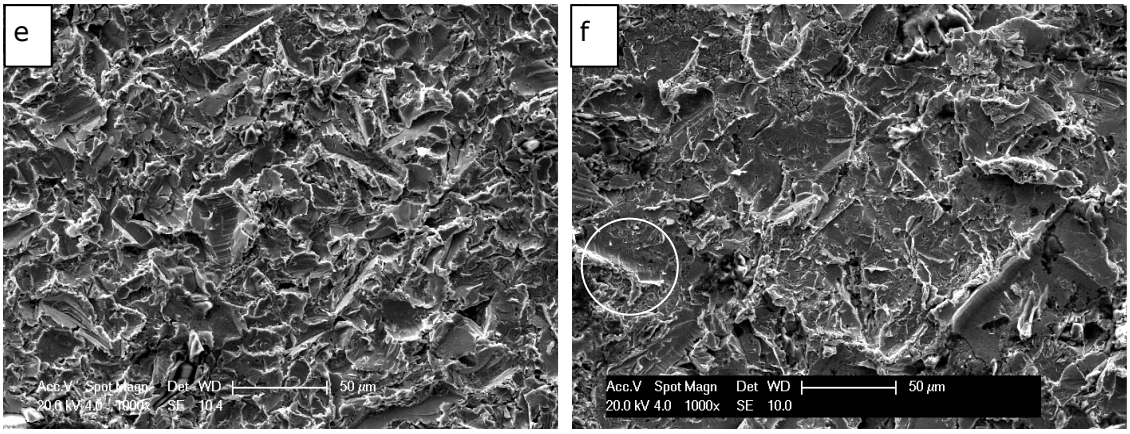

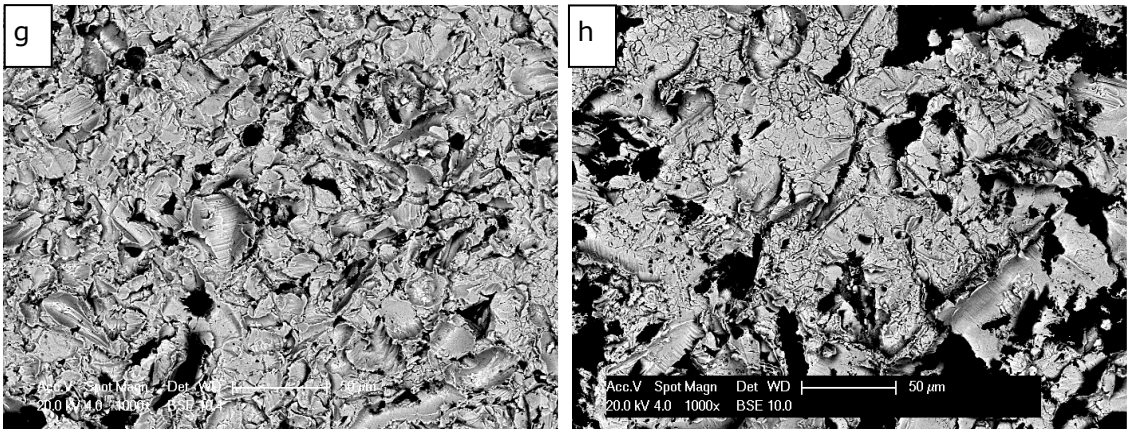

Stainless steel

Figure 5-12 SEM images of the top surfaces of carbon steel (a-d) and stainless steel (e-h) with different substrate surface preparations: cabinet grit blasted (a, c, e, g) and in-situ grit blasted (b, d, f, h)

	Cabinet grit blasted	**In-situ grit blasted**
Carbon steel	**0.15 ± 0.04**	**0.37 ± 0.02**
Stainless steel	**0.11 ± 0.01**	**0.25 ± 0.01**

Table 5-5 Microscopic analysis of the fraction of Al_2O_3 present on the substrate after grit blasting surface preparations (all measurements were taken on BSE images with a field size of 300 × 225 µm)

This change in surface preparation procedure enabled deposition of titanium using 4 passes at 800°C onto carbon steel. Figure 5-13 (a, b) show the BSE images of the cross section of the titanium coatings deposited onto in-situ grit blasted carbon steel and stainless steel. BSE images of the coating-substrate interface in Figure 5-13 (c, d) show a mechanical anchoring phenomena marked with circles. These mechanical features contributed to increase the mechanical component of the bonding mechanisms in cold spraying. Although the change in grit blasting procedure enabled mechanical anchoring, it also led to more embedded grit at the coating-substrate interface (dark grey contrast in Figure 5-13 c, d). Otherwise coating buildup was identical to that described previously with regard to a top porous layer.

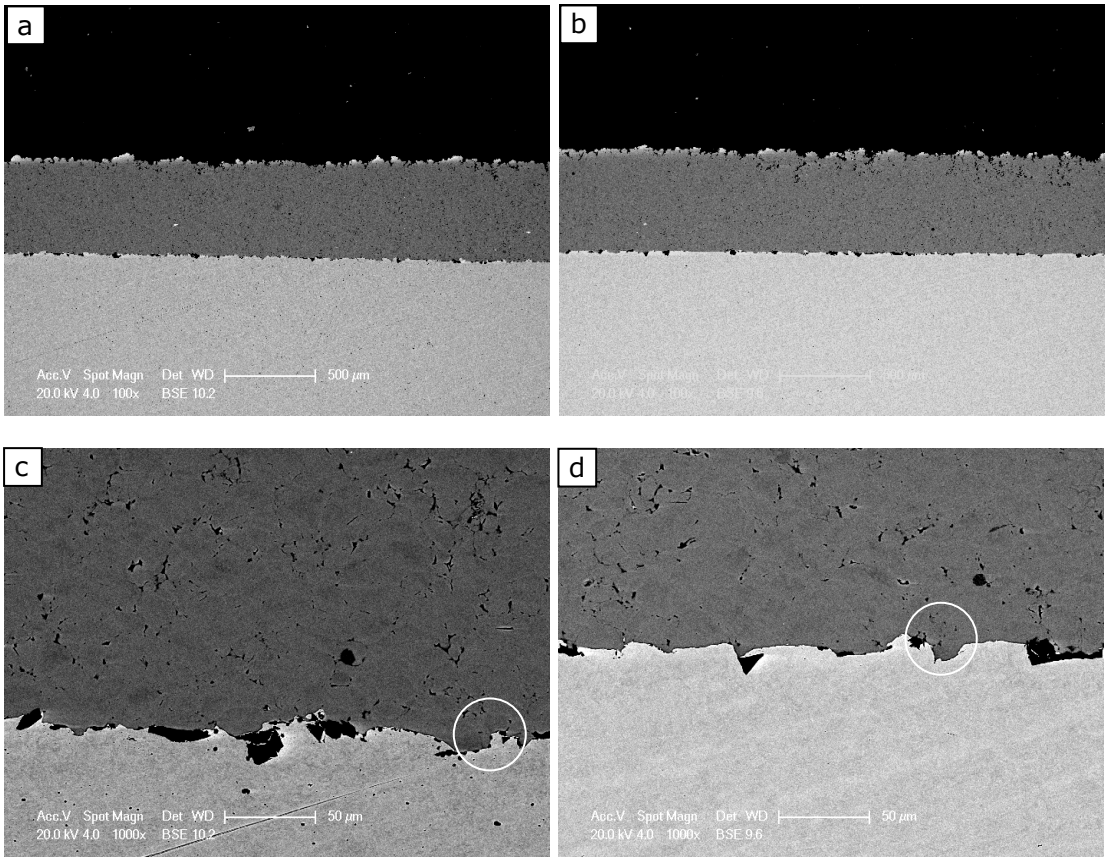

Figure 5-13 BSE image of the titanium coating deposited onto in-situ grit blasted (a) carbon steel & (b) stainless steel substrate. Coating-substrate interface of (c) carbon steel & (d) stainless steel showing embedded grits.

5.4.4 Bond strength and cohesive strength of deposits

Following the earlier work on surface preparation, ASTM C633 bond strength test samples were prepared using in-situ grit blasting for carbon and stainless steel and machined surface for Ti6Al4V. A coating of approximately 380 µm thickness was deposited for the pull-off tests. The results are summarized in Table 5-6.

Substrate	Test No.	Failure stress (MPa)	Failure Mode	Mean bond strength
Carbon Steel	A	69.02	Coating-substrate interface	71 ± 6
	B	81.36	Coating-substrate interface	
	C	61.55	Coating-substrate interface	
Stainless Steel 304	A	65.89	Coating-substrate interface	57 ± 8
	B	41.68	Coating-substrate interface	
	C	62.83	Coating-substrate interface	
Ti6Al4V	A	19.57	Coating-substrate interface	64 ± 27
	B	87.93	Coating-substrate interface	
	C	84.24	Coating-substrate interface	

Table 5-6 Pull-off bond strength values for the titanium deposited onto different substrates at 800°C gas temperature. Average bond strength of the glue after 5 tests was 88 ± 2 MPa

The fracture surfaces of all three substrate types were examined in SE and BSE modes. In the case of Ti6Al4V, the fracture surfaces are shown in Figure 5-14. Looking at the fracture surface of Ti6Al4V, it is clear that titanium particles are observed to adhere both as single particle and group of particles (Figure 5-14a). Figure 5-14 (c) shows that the impacting titanium particle deformed the substrate to some extent and created the shear lips (marked with arrows). However, during the pull-off bond strength tests these lips were probably ruptured and titanium particles were removed from the impact craters. In a similar manner, the wavy features on the outer edge of the titanium particle on the deposit sides (marked with arrow in Figure 5-14d) were probably created at the same time.

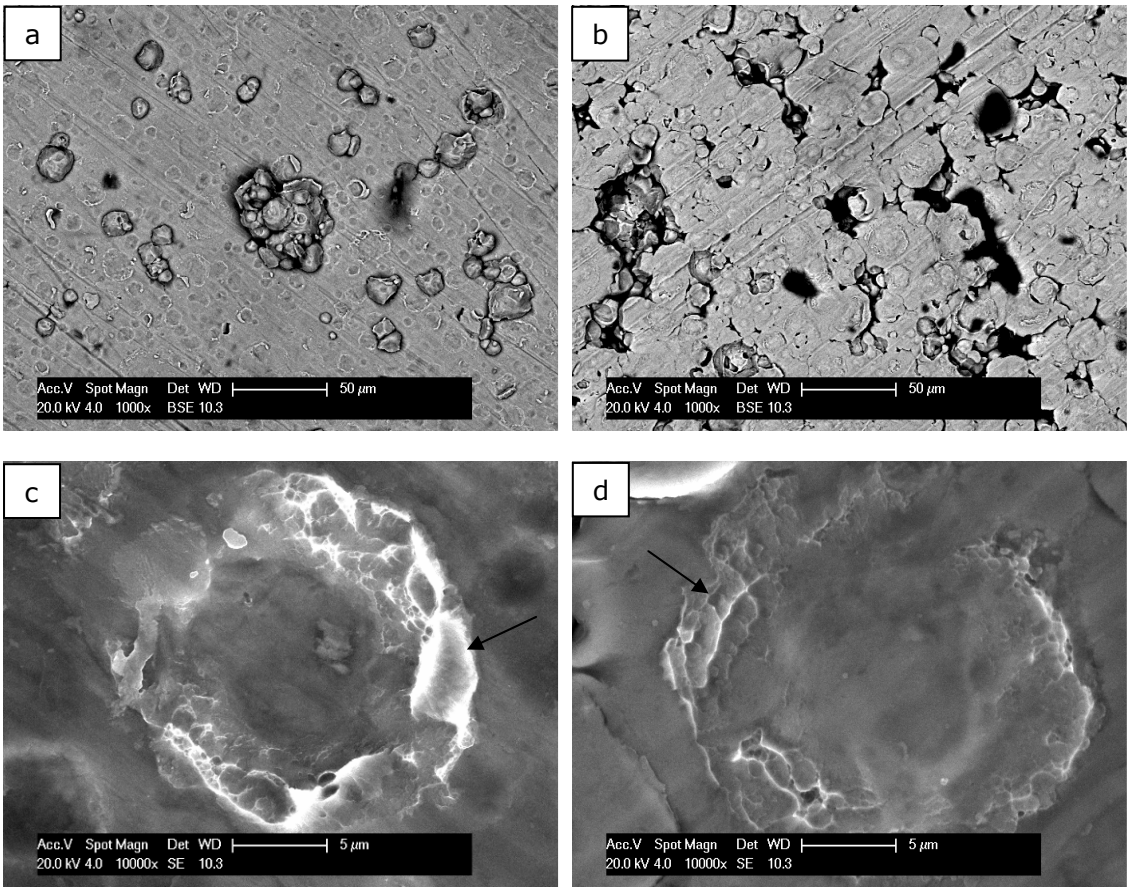

Figure 5-14 Fracture surfaces of as-machined Ti6Al4V substrate (a, c) and corresponding titanium coating (b, d)

Looking at the fracture surface of carbon steel substrate (Figure 5-15 a, c), it can be seen that there are titanium particles retained on the surface following bond-strength tests as individual particles, marked with circles. In the BSE image of the fracture surface of carbon steel (Figure 5-15c), a large number of dark contrast regions are seen which were identified as alumina from the substrate preparation methods. It is surprising to notice that on the surface of titanium coating counterpart (Figure 5-15 b, d), alumina is also present, which were pulled out from the carbon steel substrate. In a similar manner, fracture surface of stainless steel shows presence of individual titanium particles and also alumina from the substrate preparation methods (Figure 5-16 a, c). Also, the counterpart of titanium deposit shows evidence of alumina pulled out of the stainless steel substrate (Figure 5-16 b, d).

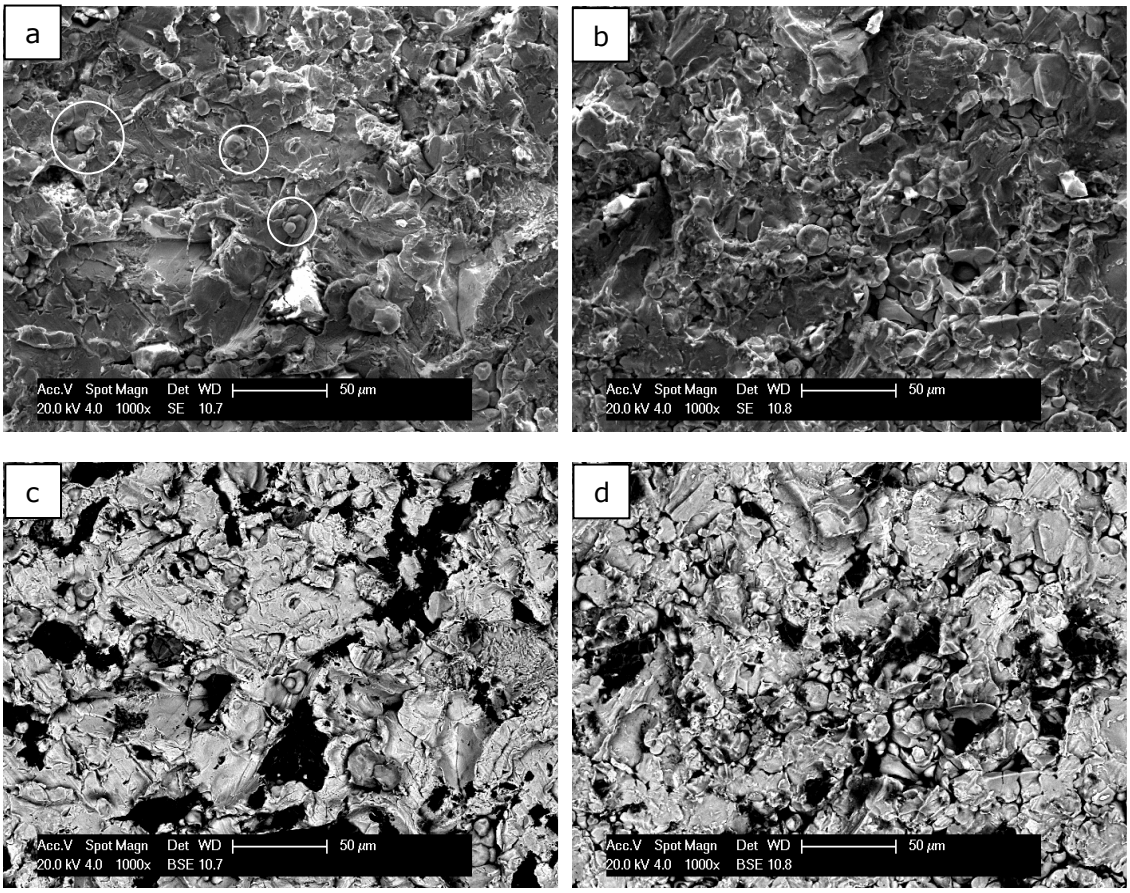

Figure 5-15 Fracture surfaces of carbon steel substrate (a, c) and corresponding titanium coating (b, d)

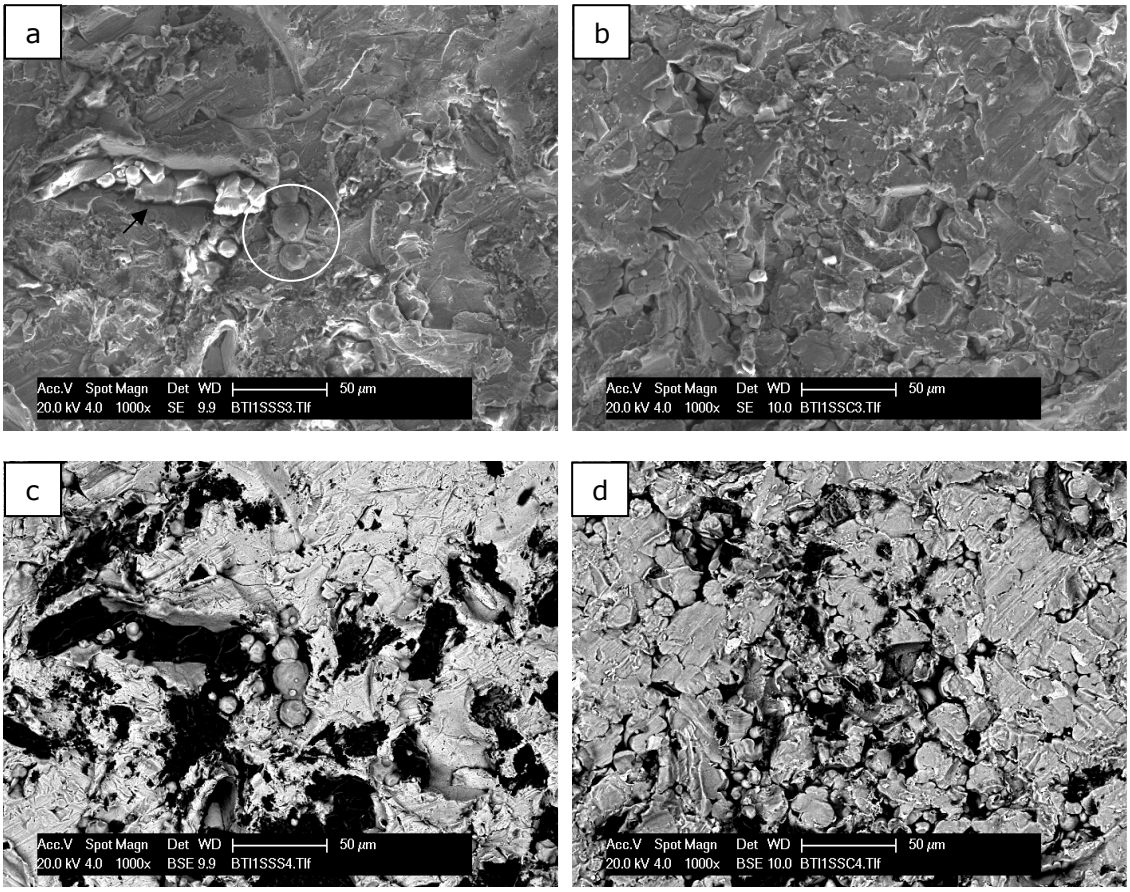

Figure 5-16 Fracture surfaces stainless steel (a, c) and corresponding titanium coating (b, e)

As all failures in the ASTM C633 test were at the coating-substrate interface it does not provide information on the cohesive strength or ductility of the coating. Hence TCT specimens were prepared and tested. The principles of the test are given in [10, 182]. Tubular coating tensile test (TCT) was performed to measure the ultimate tensile strength (UTS) of the deposits. The test does not require any post-spray machining of the deposit. Titanium was deposited onto in-situ grit blasted carbon steel surface to a thickness of ~900 µm for the TCT tests. Table 5-7 shows the failure loads and the cross-sectional area of the three different TCT samples. The mean ultimate tensile strength of three cold sprayed titanium deposits was 247 ± 15 MPa. For comparison, ultimate tensile strength of ASTM grade 1 titanium is 240 MPa [200].

Sample	Failure stress (MPa)	Ultimate tensile strength (multiplied by factor 1.7) MPa	Mean UTS / MPa
A	151	256	247 ± 15
B	128	217	
C	157	267	

Table 5-7 Tubular coating tensile test results of titanium deposited at 800°C process gas temperature

The fracture surfaces following TCT tests were examined and are shown in Figure 5-17. Lower magnification image of the fracture surface in Figure 5-17 (a) shows failure at inter-particle boundary (marked with dotted arrow) and failure within a particle (marked with solid arrows). Looking at the higher magnification images (Figure 5-17b- e) of the fracture surface, it is evidence that ductile failure occurred at certain places. Figure 5-17 (b) indicates failure modes similar to void coalescence occurred in the boxed region showing elongated voids, which deformed when load was applied and finally resulted in dimples (marked with arrow). It should be noted that in all the micrographs the spraying direction is from the top and the tensile loading direction is perpendicular to the image. In addition, figure 5-17(c) shows topography of fracture surface consisting of cusps marked with an arrow. Higher magnification images of fracture surface (Figure 5-17 d, e) show equiaxed dimples (marked with arrows) that are created during void coalescence by stress normal to the plane of fracture. Furthermore, Figure 5-17 (d) shows the fracture occurred within the particle. It is noticeable that the dimples are quite shallow on the particle surface.

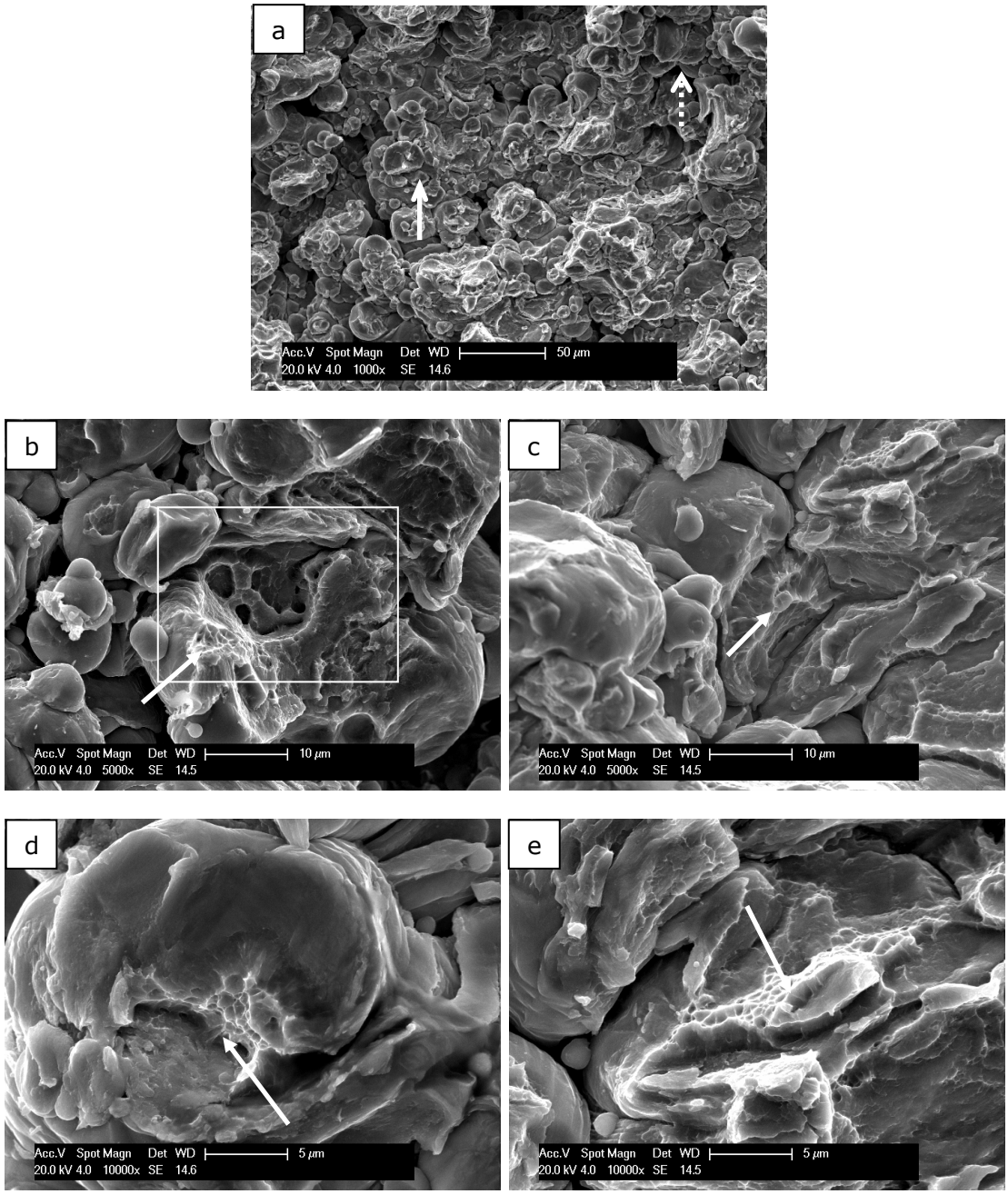

Figure 5-17 Fracture surfaces, after tubular coating tensile tests, of titanium deposits sprayed at 800°C. Direction of spraying from the top to bottom and load direction perpendicular to the paper surface

5.5 Deposit porosity and effect of post-spray processing

As mentioned previously titanium will function as a barrier coating only if there is no interconnected porosity. Also, as a free standing material, its mechanical properties will be reduced by the presence of porosity. Hence in this section work on assessing the porosity of as-sprayed deposits will be reported along with results on the effects of selected post-spray treatments namely high temperature annealing and laser surface melting.

5.5.1 Porosity of as-sprayed and heat-treated titanium deposits (mercury intrusion porosimetry)

As shown in Figure 5-5 and Figure 5-9, coatings sprayed onto stainless steel at both 600 and 800°C exhibited porosity, when examined in the optical microscope and scanning electron microscope. However, mercury intrusion porosimetry (MIP) is a better technique for quantifying and characterizing interconnected porosity as described in experimental methods section 3.11. Coating samples (with porous top layer) sprayed at 600 and 800°C were removed from the substrate and MIP was performed. Figure 5-18(a) shows the incremental mercury intrusion with respect to pore sizes of 600 and 800 °C deposits before and after heat treatment. The as-sprayed 600°C deposit has a pore size distribution of 0.3 - 8 μm. Heat treatment of the deposit altered the pore size range to 0.6 - 2.5 μm. The majority of the pores in the 800°C deposit were in the size range of 0.18 - 1.6 μm with a smaller number of very fine pores of size 0.003 - 0.004 μm. Heat treatment of 800°C showed a virtual complete elimination of larger pores and resulted in formation of very small pores of 0.006 μm to 0.013 μm.

Figure 5-18(b) shows the cumulative intrusion of mercury per gram of sample versus pore diameter. The cumulative intrusion for the as-sprayed 600°C deposit was 0.025 mL/ g with a sharp increase of cumulative intrusion curve at 2-3 μm pore sizes. The larger pores are filled up with mercury at lower pressure and smaller pores are infiltrated at higher pressure. Following heat treatment of 600°C deposit, the total amount of intruded mercury decreased to 0.01 mL/g, i.e. decrease in the total pore volume. The cumulative intrusion of as-sprayed 800°C deposit was 0.013 mL/g, which is half the amount compared to as-sprayed 600°C deposit (0.025 mL/g). The slope of the 800°C cumulative intrusion curve sharply increases at the pore sizes of 1-2 μm. After heat treatment, 800°C deposit exhibited a cumulative intrusion of only 0.004 mL/g. The equivalent volume percentages of porosity from mercury intrusion tests are shown in Table 5-8. The last two columns of the table show the volume percentages of porosity of the deposits corresponding to pore sizes below and above 1 μm. In as-sprayed and heat-treated 600 °C deposit, the pore sizes above 1 μm accounted for the majority of the porosity. However, in the as-sprayed and heat-treated 800°C deposits, the pores smaller than 1 μm accounted for the majority of the porosity. Evidently optical microscopy can only detect pores of diameter approximately ≥ 1 μm and so will not detect these very fine pores.

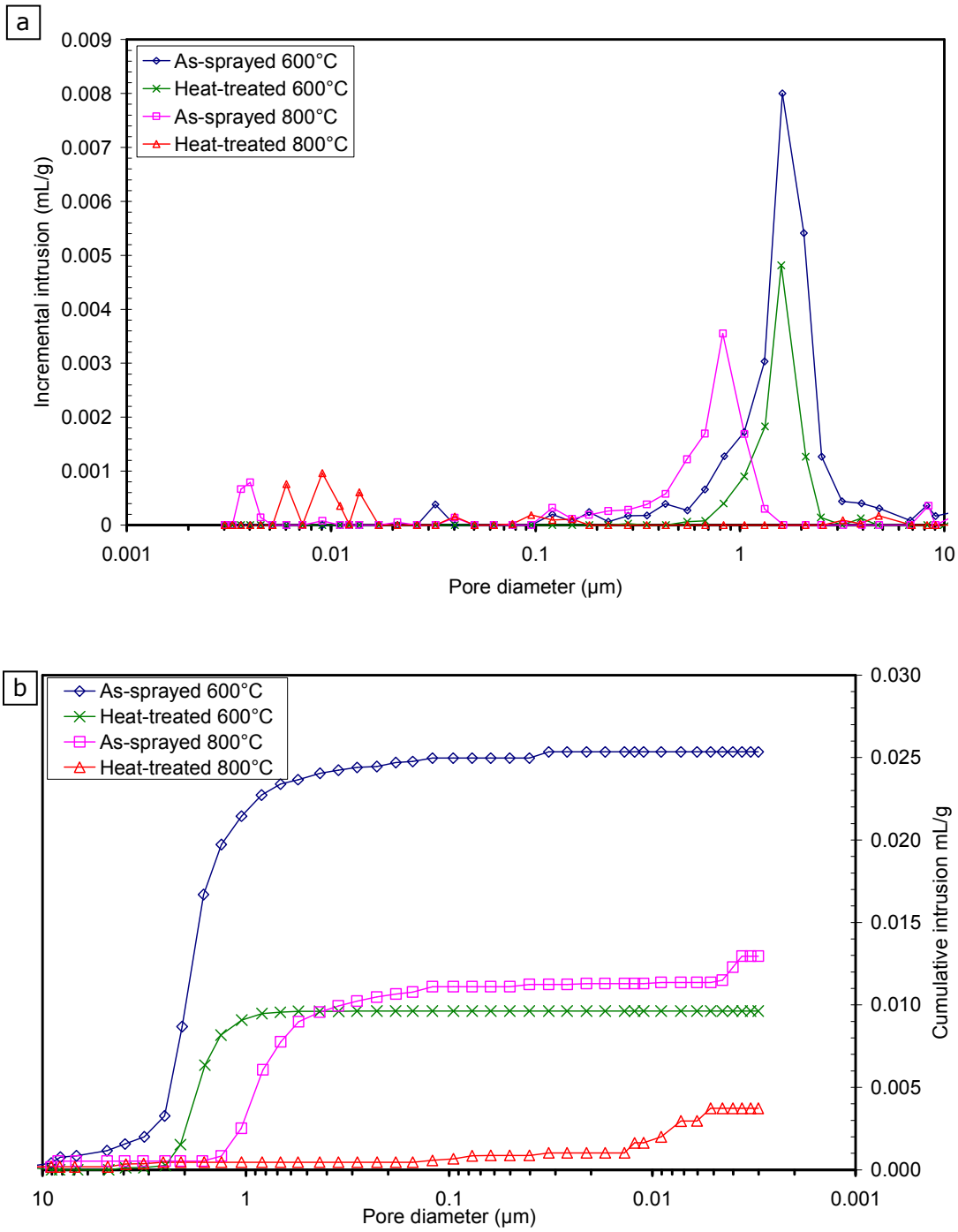

Figure 5-18 (a) Incremental intrusion of mercury vs. pore size distribution of as-sprayed and heat-treated deposits (b) Cumulative mercury intrusion of the same deposits

Process conditions	Total intrusion (mL/g)	Total volume percentage of interconnected porosity (vol. %)	Volume percentage of porosity with pore size > 1 μm (vol. %)	Volume percentage of porosity with pore size < 1 μm (vol. %)
As-sprayed 600°C	0.025	11.3	9.9	1.4
Heat-treated 600°C	0.010	4.5	4.0	0.5
As-sprayed 800°C	0.013	5.9	1.4	4.5
Heat-treated 800°C	0.004	1.8	0.2	1.6

Table 5-8 Volume fraction of open porosity of free standing 600 and 800°C deposits before and after heat treatment (Cumulative intrusion of mercury (mL/g) was converted to vol. % assuming density of titanium is 4500 kg/m^3)

5.5.2 Morphological and microstructural changes following heat treatment

Figure 5-19 (a, b) show optical images of etched as-sprayed free standing deposits (600 and 800°C) taken from near the mid-plane of the coating and Figure 5-19 (c, d) show the microstructure following heat treatment. Most of the interparticle pores in heat-treated 800°C deposit were eliminated following heat treatment due to recrystallization and grain growth at higher temperature, but a number of isolated regions of defects were still present in heat-treated 600°C deposit. X-ray diffraction (XRD) analysis of heat-treated deposits showed the presence of only α-Ti. No secondary phases were present within the limits of XRD sensitivity (i.e. 1-2 vol. %).

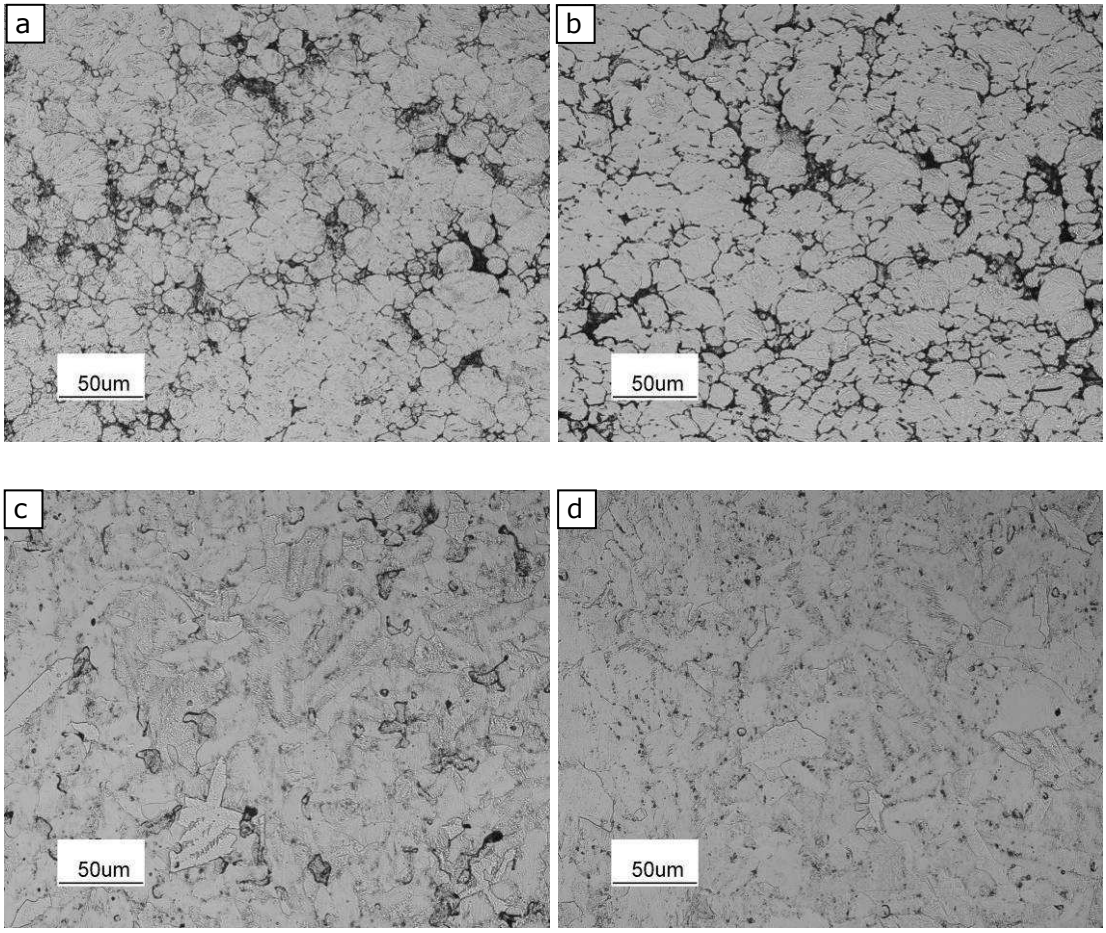

Figure 5-19 OM etched images showing changes in microstructure. As-sprayed (a) 600 & (b) 800 °C deposits. Heat-treated (c) 600 & (d) 800˚C deposits.

Figure 5-20 shows higher magnification secondary electron (SE) images of the deposits before and after heat treatment. The pores in as-sprayed 600 and 800˚C deposits (Figure 5-20a, b) are mostly at the interparticle boundaries and the gas atomized titanium powder particles show little evidence for pores within them. The heat-treated 600˚C deposit shows a reduction of interparticle voids and spheriodization of pores (Figure 5-20c). Interparticle boundaries, nearly free from defects, were observed following heat treatment of 800˚C deposit and formation of metallurgical bonds at the interparticle splats (Figure 5-20d).

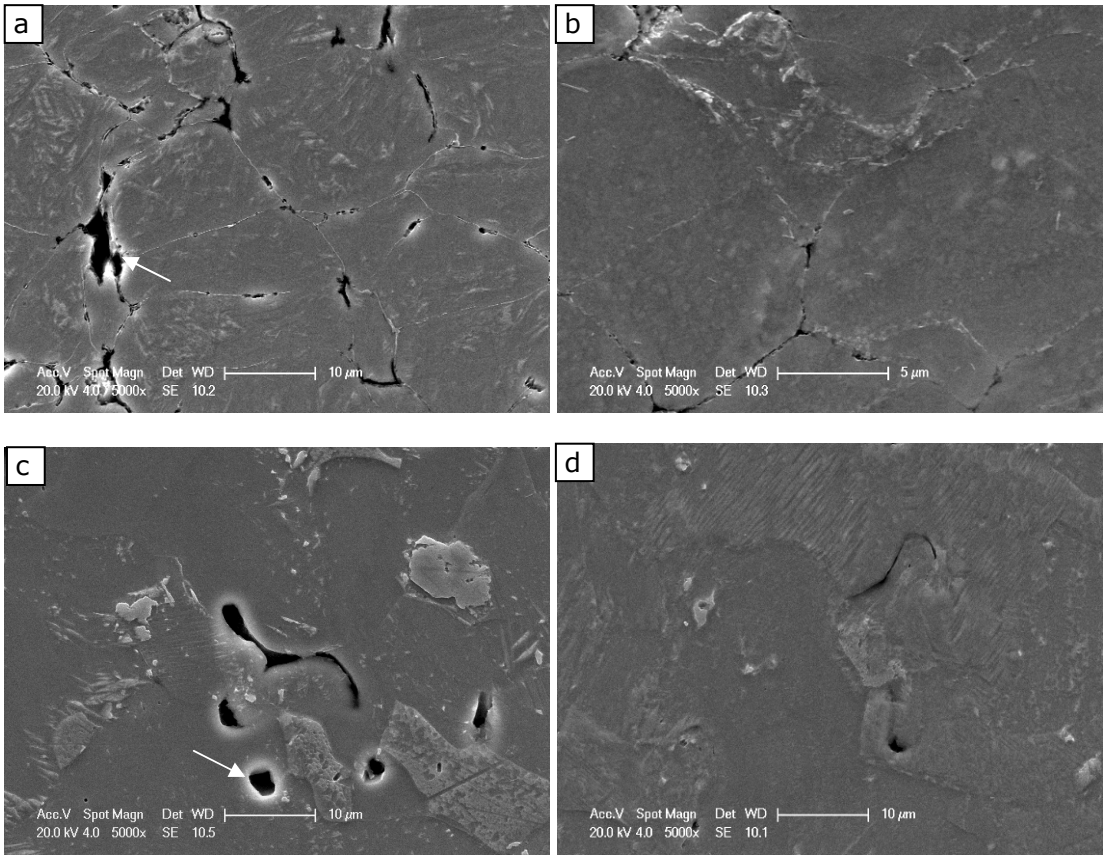

Figure 5-20 SEM images of etched samples showing changes in pore structure. As-sprayed (a) 600 & (b) 800°C deposits. Heat-treated (c) 600 & (d) 800˚C deposits (Arrows showing the interparticle pores)

Lower magnification images of heat-treated top surfaces of 600 and 800 °C deposits are shown in Figure 5-21 (a, b). The heat-treated deposits show new grain growth and elimination of previous particle boundaries. Heat-treated 600 °C deposit (Figure 5-21a) shows larger intergrain voids compared to heat-treated 800 °C deposit (Figure 5-21b). Figure 5-21 (c, d) show higher magnification images of heat-treated 600 and 800 °C deposit. In both deposits, grain growth following heat treatment shows a reduction of pores with the formation of faceted grain boundaries.

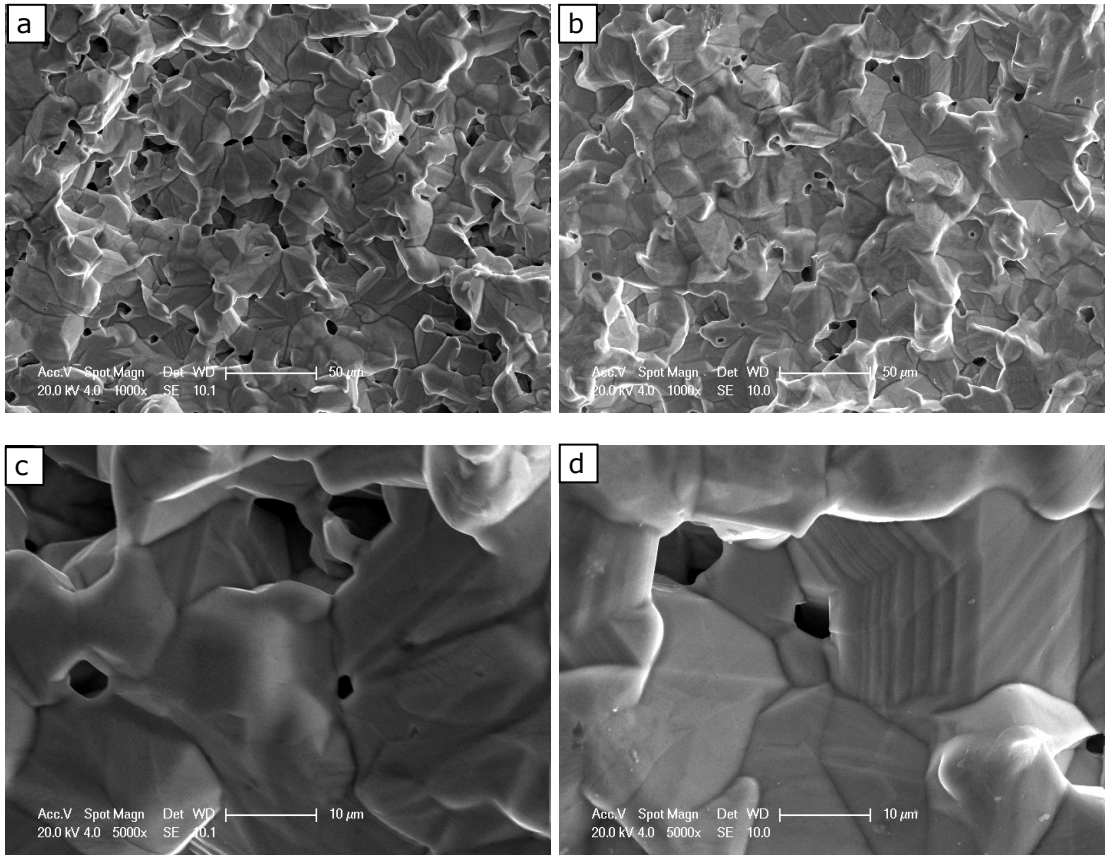

Figure 5-21 SEM images of the top view of heat-treated deposits (a) 600 & (b) 800°C. Higher magnification images of the heat-treated deposits (c) 600 & (d) 800°C

5.5.3 Laser surface melting trials

Laser surface melting (LSM) trials were performed on coatings sprayed at 800°C onto carbon steel substrates. The coating thickness was ~550 µm. In the trials, to assess the appropriate conditions to achieve surface melting without delamination, six different laser process conditions were used as listed in Table 5-9, where P' is the power of the laser beam (W), D is the spot size (mm) and U is the traverse speed (mm/s).

Run No	Power, P' (W)	Speed, U mm/s	Spot size, D (mm)	Track (melt) width, (μm)	Melted depth (μm)	$\frac{P'}{\sqrt{DU}}$ ($\times 10^5$ W $s^{1/2}$ m^{-1})
1	440	25	0.3	500	110	1.61
2	540	25	0.408	600	130	1.69
3	1000	15	1.08	1200	145	2.48
4	1000	21.6	1.08	1200	140	2.07
5	1000	31.6	1.08	1200	115	1.71
6	1000	48.3	1.08	1200	55	1.38

Table 5-9 Process parameters for laser surface treatment of titanium coatings deposited at 800°C process gas temperature

Single LSM runs were performed and cross-sections of the LSM samples are shown in Figure 5-22. The porosity present in the original deposits is readily visible and the LSM regions can be identified from the regions free from pores, having equiaxed grains. This is due to the melting of the deposit, the escape porosity moves to the free surface and the subsequent re-solidification of the track. An empirical relationship between $\frac{P'}{\sqrt{DU}}$ and melting depth was reported by Steen [178]. From run no 3 to 6, where the spot diameter was fixed, it is seen that increasing $\frac{P'}{\sqrt{DU}}$ value correlate with increasing melting depth. From Figure 5-22 (a) and (b) it can be noticed that increasing the power increases the depth and width of the melting. From Figure 5-22 (c) to (f), it is evident that as traverse speed U is increased the melted depth decreases but with less change in track width. Values of depth and width of the melting regions are given in Table 5-9.

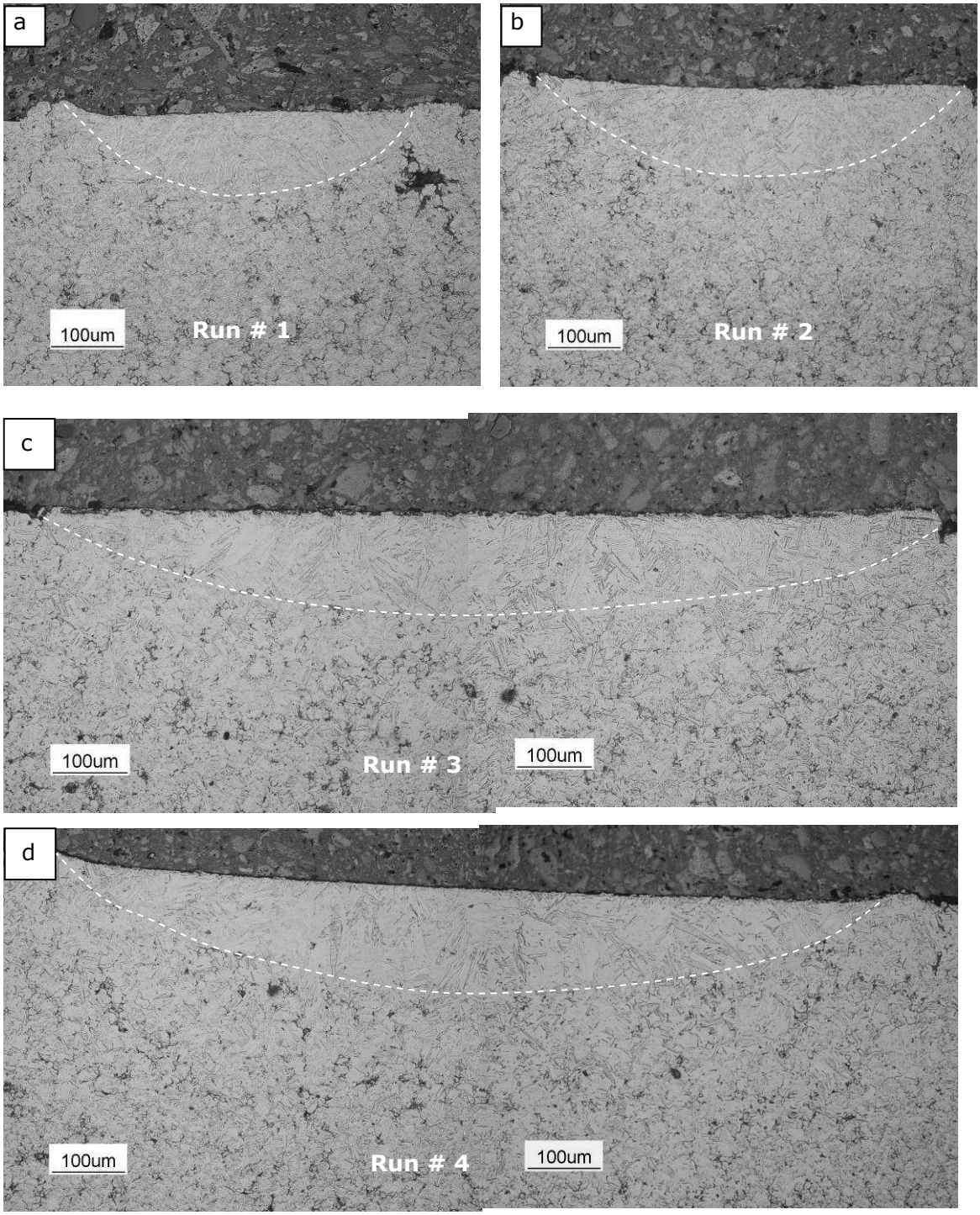
a
100um
Run # 1
b
100um
Run # 2
c
100um
Run # 3
100um
d
100um
Run # 4
100um

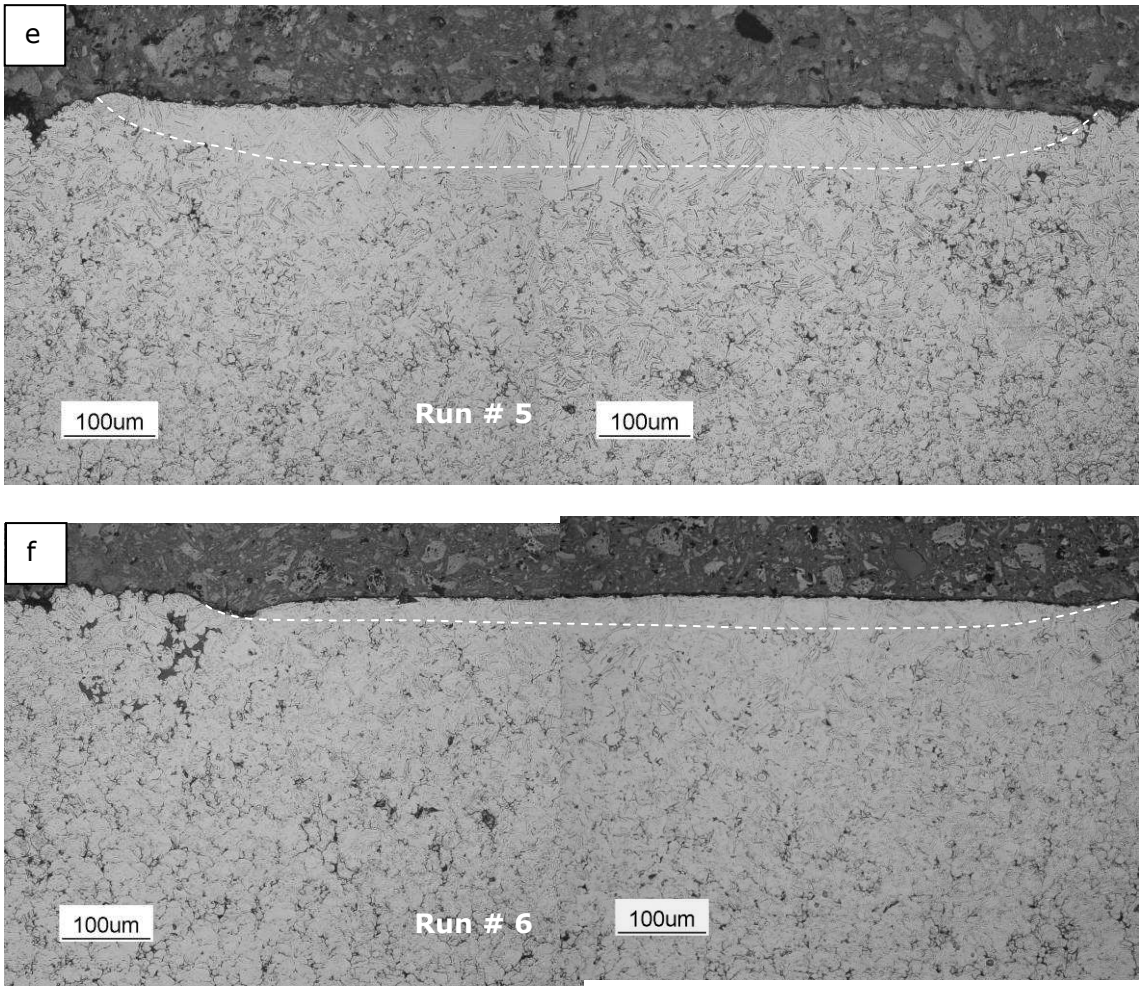

Figure 5-22 Melt pool characteristics of laser treated etched titanium coatings sprayed at 800°C process gas temperature according to the process parameters shown in Table 5-9

On the basis of these single tracks condition 4 was selected to treat an area of 16 mm ×16 mm. Overlapping track trials were performed at condition no 4 using a range of track separations from 200 to 1000 μm. Finally, 1000 μm track separation was used to produce the laser melted areas i.e., only 200 μm of the track was overlapped.

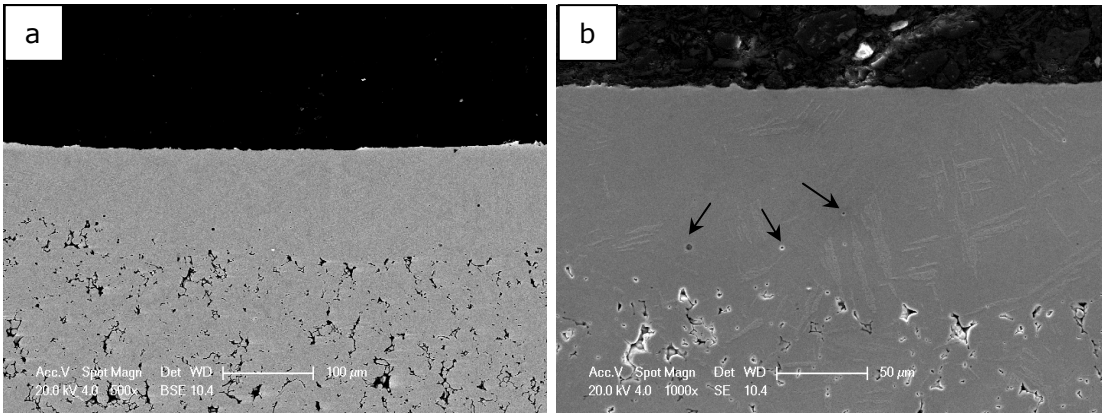

Figure 5-23 (a) Etched BSE image showing the shape of the melt pool and (b) SE image showing the microstructure of the laser treated zone (run 4)

Figure 5-23(a) shows the etched BSE image of the cross section of a laser treated coating. The depth of the laser melt pool can be identified as where the interparticle pores of the titanium coating begin. The heat affected zones in the laser treated coatings cannot be easily identified. It can be seen that at the centre of the melt pool the penetration depth is ~140 µm whereas at the edge, where two laser tracks were overlapped, is around ~100 µm. Nevertheless, the parameters of run no 4 (Table 5-9) sealed the coating surface completely without any gaps. Figure 5-23(b) shows the higher magnification SE images of the laser treated area showing the acicular microstructure of titanium and isolated rounded pores marked with arrows. Figure 5-24 shows the X-ray diffraction analysis of the laser treated coating. The laser treated coating is composed of α- titanium and no evidence of β-titanium within the detectable range of XRD was observed. However, peaks corresponding to TiO (Hongquiite) at 2- theta angle of 36°, 42° and 61° were detected in the laser treated coating. Although the laser treatment was conducted in protective atmosphere, due to high reactivity of titanium, the reaction between titanium and oxygen occurred at high temperature.

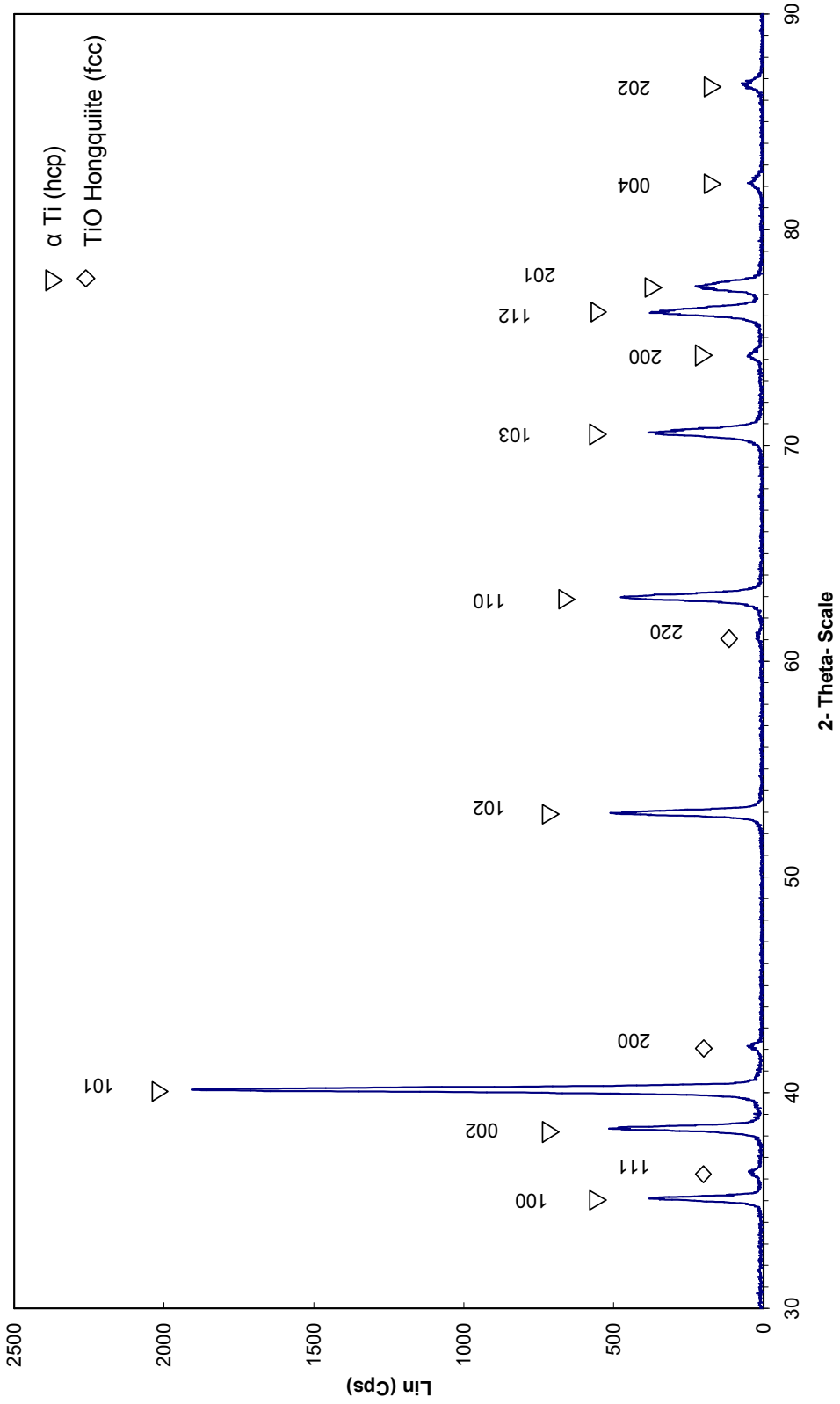

Figure 5-24 XRD analysis of a laser treated (condition 4) titanium coating sprayed at 800°C

5.6 Discussion

5.6.1 General observations

Although it is possible to produce a pore free microstructure using cold spray from ductile face centred cubic copper [201], it is more difficult to produce a pore free deposit from titanium. Titanium is more difficult to deform at high strain rate in cold spraying due to its hexagonal closed packed (hcp) crystal structure (see flow stress of Ti using Johnson-Cook parameters in Figure 4-30) and its lower density [44, 76]. A less deformed top porous layer is clearly observed in the deposits sprayed at 600 °C, whereas, this porous layer is less evident in the deposits sprayed at 800 °C. It can be argued that there are two effects taking place at the higher process gas temperature. First, the particles reach a higher in-flight velocity due to a higher Mach number inside the gun and secondly, the particles reach a higher temperature in the gas stream. According to the energy balance theory the initial kinetic energy of a particle before impact is the sum of the energy dissipated as plastic deformation plus recoverable strain energy [39]. A higher particle velocity results in a greater kinetic energy which enhances plastic deformation. Also heating of the particles changes the initial state of impacting bodies due to thermal softening that results in a decrease of flow stress. Also, the porosity of titanium deposits decreases with increasing the distance from the coating top surface because the particles at the bottom of the coating experience more of a peening effect than the particles deposited at the top surface [202].

The shear lips of the titanium particles observed at the top surface of the coating sprayed at 800 °C process gas temperature (Figure 5-10d) can be attributed to the highly localized deformation at the impacting interface. During this high strain rate plastic deformation, much of the work done is converted to heat [203]. On

the other hand, partial bonding and ruptured bonds in the deposits sprayed at 600 °C (Figure 5-10c) can be attributed to elastic relief on unloading during the impact phenomena [56]. These differences in deformation of the particles and thermal softening resulted in an open porosity of ~6 vol. % in the deposits sprayed at 800 °C compared to ~11 vol. % of the deposits sprayed at 600 °C as determined from MIP.

5.6.2 Role of substrate types and surface preparations on bonding

Building up of titanium coatings using 800°C gas onto conventionally cabinet grit blasted carbon steel substrate was not possible due to spontaneous coating delamination after two passes, unlike stainless steel and titanium alloy substrates. This indicates weak bonding of the coating to the cabinet grit blasted carbon steel surface. Previously in Chapter 4, it was observed that following deposition of titanium particles onto carbon steel substrates a metal-to-metal bond was not formed which is a reason for the ease of spallation.

It was previously proposed in Chapter 4 that there are two components of bonding in cold spraying: a mechanical component and a metallurgical component. Thus, if titanium is to be successfully deposited onto carbon steel substrate, the mechanical component of the bonding or coating-substrate "interlocking" needs to be improved. It was reported in literature that to achieve acceptable coating-substrate adhesion the surface of the substrate was prepared to a rougher surface finish using a coarse grit (350 – 764 µm) [38, 111]. Hence, in this study in-situ grit blasting was used, in which the particle velocity is higher due to process parameters compared to that of the conventional grit blasting. In-situ grit blasting of the carbon steel substrate increased the surface roughness (Ra) by a factor of two compared to that of conventional cabinet blasting, which is

likely to increase the mechanical "interlocking" at the coating-substrate interface. The adhesion strength of the first layer of coating to the substrate was thus increased to such an extent that the successive particle impact and supersonic gas stream did not debond the coating. The bond strength of the titanium deposits onto in-situ grit blasted carbon steel substrate was as up to 71 MPa. However, a large number of alumina particles were embedded at the coating-carbon steel interface. The role of these fractured alumina particles in bonding is not clear. Looking at the cross-section of the titanium coatings onto the carbon steel substrates (circles in Figure 5-13c, d) and the fracture surfaces following bond strength test samples (Figure 5-15a-d), a mechanical interlocking of the coating-substrate is evident.

It should be mentioned here that titanium coatings were also deposited onto Ti6Al4V substrates without any surface preparation steps (grinding, polishing, conventional or in-situ grit blasting) and no debonding of the coatings was observed. Although, there was little substrate deformation following deposition the bond strength was typically ~86 MPa. The metallurgical component of the bonding must have been high to allow such a high bond strength value without significant substrate deformation. This high metallurgical component of the bonding could possible be due to a similarity in chemical compositions of the coating and substrates.

5.6.3 Failure modes of titanium deposits

The mean ultimate tensile strength (UTS) derived from the cold sprayed titanium deposits was ~247 MPa. This is in reasonable agreement with the strengths of the cold sprayed titanium deposits measured by other researchers using TCT tests [140]. The tensile strength of titanium is sensitive to the impurity contents i.e., oxygen and nitrogen. The oxygen content of the powder used in this study was

0.14 wt.% and nitrogen content was <0.01 wt.%; however, following deposition the oxygen content increased to 0.35 wt.% and nitrogen content increased to 0.03 wt.%. The oxygen content of an ASTM grade 1 titanium is 0.18 wt.% (max) and nitrogen content is 0.03 wt.% (max), whereas the oxygen content of grade 3 titanium is 0.35 wt.% (max) and nitrogen content is 0.05 wt.% (max). The UTS of ASTM grade 1 titanium is 240 MPa and that of grade 3 titanium is 440 MPa [200]. With increasing impurity content, the strength of the material increases at the expense of ductility.

The fracture surfaces of titanium deposits (Figure 5-17) following TCT tests indicate a combination of cleavage fracture along pre-existing particle-particle boundaries and ductile rupture within the particle itself, (dimpling) around pores. However, the interparticle pores within the deposit act as the stress concentration sites, which grow rapidly once a critical stress level is reached and results in failure. The dimple sizes observed in the fracture surface are of sub micron sizes, which is in agreement with Bae et al.'s [139] observation of nanostructure formation during kinetic spraying of commercially pure titanium. Dimple patterns indicative of void-coalescence failure mode are observed in a number of places at the fracture surface. A schematic diagram of the process is shown in Figure 5-25. Once the voids form, the connecting material continues to deform by slip, allowing the voids to expand until they begin to connect. This mechanism develops a fracture topography consisting of cusps on each side of the fracture surface. Void coalescence by a stress normal to the surface creates equiaxed dimples. However, shallow dimples are created when a high strength material fails by void coalescence due to limited ductility of the material connecting the voids.

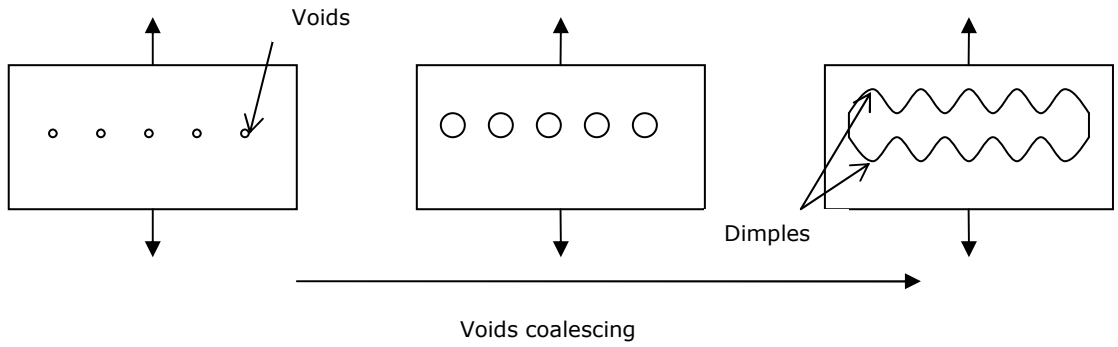

Figure 5-25 Schematic illustration of fracture by void coalescence [204]

5.6.4 Porosity of as-sprayed and heat-treated deposits

It is evidenced from the micrographs (Figure 5-19), that heat treatment of free standing titanium deposits above the β transus temperature resulted in grain growth and reduction in porosity. Titanium has an adherent oxide (TiO_2) layer which has to be disrupted to form metallurgical bonds [4, 186]. Moreover, the oxide layer on the metal surface acts as a diffusion barrier for many metals but TiO_2 does not hinder the formation of metallurgical bonds during heat treatment because both α and β phases of titanium are known to dissolve oxygen interstitially [205]. Therefore, during vacuum heat treatment new grains were formed and grain growth took place, which eliminated the sprayed particle boundaries [141]. Consequently, the interparticle pores in the as-sprayed deposits were pinned down at the new grain boundaries.

Following heat treatment, the interconnected porosity of 600° C deposit reduced from ~11 vol. % to ~5 vol. % and that of 800 °C deposit reduced from ~6 vol. % to ~2 vol. %. Healing of the incomplete interparticle interfaces and interparticle micro pores through atom diffusion and recrystallization during heat treatment process resulted in reduced porosity. Mercury intrusion porosimetry (MIP) measured the interconnected porosity of the as-sprayed and the heat-treated free

standing deposits down to a few nm of pore sizes. This is well below the resolution of an optical microscope. If an optical microscope with a typical resolution of 1 μm were to be used to measure the porosity of heat-treated 800 °C deposit, the deposit would appear to have a porosity of only ~ 0.2% because the sub-micron pores would not be resolved (Table 5-8). However, the majority of the pores in the heat-treated 800 °C were of sub-micron sizes which account for a porosity of 1.6 vol. %. Moreover, MIP has a unique advantage in measuring the volume percentage of porosity in cold sprayed coatings compared with thermally sprayed metals because the formation of oxide can be neglected. Therefore MIP cumulative intrusion values can readily be converted to volume percentage of porosity using the known density of metallic Ti. In thermally sprayed coatings, the volume percentage and density of any oxide inclusions also need to be known before the cumulative intrusion values in mL of mercury per gram of sample can be converted to volume percentage of porosity.

5.6.5 Laser surface melting of the deposits

Following laser surface melting, the interparticle porosity in the top ~140 μm of the coating was eliminated. In the laser treated zone the rounded shaped of the as-sprayed particles was eliminated and an equiaxed grain structure formed upon solidification (Figure 5-22). However, etched microstructure of the coating showed submicron sized pores which are isolated in nature (Figure 5-23). These pores are probably trapped gas pores which are typically seen in laser treatment of thermal sprayed coatings.

Titanium has a high melting temperature (1668 °C) and a high affinity to oxygen and nitrogen. Titanium goes through an allotropic phase transformation at 882 °C, where α-titanium (hcp) transforms to β-titanium (bcc). On solidification bcc β-titanium will form from the melt and cooling the solid state will give either hcp α-

titanium or martensitic α [206]. It is evident from Figure 5-24 that the hcp α-titanium formed. Peak height ratios are as expected from a random grain structure, so no preferred orientation in α-titanium is present. Presumably, columnar β-titanium formed but β to α- titanium transformation gives random grain orientation. Also, TiO instead of TiO_2 was detected in the laser treated deposits (Figure 5-24). Although the laser surface melting was performed in protective environment, oxygen contamination might have occurred. Nonetheless, the coating contains 0.34 wt.% oxygen in as-sprayed condition which can also contribute to this oxide formation during the laser surface melting.

5.7 Summary

Titanium was deposited by cold gas dynamic spraying using two different process parameters (600 and 800°C nitrogen as a propellant gas) designed to reduce porosity. The coatings were characterized using optical microscopy, SEM, surface profilometry, microhardness measurements and X-ray diffraction. The surfaces of the steel substrates were prepared in an alternative in-situ grit blasting technique to improve the adhesion of the coating to the substrate. The bond strength values of the titanium deposits on carbon steel, stainless steel and titanium alloys substrates, as well as the tensile strengths of the deposits were measured. The porosity of the deposits was characterized by mercury intrusion porosimetry. The deposits were heat treated to reduce porosity. In addition, laser surface melting was also employed to eliminate porosity from the top ~140 microns of the coatings. The summary of this chapter were as follows

- Cold sprayed 800°C titanium coatings showed a less porous microstructure, a lower surface roughness and a higher microhardness than those of 600 °C coatings because of a higher degree of particle deformation on impact.

- An in-situ grit blasting surface preparation of carbon steel enabled a deposition of 4 passes of coating at 800°C gas temperature. In-situ grit blasting provides "key like" features to enhance the mechanical component of the bonding.
- Typical bond strengths of the deposits onto carbon steel was ~70 MPa, onto stainless steel was ~60 MPa and onto Ti6Al4V was 85 MPa.
- Mean tensile strength of the deposits was 247 MPa which is similar to that of ASTM grade 1 bulk titanium. Typical failure modes involve a combination of brittle failure at the inter-particle boundaries and ductile failures by void coalescence.
- Over the range of process parameter used a pore free titanium deposit cannot be achieved. However, a vacuum heat treatment of free standing deposits significantly reduces the interconnected porosity to 1.8 vol. %, measured by mercury intrusion porosimetry.
- Optical microscope and MIP give different values of porosity because a substantial portion of porosity is submicron, i.e, in as-sprayed and heat-treated 800°C deposits 75-90% pores are submicron.
- Laser surface melting can eliminate all the interparticle pores from the top ~140 μm of the deposits.

6 Corrosion performance of cold sprayed titanium coatings and free standing deposits

6.1 Introduction

Titanium metal has excellent corrosion resistance in a number of aqueous media including salt water due to the presence of a tenacious oxide film [107] and so titanium and its alloys have been used in a number of situations to protect steel structures and components from attack [177]. However, deposition of protective coatings of titanium by thermal spraying processes is problematic due to the fact that titanium reacts readily with oxygen to form TiO_2 at elevated temperature. Hence the resultant coatings contain features such as oxide inclusions and interconnected pores which prevent the realization of the protective capabilities of titanium as a barrier coating. Cold gas dynamic spraying can be used to deposit oxygen sensitive materials, such as titanium, without significant chemical degradation of the powder. The process is thus believed to have potential for the deposition of corrosion resistant barrier coatings. However, to be effective, a barrier coating must not allow ingress of a corrosive liquid and hence must not have interconnected porosity. Therefore, there is considerable interest in developing corrosion resistant titanium coatings as barrier layers and so more recently much attention has focused on using the cold spray process to deposit titanium coatings.

The aims and objectives of the work reported in this chapter were as follows.

- To study the corrosion behaviour of free standing titanium deposits and coatings sprayed with nitrogen at 600 and 800°C.

- To investigate the role of interconnected porosity on the corrosion behaviour of the deposits and coatings.
- To assess the corrosion behaviour of the post-treated deposits and coatings.

Therefore, the results section of this work are divided into five different sections: (i) corrosion behaviour of free standing deposits; (ii) corrosion behaviour of the heat-treated free standing deposits; (iii) corrosion behaviour of the coatings on stainless steel substrate; (iv) corrosion behaviour of the coatings on carbon steel substrate, and (v) corrosion behaviour of laser surface treated coatings.

6.2 Experimental methods

The methods of qualitative corrosion performance techniques: immersion testing and salt spray testing, and quantitative electrochemical techniques: open circuit potential measurements and potentiodynamic polarization scans are described in the Experimental Methods section in chapter 3. The sample preparation procedures for all these tests are also described in the experimental chapter. The coatings were sprayed onto both carbon steel and stainless steel substrates at process gas temperatures of 600 and 800 °C. The detailed spraying process parameters are presented in chapter 5.

Results

6.3 Corrosion behaviour of free standing deposits

Open circuit potential (OCP) and potentiodynamic polarization scans of free standing deposits sprayed at temperatures of 600 and 800°C were measured in de-aerated 3.5% NaCl.

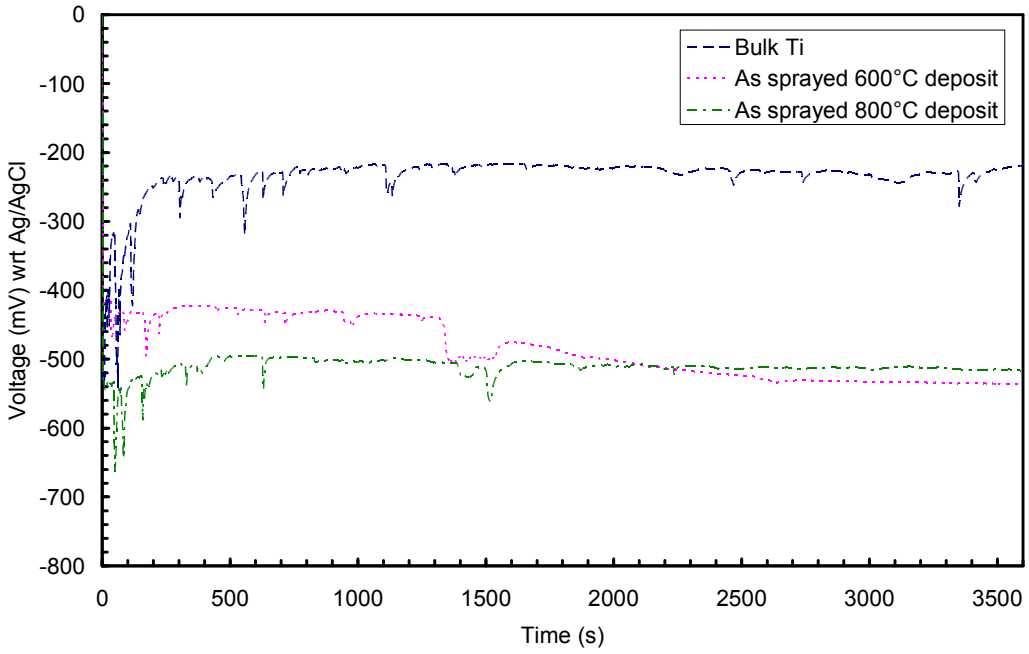

Figure 6-1 Open circuit potential of bulk titanium, as-sprayed 600 and 800 °C deposits

Figure 6-1 shows typical open circuit potential measurements of bulk titanium, as-sprayed free standing 600°C (porosity ~ 11 vol. %) and as-sprayed free standing 800 °C (porosity ~6 vol. %) deposit in de-aerated 3.5% NaCl solution for 3600 seconds. The detailed porosity measurements of the deposits sprayed at temperature of 600 and 800 °C are reported in Table 5-8. The bulk titanium reached a steady state OCP of -220 mV with respect to Ag/AgCl electrode within a few minutes of immersion. Both the open circuit potentials of as-sprayed 600 and 800 °C deposits were ~-525 mV (Ag/AgCl).

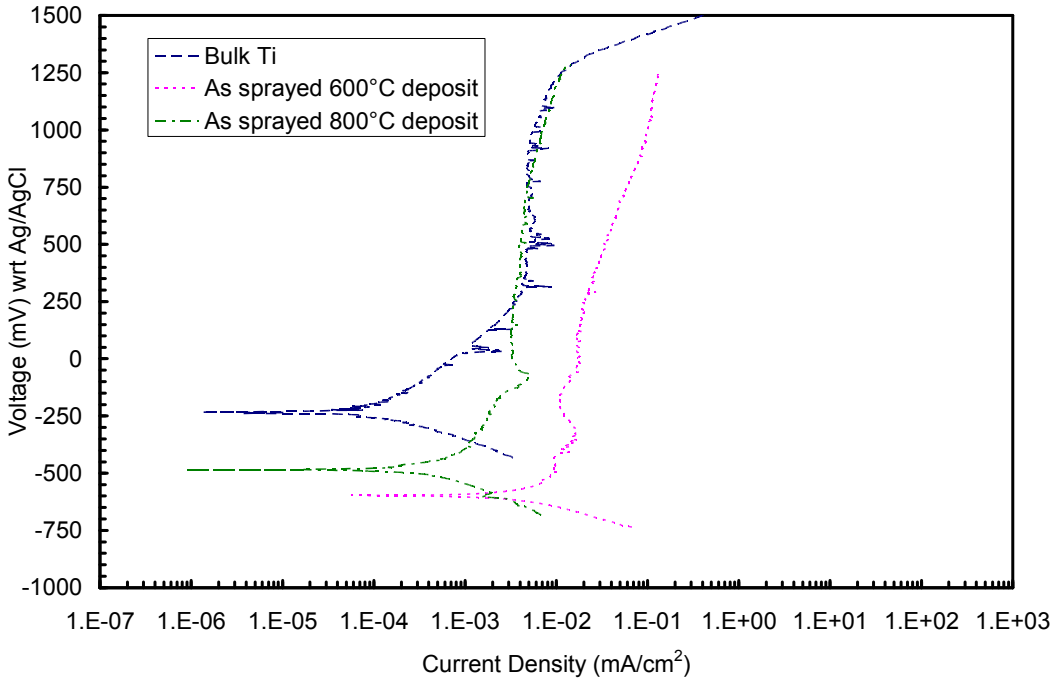

Figure 6-2 Potentiodynamic polarization scans of bulk titanium, as-sprayed 600 and 800°C deposits

Figure 6-2 shows typical potentiodynamic polarization scans of the bulk titanium, as-sprayed free standing 600 and 800 °C deposits. The scan of bulk titanium showed typical active-passive behaviour of a passivating metal. Bulk titanium had a passivation range of 250 mV to 1250 mV, after which it showed trans-passive behaviour. The passive current density (Ipp) of bulk titanium was 0.005 mA/cm^2. The as-sprayed free standing 600 °C deposit showed "passive-like" behaviour from 70mV to 1250 mV, during which the current density increased from 0.017 mA/cm^2 to 0.13 mA/cm^2. It also reached the limiting voltage value during the potentiodynamic polarization scan before the onset of trans-passive behaviour. On the other hand, the as sprayed free standing 800 °C deposit showed a decreased passive current density of 0.005 mA/cm^2 compared to free standing 600 °C deposit. It is noticeable that the passive current density of 800 °C free standing deposit is the same as the passive current density of the bulk titanium. The Ecorr and Icorr values of all the samples are shown in Table 6-1. Moreover,

the corrosion current density Icorr decreased by an order of magnitude in the 800 °C deposit compared to the 600 °C deposit.

Specimens	OCP wrt Ag/AgCl (mV)	Ecorr wrt Ag/AgCl (mV)	Corrosion current density, Icorr (mA/cm^2)	Passive current density, Ipp (mA/cm^2)
Bulk titanium	-220	-233	6.0×10^{-5}	0.005
As-sprayed 600 °C deposit	-540	-565	1.9×10^{-3}	0.017-0.13
As-sprayed 800 °C deposit	-510	-483	2.0×10^{-4}	0.005
Heat-treated 600 °C deposit	-525	-600	2.4×10^{-5}	0.007
Heat-treated 800 °C deposit	-365	-373	3.0×10^{-5}	0.005

Table 6-1 OCP, Ecorr, Icorr and Ipp values of as-sprayed and heat-treated deposits tested in de-aerated 3.5% NaCl

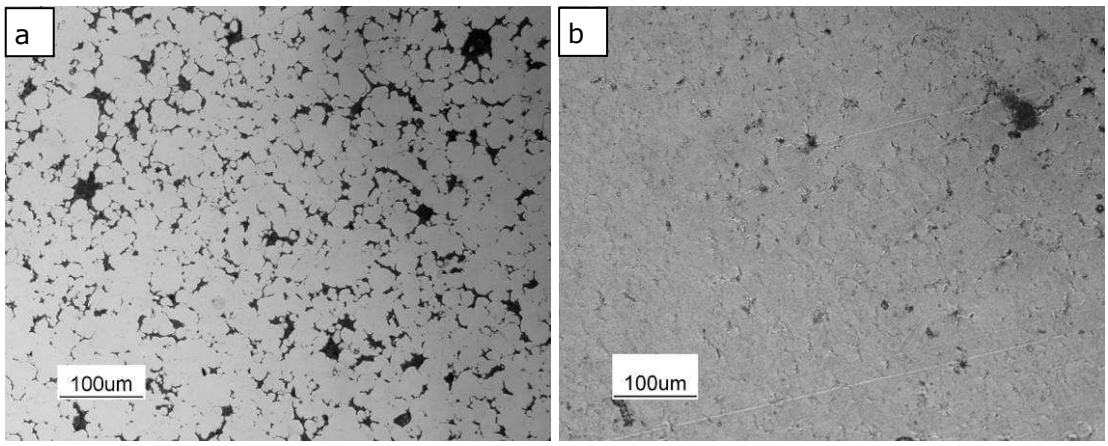

Figure 6-3 Optical microscope images of the polished surface of (a) 600 and (b) 800 °C deposits after electrochemical tests

Figure 6-3(a, b) show the plan view of the top surface, which were prepared in polished surface finish before the tests, of the free standing 600 and 800 °C deposits after OCP and potentiodynamic polarization scans. The surface of the 600 °C deposit (Figure 6-3a) shows a large number of pores at the interparticle boundaries. In contrast, the plan view of the free standing deposit 800 °C shows reduced interparticle pores compared to free standing 600 °C deposit. It is clear that increased interparticle porosity will also increase the actual area of the surface taking part in the corrosion reactions, which will be higher than the measured apparent area. This increased actual area will contribute to an increased corrosion current density of the free standing 600 °C deposit in potentiodynamic polarization scans (Figure 6-2).

6.4 Corrosion behaviour of heat-treated deposits

Samples were heat treated as described in the previous chapter in order to decrease the porosity levels. A summary of the porosity data is given in Table 5-8.

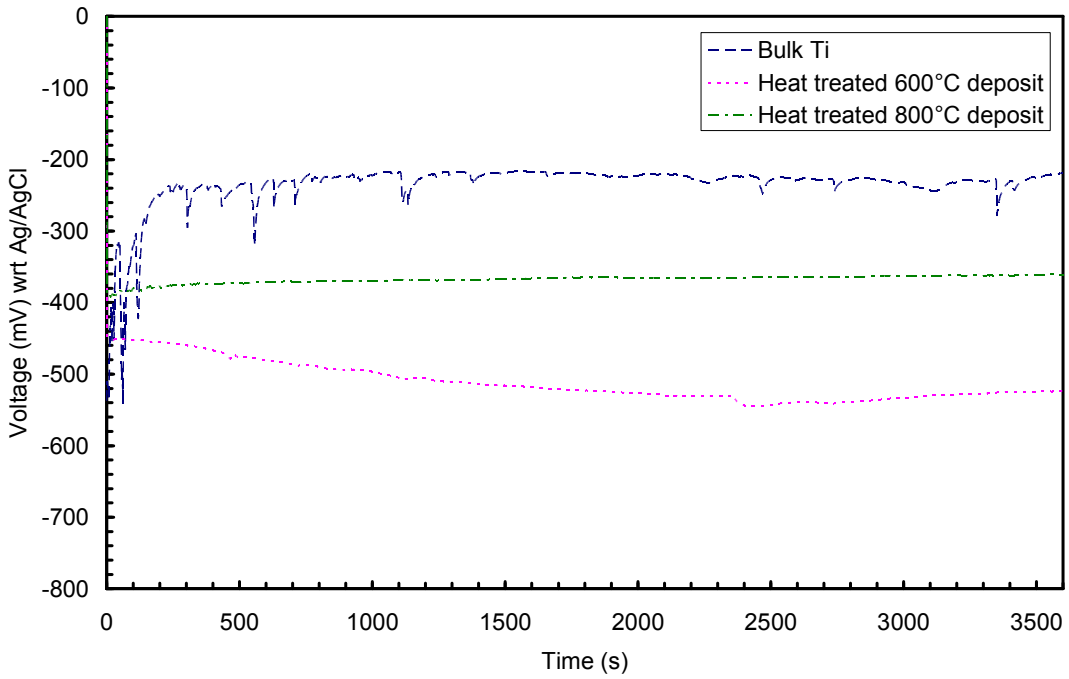

Figure 6-4 Open circuit potential of bulk titanium, heat treated 600 and 800 °C deposits

Open circuit potential measurements of heat treated free standing 600 °C (~porosity 5%) and heat treated 800 °C (~porosity 2 %) deposits in de-aerated 3.5 wt. % NaCl solution are shown in Figure 6-4. The open circuit potential of heat treated 600°C deposit was -525 mV and that of heat treated 800 °C deposit was -365 mV. The heat treatment of free standing 800 °C deposit resulted in a shift of ~145 mV in the more positive direction, towards the bulk titanium. This is a significant difference from the behaviour of heat treated 600 °C deposit, which had similar OCP before and after the heat treatment (~-525 mV).

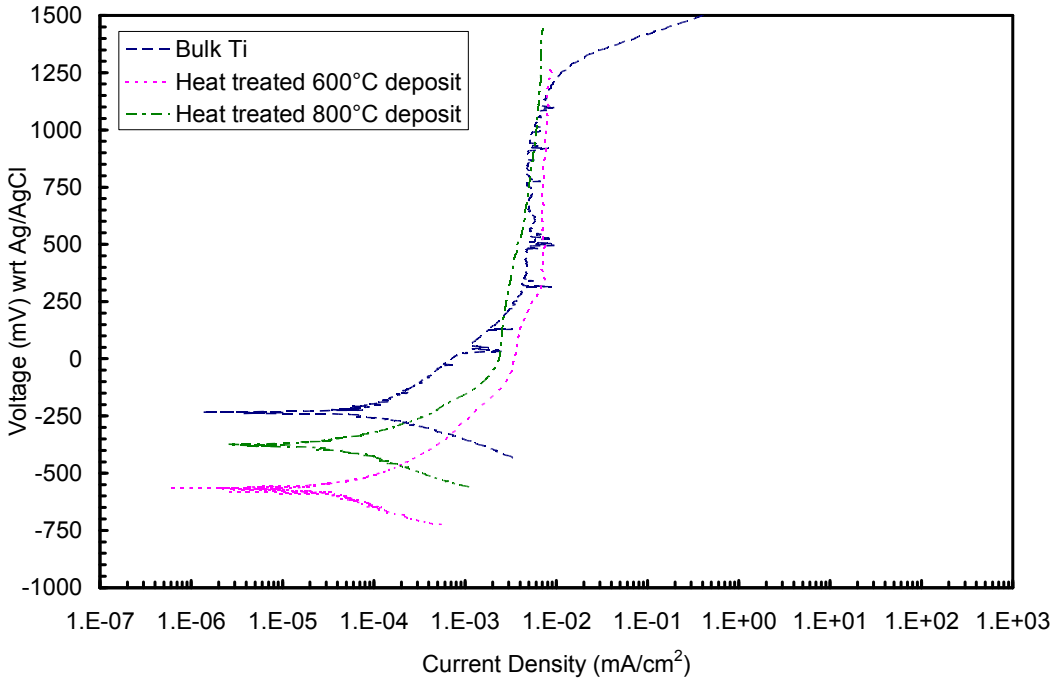

Figure 6-5 Potentiodynamic polarization scans of bulk titanium, heat treated 600 and 800°C deposits

Figure 6-5 shows the potentiodynamic polarization scans of heat treated free standing 600 and 800 °C deposits. In each case, the passive current density was similar to bulk titanium (~0.005 mA/cm^2) which means the heat treatment of free standing 600°C deposit resulted in a decrease of passive current density by 1-2 orders of magnitude. The Ecorr values of the heat treated 600 and 800 °C deposits showed similar trends to OCP measurements. The Icorr value of the 600 °C deposit reduced to 2.4 × 10^{-5} mA/cm^2 from 1.9 × 10^{-3} mA/cm^2 and Icorr value of the 800 °C deposit reduced to 3 × 10^{-5} mA/cm^2 from 2 × 10^{-4} mA/cm^2 following heat treatment. The observed differences in corrosion parameters correlate with different porosity levels.

6.5 Corrosion behaviour of Ti coatings on stainless steel

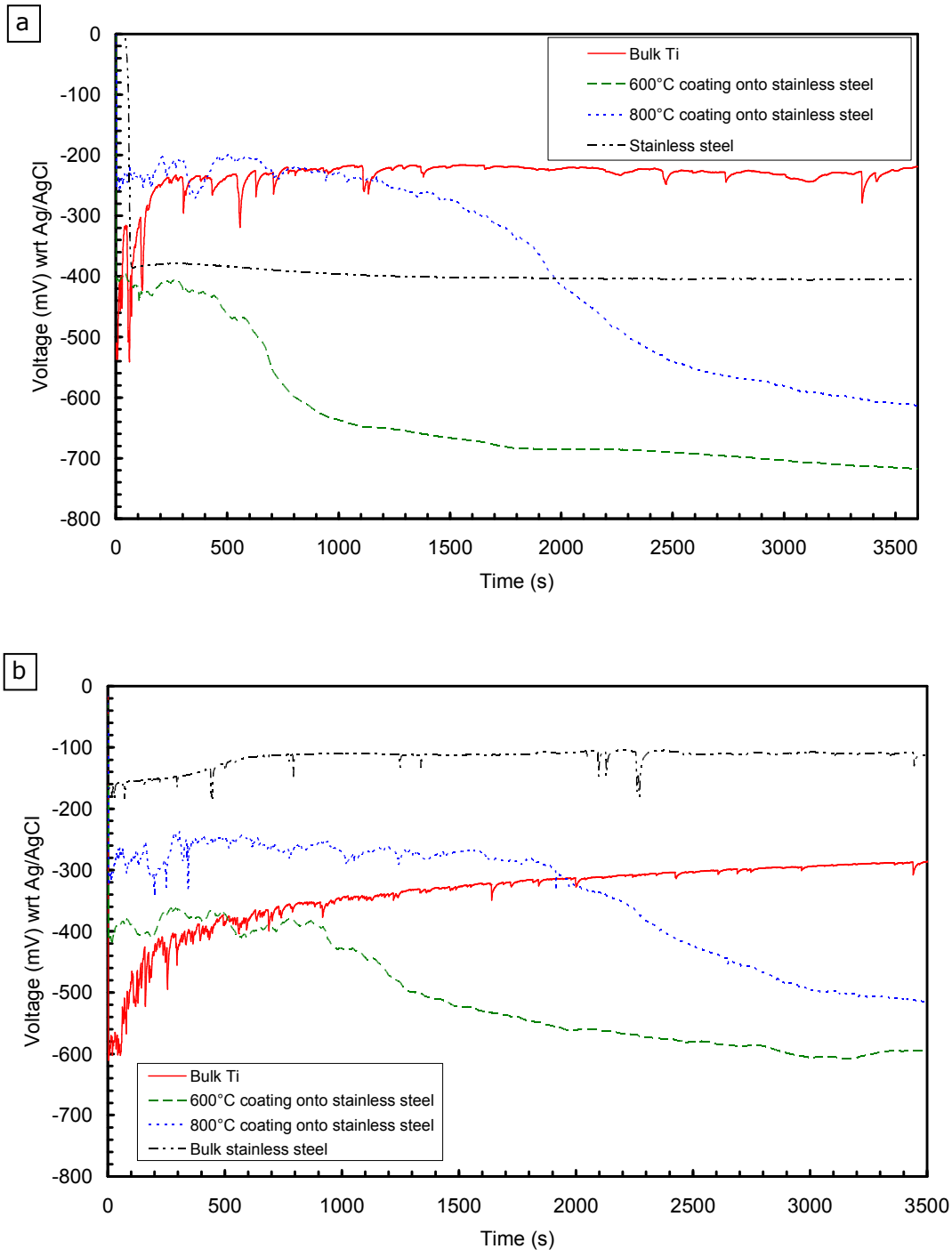

Figure 6-6 Open circuit potentials of bulk Ti, stainless steel, 600 and 800˚C coatings in (a) de-aerated (b) aerated solutions

Figure 6-6 shows the OCP of titanium coatings sprayed at 600 °C (porosity ~11 vol. %) and 800 °C (porosity ~6 vol.%) onto stainless steel along with data for bulk titanium and stainless steel in de-aerated and aerated solutions for 3600 seconds. In the de-aerated solution, the OCP of bulk titanium was -220 mV and that of stainless steel was -405 mV (Table 6-2). In the same solution, the 600 °C coating reached an OCP value of -720 mV and the 800 °C coating reached an OCP value of -610 mV after 3600 seconds. In the aerated solution, the OCP of bulk titanium was -285 mV which is a 65 mV more negative than that of de-aerated solution. However, the remainder of the samples in the aerated solution showed an increase in OCP values compared to those of the de-aerated solutions. OCP of the bulk stainless steel increased to -110 mV, which is a 300 mV shift towards the positive direction. In the same solution, the OCP of the 600°C coating was -595 mV and the OCP of the 800°C coating was -515 mV after 3600 seconds. In both solutions, the OCP values of the 800 °C coatings were higher than that of the 600 °C coatings. Also, both the coatings showed a gradual decrease in OCP values from the onset of immersion in both solutions.

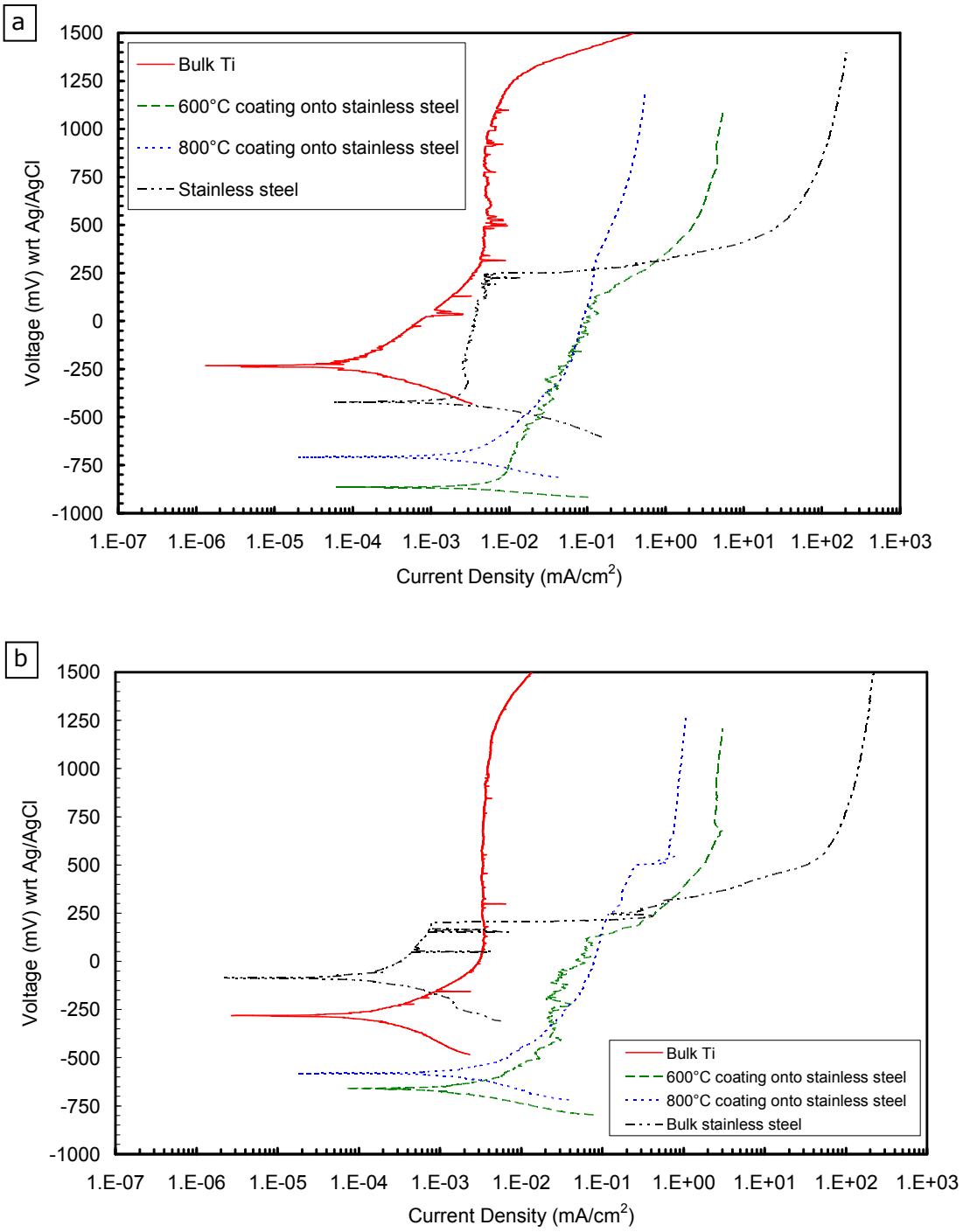

Figure 6-7 Potentiodynamic polarization scans of bulk Ti, stainless steel, 600 and 800˚C coatings in (a) de-aerated (b) aerated solutions

Potentiodynamic polarization scans of 600 and 800 °C coatings onto stainless steel, bulk titanium and stainless steel in de-aerated and aerated solutions are shown in Figure 6-7. The values of the principal corrosion parameters are listed in

Table 6-2**.** In the de-aerated solution, both bulk titanium and stainless steel had an Ipp value of 0.005 mA/cm^2, however the passivation breakdown potential of stainless steel was 245 mV, whereas that of titanium was ~1200 mV. The "passive like" corrosion current density of the 600°C coating was 4.5 mA/cm^2 and that of 800°C coating was 0.45 mA/cm^2 at a potential of 1000 mV. These current densities are 2-3 orders of magnitude higher than that of bulk titanium. The Ecorr values of the bulk materials and the coatings showed similar trends to the OCP measurements.

In the aerated solution, Ipp value of bulk titanium remained unchanged but the Ipp value of the stainless steel decreased by 10 times. However, the potential range over which the stainless steel shows passivity reduced significantly in the aerated solution. "Passive like" current density of the 600°C coating was 2.7 mA/cm^2 and that of the 800°C coating was 0.9 mA/cm^2. These values are very similar to the values measured in the de-aerated solution. However, in both solutions current densities of the 600°C coatings were higher than those of 800°C coatings.

Specimens	OCP wrt Ag/AgCl (mV)	Ecorr wrt Ag/AgCl (mV)	Icorr (mA/cm^2)	Ipp (mA/cm^2)
Bulk titanium (De)	-220	-233	6.0×10^{-5}	0.005
600°C coating (De)	-720	-705	5×10^{-3}	4.5
800°C coating (De)	-610	-865	2.0×10^{-3}	0.45
Stainless steel (De)	-405	-420	2.0×10^{-3}	0.005
Bulk titanium (Ae)	-285	-281	1×10^{-4}	0.004
600°C coating (Ae)	-595	-660	1.5×10^{-3}	2.7
800°C coating (Ae)	-515	-581	1.5×10^{-3}	0.9
Stainless steel (Ae)	-110	-85	1.5×10^{-4}	0.0008

Table 6-2 Corrosion parameters of 600 and 800˚C coatings onto stainless steel

Immersion tests of the 600 and 800 ˚C coatings were performed in aerated 3.5 wt.% NaCl solution at 80 ˚C.

Figure 6-8 (a, b) show the surface of the titanium coatings sprayed at 600 and 800°C gas temperatures onto stainless steel substrates before immersion.

Figure 6-8 (c, d) show both the samples after 30 hours of exposure. The surface of the 600 °C coating shows discolouration (on the upper right corner) whereas the 800 °C coating shows specs of brown rust, marked with arrow.

Figure 6-8 (e, f) show the surface of the coatings following 165 hours of exposure. Three quarters of the 600 °C coating was tarnished and dark red corrosion products are seen on the surface (

Figure 6-8e) , whereas the 800 °C coating shows only a number of small corrosion spots all across the surface (

Figure 6-8f). The images suggest very different degree of corrosion attack of the two coatings under these particular conditions.

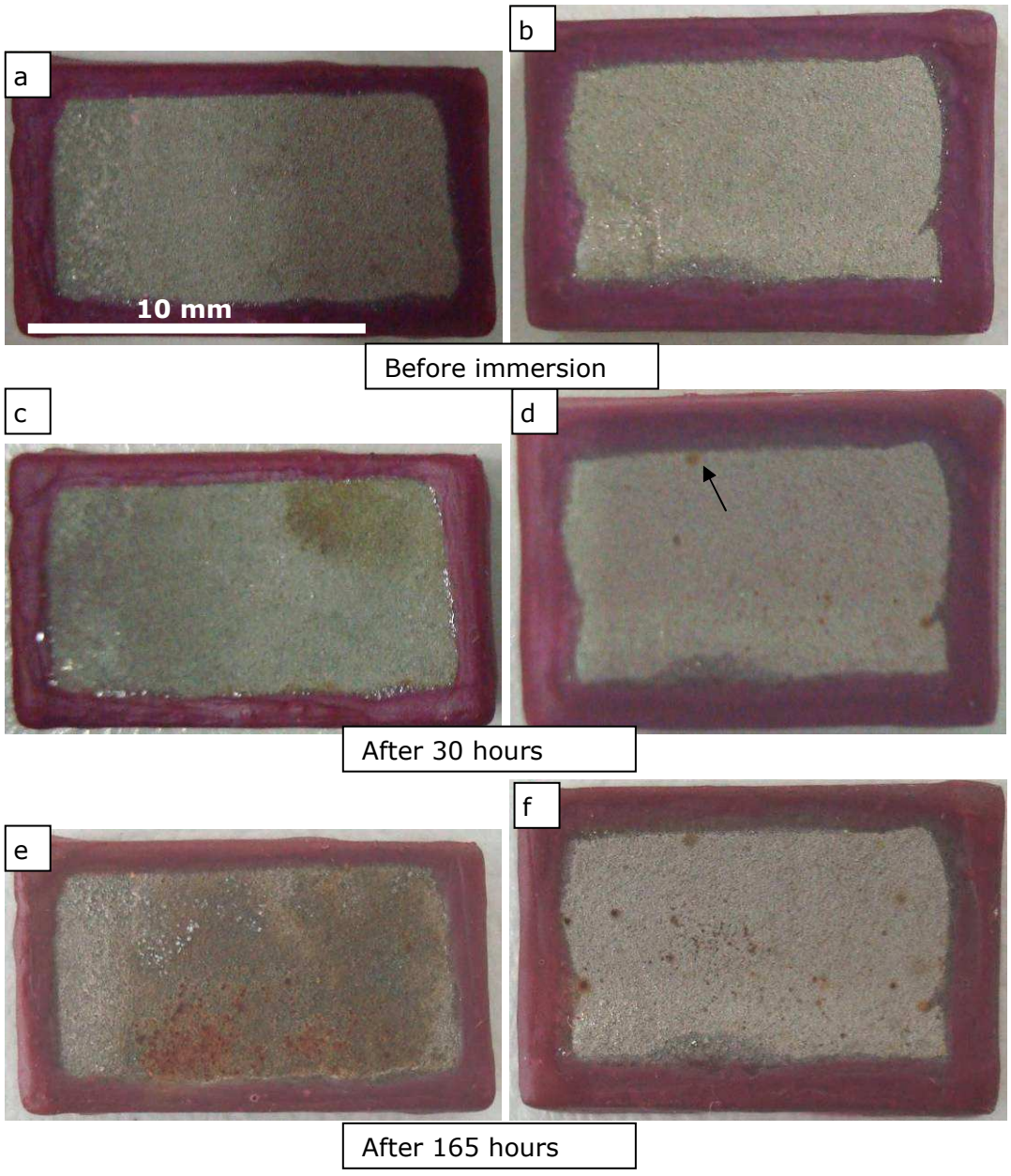

Figure 6-8 Immersion tests of 600°C (a, c, e) and 800°C (b, d, f) Ti coatings on stainless steel (a, b) before immersion (c, d) after 30 hours and (e, f) after 165 hours

Figure 6-9 (a, b) show cross sections of the 600 and 800 °C coatings following the immersion test for 165 hours. It can be seen that the coating-substrate interface of the 600 °C sample is severely attacked by the corrosive solution and corrosion product is present at the interface (darker circular region in the BSE image in Figure 6-9a)**.** Energy dispersive X-ray analysis in the SEM showed the corrosion products in the dark region were composed of oxygen, sodium, chlorine and iron. The higher magnification image of the 600 °C coating, Figure 6-9 (c), shows formation of the pits along the coating-substrate interface, marked with an arrow. In contrast to the 600 °C coating, the cross-section of the 800 °C coating shows a lower extent of corrosion attack, as can be seen from Figure 6-9 (b). A small fraction of the coating-substrate interface in Figure 6-9 (b) shows defects (marked with an arrow). Moreover, cracks at the stainless steel substrate following the immersion tests are seen in Figure 6-9 (d), marked with a circle.

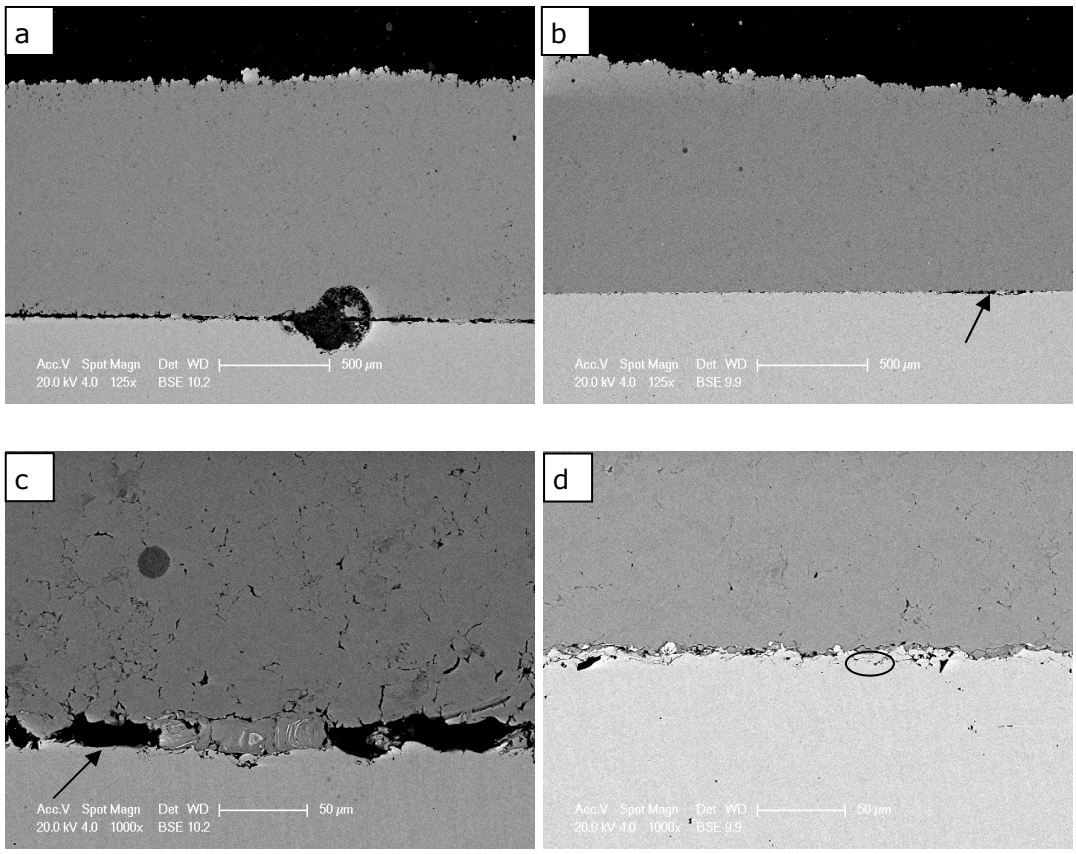

Figure 6-9 SEM images of the cross section of 600°C coating (a, c) and 800 °C coating (b, d) after immersion tests of 165 hours.

6.6 Corrosion behaviour of Ti coatings on carbon steel

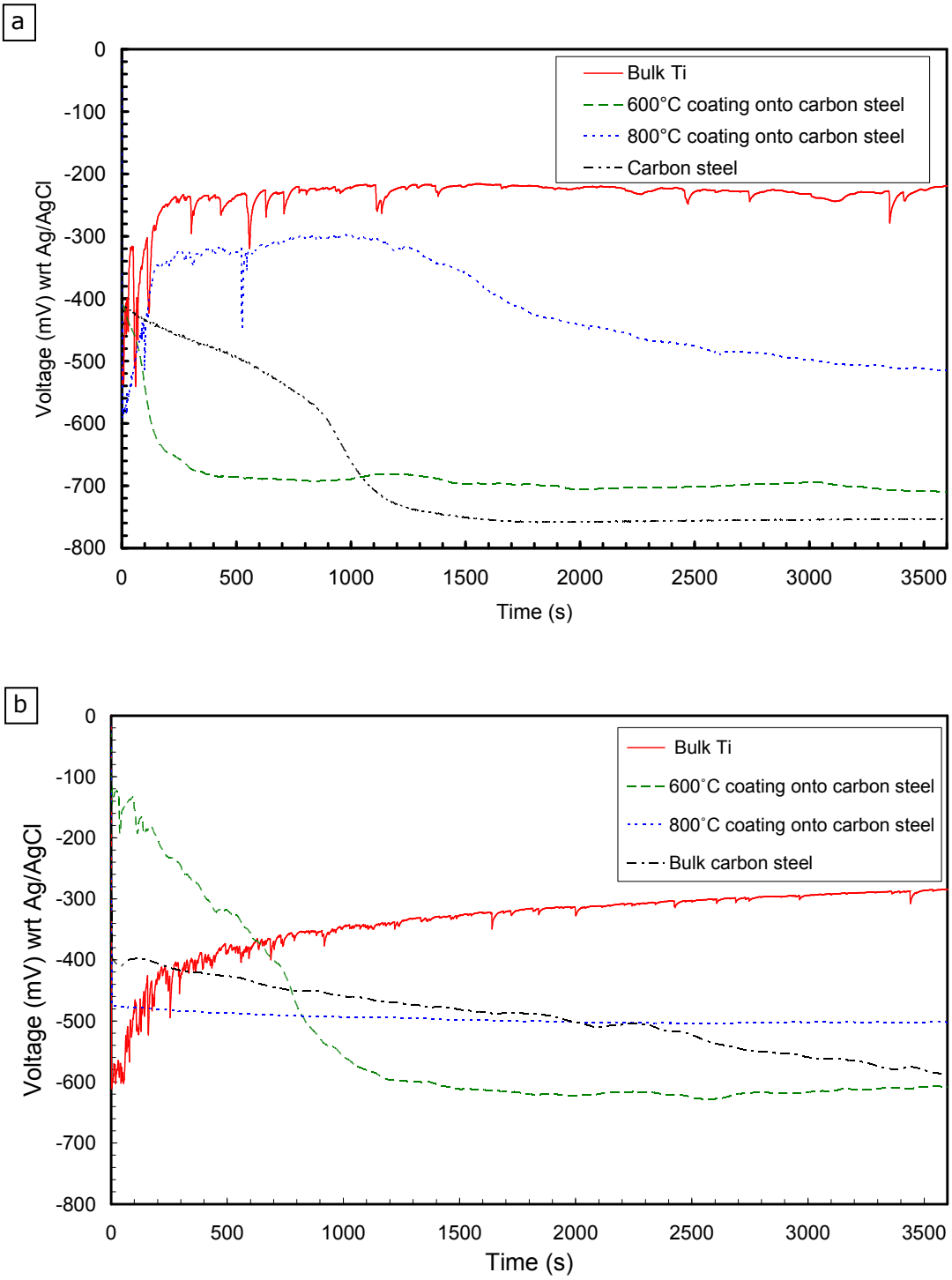

Figure 6-10 Open circuit potentials of bulk Ti, carbon steel, 600 and 800 ˚C coatings in (a) de-aerated (b) aerated solutions

Figure 6-10 shows the OCP of the 600 °C (porosity ~11 vol. %) and 800 °C (porosity ~6 vol.%) coatings onto carbon steel along with data for bulk titanium and bulk carbon steel in de-aerated and aerated solutions for 3600 seconds. In the de-aerated solution, carbon steel reached a steady state OCP of -750 mV after 1200 seconds of immersion. Also, the 600 °C coating reached a steady state OCP of -700 mV after 200 seconds of immersion and remained at that level during the full length of the experiment. The 800 °C coating showed an OCP value of -320 mV upon immersion, which is closer to bulk titanium, and gradually dropped to -500 mV after 3600 seconds. In aerated solution, carbon steel showed a decreasing trend of the OCP, which reached -590 mV after 3600 seconds. In the same solution, the OCP of the 800°C coating was -500 mV and OCP of 600°C coating was -605 mV after 3600 seconds. In both solutions, the OCP values of coatings sprayed at 800°C were higher than those of coatings sprayed at 600°C.

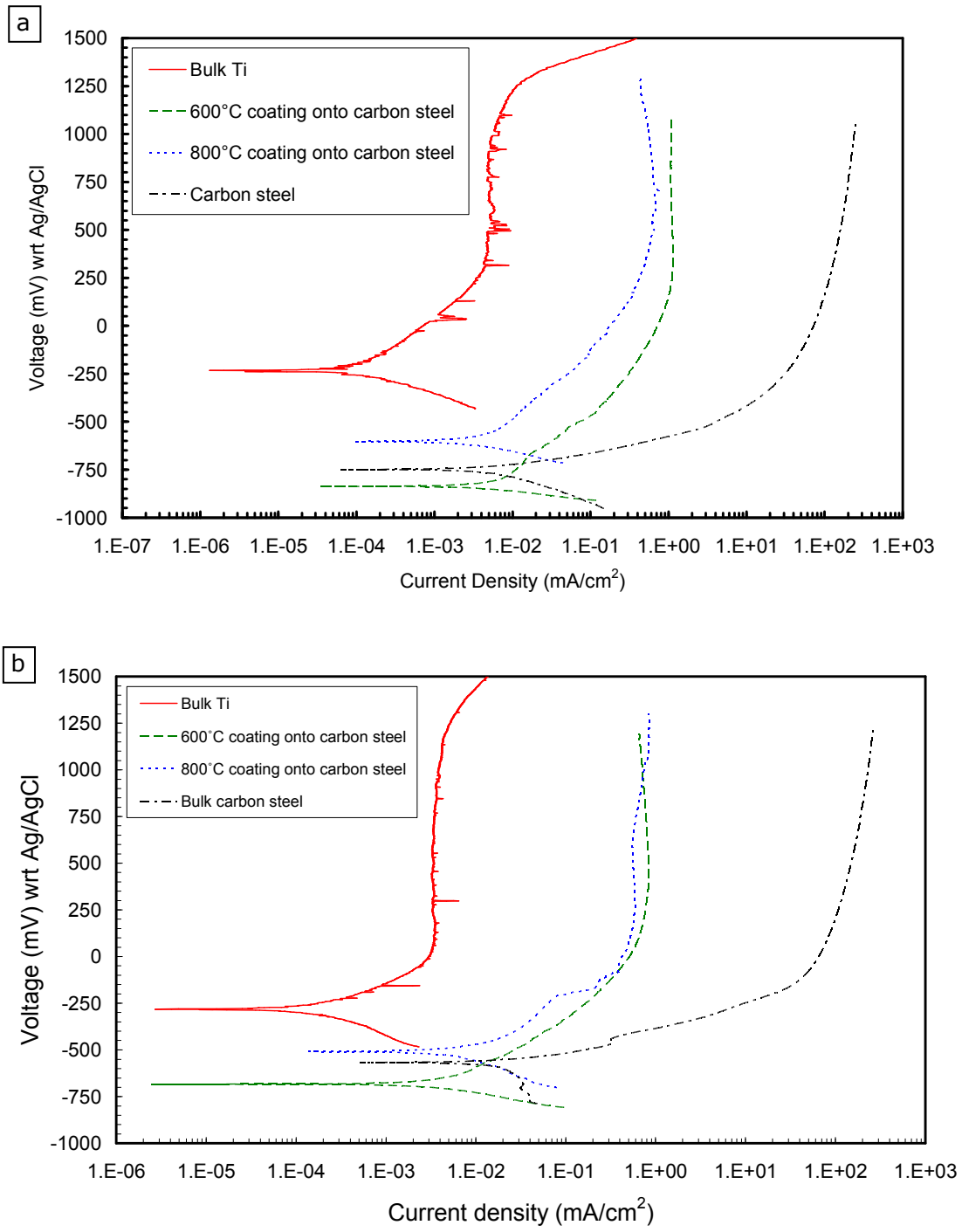

Figure 6-11 Potentiodynamic polarization scans of bulk Ti, carbon steel, 600 and 800 ˚C coatings in (a) de-aerated (b) aerated solutions

Potentiodynamic polarization scans of 600 and 800 °C coatings onto carbon steel, bulk titanium and carbon steel in de-aerated and aerated solutions are shown in Figure 6-11. In de-aerated solution, 600 °C coating showed an Icorr value of 3.5

× 10^{-3} mA/cm^2 and Ecorr value of -836 mV; and 800 °C coating showed an Icorr value of 2 × 10^{-3} mA/cm^2 and Ecorr value of -603 mV (Table 6-3). 600 °C coating showed "passive like" corrosion current density of 1.1 mA/cm^2 and 800 °C coating showed a value of 0.7 mA/cm^2; these are around two orders of magnitude greater than bulk titanium passive current density of 0.005 mA/cm^2. A piece of carbon steel substrate was also tested under similar conditions for reference. Carbon steel had an Icorr value of 3 × 10^{-3} mA/cm^2 and Ecorr value of -750mV. The current density of carbon steel increased rapidly with overpotential and reached a limiting value of 1000 mA/cm^2 at 1050 mV. In aerated solution, 600°C coating showed an Icorr value of 3.5 × 10^{-3} mA/cm^2 and 800°C coating showed an Icorr value of 5 × 10^{-3} mA/cm^2, both of which are again an order of magnitude higher than that of bulk titanium. The Ipp of 600°C coating was 0.8 mA/cm^2 and that of 800°C coating was 0.6 mA/cm^2, which are also several times higher than bulk titanium current density. The values of Icorr and Ipp of both coatings in de-aerated and aerated solutions were very similar. Keeping in mind the nature of potentiodynamic tests, the only observable difference was in the values of Ecorr. In aerated solution, Ecorr values of both the coatings were less negative than that of the de-aerated solution.

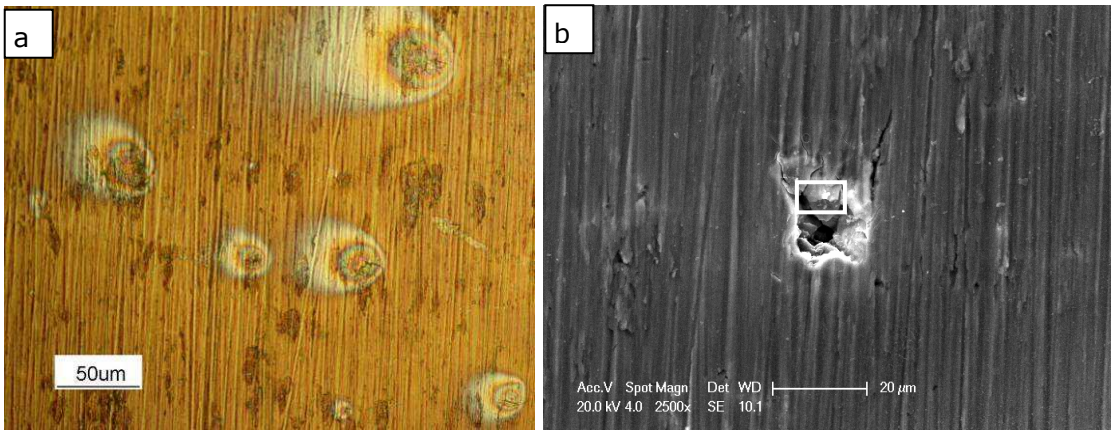

Figure 6-12 (a) Optical microscope image of 600°C coating following electrochemical tests (b) SEM image of localized corrosion

Figure 6-12 (a, b) show low and high magnifications of the plan view of the ground top surface of 600 °C coating after OCP measurements and potentiodynamic polarization test. The optical microscope image of Figure 6-12(a) shows evidence of localized corrosion on the sample surface, where the electrolyte percolated through the coating and attacked the carbon steel substrate. Figure 6-12(b) shows a higher magnification SEM image of one of the localized corrosion regions. Energy dispersive X-ray analysis in the SEM of the boxed region showed presence of iron, oxygen, sodium and chlorine on the titanium coating surface.

Specimens	OCP wrt Ag/AgCl (mV)	Ecorr wrt Ag/AgCl (mV)	Icorr (mA/cm^2)	Ipp (mA/cm^2)
Bulk titanium (De)	-220	-233	6.0×10^{-5}	0.005
600°C coating (De)	-700	-836	3.5×10^{-3}	1.1
800°C coating (De)	-500	-603	2.0×10^{-3}	0.7
Carbon steel (De)	-750	-740	3.0×10^{-3}	-
Bulk titanium (Ae)	-285	-281	1×10^{-4}	0.004
600°C coating (Ae)	-605	-683	3.5×10^{-3}	0.8
800°C coating (Ae)	-500	-507	5×10^{-3}	0.6
Carbon steel (Ae)	-590	-567	2×10^{-2}	-

Table 6-3 Corrosion parameters of 600 and 800˚C coatings onto carbon steel

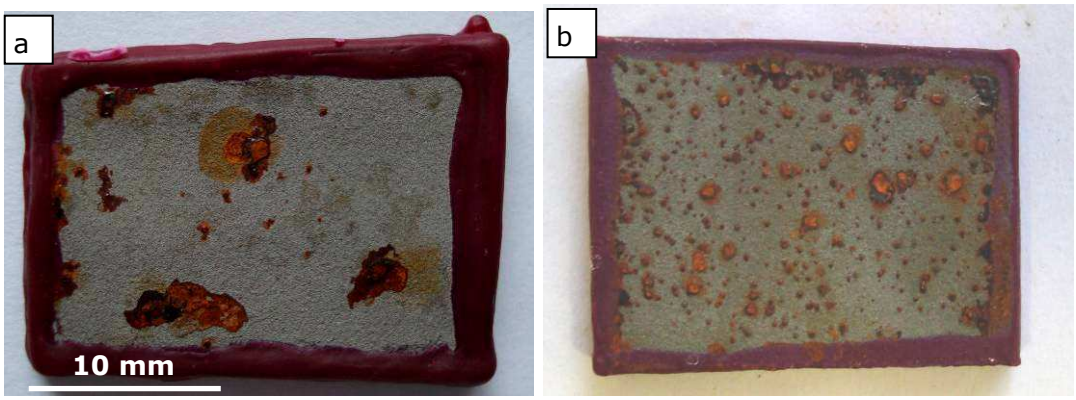

Figure 6-13 Salt spray (fog) samples of Ti coatings on carbon steel after 24 hours of exposure (a) 600 (b) 800 °C coatings

Figure 6-13 (a, b) show the salt spray (fog) test results of 600 and 800 °C coatings onto carbon steel after 24 hours of exposure. The 600 °C coating shows severe attack with pits on the surface, where distinctive yellow rust from the corrosion of carbon steel substrate was present. The surface of the 800 °C coating showed a large number of small corrosion spots after the test. The 800 °C coating shows uniformly distributed corrosion product over the entire surface as opposed to a few large corrosion pits in the 600 °C coating. These coatings were tested in the as-sprayed surface conditions. A further set of tests was performed on coatings which were ground with p1200 grit prior to testing.

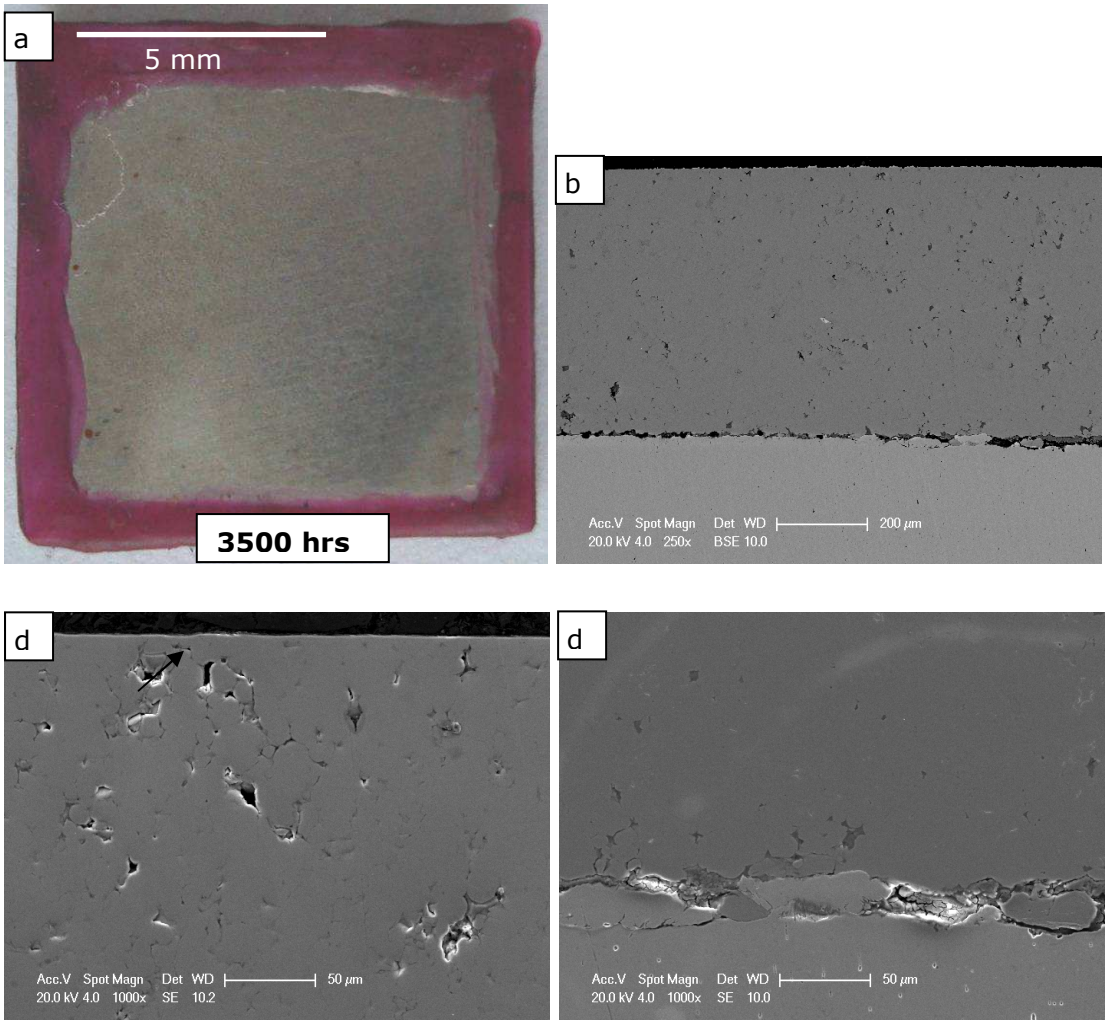

Figure 6-14 (a) Optical image of 600 °C Ti coating on carbon steel after 3500 hours of exposure in salt spray (fog). (b) BSE image of the cross-section. SE images of (c) the top region (d) coating-substrate interface.

Figure 6-14 shows the salt spray test results for the ground surface samples. Very small corrosion spots without any large pits were seen after 3500 hours of exposure, whereas the as-sprayed surface showed signs of corrosion in less than 24 hours (Figure 6-13 a). However, the cross-section of the coating, examined in BSE mode, still shows defects along the coating-substrate interface (Figure 6-14b). These indicate that the substrate was attacked by the aqueous solution. It is evident that grinding the top surface of the coating extended the life of the coating by a few thousand hours but it failed to provide barrier-like properties.

High magnification images of the top section of the coating show folding of particles and sealing the pores following surface grinding (marked with an arrow in Figure 6-14c). It can also be seen that interparticle pores still exist in the coating but the top layer of the coating is virtually sealed due to grinding. Figure 6-14 (d) shows the coating-substrate interface after 3500 hours of exposure, where formation of localized pits in the carbon steel substrate is seen.

6.7 Corrosion behaviour of laser treated Ti coatings on carbon steel

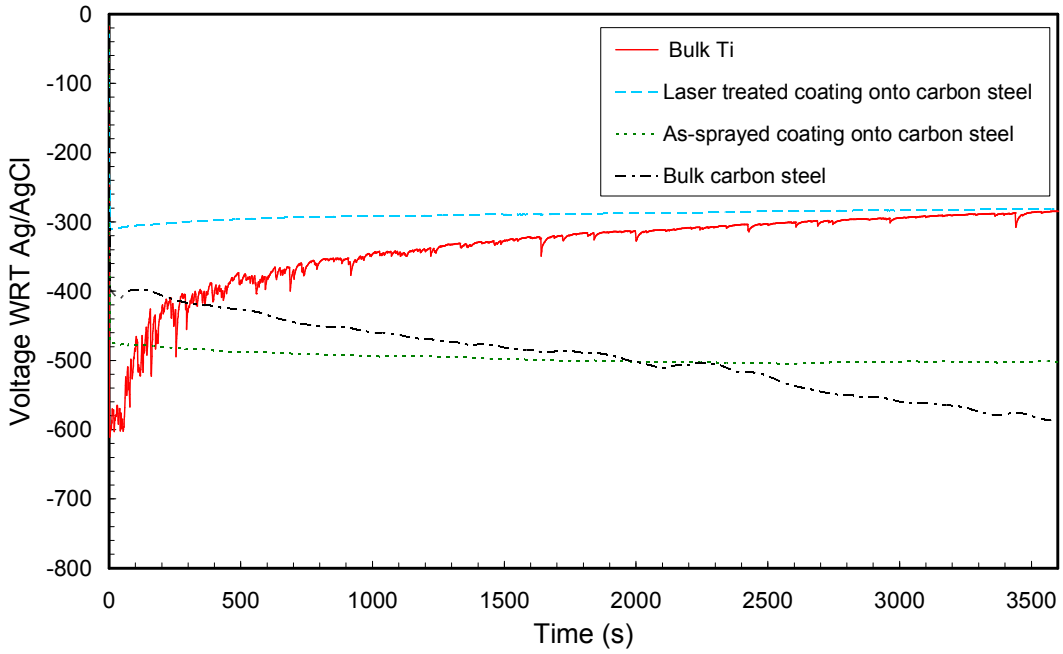

Figure 6-15 Open circuit potential of bulk Ti, carbon steel, 800 °C coating onto carbon steel and laser treated coating in aerated 3.5% NaCl

Figure 6-15 shows the OCP values of bulk titanium, carbon steel, as-sprayed coating onto carbon steel and a laser treated coating on carbon steel substrates in aerated solution for 3600 seconds. Due to the small number of laser treated samples produced, the tests could only be performed in aerated solution. OCP of bulk titanium was -285mV and carbon steel reached an OCP of -590 mV after

3600 seconds. As-sprayed 800°C coating onto carbon steel had a steady state OCP of -500mV and remained at that level during the full length of the experiment. The laser treated titanium coating onto carbon steel showed a steady state OCP of -285 mV after 3600 seconds, which is the same as that of the bulk titanium. Therefore, the laser surface treatment of the coating shifted the OCP by -210 mV in the more positive direction, towards the bulk titanium value.

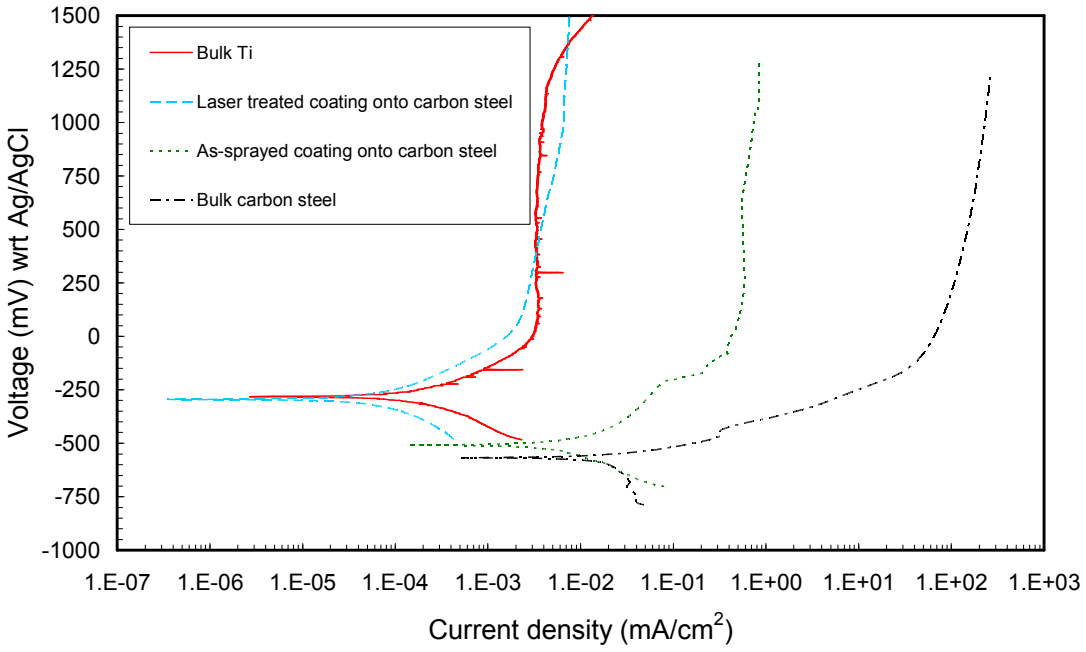

Figure 6-16 Potentiodynamic polarization scans of bulk Ti, carbon steel, 800 °C coating onto carbon steel and laser treated coating in aerated 3.5% NaCl

Potentiodynamic polarization scans of as-sprayed coatings onto carbon steel, laser treated coatings onto carbon steel, bulk titanium and carbon steel are shown in Figure 6-16**.** Bulk titanium shows an Ipp of 0.004 mA/cm^2 but the as-sprayed titanium coating shows a "passive like" current density of 0.6 mA/cm^2 which is two orders of magnitude greater than the bulk titanium. However, laser treated coating shows an Ipp of 0.005 mA/cm^2 which is virtually the same as that of bulk titanium. Laser treatment of the coatings resulted in a decrease in passive

current density by two orders of magnitude. In addition, as-sprayed coating had an Icorr value of 5×10^{-3} mA/cm^2, which changed to 5×10^{-5} following laser treatment (Table 6-4), which is two orders of magnitude smaller than as-sprayed Icorr. It should be mentioned here that the corrosion current density is directly proportional to the corrosion rate of the metals. Ecorr values of all the samples showed similar trend to the OCP measurements.

Specimens	OCP wrt Ag/AgCl (mV)	Ecorr wrt Ag/AgCl (mV)	Icorr (mA/cm^2)	Ipp (mA/cm^2)
Bulk titanium	-285	-281	1×10^{-4}	0.004
As-sprayed 800 °C coating onto carbon steel	-500	-507	5×10^{-3}	0.6
Laser treated 800 °C coating onto carbon steel	-285	-294	5×10^{-5}	0.005
Carbon steel	-590	-567	2×10^{-2}	-

Table 6-4 Corrosion parameters of as-sprayed and laser treated 800 ˚C coatings onto carbon steel in aerated 3.5% NaCl

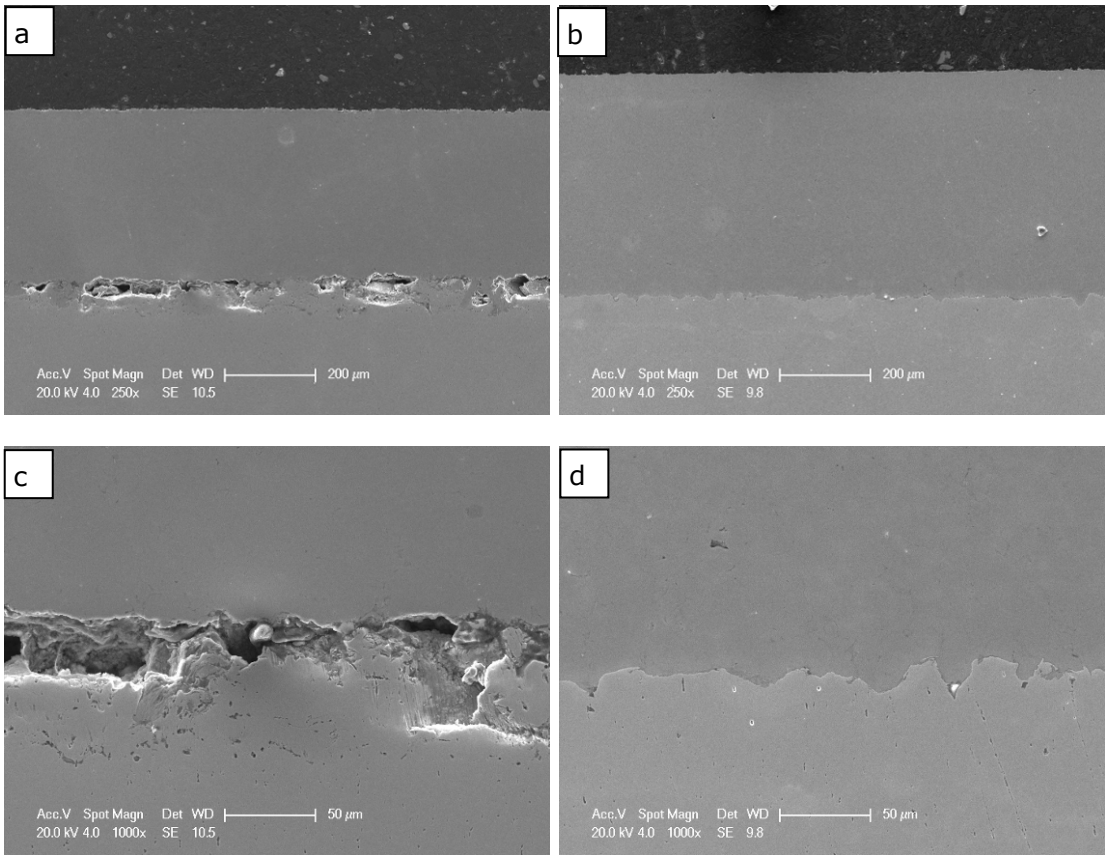

Figure 6-17 SE images of (a) as-sprayed (b) laser treated coatings onto carbon steel after electrochemical tests. Corresponding high magnification images of the interface (c) and (d)

Figure 6-17 (a, b) show the cross section of the as-sprayed coating onto carbon steel substrate and laser treated coating onto carbon steel substrate after OCP and potentiodynamic scans in aerated solution. It is evident that the coating-substrate interface of the as-sprayed sample shows severe pitting following the electrochemical tests, whereas the laser treated coating-substrate interface is free from any defect or pitting as such. Figure 6-17 (c, d) show higher magnification images of the coating-substrate interface of the as-sprayed coating and the laser treated coating. It can be seen the as-sprayed coating substrate interface shows significant corrosion attack of the carbon steel substrate through the interconnected pores in the coating. On the other hand, the coating-substrate

interface of the laser treated sample appears unaffected following the corrosion tests.

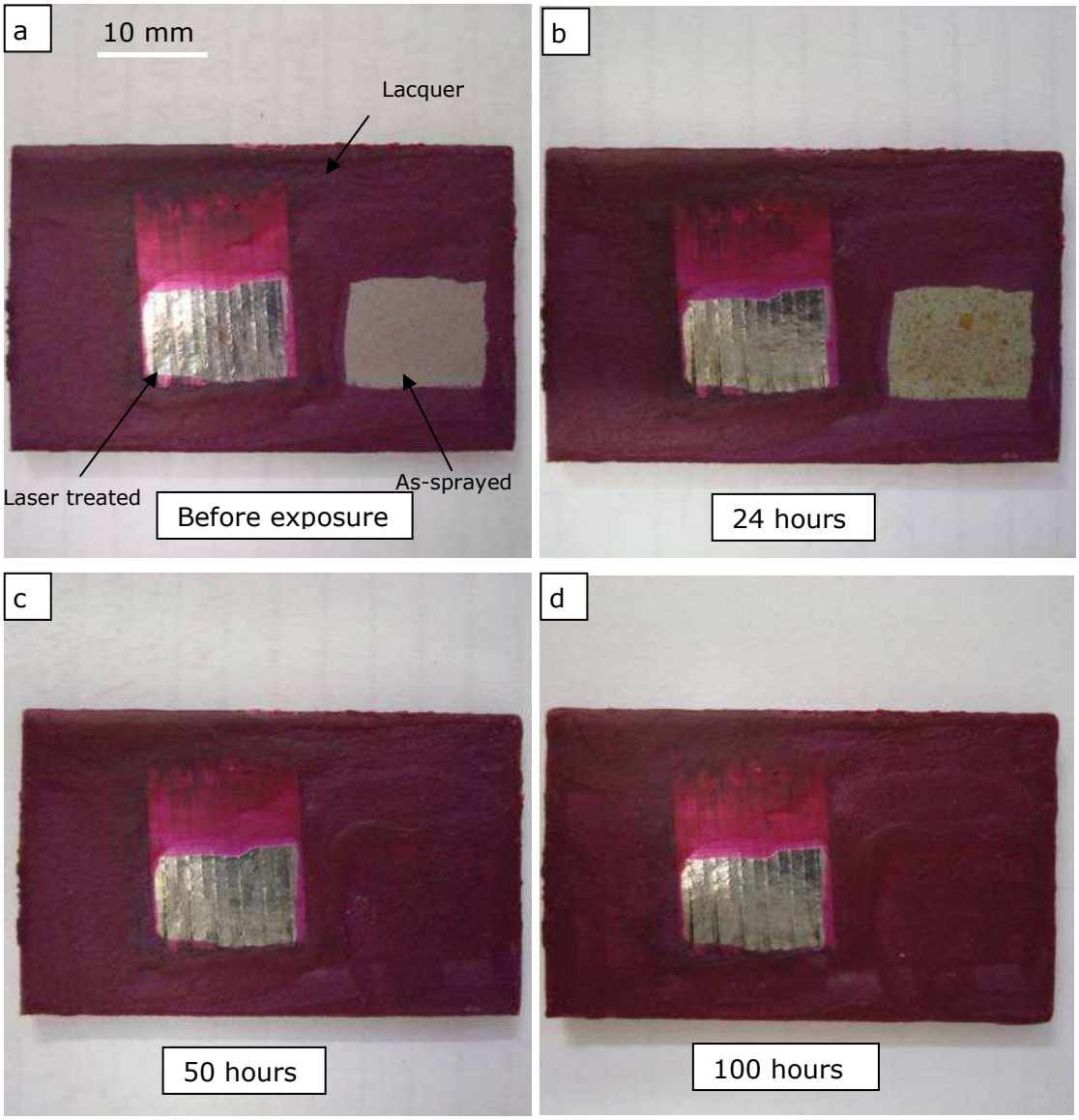

Figure 6-18 Salt spray (fog) sample sprayed at 800˚C: (left) laser treated and (right) as-sprayed (a) before exposure (b) after 24 hours. Only laser treated section after (c) 50 hours (d) 100 hours.

Figure 6-18(a) shows the sample surface of the laser treated and as-sprayed coating onto carbon steel before the salt spray tests. Two sections on the sample were selected for the salt spray test to eliminate any sample to sample variations during the test. The as-sprayed section was covered with lacquer after 24 hours to avoid any further corrosion of the sample. Figure 6-18(b) shows the surfaces

of the sample after 24 hours of exposure in salt spray (fog). The as-sprayed coating shows yellow rust from from the carbon steel on the surface, whereas the laser treated coating was free from any yellow rust. The sample surface of the as-sprayed coating after 24 hours of exposure is very similar to Figure 6-13(b), which was also exposed for 24 hours. Figure 6-18(c, d) show the surface of the laser treated section after 50 hours of exposure and 100 hours of exposure in the salt spray test. It can be seen that there was no sign of yellow rust in any of the laser treated samples. However, a slight change in colour in between the overlapping laser tracks is noticeable.

6.8 Discussion

6.8.1 Corrosion behaviour of free standing deposits

In thermally sprayed coatings open circuit potential measurements and potentiodynamic polarization scans have been widely used to evaluate the corrosion behaviour [207-210]. In the present potentiodynamic experiments, heat treated 600 °C deposit, as-sprayed 800 °C deposit, and heat treated 800 °C deposit show a passive current density similar to the bulk titanium, which means that the change in porosity level from ~6 vol. % to ~2 vol. % does not have a significant effect on the passive current density. However, the as-sprayed 600 °C deposit with a porosity of ~11 vol. % shows an increased passive current density (by 1-2 orders of magnitude). This could in part be due to an increase in "true surface area" taking part in the corrosion reactions. In support of this, a similar increase in passive current density with increasing porosity in sintered and warm sprayed titanium has also been reported in literature [175, 211]. Moreover, in contrast to APS, arc, or flame sprayed titanium deposits, cold sprayed titanium deposits are apparently free from oxides and nitrides, and hence the increase in passive current density is unlikely to arise from the presence of such phases.

In this study, the open circuit potentials of all the deposits show more negative values compared to the bulk titanium, which means that the deposits had active surfaces and higher thermodynamic tendency to corrosion [174]. Also, the open circuit potentials of the deposits did not show any decreasing trend with time because of the stability of the protective oxide film [164]. Also it would appear that OCP and Ecorr values are more sensitive to small amounts of porosity than are passive current densities. In Figure 6-4, the heat treated deposit 800 °C deposit is seen to be cathodic with respect to bulk titanium whereas Figure 6-5 shows a very similar current density.

Corrosion current density (Icorr) is directly proportional to the corrosion rate of the material if the corrosion is uniform over the surface. This might not be the case in this study; nonetheless, Icorr values will provide a baseline for comparison of corrosion rates. Potentiodynamic polarization scans showed that Icorr of free standing 800°C deposit (~6 vol. % porosity) is an order of magnitude smaller than as-sprayed 600 °C deposit (~11 vol. %). In addition, heat treatment of both 600 and 800 °C deposits reduced the Icorr by 1-2 orders of magnitude. Heat treatment of porous titanium deposits eliminates the smaller pores to produce a more homogenous structure and the surface oxide of the particles is removed during heat treatment in a vacuum [208, 212]. Moreover, cold sprayed deposits contain highly deformed particles [82]. These highly deformed particles could act as preferential sites for corrosion [21]. Heat treatment of the as-sprayed deposits also eliminates these high stressed regions and thus reduces the preferential corrosion attack.

6.8.2 Corrosion behaviour of coatings on stainless steel

Titanium and stainless steel are both, on their own, passivating materials which show typical active-passive behaviour in suitable environment. Passivation in a material occurs due to formation of a very thin film on its surface. In the de-aerated solution, the OCP of the bulk stainless steel was less noble than that of the bulk titanium and vice versa in aerated solution. The OCP values of 600 and 800°C (Figure 6-6) coatings were less noble than those of bulk titanium and stainless steel in both aerated and de-aerated solutions indicating that coatings were not performing as impermeable barriers. This is due to the active state of the stainless steel. Stainless steel can show both active and passive material behaviour in the same solution [158]. According to ASM Handbook, stainless steel (304), when in passive state has an OCP of -120 mV and when in active state has a potential of -570 mV (Ag/AgCl) in flowing sea water. In both the coatings, the underlying stainless steel substrates were in an active state which led to these high negative potentials. Moreover, both the coatings showed a gradual decrease in OCP values over time, presumably when the solution started percolation through the coatings. However, the OCP of 800°C coatings were always higher than that of the 600 °C coatings. This indicates a better degree of protection of the substrate by the 800°C coating. A superior corrosion protection of the 800°C coatings was also observed in the immersion test (Figure 6-8). The difference in the corrosion performance can be correlated to the porosity of the coatings: 600 °C coating has a porosity of 11 vol. % and 800 °C coating has a porosity of 6 vol. %. In the potentiodynamic tests, the Icorr and Ipp values of both 600 and 800°C coatings were even higher than that of bulk stainless steel. The high Icorr and Ipp values are due to galvanic corrosion at the coating-substrate interface. Bomberger et al. [165] also reported that the corrosion rate of stainless steel

increases in marine environment when coupled with titanium compared to their uncoupled state.

6.8.3 Corrosion behaviour of coatings on carbon steel

In this study, the coated samples sprayed at both 600 and 800 °C had OCP values between bulk titanium and carbon steel substrate, which indicates salt solution percolation through the coatings. 800 °C coating (porosity ~6 vol. %) had an OCP closer to bulk titanium for first few hundred seconds and then the OCP decreased; presumably when the solution started percolating through the coating and attacking the substrate. However, with 600 °C coating (porosity ~11 vol. %) the OCP decreased to the carbon steel value within a few tens of seconds of immersion. Furthermore, the 600 °C coating had a coarser pore size distribution (0.3- 8 μm) than that of 800 °C (0.18- 1.6) which possibly allowed the solution to percolate through the coating readily. It should also be mentioned that although 600 °C coating was thicker than 800 °C coating, by around ~300 μm, this increased thickness did not provide any increased corrosion resistance. Clearly, therefore less interconnected porosity in coatings plays the major role in corrosion resistance over increased thickness.

Salt spray test results also confirmed the lack of barrier like properties of coatings sprayed at 600 and 800 °C (Figure 6-13 a, b). It is clear that 600 °C coating, which had a higher porosity and larger pores, exhibited only a few but large corrosion spots compared to 800 °C coating. One explanation for this is that once the corrosion of the substrate started due to galvanic effect, it had a higher driving force to continue corroding at the attacked sites instead of forming new pits. In aggressive environments such as salt spray test, micro galvanic cells are

formed across the titanium- carbon steel interface (Figure 6-14), which ultimately results in delamination of the coating.

Potentiodynamic polarization scans of the coatings on carbon steel resulted in a higher Icorr compared to the bulk titanium sheet. The lower amount of porosity in the 800 °C coating compared to the 600 °C coating resulted in a decrease in anodic current. A study by Wang et al. [125] also showed that cold sprayed titanium coating with a lower porosity resulted in a lower Icorr in aerated salt solution. The coating with least porosity (1.6%) in that study, which was measured using image analysis techniques, had an Icorr value ~100 times that of bulk titanium.

In addition, bulk titanium is only susceptible to crevice corrosion in salt solutions at higher temperature. However, in presence of interconnected porosity in coatings, crevice corrosion can also take place at lower temperature. The chloride ions penetrate the open porosity which acts as a crevice (Figure 6-12a). In tight crevices, the concentration of chloride ion increases and corrosion occurs within the pore by depletion of oxygen. The complementary oxygen reduction occurs at the material surface.

6.8.4 Corrosion behaviour of laser treated coatings

Laser surface treatment eliminated the surface connected pores and hence the possibility of the occurrence of crevice corrosion. The result was a shift of 215 mV in the OCP and Ecorr values in the noble direction and a decrease of two orders of magnitude in Ipp value from the as-sprayed condition. Also OCP did not decrease over time and remained close to the bulk titanium level. Hence resolidified surface layer provides impermeable barrier and behaviour of solidified material not different for bulk, wrought sheet. Post-spray laser treatment has also

been reported to improve the corrosion performance of the plasma sprayed titanium coatings [164, 169, 170, 172]. Although TiO was observed to be present in the solidified surface (Figure 5-24), behaviour of the laser treated surface was not different from bulk sheet in solution. In presence of interconnected pores in the coating, large pits are formed at the coating-substrate interface (Figure 6-17). However, laser surface melting seals the surface of the top ~140 μm of the coating during the resolidification of the melt pool and thus, stopping the corrosive liquid to percolate through the coating.

6.9 Summary

Corrosion behaviour of cold sprayed (one sprayed at 600°C and the other sprayed at 800°C) free standing titanium deposits and coatings were studied in 3.5 wt.% NaCl solution in this chapter. The free standing deposits were heat treated to reduce porosity and the effect of porosity on the corrosion performance was studied. Corrosion behaviour of the titanium coatings onto carbon steel and stainless steel were also investigated in de-aerated and aerated conditions using electrochemical methods. In addition, immersion and salt spray (fog) tests were conducted to verify the electrochemical results. Moreover, laser surface melted coatings were studied using electrochemical methods in aerated solution and salt spray tests. The summary of the study on corrosion were as follows

Free standing deposits

- Open circuit potential (OCP) values of the free standing titanium deposits were, in all cases, less noble than that of bulk titanium. OCP and rest potentials (Ecorr) are more sensitive to small amounts of porosity than are passive current densities (Ipp).

Coatings

- The passive current density (Ipp) and corrosion current (Icorr) of both 600 and 800°C titanium coatings onto steel substrates were higher compared

to bulk titanium. Electrochemical corrosion studies of the titanium coatings on steel substrates showed significant substrate influence at the levels of porosity arising from deposition at both 600 and 800 °C. Salt spray tests also confirmed the presence of interconnected porosity in these coatings.

- Coatings sprayed at 800°C gas temperature onto both carbon steel and stainless steel substrates can provide a better corrosion protection than coatings sprayed at 600 °C due to a decreased level of porosity.

Surface treatment effects

- Mechanical grinding and polishing of the coating top layer can improve the corrosion behaviour of the coatings by slowing down the degree of corrosion attack. However, the grinding and polishing cannot eliminate all the surface connected pores.
- Laser surface melted coatings show similar OCP, Ecorr and Ipp values to bulk titanium in the electrochemical corrosion studies. A barrier coating layer can be achieved by laser surface melting to protect carbon steel substrates in corrosive environment.

7 General conclusions

The research work in this thesis was primarily focused on: (i) investigating the bonding mechanisms at the coating-substrate interface in cold sprayed deposits; (ii) optimizing the processing conditions to deposit a pore free titanium coating; and (iii) studying the corrosion behaviour of cold sprayed titanium coatings and free standing deposits. The general conclusions of the research work presented in this thesis are summarized below.

The bonding mechanisms were investigated in this thesis using copper, aluminium and titanium powders on aluminium, copper and steel substrates respectively. Experimental observations of bonding of copper coatings onto aluminium substrate led to the proposal of a bonding model with two components: namely metallurgical bonding between the substrate the coating material and mechanical "interlocked" substrate material within the coating structure. The metallurgical bonding between aluminium and copper can be assessed via an intermetallic growth method, i.e, intermetallics would only form at regions where true metal to metal bonding had occurred during deposition process. When the metallurgical bonding between the coating and substrate is low, the bond strength is dictated by the strength of the interlocked material. However, when the metallurgical bonding is high, the strength is dictated by the metallurgical component. In aluminium coating-copper substrate system, it is clear that the metallurgical component of the bonding is relatively low compared to the copper coating-aluminium substrate system, due to a lower momentum of the aluminium particles and no evidence of "interlocking" of substrate material with the coating occurs. Thus, the overall bond strength of the aluminium coating- copper substrate is low compared to copper coating-aluminium substrate. Grit blasting of low hardness substrates like copper and aluminium are detrimental to the

bonding process. It is postulated that the grit blasting of the substrates shows a less effective jet formation upon impact and hence a weaker metallurgical bond.

The cold spraying of titanium onto low carbon steel (0.04% C) and Armco iron (<0.005% C) shows presence of a barrier to form metal-to-metal contact at the particle-substrate interface which is not removed by the deposition or the consequent heat treatment. However, the barrier is removed following deposition onto stainless steel either during impact or possibly during heat treatment and a metal-to-metal contact is established. The efficient removal of the barrier could be associated with plastic deformation taking place in both the particle and substrate. Also, the metal-to-metal contact at the interface of the particle-substrate can be increased by increasing the deformation of the particle and substrate, and the deformation in cold spraying can be increased by increasing the particle velocity and/or temperature.

This study has also shown that thick titanium coatings can be successfully produced using cold spraying with heated nitrogen as propellant gas. A less porous microstructure of the titanium coating can be achieved by increasing the degree of particle deformation. The bond strength of the titanium coatings onto conventional grit blasted carbon steel substrates was weak which does not allow building up of well bonded deposits. However, changing the surface roughness of the substrates using an in-situ grit blasting can resolve this issue. Cold spraying is capable of producing titanium coatings onto carbon steel, stainless steel and titanium alloy substrates with good bond strength (~70-80 MPa) for industrial applications. In addition, the cold sprayed titanium deposits have a high cohesive tensile strength value, similar to the grade 1 bulk titanium, as determined by the TCT test.

However, porosity remains a barrier in using cold sprayed titanium coatings for corrosion resistant applications. The least porous coating achieved in this study using 800°C gas temperature had a porosity level of 6 vol.%, measured using mercury intrusion porosity. The porosity in the cold sprayed titanium coatings are mostly of submicron size which cannot be accurately measured using image analysis technique.

The corrosion behaviour of all the as-sprayed titanium coatings onto carbon steel substrates show open circuit potential more negative than that of bulk titanium and passive current density higher than that of bulk titanium. The interconnected porosity in the as-sprayed titanium coatings allows percolation of the solution through the coating and results in substrate dissolution. A coating with lower amount of interconnected porosity generally provides a better corrosion protection to the substrate, i.e. in this study 800°C coating showed a higher corrosion resistance (low current density) than that of 600°C coating.

To eliminate interconnected porosity of the as-sprayed titanium deposits post-spray processing needs to be performed. Vacuum heat treatment of the free standing deposits can reduce the porosity of the coatings significantly, i.e, the porosity of the 800°C deposit was reduced to 2 vol.% from 6 vol.% following heat treatment. Open circuit potentials of all free standing deposits were still less noble than bulk titanium due to porosity. Open circuit potentials are found to be more sensitive to small amounts of porosity in deposits than are passive current densities.

Laser surface melting of the titanium coatings can eliminate all the interconnected porosity in the top ~140 μm of the coatings without any deleterious effect on the substrate. The laser surface melted titanium coatings also behave like a barrier layer coating and have corrosion parameters very close to those of bulk titanium.

This thesis ultimately shows that the bonding mechanism in cold spraying is not only metallurgical bonding, but there also exists a mechanical component which also contributes to the overall bonding of the cold sprayed coatings with the substrate. This study has also shown that over the ranges of parameters investigated, an interconnected pore free titanium deposit cannot be achieved by cold spraying alone. However, the laser surface melting of the coatings can eliminate all the interconnected porosity from the top hundred microns of the coating and this laser treated coating can provide excellent corrosion protection in 3.5 wt% NaCl solution.

8 Future work

This chapter presents the future work relevant to the main theme of this thesis to further enhance our understanding of cold spraying technology. It is divided into three main sections corresponding to the three results chapters of the thesis.

8.1 Bonding mechanisms in cold spraying

The bonding mechanisms in cold spraying are of primary interest to the scientific community. A clear understanding of the bonding mechanisms will not only provide a useful ground to develop better coatings but also to explore the difficult to spray materials. In this study, only copper and aluminium coatings were heat treated to identify the regions of metal-to-metal bonding. In addition, wipe test samples of copper and aluminium particles can also be heat treated to identify the regions of metallurgical bond formation at the interface. This will show how the individual particle deformation behaviour is associated with the oxide layer break-up.

Focused ion beam (FIB) lift out of copper, aluminium and titanium particles can be performed and the interface of the particle-substrate can be analysed using transmission electron microscope (TEM). TEM analysis will provide useful information about the grain structure and deformation near the jetted out region and at the centre of the particles. TEM can also be utilized to complement the metal-to-metal bond formation experiments at the interface of the particle, which was proven in this thesis using intermetallic formation. It is time consuming to prepare samples for the TEM analysis; nonetheless, it will provide useful information about the state of the oxides at the interface. FIB milling can be performed to identify the deformation upon impact on different substrates. To

complement FIB, con-focal microscopy can also be used to measure the volume of the deposited particles and calculate the deformation parameters.

The role of different substrate surface preparations in cold spraying has been investigated using copper and aluminium substrate in this thesis. The residual stress state of the substrates can also be investigated using different residual stress measurements techniques, e.g. X-ray diffraction and neutron diffraction etc. The residual stress state of the prepared surface will aid in understanding the bonding behaviour of the particles.

In addition, 3D finite element modelling (FEM) of substrates and particle may be considered to understand the deformation behaviour of particles. Most of the finite element models in cold spraying are axi-symmetrical which does not take into account of the surface roughness of the substrate and the oxides on the surface. Three dimensional modelling of bonding onto different substrate, e.g., polished, ground and grit blasted surface will help in a better understanding of the bonding mechanisms. Johnson-cook parameter for materials, like copper and aluminium are readily available in literature at high strain rate, however a large number of discrepancies in J-C parameters of titanium exist in literature. If possible high strain data of titanium for the model should be determined experimentally.

8.2 Process-structure optimization of titanium coatings

Spraying of titanium coating is a niche area for the cold spraying technology. In this thesis two different process conditions: 600 and 800°C gas temperatures using a commercially available cold spray system was used. Particle image

velocity (PIV) measurement can be used to provide velocity information of the particles in the spray plume. PIV methods for cold spraying e.g., spray watch, oxford laser etc, are not able to measure the temperature of in-flight particles. However, one dimensional isentropic gas flow models with particle acceleration can simulate the effect of processing gas temperature on the particle temperature. In addition, computational fluid dynamics (CFD) code FLUENT can also be used to model the flow of the jet stream.

The mechanical properties of the cold sprayed titanium deposits are critical for commercial applications. Tensile test should be performed to find the stress-strain behaviour of the material. Also, Young's modulus of the deposits should be investigated. Porosity within the deposits makes it difficult to measure the microhardness. Nanohardness measurement should be used to provide reliable hardness measurements. Nanoindentation can also measure the Young's modulus of the deposits.

The post-spray treatments of the titanium deposits were performed using a carbon dioxide laser. However, a diode laser with a wider beam size will be ideal to seal the surface porosity of the coatings. Trials should be conducted using a wider spot diameter to seal the surface which will induce less heat energy to the deposit and subsequently lower chance of coating delamination.

8.3 Corrosion behaviour of cold sprayed titanium coatings

In this thesis open circuit potential and potentiodynamic polarization scans were used to study the corrosion behaviour of the titanium deposits and coatings. In addition, cyclic polarization scans of the coatings can be performed which will

provide additional information on localized corrosion behaviour, i.e., repassivation potential and type of hysteresis loops: forward/ reverse etc. Electrochemical impedance spectroscopy (EIS) measurements will also provide a better understanding of the corrosion behaviour of the porous coatings.

Laser surface melted titanium coatings showed promising results in corrosion protection of the carbon steel substrates. However, due to a shortage of samples, laser treated coatings were only scanned in the aerated NaCl solution. The scans should also be performed in de-aerated NaCl solution. In addition, the thickness of the coating was 550 µm and the laser melt pool depth was only ~140 µm. Future trials should be conducted with a thinner coating layer, which will save material and thus the cost of spraying. It was also found in this study that mechanical grinding of the top layer of the coating surface provides a better corrosion protection. Therefore, shot peening of the top porous layer should be investigated to improve the corrosion behaviour. Shot peening may be able to deform the particles on the top layer to form a barrier layer in corrosion reactions. Future work to improve the corrosion performance of cold sprayed titanium coating should thus focus on enhancing the particle deformation during cold spraying to ensure the elimination of even sub-micron porosity.

References

1. Assadi, H., Gartner, F., Stoltenhoff, T., and Kreye, H., *Bonding Mechanism in Cold Gas Spraying.* Acta Materialia, 2003. 51(15): p. 4379-4394.
2. Ghosh, M. and Chatterjee, S., *Characterization of Transition Joints of Commercially Pure Titanium to 304 Stainless Steel.* Materials Characterization, 2002. 48(5): p. 393-399.
3. Kale, G.B., Patil, R.V., and Gawade, P.S., *Interdiffusion Studies in Titanium 304 Stainless Steel System.* Journal of Nuclear Materials, 1998. 257(1): p. 44-50.
4. Price, T.S., Shipway, P.H., McCartney, D.G., Calla, E., and Zhang, D., *A Method for Characterizing the Degree of Inter-Particle Bond Formation in Cold Sprayed Coatings.* Journal of Thermal Spray Technology, 2007. 16(4): p. 566-570.
5. Papyrin, A.N., *Cold Spray Technology* 2007: Elsevier.
6. Marrocco, T., Development of Improved Cold Spray and HVOF Deposited Coatings, PhD Thesis, University of Nottingham, 2008.
7. Davis, J.R., *Handbook of Thermal Spray Technology* 2004: TSS/ASM International.
8. McCune, R.C., Hall, J.N., Papyrin, A.N., Riggs II, W.L., and Zajchowski, P.H., *An Exploration of the Cold Gas-Dynamic Spray Method for Several Materials System*, in *Advances in Thermal Spray Science and Technology*, C. C. Berndt and S. Sampath, Editors. 1995, ASM International: Houston, TX. p. 1-5.
9. Grujicic, M., Zhao, C.L., DeRosset, W.S., and Helfritch, D., *Adiabatic Shear Instability Based Mechanism for Particles/Substrate Bonding in the Cold-Gas Dynamic-Spray Process.* Materials & Design, 2004. 25(8): p. 681-688.
10. Schmidt, T., Gaertner, F., and Kreye, H., *New Developments in Cold Spray Based on Higher Gas and Particle Temperatures.* Journal of Thermal Spray Technology, 2006. 15(4): p. 488-494.
11. Schmidt, T., Gartner, F., Assadi, H., and Kreye, H., *Development of a Generalized Parameter Window for Cold Spray Deposition.* Acta Materialia, 2006. 54(3): p. 729-742.
12. GmbH, C.G.T. *Cgt- Cold Gas Technology*. 2010 [cited 2010 Sep 27]; Available from: http://www.cgt-gmbh.com/.
13. Inovati. *Inovati- Home of Kinetic Metallization*. 2010 [cited 2010 Sep 27]; Available from: http://www.inovati.com/.
14. Technology, S.S. *Centerline Supersonic Spray Technology (Sst)- Practical Cold Spray Solutions*. 2010 [cited 2010 Sep 27]; Available from: http://www.supersonicspray.com/.
15. Karthikeyan, J., *The Advantages and Disadvantages of the Cold Spray Coating Process*, in *The Cold Spray Materials Deposition Process : Fundamentals and Applications* Victor K. Champagne, Editor. 2007, Woodhead ; CRC Press. p. 62-71.
16. Wong, W., Irissou, E., Legoux, J.-G., and Yue, S., *Influence of Helium and Nitrogen Gases on the Properties of Cold Gas Dynamic Sprayed Pure Titanium Coatings*, in *Thermal spray: Global Solutions for Future Application*, B. R. Marple, A. Agarwal, M. M. Hyland, Y. -C. Lau, C.-J. Li, R. S. Lima, and G. Montavon, Editors. 2010, ASM International: Singapore.
17. Davis, J.R., *Handbook of Thermal Spray Technology*. 2004: TSS/ASM International.
18. Borchers, C., Gartner, F., Stoltenhoff, T., Assadi, H., and Kreye, H., *Microstructural and Macroscopic Properties of Cold Sprayed Copper Coatings.* Journal of Applied Physics, 2003. 93(12): p. 10064-10070.

19. Haynes, J., Pandey, A., Karthikeyan, J., and Kay, A., *Cold Sprayed Discontinuously Reinforced Alumina (Dra)* in *Thermal Spray: Building on 100 Years of Success*, B. R. Marple, M. M. Hyland, Y. Lau, R. S. Lima, and J. Voyer, Editors. 2006, ASM International: Seattle, WA.
20. Koivuluoto, H., Näkki, J., and Vuoristo, P., *Corrosion Properties of Cold-Sprayed Tantalum Coatings.* Journal of Thermal Spray Technology, 2009. 18(1): p. 75-82.
21. Balani, K., Laha, T., Agarwal, A., Karthikeyan, J., and Munroe, N., *Effect of Carrier Gases on Microstructural and Electrochemical Behavior of Cold-Sprayed 1100 Aluminum Coating.* Surface & Coatings Technology, 2005. 195(2-3): p. 272-279.
22. Dykhuizen, R.C. and Smith, M.F., *Gas Dynamic Principles of Cold Spray.* Journal of Thermal Spray Technology, 1998. 7(2): p. 205-212.
23. Alkhimov, A., Kosarev, V., and Klinkov, S., *The Features of Cold Spray Nozzle Design.* Journal of Thermal Spray Technology, 2001. 10(2): p. 375-381.
24. Price, T.S., Cold Gas Dynamic Spraying of Titanium Coatings, PhD Thesis, University of Nottingham, 2008.
25. Oosthuizen, P.H. and Carscallen, W.E., *Compressible Fluid Flow* Mcgraw-Hill Series in Aeronautical and Aerospace Engineering. 1997: McGraw-Hill.
26. Grujicic, M., Zhao, C.L., Tong, C., DeRosset, W.S., and Helfritch, D., *Analysis of the Impact Velocity of Powder Particles in the Cold-Gas Dynamic-Spray Process.* Materials Science and Engineering A, 2004. 368(1-2): p. 222-230.
27. Grujicic, M., Tong, C., DeRosset, W., and Helfritch, D., *Flow Analysis and Nozzle-Shape Optimization for the Cold-Gas Dynamic-Spray Process.* Proceedings of the Institution of Mechanical Engineers, Part B: Journal of Engineering Manufacture, 2003. 217(11): p. 1603-1613.
28. Lee, J., Shin, S., Kim, H., and Lee, C., *Effect of Gas Temperature on Critical Velocity and Deposition Characteristics in Kinetic Spraying.* Applied Surface Science, 2007. 253(7): p. 3512-3520.
29. Li, W.Y., Zhang, C., Guo, X.P., Zhang, G., Liao, H.L., Li, C.J., and Coddet, C., *Effect of Standoff Distance on Coating Deposition Characteristics in Cold Spraying.* Materials & Design, 2008. 29(2): p. 297-304.
30. Gartner, F., Stoltenhoff, T., Schmidt, T., and Kreye, H., *The Cold Spray Process and Its Potential for Industrial Applications.* Journal of Thermal Spray Technology, 2006. 15(2): p. 223-232.
31. Van Steenkiste, T. and Smith, J.R., *Evaluation of Coatings Produced Via Kinetic and Cold Spray Processes.* Journal of Thermal Spray Technology, 2004. 13(2): p. 274-282.
32. Gilmore, D.L., Dykhuizen, R.C., Neiser, R.A., Roemer, T.J., and Smith, M.F., *Particle Velocity and Deposition Efficiency in the Cold Spray Process.* Journal of Thermal Spray Technology, 1999. 8(4): p. 576-582.
33. Pattison, J., Celotto, S., Khan, A., and O'Neill, W., *Standoff Distance and Bow Shock Phenomena in the Cold Spray Process.* Surface and Coatings Technology, 2008. 202(8): p. 1443-1454.
34. Samareh, B., Stier, O., Lüthen, V., and Dolatabadi, A., *Assessment of CFD Modeling Via Flow Visualization in Cold Spray Process.* Journal of Thermal Spray Technology, 2009. 18(5): p. 934-943.
35. Stoltenhoff, T., Kreye, H., and Richter, H.J., *An Analysis of the Cold Spray Process and Its Coatings.* Journal of Thermal Spray Technology, 2002. 11(4): p. 542-550.
36. Yin, S., Wang, X.-f., Li, W.-y., and Xu, B.-p., *Numerical Study on the Effect of Substrate Angle on Particle Impact Velocity and Normal Velocity Component in Cold Gas Dynamic Spraying Based on CFD.* Journal of Thermal Spray Technology.

37. Morgan, R., Fox, P., Pattison, J., Sutcliffe, C., and O'Neill, W., *Analysis of Cold Gas Dynamically Sprayed Aluminium Deposits.* Materials Letters, 2004. 58(7-8): p. 1317-1320.
38. Bae, G., Kumar, S., Yoon, S., Kang, K., Na, H., Kim, H.-J., and Lee, C., *Bonding Features and Associated Mechanisms in Kinetic Sprayed Titanium Coatings.* Acta Materialia, 2009. 57(19): p. 5654-5666.
39. Bae, G., Xiong, Y., Kumar, S., Kang, K., and Lee, C., *General Aspects of Interface Bonding in Kinetic Sprayed Coatings.* Acta Materialia, 2008. 56(17): p. 4858-4868.
40. Grujicic, M., Saylor, J.R., Beasley, D.E., DeRosset, W.S., and Helfritch, D., *Computational Analysis of the Interfacial Bonding between Feed-Powder Particles and the Substrate in the Cold-Gas Dynamic-Spray Process.* Applied Surface Science, 2003. 219(3-4): p. 211-227.
41. Li, C.J., Li, W.Y., and Liao, H.L., *Examination of the Critical Velocity for Deposition of Particles in Cold Spraying.* Journal of Thermal Spray Technology, 2006. 15(2): p. 212-222.
42. Li, W.Y., Liao, H.L., Li, C.J., Bang, H.S., and Coddet, C., *Numerical Simulation of Deformation Behavior of Al Particles Impacting on Al Substrate and Effect of Surface Oxide Films on Interfacial Bonding in Cold Spraying.* Applied Surface Science, 2007. 253(11): p. 5084-5091.
43. Li, W.Y., Liao, H.L., Li, C.J., Li, G., Coddet, C., and Wang, X.F., *On High Velocity Impact of Micro-Sized Metallic Particles in Cold Spraying.* Applied Surface Science, 2006. 253(5): p. 2852-2862.
44. Vlcek, J., Gimeno, L., Huber, H., and Lugscheider, E., *A Systematic Approach to Material Eligibility for the Cold-Spray Process.* Journal of Thermal Spray Technology, 2005. 14(1): p. 125-133.
45. Yokoyama, K., Watanabe, M., Kuroda, S., Gotoh, Y., Schmidt, T., and Gartner, F., *Simulation of Solid Particle Impact Behavior for Spray Processes.* Materials Transactions, 2006. 47(7): p. 1697-1702.
46. King, P., Bae, G., Zahiri, S., Jahedi, M., and Lee, C., *An Experimental and Finite Element Study of Cold Spray Copper Impact onto Two Aluminum Substrates.* Journal of Thermal Spray Technology, 2010. 19(3): p. 620-634.
47. Li, W.-Y., Zhang, C., Li, C.-J., and Liao, H., *Modeling Aspects of High Velocity Impact of Particles in Cold Spraying by Explicit Finite Element Analysis.* Journal of Thermal Spray Technology, 2009. 18(5): p. 921-933.
48. Schmidt, T., Assadi, H., Gärtner, F., Richter, H., Stoltenhoff, T., Kreye, H., and Klassen, T., *From Particle Acceleration to Impact and Bonding in Cold Spraying.* Journal of Thermal Spray Technology, 2009. 18(5): p. 794-808.
49. Assadi, H., Richter, H.J., Gartner, F., Schmidt, T., Stoltenhoff, T., Kreye, H., and Klassen, T., *Particle Acceleration, Impact and Coating Formation in Cold Spraying*, in *8th Colloquium High Velocity Oxy-fuel Flame Spray*, Christian Penszior and Peter Heinrich, Editors. 2009, Gemeinschaft Thermisches Spritzen e.V. (Association of Thermal Sprayers): Erding near Munich. p. 27-36.
50. Xiong, Y., Bae, G., Xiong, X., and Lee, C., *The Effects of Successive Impacts and Cold Welds on the Deposition Onset of Cold Spray Coatings.* Journal of Thermal Spray Technology. 19(3): p. 575-585.
51. Guetta, S., Berger, M., Borit, F., Guipont, V., Jeandin, M., Boustie, M., Ichikawa, Y., Sakaguchi, K., and Ogawa, K., *Influence of Particle Velocity on Adhesion of Cold-Sprayed Splats.* Journal of Thermal Spray Technology, 2009. 18(3): p. 331-342.
52. Johnson, G.R. and Cook, W.H., *Fracture Characteristics of Three Metals Subjected to Various Strains, Strain Rates, Temperatures and Pressures.* Engineering Fracture Mechanics, 1985. 21(1): p. 31-48.

53. Klinkov, S.V., Kosarev, V.F., and Rein, M., *Cold Spray Deposition: Significance of Particle Impact Phenomena.* Aerospace Science and Technology, 2005. 9(7): p. 582-591.
54. Schmidt, T., Gartner, F., Kreye, H., and Klassen, T., *Correlation of Particle Impact Conditions and Coating Properties in Cold Spraying*, in *Thermal Spray: Global Coating Solutions*, E. Lugscheider, Editor 2008, ASM International: Maastricht, The Netherlands. p. 724-731.
55. Bae, G., Kang, K., Na, H., and Lee, C., *Thermally Enhanced Kinteic Sprayed Titanium Coating: Microstructure and Property Improvement for Potential Application*, in *Thermal Spray 2009: Expanding Thermal Spray Performance to New Markets and Applications*, B. R. Marple, M. M. Hyland, Y. -C. Lau, C. -J. Li, R. S. Lima, and G. Montavon, Editors. 2009, ASM International: Las Vegas, NV. p. 290-295.
56. Wu, J.W., Fang, H.Y., Yoon, S., Kim, H., and Lee, C., *The Rebound Phenomenon in Kinetic Spraying Deposition.* Scripta Materialia, 2006. 54(4): p. 665-669.
57. Yin, S., Wang, X.-f., Xu, B.-p., and Li, W.-y., *Examination on the Calculation Method for Modeling the Multi-Particle Impact Process in Cold Spraying.* Journal of Thermal Spray Technology.
58. Kurochkin, Y.V., Demin, Y.N., and Soldatenkov, S.I., *Demonstration of the Method of Cold Gasdynamic Spraying of Coatings.* Chemical and Petroleum Engineering, 2002. 38(3): p. 245-248.
59. Alkhimov, A., Klinkov, S., and Kosarev, V., *Experimental Study of Deformation and Attachment of Microparticles to an Obstacle Upon High-Rate Impact.* Journal of Applied Mechanics and Technical Physics, 2000. 41(2): p. 245-250.
60. Barradas, S., Guipont, V., Molins, R., Jeandin, M., Arrigoni, M., Boustie, M., Bolis, C., Berthe, L., and Ducos, M., *Laser Shock Flier Impact Simulation of Particle-Substrate Interactions in Cold Spray.* Journal of Thermal Spray Technology, 2007. 16(4): p. 548-556.
61. Barradas, S., Molins, R., Jeandin, M., Arrigoni, M., Boustie, M., Bolis, C., Berthe, L., and Ducos, M., *Application of Laser Shock Adhesion Testing to the Study of the Interlamellar Strength and Coating-Substrate Adhesion in Cold-Sprayed Copper Coating of Aluminum.* Surface and Coatings Technology, 2005. 197(1): p. 18-27.
62. Champagne, V.K., Helfritch, D., Leyman, P., Ahl, S.G., and Klotz, B., *Interface Material Mixing Formed by the Deposition of Copper on Aluminum by Means of the Cold Spray Process.* Journal of Thermal Spray Technology, 2005. 14(3): p. 330-334.
63. Christoulis, D.K., Borit, F., Guipont, F., and Jeandin, M., *Evidence of the 2-Stage Build-up Process in Cold Spray from the Study of Influence of Powder Characteristics on Ti-6Al-4V Coating*, in *Thermal Spray: Global Coating Solutions*, E. Lugscheider, Editor 2008, ASM International: Maastricht, The Netherlands.
64. Dykhuizen, R.C., Smith, M.F., Gilmore, D.L., Neiser, R.A., Jiang, X., and Sampath, S., *Impact of High Velocity Cold Spray Particles.* Journal of Thermal Spray Technology, 1999. 8(4): p. 559-564.
65. Kang, K., Yoon, S., Ji, Y., and Lee, C., *Oxidation Dependency of Critical Velocity for Aluminum Feedstock Deposition in Kinetic Spraying Process.* Materials Science and Engineering a-Structural Materials Properties Microstructure and Processing, 2008. 486(1-2): p. 300-307.
66. Li, C.J., Wang, H.T., Zhang, Q., Yang, G.J., Li, W.Y., and Liao, H., *Influence of Spray Materials and Their Surface Oxidation on the Critical Velocity in Cold Spraying.* Journal of Thermal Spray Technology. 19(1): p. 95-101.

67. Li, W., Guo, X., Yu, M., Liao, H., and Coddet, C., *Investigation of Impact Behavior of Cold-Sprayed Large Annealed Copper Particles and Characterization of Coatings.* Journal of Thermal Spray Technology.
68. Shkodkin, A., Kashirin, A., Klyuev, O., and Buzdygar, T., *Metal Particle Deposition Stimulation by Surface Abrasive Treatment in Gas Dynamic Spraying.* Journal of Thermal Spray Technology, 2006. 15(3): p. 382-386.
69. Shukla, V., Elliott, G.S., Kear, B.H., and McCandlish, L.E., *Hyperkinetic Deposition of Nanopowders by Supersonic Rectangular Jet Impingement.* Scripta Materialia, 2001. 44(8-9): p. 2179-2182.
70. Tokarev, A.O., *Structure of Aluminum Powder Coatings Prepared by Cold Gasdynamic Spraying.* Metal Science and Heat Treatment, 1996. 38(3-4): p. 136-139.
71. Van Steenkiste, T.H., Smith, J.R., and Teets, R.E., *Aluminum Coatings Via Kinetic Spray with Relatively Large Powder Particles.* Surface & Coatings Technology, 2002. 154(2-3): p. 237-252.
72. Van Steenkiste, T.H., Smith, J.R., Teets, R.E., Moleski, J.J., Gorkiewicz, D.W., Tison, R.P., Marantz, D.R., Kowalsky, K.A., Riggs, W.L., Zajchowski, P.H., Pilsner, B., McCune, R.C., and Barnett, K.J., *Kinetic Spray Coatings.* Surface & Coatings Technology, 1999. 111(1): p. 62-71.
73. Papyrin, A.N., Klinkov, S.V., and Kosarev, V.F., *Effect of Substrate Activation on the Process of Cold Spray Coating Formation*, in *Thermal spray: Exploring its surfacing potential*, E. Lugscheider, Editor 2005, ASM International: Basel, Switzerland.
74. King, P., Zahiri, S., and Jahedi, M., *Copper Particle Impact onto Aluminium by Cold Spray*, in *Thermal Spray: Global Coating Solutions*, E. Lugscheider, Editor 2008, ASM International: Maastricht, The Netherlands.
75. Balani, K., Agarwal, A., Seal, S., and Karthikeyan, J., *Transmission Electron Microscopy of Cold Sprayed 1100 Aluminum Coating.* Scripta Materialia, 2005. 53(7): p. 845-850.
76. Marrocco, T., McCartney, D.G., Shipway, P.H., and Sturgeon, A.J., *Production of Titanium Deposits by Cold-Gas Dynamic Spray: Numerical Modeling and Experimental Characterization.* Journal of Thermal Spray Technology, 2006. 15(2): p. 263-272.
77. Wu, J.W., Yang, J.G., Fang, H.Y., Yoon, S., and Lee, C., *The Bond Strength of Al-Si Coating on Mild Steel by Kinetic Spraying Deposition.* Applied Surface Science, 2006. 252(22): p. 7809-7814.
78. H. Mäkinen, J. Lagerbom, and P. Vuoristo, *Adhesion of Cold Sprayed Coatings: Effect of Powder, Substrate, and Heat Treatment*, in *Thermal Spray: Global Coating Solutions*, B.R. Marple, M.M. Hyland, Y. Lau, C. Li, R.S. Lima, and G. Montavon, Editors. 2007, ASM International: Beijing, People's Republic of China. p. 31-36.
79. K. Sakaki, T. Tajima, H. Li, S. Shinkai, and Y. Shimizu, *Influence of Substrate Conditions and Traverse Speed on Cold Sprayed Coatings*, in *Thermal Spray: Advances in Technology and Application* 2004, ASM International: Osaka, Japan. p. 358–362.
80. P. Richer, B. Jodoin, K. Taylor, E. Sansoucy, M. Johnson, and L. Ajdelsztajn, *Effect of Particle Geometry and Substrate Preparation in Cold Spray*, in *Thermal spray: Exploring its surfacing potential*, E. Lugscheider, Editor 2005, ASM International: Basel, Switzerland.
81. King, P., Zahiri, S., and Jahedi, M., *Microstructural Refinement within a Cold-Sprayed Copper Particle.* Metallurgical and Materials Transactions A, 2009. 40(9): p. 2115-2123.
82. McCune, R.C., Donlon, W.T., Popoola, O.O., and Cartwright, E.L., *Characterization of Copper Layers Produced by Cold Gas-Dynamic Spraying.* Journal of Thermal Spray Technology, 2000. 9(1): p. 73-82.

83. Borchers, C., Gartner, F., Stoltenhoff, T., and Kreye, H., *Microstructural Bonding Features of Cold Sprayed Face Centered Cubic Metals.* Journal of Applied Physics, 2004. 96(8): p. 4288-4292.
84. Koivuluoto, H., Lagerbom, J., and Vuoristo, P., *Microstructural Studies of Cold Sprayed Copper, Nickel, and Nickel-30% Copper Coatings.* Journal of Thermal Spray Technology, 2007. 16(4): p. 488-497.
85. Kairet, T., Degrez, M., Campana, F., and Janssen, J.P., *Influence of the Powder Size Distribution on the Microstructure of Cold-Sprayed Copper Coatings Studied by X-Ray Diffraction.* Journal of Thermal Spray Technology, 2007. 16(5): p. 610-618.
86. Stoltenhoff, T., Borchers, C., Gartner, F., and Kreye, H., *Microstructures and Key Properties of Cold-Sprayed and Thermally Sprayed Copper Coatings.* Surface & Coatings Technology, 2006. 200(16-17): p. 4947-4960.
87. Calla, E., McCartney, D.G., and Shipway, P.H., *Effect of Deposition Conditions on the Properties and Annealing Behavior of Cold-Sprayed Copper.* Journal of Thermal Spray Technology, 2006. 15(2): p. 255-262.
88. Fukumoto, M., Mashiko, M., Yamada, M., and Yamaguchi, E., *Deposition Behavior of Copper Fine Particles onto Flat Substrate Surface in Cold Spraying.* Journal of Thermal Spray Technology. 19(1): p. 89-94.
89. Triantou, K.I., Sarafoglou, C.I., Pantelis, D.I., Christoulis, D.K., Guipont, V., Jeandin, M., Zaroulias, A., and Vardavoulias, M., *A Microstructural Study of Cold Sprayed Cu Coatings on 2017 Al Alloy*, in *Thermal Spray: Global Coating Solutions*, E. Lugscheider, Editor 2008, ASM International: Maastricht, The Netherlands.
90. King, P.C., Zahiri, S.H., and Jahedi, M., *Focused Ion Beam Micro-Dissection of Cold-Sprayed Particles.* Acta Materialia, 2008. 56(19): p. 5617-5626.
91. Koivuluoto, H., Honkanen, M., and Vuoristo, P., *Cold-Sprayed Copper and Tantalum Coatings -- Detailed FESEM and TEM Analysis.* Surface and Coatings Technology, 2010. 204(15): p. 2353-2361.
92. Gärtner, F., Stoltenhoff, T., Voyer, J., Kreye, H., Riekehr, S., and Koçak, M., *Mechanical Properties of Cold-Sprayed and Thermally Sprayed Copper Coatings.* Surface and Coatings Technology, 2006. 200(24): p. 6770-6782.
93. Zhang, D., Shipway, P.H., and McCartney, D.G., *Cold Gas Dynamic Spraying of Aluminum: The Role of Substrate Characteristics in Deposit Formation.* Journal of Thermal Spray Technology, 2005. 14(1): p. 109-116.
94. Choi, W.B., Li, L., Luzin, V., Neiser, R., Gnaupel-Herold, T., Prask, H.J., Sampath, S., and Gouldstone, A., *Integrated Characterization of Cold Sprayed Aluminum Coatings.* Acta Materialia, 2007. 55(3): p. 857-866.
95. Irissou, E. and Arsenault, B., *Corrosion Study of Cold Sprayed Aluminium Coatings onto Al 7075 Alloy*, in *Thermal Spray: Global Coating Solutions*, B. R. Marple, M. M. Hyland, Y.-C. Lau, C.-J. Li, R. S. Lima, and G. Montavon, Editors. 2007, ASM International: Beijing, People's Republic of China. p. 549-554.
96. Hall, A., Yang, P., Brewer, L., Buchheit, T., and Roemer, T., *Preparation and Mechanical Properties of Cold Sprayed Nanocrystalline Aluminium*, in *Thermal Spray: Global Coating Solutions*, E. Lugscheider, Editor 2008, ASM International: Maastricht, The Netherlands.
97. King, P.C. and Jahedi, M., *Relationship between Particle Size and Deformation in the Cold Spray Process.* Applied Surface Science. 256(6): p. 1735-1738.
98. Rech, S., Trentin, A., Vezzu, S., Legoux, J.G., Irissou, E., and Guagliano, M., *Study of the Influence of Pre-Heated Al6061 Substrate Temperature on Al Coatings Deposited by Cold Spray*, in *Thermal spray: Global Solutions for Future Application*, B. R. Marple, A. Agarwal, M. M. Hyland, Y. -C. Lau,

C.-J. Li, R. S. Lima, and G. Montavon, Editors. 2010, ASM International: Singapore.
99. Calvo, F.A., Urena, A., Desalazar, J.M.G., and Molleda, F., *Special Features of the Formation of the Diffusion Bonded Joints between Copper and Aluminum.* Journal of Materials Science, 1988. 23(6): p. 2273-2280.
100. Funamizu, Y. and Watanabe, K., *Interdiffusion in Al-Cu System.* Transactions of the Japan Institute of Metals, 1971. 12(3): p. 147-&.
101. Manna, I. and Majumdar, J.D., *Enhanced Kinetics of Diffusion Coating of Aluminum on Copper by Boundary Diffusion.* Journal of Materials Science Letters, 1993. 12(12): p. 920-922.
102. Takahashi, Y., Nakamura, T., and Nishiguchi, K., *Dissolution Process of Surface Oxide Film During Diffusion Bonding of Metals.* Journal of Materials Science, 1992. 27(2): p. 485-498.
103. ASM, *ASM Handbook/ Alloy Phase Diagrams*. Metals Handbook. 1992: ASM International.
104. Xia, C.Q. and Jin, Z.P., *On the Evolution of Microstructure and Diffusion Paths in the Titanium-Steel Explosion Weld Interface During Heat-Treatment.* Journal of the Less-Common Metals, 1990. 162(2): p. 315-322.
105. Momono, T., Enjo, T., and Ikeuchi, K., *Effect of Carbon Content on the Diffusion Bonding of Iron and Steel to Titanium* Tetsu to Hagane-Journal of the Iron and Steel Institute of Japan, 1987. 73(11): p. 1590-1597.
106. Segall, A.E., Papyrin, A.N., Conway, J.C., and Shapiro, D. *A Cold-Gas Spray Coating Process for Enhancing Titanium*. in *TMS Annual Meeting*. 1998. San Antonio, Texas: Minerals Metals Materials Soc.
107. Sun, J.F., Han, Y., and Cui, K., *Innovative Fabrication of Porous Titanium Coating on Titanium by Cold Spraying and Vacuum Sintering.* Materials Letters, 2008. 62(21-22): p. 3623-3625.
108. Dosta, S., Cinca, N., Garcia, J., Salito, A., and Guilemany, J.M., *Cold Spray Perspectives in Medical Engineering*, in *8th Colloquium High Velocity Oxy-fuel Flame Spray*, Christian Penszior and Peter Heinrich, Editors. 2009, Gemeinschaft Thermisches Spritzen e.V. (Association of Thermal Sprayers): Erding near Munich. p. 151-156.
109. Li, W.Y., Zhang, C., Wang, H.T., Guo, X.P., Liao, H.L., Li, C.J., and Coddet, C., *Significant Influences of Metal Reactivity and Oxide Films at Particle Surfaces on Coating Microstructure in Cold Spraying.* Applied Surface Science, 2007. 253(7): p. 3557-3562.
110. Li, C.-J. and Li, W.-Y., *Deposition Characteristics of Titanium Coating in Cold Spraying.* Surface and Coatings Technology, 2003. 167(2-3): p. 278-283.
111. Wong, W., Rezaeian, A., Irissou, E., Legoux, J.-G., and Yue, S., *Cold Spray Characteristics of Commercially Pure Ti and Ti-6Al-4V.* Advanced Materials Research, 2010. 89-91: p. 639-644.
112. Wong, W., Rezaeian, A., Yue, S., and Legoux, J.G., *Effects of Gas Temperature, Gas Pressure and the Particle Characteristics on Cold Sprayed Pure Titanium Coatings*, in *Thermal Spray 2009: Expanding Thermal Spray Performance to New Markets and Applications*, B. R. Marple, M. M. Hyland, Y. -C. Lau, C. -J. Li, R. S. Lima, and G. Montavon, Editors. 2009, ASM International: Las Vegas, NV. p. 231-236.
113. Gulizia, S., Trentin, A., Vezzu, S., Rech, S., King, P., Jahedi, M., and Guagliano, M., *Microstucture and Mechanical Properties of Cold Spray Titanium Coatings*, in *Thermal spray: Global Solutions for Future Application*, B. R. Marple, A. Agarwal, M. M. Hyland, Y. -C. Lau, C.-J. Li, R. S. Lima, and G. Montavon, Editors. 2010, ASM International: Singapore.
114. Grenier, S., Brzezinski, T., Allaire, F., and Tsantrizos, P., *Vps Deposition of Spherical Ti-Based Powders Produced by Plasma Atomization* in *Thermal*

Spray: Meeting the Challenges of the 21st Century, C. Coddet, Editor 1998, ASM International: Nice, France. p. 1277-1282.
115. Yule, A.J. and Dunkley, J.J., *Atomization of Melts : For Powder Production and Spray Deposition* Oxford Series on Advanced Manufacturing ; 11. 1994: Oxford University Press.
116. Alagheband, A. and Brown, C., *Plasma Atomization Goes Commercial.* Metal Powder Report, 1998. 53(11): p. 26-28.
117. Blose, R.E., *Spray Forming Titanium Alloys Using the Cold Spray Process.*, in *Thermal spray: Exploring its surfacing potential*, E. Lugscheider, Editor 2005, ASM International: Basel, Switzerland.
118. Blose, R.E., Walker, B.H., Walker, R.M., and Froes, S.H., *New Opportunities to Use Cold Spray Process for Applying Additive Features to Titanium Alloys.* Metal Powder Report, 2006. 61(9): p. 30-37.
119. Blose, R.E., Walker, B.H., Walker, R.M., and Froes, S.H., *Depositing Titanium Alloy Additive Features to Forgings and Extrusions Using the Cold Spray Process*, in *Thermal Spray: Building on 100 Years of Success*, B. R. Marple, M. M. Hyland, Y. Lau, R. S. Lima, and J. Voyer, Editors. 2006, ASM International: Seattle, WA.
120. Razaeian, A., Chromik, R.R., Yue, S., Irissou, E., and Legoux, J.G., *Characterization of Cold-Sprayed Ni, Ti and Cu Coating Properties for Their Optimizations*, in *Thermal Spray: Global Coating Solutions*, E. Lugscheider, Editor 2008, ASM International: Maastricht, The Netherlands.
121. Chromik, R.R., Goldbaum, D., Shockley, J.M., Yue, S., Irissou, E., Legoux, J.-G., and Randall, N.X., *Modified Ball Bond Shear Test for Determination of Adhesion Strength of Cold Spray Splats.* Surface and Coatings Technology. In Press, Accepted Manuscript.
122. Zahiri, S.H., Jahedi, M., and Yang, W., *Particle Image Velocimetry of Cold Spray Cp Titanium*, in *Thermal Spray: Global Coating Solutions*, E. Lugscheider, Editor 2008, ASM International: Maastricht, The Netherlands.
123. Lima, R.S., Kucuk, A., Berndt, C.C., Karthikeyan, J., Kay, C.M., and Lindemann, J., *Deposition Efficiency, Mechanical Properties and Coating Roughness in Cold-Sprayed Titanium.* Journal of Materials Science Letters, 2002. 21(21): p. 1687-1689.
124. Zahiri, S.H., Yang, W., and Jahedi, M., *Characterization of Cold Spray Titanium Supersonic Jet.* Journal of Thermal Spray Technology, 2009. 18(1): p. 110-117.
125. Wang, H.-R., Hou, B.-R., Wang, J., Wang, Q., and Li, W.-Y., *Effect of Process Conditions on Microstructure and Corrosion Resistance of Cold-Sprayed Ti Coatings.* Journal of Thermal Spray Technology, 2008. 17(5): p. 736-741.
126. Li, W.Y., Zhang, C., Guo, X.P., Li, C.J., Liao, H.L., and Coddet, C., *Study on Impact Fusion at Particle Interfaces and Its Effect on Coating Microstructure in Cold Spraying.* Applied Surface Science, 2007. 254(2): p. 517-526.
127. Price, T., Shipway, P., and McCartney, D., *Effect of Cold Spray Deposition of a Titanium Coating on Fatigue Behavior of a Titanium Alloy.* Journal of Thermal Spray Technology, 2006. 15(4): p. 507-512.
128. Zahiri, S.H., Antonio, C.L., and Jahedi, M., *Elimination of Porosity in Directly Fabricated Titanium Via Cold Gas Dynamic Spraying.* Journal of Materials Processing Technology, 2009. 209(2): p. 922-929.
129. Zahiri, S.H., Mayo, S.C., and Jahedi, M., *Characterization of Cold Spray Titanium Deposits by X-Ray Microscopy and Microtomography.* Microscopy and Microanalysis, 2008. 14(3): p. 260-266.
130. Ilavsky, J., *Characterization of Complex Thermal Barrier Deposits Pore Microstructures by a Combination of Imaging, Scattering, and Intrusion Techniques.* Journal of Thermal Spray Technology, 2010. 19(1): p. 178-189.

131. Moy, C.K.S., Cairney, J., Ranzi, G., Jahedi, M., and Ringer, S.P., *Investigating the Microstructure and Composition of Cold Gas-Dynamic Spray (Cgds) Ti Powder Deposited on Al 6063 Substrate.* Surface and Coatings Technology, 2010. 204(23): p. 3739-3749.
132. Zahiri, S.H., Fraser, D., and Jahedi, M., *Recrystallization of Cold Spray-Fabricated CP Titanium Structures.* Journal of Thermal Spray Technology, 2009. 18(1): p. 16-22.
133. Li, W.Y., Zhang, C., Guo, X., Xu, J., Li, C.J., Liao, H., Coddet, C., and Khor, K.A., *Ti and Ti-6Al-4V Coatings by Cold Spraying and Microstructure Modification by Heat Treatment.* Advanced Engineering Materials, 2007. 9(5): p. 418-423.
134. Gulizia, S., Tiganis, B., Jahedi, M.Z., Wright, N., Gengenbach, T., and MacRae, C., *Effects of Cold Spray Process Gas Temperature on Cp Titanium Structure*, in *Thermal Spray 2009: Expanding Thermal Spray Performance to New Markets and Applications*, B. R. Marple, M. M. Hyland, Y. -C. Lau, C. -J. Li, R. S. Lima, and G. Montavon, Editors. 2009, ASM International: Las Vegas, NV. p. 237-242.
135. Watts, J.F. and Wolstenholme, J., *An Introduction to Surface Analysis by XPS and AES*. 2003: J. Wiley.
136. King, P.C. and Jahedi, M., *Transmission Electron Microscopy of Cold Sprayed Titanium*, in *Thermal spray: Global Solutions for Future Application*, B. R. Marple, A. Agarwal, M. M. Hyland, Y. -C. Lau, C.-J. Li, R. S. Lima, and G. Montavon, Editors. 2010, ASM International: Singapore. p. May 3- 5.
137. Rafaja, D., Schucknecht, T., Klemm, V., Paul, A., and Berek, H., *Microstructural Characterisation of Titanium Coatings Deposited Using Cold Gas Spraying on Al2O3 Substrates.* Surface and Coatings Technology, 2009. 203(20-21): p. 3206-3213.
138. Cullity, B.D. and Stock, S.R., *Elements of X-Ray Diffraction* 2001: Prentice Hall.
139. Bae, G., Kang, K., Kim, J.-J., and Lee, C., *Nanostructure Formation and Its Effects on the Mechanical Properties of Kinetic Sprayed Titanium Coating.* Materials Science and Engineering: A, 2010. In Press, Corrected Proof.
140. Binder, K., Gartner, F., and Klassen, T., *Ti-Parts for Aviation Industry Produced by Cold Spraying*, in *Thermal spray: Global Solutions for Future Application*, B. R. Marple, A. Agarwal, M. M. Hyland, Y. -C. Lau, C.-J. Li, R. S. Lima, and G. Montavon, Editors. 2010, ASM International: Singapore.
141. Jazi, H.R.S., Coyle, T.W., and Mostaghimi, J., *Understanding Grain Growth and Pore Elimination in Vacuum-Plasma-Sprayed Titanium Alloy.* Metallurgical and Materials Transactions A-Physical Metallurgy and Materials Science, 2007. 38A(3): p. 476-484.
142. Li, C.-j. and Li, W.-y., *Microstructure Evolution of Cold-Sprayed Coating During Deposition and through Post-Spraying Heat Treatment.* Transactions of Nonferrous Metals Society of China 2004. 14(2): p. 49-55.
143. Kim, K., Watanabe, M., Kawakita, J., and Kuroda, S., *Effects of Temperature of in-Flight Particles on Bonding and Microstructure in Warm-Sprayed Titanium Deposits.* Journal of Thermal Spray Technology, 2009.
144. Kim, K., Watanabe, M., Kawakita, J., and Kuroda, S., *Grain Refinement in a Single Titanium Powder Particle Impacted at High Velocity.* Scripta Materialia, 2008. 59(7): p. 768-771.
145. Kim, K., Watanabe, M., and Kuroda, S., *Bonding Mechanisms of Thermally Softened Metallic Powder Particles and Substrates Impacted at High Velocity.* Surface and Coatings Technology. 204(14): p. 2175-2180.
146. Kim, K., Watanabe, M., and Kuroda, S., *Thermal Softening Effect on the Deposition Efficiency and Microstructure of Warm Sprayed Metallic Powder.* Scripta Materialia, 2009. 60(8): p. 710-713.

147. Kim, K., Watanabe, M., and Kuroda, S., *Jetting-out Phenomenon Associated with Bonding of Warm-Sprayed Titanium Particles onto Steel Substrate.* Journal of Thermal Spray Technology, 2009. 18(4): p. 490-499.
148. Kim, K., Watanabe, M., Mitsuishi, K., Iakoubovskii, K., and Kuroda, S., *Impact Bonding and Rebounding between Kinetically Sprayed Titanium Particle and Steel Substrate Revealed by High-Resolution Electron Microscopy.* Journal of Physics D-Applied Physics, 2009. 42(6): p. 5.
149. Kawakita , J., Watanabe, M., and Kuroda, S., *Densification of Ti Coatings by Bi-Modal Size Distribution of Feedstock Powder During Warm Spraying*, in *Thermal Spray: Global Coating Solutions*, B. R. Marple, M. M. Hyland, Y.-C. Lau, C.-J. Li, R. S. Lima, and G. Montavon, Editors. 2007, ASM International: Beijing, People's Republic of China. p. 43-47.
150. Deng, C.M., Deng, C.G., Liu, M., Huang, J., Zhou, K.S., Chen, Z.K., Wank, A., and Schwenk, A., *Corrosion of Ti Coating Prepared by Modified HVOF Process*, in *Thermal spray: Global Solutions for Future Application*, B. R. Marple, A. Agarwal, M. M. Hyland, Y. -C. Lau, C.-J. Li, R. S. Lima, and G. Montavon, Editors. 2010, ASM International: Singapore.
151. Kawakita, J., Kuroda, S., Fukushima, T., Katanoda, H., Matsuo, K., and Fukanuma, H., *Dense Titanium Coatings by Modified HVOF Spraying.* Surface & Coatings Technology, 2006. 201(3-4): p. 1250-1255.
152. Callister, W.D., *Materials Science and Engineering : An Introduction* 2007: John Wiley & Sons.
153. Fontana, M.G., *Corrosion Engineering*. Mcgraw-Hill Series in Materials Science and Engineering. 1986: McGraw-Hill.
154. Stansbury, E.E. and Buchanan, R.A., *Fundamentals of Electrochemical Corrosion* 2000: ASM International.
155. Trethewey, K.R. and Chamberlain, J., *Corrosion : For Science and Engineering*. Corrosion : For Students of Science and Engineering. 1995: Longman.
156. Tait, W.S., *An Introduction to Electrochemical Corrosion Testing for Practicing Engineers & Scientists*. 1994: Pair O Docs Pubns.
157. Ahmed, N., Characterisation of Different Forms of Inconel 625 for Determining the Effects of Microstructural Modifications on Electrochemical Behaviour, University of Nottingham, 2008.
158. Schutz, R.W., *Corrosion of Titanium and Titanium Alloys*, in *ASM Handbook. Vol. 13b, Corrosion : Materials*, Charles Moosbrugger and Elizabeth Marquand, Editors. 2005, ASM: Materials Park, Ohio. p. 252-299.
159. Valente, T. and Galliano, F.P., *Corrosion Resistance Properties of Reactive Plasma-Sprayed Titanium Composite Coatings.* Surface & Coatings Technology, 2000. 127(1): p. 86-92.
160. Riskin, I.V., Torshin, V.B., Skuratnik, Y.B., and Dembrovsky, M.A., *Corrosion of Titanium by Cathodic Currents in Chloride Solutions.* Corrosion, 1984. 40(6): p. 266-271.
161. Hackerman, N. and Hall, J.C.D., *Electrochemical Polarization of Titanium in Aqueous Solutions of Sodium Chloride.* Journal of the Electrochemical Society, 1954. 101(6): p. 321-327.
162. Feige, N.G. and Murphy, T.J., *Environmental Effects on Titanium Alloys.* Corrosion, 1966. 22(11): p. 320-&.
163. Bomberger, H.B., Beck, F.H., and Fontana, M.G., *Polarization Studies of Copper, Nickel, Titanium, and Some Copper and Nickel Alloys in Three Per Cent Sodium Chloride.* Journal of the Electrochemical Society, 1955. 102(2): p. 53-58.
164. Ayers, J.D., Schaefer, R.J., Bogar, F.D., and McCafferty, E., *Corrosion Behavior of Laser Consolidated Titanium Coated Steel in Sea-Water.* Corrosion, 1981. 37(1): p. 55-57.

165. Bomberger, H.B., Cambourelis, P.J., and Hutchinson, G.E., *Corrosion Properties of Titanium in Marine Environments.* Journal of the Electrochemical Society, 1954. 101(9): p. 442-447.
166. Golden, L.B., Lane, I.R., Jr., and Acherman, W.L., *Corrosion Resistance of Titanium, Zirconium, and Stainless Steel Mineral Acids.* Industrial and Engineering Chemistry 1952. 44(8): p. 1930-1935.
167. Griess, J.C., Jr., *Crevice Corrosion of Titanium in Aqueous Salt Solutions.* Corrosion, 1968. 24(4): p. 96-109.
168. Mckay, P. and Mitton, D.B., *Electrochemical Investigation of Localized Corrosion on Titanium in Chloride Environments.* CORROSION, 1985. 41(1): p. 52-60.
169. Kinos, T., Chen, S.L., Siitonen, P., and Kettunen, P., *Corrosion Properties of Shrouded Plasma Sprayed Titanium Coatings*, in *Thermal Spraying: Current Status and Future Trends*, Akira Ohmori, Editor 1995, High Temperature Society of Japan: Kobe, Japan. p. 573-576.
170. Kinos, T., Chen, S., Siitonen, P., and Kettunen, P., *Densification of Plasma-Sprayed Titanium and Tantalum Coatings.* Journal of Thermal Spray Technology, 1996. 5(4): p. 439-444.
171. Steffens, H.D., Erturk, E., and Busse, K.H., *A Comparison of Low-Pressure Arc and Low-Pressure Plasma Sprayed Titanium Coatings.* Journal of Vacuum Science & Technology A-Vacuum Surfaces and Films, 1985. 3(6): p. 2459-2463.
172. Steffens, H.D., Wilden, J., and Buchmann, C., *Laser Beam Nitriding of Thermally Sprayed Titanium Coatings*, in *Thermal Spraying: Current Status and Future Trends*, Akira Ohmori, Editor 1995, High Temperature Society of Japan: Kobe, Japan. p. 981- 986.
173. Ishikawa, K., Suzuki, T., Kitamura, Y., and Tobe, S., *Corrosion Resistance of Thermal Sprayed Titanium Coatings in Chloride Solution.* Journal of Thermal Spray Technology, 1999. 8(2): p. 273-278.
174. Zhao, W.-m., Liu, C., Dong, L.-x., and Wang, Y., *Effects of Arc Spray Process Parameters on Corrosion Resistance of Ti Coatings.* Journal of Thermal Spray Technology, 2009. 18(4): p. 702-707.
175. Kawakita, J., Katanoda, H., Watanabe, M., Yokoyama, K., and Kuroda, S., *Warm Spraying: An Improved Spray Process to Deposit Novel Coatings.* Surface and Coatings Technology, 2008. 202(18): p. 4369-4373.
176. Kawakita, J., Fukushima, T., Kuroda, S., and Kodama, T., *Corrosion Behaviour of HVOFf Sprayed Sus316l Stainless Steel in Seawater.* Corrosion Science, 2002. 44(11): p. 2561-2581.
177. Wang, H.-R., Li, W.-Y., Ma, L., Wang, J., and Wang, Q., *Corrosion Behavior of Cold Sprayed Titanium Protective Coating on 1cr13 Substrate in Seawater.* Surface and Coatings Technology, 2007. 201(9-11): p. 5203-5206.
178. Steen, W.M., *Laser Material Processing* 2003: Springer.
179. Ion, J.C., *Laser Processing of Engineering Materials : Principles, Procedure and Industrial Application* 2005: Elsevier Butterworth-Heinemann.
180. Calla, E., Cold Gas Spraying of Copper and Tin onto Metallic and Non Metallic Substrates, PhD Thesis, University of Nottingham, 2005.
181. Leigh, S. and Berndt, C., *A Test for Coating Adhesion on Flat Substrates—a Technical Note.* Journal of Thermal Spray Technology, 1994. 3(2): p. 184-190.
182. Schmidt, T., Gartner, F., and Kreye, H. *Tubular Coating Tensile Test (Tct)*. 2010 [cited 2010 August 25]; Available from: http://www.hsu-hh.de/werkstoffkunde/index_X2D7URlyQyLhkjJJ.html.
183. Li, W.Y., Zhang, C., Guo, X.P., Xu, J.L., Li, C.J., Liao, H.L., Cocidet, C., and Khor, K.A., *Ti and Ti-6Al-4V Coatings by Cold Spraying and Microstructure Modification by Heat Treatment.* Advanced Engineering Materials, 2007. 9(5): p. 418-423.

184. Bray, M., Cockburn, A., and O'Neill, W., *The Laser-Assisted Cold Spray Process and Deposit Characterisation.* Surface and Coatings Technology, 2009. 203(19): p. 2851-2857.
185. Dykhuizen, R.C. and Neiser, R.A., *Optimizing the Cold Spray Process*, in *Thermal Spray: Advancing the science and Applying the technology*, B.R. Marple and C. Moreau, Editors. 2003, ASM International: Orlando, Florida, USA. p. 19-26.
186. Hussain, T., McCartney, D.G., Shipway, P.H., and Zhang, D., *Bonding Mechanisms in Cold Spraying: The Contributions of Metallurgical and Mechanical Components.* Journal of Thermal Spray Technology, 2009. 18(3): p. 364-379.
187. International, ASM, *ASM Handbook Vol. 3: Alloy Phase Diagrams*. Metals Handbook. 1992: ASM International.
188. Itabashi, M. and Kawata, K., *Carbon Content Effect on High-Strain-Rate Tensile Properties for Carbon Steels.* International Journal of Impact Engineering, 2000. 24(2): p. 117-131.
189. Hutchings, I.M., *Strain Rate Effects in Microparticle Impact.* Journal of Physics D: Applied Physics, 1977. 10(14): p. L179.
190. Shaw, M.C., *Metal Cutting Principles*. Oxford Series on Advanced Manufacturing. 1984: Clarendon.
191. Yang, Y., Xinming, Z., Zhenghua, L., and Qingyun, L., *Adiabatic Shear Band on the Titanium Side in the Ti/Mild Steel Explosive Cladding Interface.* Acta Materialia, 1996. 44(2): p. 561-565.
192. Xue, Q., Nesterenko, V.F., and Meyers, M.A., *Evaluation of the Collapsing Thick-Walled Cylinder Technique for Shear-Band Spacing.* International Journal of Impact Engineering, 2003. 28(3): p. 257-280.
193. Textor, M., Sitting, C., Frauchiger, V., Tosatti, S., and Brunette, D.M., *Properties and Biological Significance of Natural Oxide Films on Titanium and Its Alloy*, in *Titanium in Medicine : Material Science, Surface Science, Engineering, Biological Responses, and Medical Applications*, D. M. Brunette, P. Tengvall, M. Textor, and P. Thomsen, Editors. 2001, Springer. p. 171-230.
194. Fursey, A., *Oxide Films on Mild Steel.* Nature, 1965. 207(4998): p. 747-748.
195. Suzuki, S. and Suzuki, K., *AES/GDS Characterization of Thin Oxide-Films on Fe-Cr Sheet Steels.* Surface and Interface Analysis, 1991. 17(8): p. 551-555.
196. Birks, N. and Meier, G.H., *Introduction to High Temperature Oxidation of Metals*. 1983: Edward Arnold.
197. Kim, K., Watanabe, M., and Kuroda, S., *Bonding Mechanisms of Thermally Softened Metallic Powder Particles and Substrates Impacted at High Velocity.* Surface and Coatings Technology, 2010. 204(14): p. 2175-2180.
198. Aleman, B., Gutierrez, I., and Urcola, J.J., *Interface Microstructures in-Diffusion Bonding of Titanium-Alloys to Stainless and Low-Alloy Steels.* Materials Science and Technology, 1993. 9(8): p. 633-641.
199. Wong, W., Rezaeiann, A., Irissou, E., Legoux, J.G., and Yue, S., *Cold Spray Characteristics of Commercially Pure Ti and Ti-6Al-4V.* Advanced Materials Research, 2010. 89-91: p. 639-644.
200. Lampman, S., *Wrought Titanium and Titanium Alloys*, in *Metals Handbook / Properties and Selection: Nonferrous Alloys and Special-Purpose Materials*, ASM International Handbook Committee, Editor. 1990, American Society for Metals International: Ohio. p. 592- 633.
201. Koivuluoto, H., Honkanen, M., and Vuoristo, P., *Cold-Sprayed Copper and Tantalum Coatings -- Detailed FESEM and TEM Analysis.* Surface and Coatings Technology. 204(15): p. 2353-2361.
202. Li, C.J. and Li, W.Y., *Microstructure Evolution of Cold-Sprayed Coating During Deposition and through Post-Spraying Heat Treatment.*

Transactions of Nonferrous Metals Society of China (English Edition), 2004. 14(SUPPL. 2): p. 49-54.
203. Kapoor, R. and Nemat-Nasser, S., *Determination of Temperature Rise During High Strain Rate Deformation.* Mechanics of Materials, 1998. 27(1): p. 1-12.
204. Brooks, C.R. and Choudhury, A., *Failure Analysis of Engineering Materials* 2002: McGraw-Hill.
205. Waldner, P., *Modelling of Oxygen Solubility in Titanium.* Scripta Materialia, 1999. 40(8): p. 969-974.
206. Danielson, P., Wilson, R., and Alman, D., *Microstructure of Titanium Welds.* Advanced Materials & Processes, 2003. 161(2): p. 39-42.
207. Chidambaram, D., Clayton, C.R., and Dorfman, M.R., *Evaluation of the Electrochemical Behavior of HVOF-Sprayed Alloy Coatings--Ii.* Surface and Coatings Technology, 2005. 192(2-3): p. 278-283.
208. Bolelli, G., Lusvarghi, L., and Barletta, M., *Heat Treatment Effects on the Corrosion Resistance of Some HVOF-Sprayed Metal Alloy Coatings.* Surface and Coatings Technology, 2008. 202(19): p. 4839-4847.
209. Siitonen, P., Chen, S.L., Niemi, K., and Vuoristo, P., *Electrochemical Method for Evaluating the Corrosion Resistance and Porosity of Thermal Sprayed Coatings*, in *Thermal Spray: International Advances in Coatings Technology*, C.C. Berndt, Editor 1992, ASM International: Orlando, FL. p. 853–858.
210. Hofman, R., Vreijling, M.P.W., Ferrari, G.M., and de Wit, J.H.W., *Electrochemical Methods for Characterisation of Thermal Spray Corrosion Resistant Stainless Steel Coatings*, in *Electrochemical Methods in Corrosion Research Vi, Pts 1 and 2*, P. L. Bonora and F. Deflorian, Editors. 1998, Trans Tech Publications Ltd: Zurich-Uetikon. p. 641-653.
211. Ahmed, N., Bakare, M.S., McCartney, D.G., and Voisey, K.T., *The Effects of Microstructural Features on the Performance Gap in Corrosion Resistance between Bulk and HVOF Sprayed Inconel 625.* Surface and Coatings Technology, 2010. 204(14): p. 2294-2301.
212. Kawakita, J., Kuroda, S., Fukushima, T., and Kodama, T., *Development of Dense Corrosion Resistant Coatings by an Improved HVOF Spraying Process.* Science and Technology of Advanced Materials, 2003. 4(4): p. 281-289.

9 Appendix

9.1 Deposition efficiency measurement

Deposition efficiency of the cold sprayed titanium coatings onto different steel and titanium alloy substrates were measured by weighing the substrates before and after spraying using a digital scale. To measure powder feed rate (PFR), the powder feed line was disconnected from the spraying gun and attached to a plastic collection bag. This method assumes that the powder feed rate is not affected by the back pressure generated by the nozzle. The sealed plastic bag collected powder for two minutes and dividing the weight of the collected powder by time, powder feed rate was calculated. Deposition efficiency of titanium onto different substrates was determined using the following formula:

Deposition efficiency = Weight of the powder adhering to the substrate/ Weight of the powder striking the substrate in a given time

The samples were mounted on the rotation table and the gun scanned the surface of the substrates in vertical direction. A sample deposition efficiency calculation onto carbon steel substrate is shown here. The following variables are known

Dimension of the substrate= 43 mm × 26 mm

Traverse speed of the gun = 0.44 mm/s

RPM of the rotating table = 35 rev /min = 0.5833 rev /s

Total number of scans of the gun = 4

Measured weight of the deposit at the end of the spray= 2.68 g

Measured weight of the powder sprayed in 2 minutes =36.21 g

∴ Powder feed rate (PFR) = 0.3018 g/s

Now,

Time taken for 1 pass = length of the substrate/ traverse speed of the gun

= 43/0.44

= 97.7272 s

Amount of powder sprayed in that time = 97.7272 * PFR

= 97.7272*0.3018

= 29.4974 g

Circumferential velocity of the table = RPM*π*diameter of the table/ 60

= 35*π*360 / 60

= 659.7345 mm/s

Number of times the substrate passes the gun = time taken for 1 pass * RPS

= 97.7272 * 0.5833

= 57.0076

Each time the substrate passes the gun, the substrate is exposed to powder for

= width of the substrate / circumferential velocity

= 26 / 659.7345

= 0.0394 s

Total exposure to powder = no of times the substrate passes the gun * time

= 57.0076 * 0.0394

= 2.2467 s

On each pass, amount of powder impacting the substrate

= PFR * total exposure to powder

= 0.3018 * 2.2467

= 0.6781 g

Total powder impacting the substrate in 4 scans = 4 * 0.6781 g = 2.7125 g

Deposition efficiency = Weight of the powder adhering to the substrate/ weight of the powder striking the substrate

= 2.68/2.7125

= 98.80 %

Deposition efficiency of the titanium coating sprayed onto in-situ grit blasted carbon steel, in-situ grit blasted stainless steel and as-machined titanium alloy (Ti6Al4V) are shown in Table 9-1. It can be seen that the deposition efficiency of all the substrates sprayed at 800 °C process gas temperature was 98.8 - 100 %, which means virtually all the powder impacting the substrate during the spray resulted in adhesion and build up of coating. Moreover, the deposition efficiency on steel substrate was around a percent lower than titanium alloy substrates but this is not a significant difference provided the nature of measuring deposition efficiencies.

Substrate	PFR, g/min	Gun speed, mm/s	Length, mm	Width, mm	Turn-table RPM,/ s	Turn-table Dia, mm	No of passes	Total impacted wt, g	Total deposited wt, g	DE %
Carbon Steel	18.11	0.44	43	26	35	360	4	2.71	2.68	98.8
Stainless Steel	18.11	0.44	42	25	35	360	4	2.55	2.53	99.3
Ti6Al4V	18.11	0.44	40	25	35	360	2	1.21	1.21	100

Table 9-1 Deposition efficiency measurement of titanium coatings sprayed at 800°C process gas temperatures onto in-situ grit blasted carbon steel, stainless steel and Ti6Al4V substrates

9.2 Substrate temperature measurement

The temperature of the substrates was measured using temperature sensitive adhesive tapes (Thermax, TMC Hallcrest Ltd, Flintshire, UK) attached to the back of the samples during spraying. Temperature sensitive tapes are divided into different temperature ranges and when the surface of the sample reaches a certain temperature, the corresponding colour in the tape changes. The colour change of the tapes is irreversible; thus, the temperature sensitive tapes can measure the maximum temperature reached on that substrate surface.

Substrates	Temperature (°C)
Carbon steel	121
Stainless steel	132- 138
Ti6Al4V	177- 182

Table 9-2 Temperatures measured at the back of the carbon steel, stainless steel and Ti6Al4V substrates during spraying of titanium at 800°C process gas temperature

Table 9-2 shows the temperature of the substrates measured using temperature sensitive tapes at the back of the 2 mm thick substrates. It can be seen that the temperature of the Ti6Al4V substrate was raised to ~180 °C and that of carbon steel was raised to 121 °C when sprayed using a gas temperature of 800 °C. It should be noted that the thermal conductivity of carbon steel is 42.7 W/m K, stainless steel (304) is 16.2 W/m K and Ti6Al4V is 6.6 W/m K. The heat generated from the impact of a hot gas stream and deposition of coating is lost to the surrounding through convection and conduction through the sample holder assembly. Due to this very low thermal conductivity of Ti6Al4V alloy the temperature is raised higher during the spraying process, whilst the higher thermal conductivity of carbon steel dissipated the heat better, thus resulting in a lower average temperature.

9.3 Williamson-Hall analysis

The peak broadening in X-ray diffraction analysis can be attributed to instrumental broadening, microstrain and sub-micron coherent diffracting cell sizes. Equipment broadening can be measured by scanning a well annealed sample with large grain size. Following correction of equipment broadening, the rest of the broadening can be attributed to microstrain and fine grain/ sub-grain size. Table 9-3 shows the full width at half maximum (FWHM) values of the powder, 600 & 800°C as-sprayed deposits and vacuum heat treated (at 1050°C for 60 minutes) deposits. X-ray diffraction analysis was performed with Cu Kα radiation with a step size of 0.05° and a dwell time of 5s per step.

Peak position (maximum) 2θ (°)	Powder FWHM, 2θ(°)	As-sprayed 600°C deposit FWHM, 2θ(°)	Heat treated 600°C deposit FWHM, 2θ(°)	As-sprayed 800°C deposit FWHM, 2θ(°)	Heat treated 800°C deposit FWHM, 2θ(°)
35.094	0.229	0.306	0.163	0.336	0.146
38.422	0.205	0.275	0.153	0.275	0.163
40.171	0.227	0.279	0.173	0.349	0.149
53.005	0.222	0.318	0.178	0.416	0.16
62.951	0.277	0.401	0.154	0.504	0.152
70.663	0.284	0.519	0.211	0.503	0.191
74.16	0.394	0.307	0.181	0.432	0.162
76.221	0.321	0.489	0.185	0.552	0.168

Table 9-3 FWHM values of titanium powder, as-sprayed and heat treated 600 and 800°C deposits

Equation 9.1 shows the relationship of measured broadening with instrumental broadening

$$B = \sqrt{B_M^2 - B_I^2} \quad \text{equation 9.1}$$

where, B_M is measured 2θ FWHM, B_I is instrumental 2θ FWHM and B is the corrected 2θ FWHM. The instrumental broadening B_I was taken as the average of the two heat treated deposits i.e., strain free and large grain size. The corrected peak broadening values can be separated into two components: the effect of size and micro strain of crystals by using a Williamson- Hall plot [138].

$$B\cos\theta = \frac{0.9\,\lambda}{t} + m \cdot \sin\theta \quad \text{equation 9.2}$$

where, t is the crystallite size and λ is the wavelength. The wavelength of the X-ray used in the experiment was 0.15406 nm for Cu Kα radiation. In a Williamson-Hall plot, B (cos θ) / λ is plotted against sin θ / λ. The intercept of the Williamson-Hall plot is related to the crystallite size and written as follows

$$B (\cos\theta) / \lambda = 0.9 / t \quad \text{equation 9.3}$$

The slope, m, of the Williamson- Hall plot has the following relationship with strain

$$m = 2 (\Delta d/d) \quad \text{equation 9.4}$$

This equation allows the strain, Δd/d, to be calculated from the observed broadening.

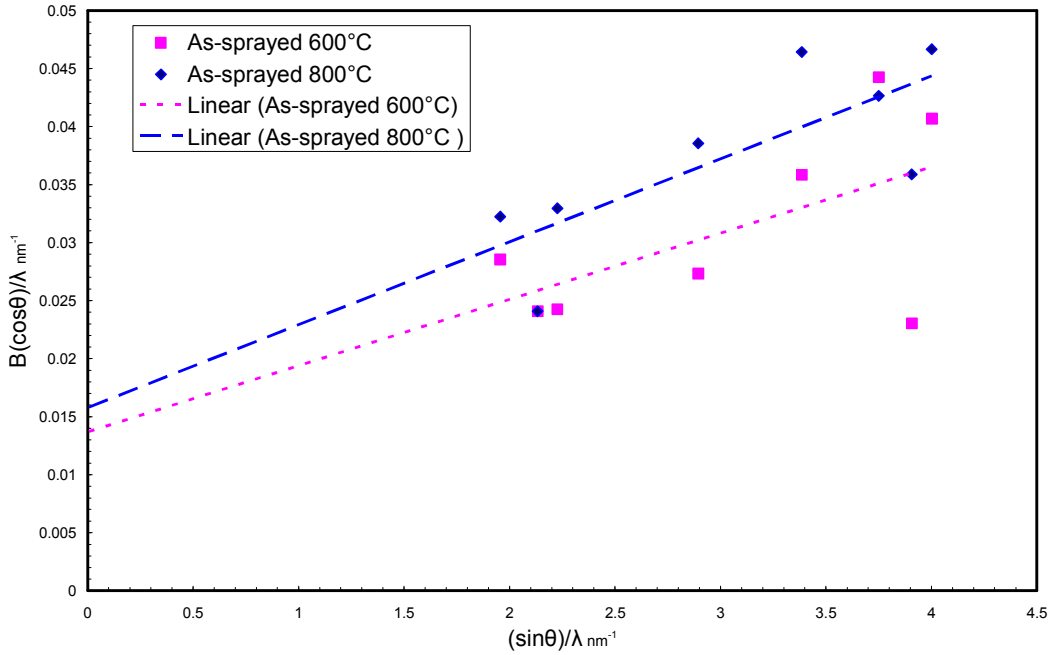

Figure 9-1 Williamson- Hall plot for as-sprayed 600 & 800°C titanium deposits.

If the size broadening was the only significant contribution to the peak width then B cosθ is constant for all the peaks- the plot is a horizontal line. If strain broadening is the important contribution then B cosθ is a linear function of sinθ [138]. Figure 9-1 shows the Williamson- Hall plot for as-sprayed 600 and 800 °C deposits.

Samples	Regression coefficients (R^2)	Crystallite size (nm)	Strain (ε)
As-sprayed 600 °C deposit	0.35	65	2.9×10^{-3}
As-sprayed 800 °C deposit	0.60	57	3.6×10^{-3}

Table 9-4 Grain size and microstrain determination of as-sprayed deposits using Williamson-Hall plots

Table 9-4 shows the crystallite size and microstrain of the as-sprayed 600 and 800 °C deposits calculated from the intercept and slope of the Williamson- Hall plot in Figure 9-1 using equations 9.2 & 9.3. A small increase in strain of the as-sprayed 800 °C coating is noticed which might be due to a greater particle deformation evidenced in the microstructural investigations. Furthermore, a recent study by Moy et al. [131] also reported a microstrain of 4.5×10^{-3} in cold sprayed titanium deposits prepared from angular powders, which was measured using X-ray diffraction of peak broadening and is in good agreement with the present analysis.